Search for Supersymmetry using a Higgs boson in the decay cascade with the ATLAS detector at the Large Hadron Collider

by

Claire David
M.Eng., Institut National des Sciences Appliquées de Toulouse, France, 2010

A Dissertation Submitted in Partial Fulfillment of the
Requirements for the Degree of

DOCTOR OF PHILOSOPHY

in the Department of Physics and Astronomy

Search for Supersymmetry using a Higgs boson in the decay cascade with the ATLAS detector at the Large Hadron Collider

by

Claire David
M.Eng., Institut National des Sciences Appliquées de Toulouse, France, 2010

Supervisory Committee

Dr. R. McPherson, Co-supervisor
(Department of Physics and Astronomy)

Dr. M. Lefebvre, Co-supervisor
(Department of Physics and Astronomy)

Dr. A. Ritz, Departmental Member
(Department of Physics and Astronomy)

Dr. I. Putnam, Outside Member
(Department of Mathematics and Statistics)

Supervisory Committee

Dr. R. McPherson, Co-supervisor
(Department of Physics and Astronomy)

Dr. M. Lefebvre, Co-supervisor
(Department of Physics and Astronomy)

Dr. A. Ritz, Departmental Member
(Department of Physics and Astronomy)

Dr. I. Putnam, Outside Member
(Department of Mathematics and Statistics)

ABSTRACT

The Standard Model of particle physics is a successful theory, yet it is incomplete. Supersymmetry is one of the favoured extensions of the Standard Model, elegantly addressing several unresolved issues. This thesis presents a search for the pair production of supersymmetric particles $pp \to \tilde{\chi}_1^{\pm}\tilde{\chi}_2^0$, where the neutralino two $\tilde{\chi}_2^0$ decays to the lightest neutralino and the 125 GeV Higgs boson. The final states considered for the search have large missing transverse momentum, an isolated lepton and two jets identified as originating from bottom quarks ($h \to b\bar{b}$ channel). The analysis is based on 20.3 fb^{-1} of $\sqrt{s} = 8$ TeV proton–proton collision data delivered by the Large Hadron Collider and recorded with the ATLAS detector. No excess over Standard Model predictions is observed. The analysis has been combined with three independent searches that probe other decay modes of the Standard Model Higgs boson. Limits are set at 95% confidence level in the context of a simplified supersymmetric model. Common masses of $\tilde{\chi}_1^{\pm}$ and $\tilde{\chi}_2^0$ are excluded up to 250 GeV for $m(\tilde{\chi}_1^0) = 0$. The analysis of this dissertation ($h \to b\bar{b}$ channel) has been reinterpreted in the context of a large scan of the phenomenological Minimal Supersymmetric Standard Model, along with 22 other ATLAS Run 1 searches. The resulting summary paper represents the most comprehensive assessment of the ATLAS constraints on Supersymmetry models to date.

I dedicate this thesis to all curious Earthlings willing to understand about the Universe and nurture their thirst for knowledge. It has become more and more precious on this fragile marble. To those pursuing an academic career in the field, receive my encouragements. I wish you joy, tenacity and marvel;
the journey is worth it.

Acknowledgements

This Ph.D. adventure has been much more than fulfilling a dream. I have always wanted to work on one of the giant detectors at the Large Hadron Collider. It was a privilege to join the ATLAS Collaboration at such an exciting time! This enriching journey would not have been possible without the precious input of numerous people.

First and foremost, I would like to send my biggest acknowledgements to my supervisors Robert McPherson and Michel Lefebvre. It has been a chance to learn from two extremely knowledgeable scientists. They provided all the guidance and reassurance I needed, the freedom in my research projects and excellent working conditions. I am grateful for their understanding and flexibility regarding my location and travels. It was very inspiring to see how Rob could spot right away where things went wrong. I enjoyed our enriching discussions on Supersymmetry, the LHC complex, the ATLAS machine... and how mean raccoons can be. Despite an incredibly busy schedule, Rob still found time for me and even flew from Geneva to attend my defense in person! Michel Lefebvre is a teaching star at UVic. As an advisor, he is fun to work with. I highly appreciate his frankness and fatherly dedication, enabling understanding. He picks up all the exciting subtleties in physics with an incredible sense of wonder. I learned so much. His endless enthusiasm makes all his explanations captivating.

I would like to thank Isabel for considering, back in 2010, my application[1] and for her kind support. Thanks to Dave for his infallible good mood, his wise advise and witty statements.

I am indebted to the members of the SUSY $1\ell bb$ analysis group. The ATLAS learning curve is less daunting within a team and I could learn a lot while contributing. Thanks in particular to Andrée for her cheerfulness that made the stress vanish, to Bart for his debugging help, to Matthew for saving me countless hours with HistFitter and to Michael for his expertise in b-tagging and the many discussions that punctuated tough times with entertaining derision. The level of dedication from Anadi and Zoltan is impressive and I am grateful for their guidance. I am indebted to Brian Petersen, who gave me all the keys to contribute to the pMSSM summary paper and it was enriching to work under his leadership for such a successful publication.

Brilliants scientists at CERN offered precious help: I express my gratitude to Caterina, Dag and Zach. Thanks to Quentin for the "strategy tips" and Kate for her amazing cheer-up.

---

[1] A five month internship to complete my engineering studies... I ended up staying much longer!

The UVic secretaries made all the bureaucratic work so smooth that I wonder what can shake their constant friendliness. I always felt so welcome in Victoria that I almost forgot I was an off-campus student. Thanks to Frank “The Legend” for everything, Kayla for her useful report, Matthias for his theoretico-philosophical input, and Tony and Alison for the superb defense prep!

TRIUMF is an awesome lab. I will miss the joyful atmosphere in the ATLAS Data Analysis Centre. Thanks to my office mates Ewan, Félix, Matt & Matt, Matthieu, Sébastien, Simon, Stephens. It was fun to hunt for free food, support each others and get excited about geeky things together.

Sara Ellison deserves to be mentioned here for being a role model and for contaminating me with the race bug. I never thought I would do a triathlon so early! The TRIUMF Running Club kept me sane thanks to the regular workouts in the beautiful Vancouver forests. Thanks to Robert Watt for making us all improve with his serene but efficient coaching.

Alex and André were awesome flatmates; their treats and encouragements count among my best memories of my stay in Canada. I send warm thanks to my supporting friends spread all around the world: Andri, Babak, Bahar, Draco, Maryam, Loïc, Lotfi, Mélodie, Minna, Paul, Pratik, Sarah, Tarzan and ToToM.

Mes parents ont tout fait pour que je puisse étudier dans les meilleures conditions. Je les remercie du fond du cœur pour toutes les activités qu’ils m’ont offertes et qui ont construit ma personnalité, en particulier les colonies scientifiques. Ces camps d’été furent déclencheurs. Je remercie ma mère pour m’avoir appris la rigueur et le goût du travail bien fait. La fascination de mon père — mon geek préféré — pour les objets techniques et ses nombreuses explications, que ce soit sur un mini moteur électrique ou près d’un télésiège débrayable, ont innocemment modelé la scientifique que je suis devenue.

Gabriel: thank you for your reassuring calmness, your healthy meals and your pragmatic encouragements. You never doubted my success and you kept my life surprisingly balanced during tough times. Thank you for reminding me everyday that the world is a complicated place and that knowledge is key to improving it. We survived the distance, many stressful moments and I foresee in the future a lot of adventures together, challenging ourselves, learning more and more about everything, racing faster, helping others. *Gracias a ti y a tu familia que se ríen de todo en un ambiente de alegría: algo que quiero reproducir en mi familia, contigo.*

"Seul l'inconnu épouvante les hommes.
Mais, pour quiconque l'affronte,
il n'est déjà plus l'inconnu."

Antoine de Saint-Exupéry, *Terre des Hommes*, 1939

Contents

List of Tables

List of Figures

Chapter 1

Introduction

Particle physics is all about the basics: how do the elementary constituents of matter interact with each other? The discipline has lately gained popularity with the construction of the most complex machine on Earth: the Large Hadron Collider. In a giant circular tunnel, protons are slammed together at record energies in order to create, in the laboratory, new particles.

The current theoretical achievement of this field, the Standard Model, brilliantly describes three fundamental forces. Some of its predictions and measurements reach unequalled precision. Yet important issues remain.

On July 4th 2012, the LHC validated the first success of its research program: the multipurpose detectors ATLAS and CMS reported the discovery of the Standard Model missing piece, the Higgs boson. An entire field of science was hinged on this event, directly witnessed at CERN by the author of this dissertation. More than the end of a successful quest, the celebration was about the start of a new area.

LHC data shall provide answers to the many speculations about the presence of physics beyond the Standard Model. The favoured theory to be probed, Supersymmetry, postulates the existence of superpartners for each existing particle. What started as a generalization in the theoretical formalism in particle physics can eventually address, if experimentally confirmed, many of the current Standard Model shortcomings, providing even a candidate for dark matter.

This thesis presents a search for supersymmetric particles using proton–proton collision data delivered by the LHC in 2012, as part of the Run 1 period, and recorded with the ATLAS detector. The considered events contain as final states one lepton, two hadronic jets coming from a bottom-antibottom quark pair $b\bar{b}$ and missing transverse momentum. For the first time at the LHC, the presence of a SM-like Higgs boson in a supersymmetric decay chain, and its resonance in the $h \rightarrow b\bar{b}$ channel, are exploited. This scenario would thus probe the Higgs boson couplings with both the predicted superpartners and Standard Model fermions.

This dissertation starts with a brief review of the theoretical foundations in Chapter 2. The ATLAS detector is presented in Chapter 3 and the reconstruction of objects is detailed in Chapter 4. The motivations, event selection and optimization of the search are articulated in Chapter 5. The following chapter summarizes studies to improve the sensitivity. The systematic uncertainties and their derivation methods are listed in Chapter 7, while the statistical tools and final results are the object of Chapter 8. The final Chapter 9 presents the reinterpretation of the analysis as part of a summary work assessing the ATLAS constraints on Supersymmetry after the LHC Run 1.

Chapter 2

Beyond the Standard Model: Supersymmetry

The experimental work presented in this dissertation challenges a very successful theoretical model. The Standard Model (SM) of particle physics is the most accurate and precise theory describing non-gravitational interactions. Its development started in the 60s through a series of theoretical breakthroughs and experimental discoveries. Although a chronological description would be interesting, only the final formulation of the SM will be described here for conciseness. Despite its successes, this current model is not a complete theory of fundamental interactions and leaves some phenomena unexplained. Most of these open questions are elegantly addressed by Supersymmetry (SUSY), a candidate theory extending the current Standard Model. Of interest in this dissertation is the phenomenological Minimum Supersymmetric Standard Model (pMSSM), presented at the end of this chapter.

2.1 The Standard Model

The Standard Model of particle physics [1–3] describes the interactions between particles of matter (fermions) through the exchange of “force-carriers” (bosons). The important achievements of twentieth-century physics, such as quantum mechanics and special relativity, are encapsulated into a single theoretical framework where the notion of symmetry plays a key role. The SM successfully models three fundamental forces in nature: the strong force, the weak interaction and electromagnetism.

Table 2.1: Elementary fermions – fundamental particles of spin 1/2 – of the Standard Model, organized in three successively heavier generations (rows) and different type (columns): quarks and leptons. The numbers below the names give an approximation of their masses, indicated in eV. The values reported for neutrino masses correspond to limits on the sum of neutrino masses as presented in Reference [4].

	Quarks		Leptons	
Charge [e]	+2/3	-1/3	-1	0
First generation	Up u 2.3 MeV	Down d 4.8 MeV	Electron e 0.51 MeV	Electron neutrino ν_e < 2.3 eV
Second generation	Charm c 1.3 GeV	Strange s 95 MeV	Muon μ 106 MeV	Muon neutrino ν_μ < 0.19 MeV
Third generation	Top t 173 GeV	Bottom b 4.7 GeV	Tau τ 1.8 GeV	Tau neutrino ν_τ < 18.2 MeV

2.1.1 Particle content

Particles with a spin in half-integer units of the reduced Planck constant $\hbar$ are fermions. The SM counts 12 elementary fermions of matter, divided into quarks and leptons, all arranged in three successively heavier generations. Each generation contains a lepton with -1 of electrical charge,[1] an uncharged lepton called neutrino, a quark with a charge of +2/3 and another with $-1/3$. Table 2.1 shows the organization of fermions in each generation, with their approximate masses in electrovolts.[2] These fermions compose matter. Each of them has an identical "twin" of equal mass but with opposite sign for each additive quantum number: these are the 12 anti-fermions forming anti-matter.

Particles with integer spin are bosons. Some are massless, like the gluons and the photon, whereas some are massive, which is the case for the W^+, W^-, Z bosons and the Higgs boson H. Their electrical charge and mass are displayed in Table 2.2, along with the fermions and bosons they interact with.

These particles – of several types, different charge and properties – have specific rules while interacting with each other. To understand how these interactions are

---

[1] Electrical charge is expressed in units of the fundamental charge $e = 1.602 \times 10^{-19}$ C.

[2] Natural units where $c = \hbar = 1$ are used in this thesis. Energy, masses and momenta are expressed in powers of electrovolts (eV): 1 eV corresponds to the kinetic energy of an electron accelerated through a potential difference of one volt.

Table 2.2: Elementary bosons – fundamental particles of integer spin – of the Standard Model, listed according to their electrical charge and arranged in increasing masses, indicated in GeV [4]. The particles these bosons interact with are specific to the fundamental force in question (these interactions will be presented later).

Name	Gluon	Photon γ	$W^{\pm}$	Z	H
Spin	1	1	1	1	0
Mass [GeV]	0	0	80	91	125
Force or mechanism	Strong interaction	Electro-magnetism	Weak interaction		Mass generation
Interacts with	quarks + itself	all charged particles	all particles except gluons		massive particles

described, it is important to introduce the formalism first.

2.1.2 Theoretical construction: the key notion of symmetry

The Standard Model is written in the mathematical language of quantum field theory (QFT), which is consistent with both quantum mechanics and special relativity. In this paradigm, space is filled with fields, whose quanta of excitations represent elementary particles. To each fermion (boson) listed above is associated a quantized fermionic (bosonic) field.

All the dynamics and kinematics are summarized in a Lagrangian density $\mathcal{L}$. The methodology followed to build particle physics theories is to write the most general Lagrangian that satisfies several requirements arising from observations. The essential requirements are the symmetries: the Lagrangian needs to remain invariant under external transformations such as Lorentz boosts (as the theory is assumed to be relativistic) and under internal symmetries. The internal symmetries that are local (spacetime dependent) and continuous are gauge symmetries. They are of particular importance: more than a simple constraint, they dictate the Lagrangian. These gauge symmetries impose the inclusion of gauge fields to ensure the invariance under the considered local group transformations. They give rise to the fundamental interactions of fermionic matter fields, which are mediated by the quanta of the gauge fields: the bosons.

The Standard Model is defined by the gauge symmetry $SU(3)_C \times SU(2)_L \times U(1)_Y$.

The factors correspond to three fundamental interactions, where the subscripts indicate the conserved quantum numbers. The $SU(3)_C$ gauge group gives rise to the strong force; the associated bosons are the gluons. The C refers to the "colour" charge, which is conserved under global $SU(3)_C$ invariance. The $SU(2)_L$ symmetry is associated to the conservation of weak isospin. The L subscript is not a quantum number but refers to the chirality of this transformation, which affects only left-handed fermions (see Section 2.1.3). The $U(1)_Y$ group conserves the weak hypercharge Y. Together, the two symmetries $SU(2)_L \times U(1)_Y$ give rise to the electroweak interaction, mediated by the electroweak boson fields W^1, W^2, W^3 and B. It will be seen later that this force splits into two: the weak interaction and electromagnetism.

2.1.3 Theoretical formulation

The Lagrangian formalism will be succintly presented, with an emphasis on the role of the Higgs boson, which is used in the decay cascade considered in this thesis.

The strong force

The strong force refers to the interactions between quarks and gluons, the particles possessing a type of charge called "colour". The colour charge comes in three type: red, green and blue (anti-red, anti-green and anti-blue are the equivalent colours for anti-particles). It is described by quantum chromodynamics (QCD), a non-Abelian gauge theory based on the local group $SU(3)$. The Lagrangian is of the form:

$$\mathcal{L}_{\text{QCD}} = \sum_{\text{quark flavors}} \bar{\psi}_f (i\gamma_\mu D^\mu - m_f)\psi_f - \frac{1}{4} G^{\,a}_{\mu\nu} G^{\,\mu\nu}_{a}, \tag{2.1}$$

where ψ_f are the fermion field for each quark flavor f, $\bar{\psi}_f$ the corresponding anti-fermion field and m_f the fermion's mass. The covariant derivative D_μ, required to ensure that the Lagrangian in Equation 2.1 stays invariant under the local $SU(3)_C$ transformation, is defined as:

$$D_\mu = \partial_\mu + i g_s \, t^a \, G^a_\mu, \tag{2.2}$$

where t^a are the eight generators of $SU(3)$, G^a_μ is the gluon field and g_s the strong coupling constant, to which all QCD interactions are proportional. The field strength tensor of QCD is:

$$G^a_{\mu\nu} = \partial_\mu G^a_\nu - \partial_\nu G^a_\mu + g_s\, f^{abc}\, G^b_\mu G^c_\nu, \tag{2.3}$$

with f^{abc} the structure constants of $SU(3)$.

The last term in Equation 2.3 corresponds to gluon self-interactions. Since gluons carry colour charge, they can indeed interact with each other. From the experimental fact that particles of colours can be observed only if they form a colour singlet (zero net colour charge), it follows that QCD must be confining. This phenomenon, known as confinement, restricts the range of the strong force to the size of a nucleon and causes quarks to hadronize, as it will be further explained in Chapter 4.

The electroweak force

The electroweak interaction arises from the $SU(2)_L \times U(1)_Y$ symmetry acting on the fermion fields. The weak isospin $SU(2)_L$ has the particularity of coupling differently depending on the fermion's chirality. A fermion field ψ can be expressed as the sum of its right-handed ψ_R (positive chirality) and left-handed ψ_L (negative chirality) projections. Under $SU(2)_L$ and for each generation i, the left-handed part of the leptons ν^i_L and ℓ^i_L forms a doublet, whereas the right-handed charged leptons ℓ^i_R are singlets.[3] Similarly for the quarks: $SU(2)_L$ couples left-handed up-type quarks u^i_L to left-handed down-type quarks d^i_L, leaving right-handed quarks (u^i_R and d^i_R) unchanged. The fermion fields are arranged then in the following way:

$$\text{Leptons:} \quad \begin{pmatrix} \nu^i_L \\ \ell^i_L \end{pmatrix},\ \ell^i_R \qquad\qquad \text{Quarks:} \quad \begin{pmatrix} u^i_L \\ d^i_L \end{pmatrix},\ u^i_R\,,\ d^i_R. \tag{2.4}$$

For more compact equations, all lepton and quark fields are labelled together as ψ_L and ψ_R, with the subscript indicating their handedness. Summing over all left-handed fermions f_L and right-handed ones f_R separately, the Lagrangian in the electroweak sector is then:

$$\mathcal{L}_E W = -\frac{1}{4} W^k_{\mu\nu} W^{k\,\mu\nu} - \frac{1}{4} B_{\mu\nu} B^{\mu\nu} + \sum_{f_L} \bar{\psi}_L\, i\gamma_\mu D^\mu_L\, \psi_L\, + \sum_{f_R} \bar{\psi}_R\, i\gamma_\mu D^\mu_R\, \psi_R, \tag{2.5}$$

where the gauge field strength tensors $W^k_{\mu\nu}$ ($k = 1, 2, 3$) and $B_{\mu\nu}$ ensue from $SU(2)_L$ and $U(1)_Y$ symmetries respectively. Their definitions with the electroweak boson

---

[3] In the Standard Model, neutrinos do not have any right-handed component since they are assumed massless.

fields W^1_μ, W^2_μ, W^3_μ and B_μ are given by:

$$W^k_{\mu\nu} = \partial_\mu W^k_\nu - \partial_\nu W^k_\mu + g\,\varepsilon^{klm}\,W^l_\mu W^m_\nu \qquad\qquad B_{\mu\nu} = \partial_\mu B_\nu - \partial_\nu B_\mu, \tag{2.6}$$

with ε^{klm} the totally antisymmetric structure constants of $SU(2)_L$, of gauge coupling constant g. The covariant derivatives, required to maintain the Lagrangian in Equation 2.5 invariant under $SU(2)_L \times U(1)_Y$, need to be defined differently depending on the chirality:

$$D_{\mu,L} = \partial_\mu \; - i\,g\,\frac{\sigma^k}{2}\,W^k_\nu - \; i\,g' Y B_\mu \qquad\qquad D_{\mu,R} = \partial_\mu \; - \; i\,g' Y B_\mu, \tag{2.7}$$

where σ^k are the three Pauli matrices, g' is the gauge coupling constant from $U(1)_Y$ symmetry, and Y is the hypercharge, a conserved quantum number relating electric charge and weak isospin.

Because of the absence of left-right symmetry in the Standard Model, fermion and boson masses can not be expliciteely added “by hand” in the Lagrangian. Terms in the form $m\bar{\psi}\psi$ would violate $SU(2)_L$ gauge invariance. The Standard Model described so far assumes all fundamental particles to be massless. This directly contradicts experimental observations of massive fermions and the large observed masses of weak bosons $W^\pm$ and Z. The solution to this massive problem – no pun intended – relies in the Higgs mechanism.

The Higgs mechanism

To allow massive particles to exist without violating gauge invariance, a $SU(2)_L$ doublet of complex scalar fields ϕ is introduced, with hypercharge set to $Y = 1$. This complex doublet, the so-called “Brout-Englert-Higgs field” [5–7], contains four degrees of freedom:

$$\phi = \begin{pmatrix} \phi^+ \\ \phi^0 \end{pmatrix} = \frac{1}{\sqrt{2}} \begin{pmatrix} \phi_1 + i\phi_2 \\ \phi_3 + i\phi_4 \end{pmatrix}, \tag{2.8}$$

The Lagrangian in the Higgs sector is of the form:

$$\mathcal{L}^{\text{Higgs}} = \underbrace{(D_\mu\phi)^\dagger(D^\mu\phi)}_{\text{kinetic}} \; - \; \underbrace{\mu^2(\phi^\dagger\phi) - \lambda\,(\phi^\dagger\phi)^2 \; - \; \frac{\mu^4}{4\lambda}}_{\text{potential}}\,. \tag{2.9}$$

The covariant derivative D_μ in the kinetic term is defined as $D_{\mu,L}$ in Equation 2.7. This Lagrangian is invariant under $SU(2)_L \times U(1)_Y$ and the Higgs field has no colour charge in order to maintain $SU(3)_C$ invariance. The interesting part resides in the presence of a quartic potential associated with the Higgs field. If $\mu^2 < 0$ and $\lambda > 0$, the minimum energy configuration does not correspond a vanishing field. Rather, the field acquires a non-zero value v, called vacuum expectation value (vev). The squared magnitude of the ground state ϕ^0 is then:

$$\phi^{0\,\dagger}\,\phi^0 = \frac{1}{2}(\phi_1^2 + \phi_2^2 + \phi_3^2 + \phi_4^2) = \frac{v^2}{2} \qquad \text{with} \qquad v = \sqrt{-\frac{\mu^2}{\lambda}}, \tag{2.10}$$

This fundamental state is not unique but degenerate.[4] Thus there exists a $SU(2)_L \times U(1)_Y$ gauge transformation to rotate the vev and align it along an arbitrary direction, *e.g.* ϕ_3:

$$\phi^0 = \frac{1}{\sqrt{2}}\begin{pmatrix} 0 \\ v \end{pmatrix}, \tag{2.11}$$

where the neutral component (to conserve electric charge) ϕ_3 develops a non-zero value. If all directions are valid, choosing one while fixing the gauge inevitably breaks, or rather hides the electroweak $SU(2)_L \times U(1)_Y$ invariance. In order to expand the ground state around the vev, the complex field ϕ can be parametrized as:

$$\phi = \begin{pmatrix} \xi_1 + i\xi_2 \\ \frac{1}{\sqrt{2}}(v+h) - i\xi_3 \end{pmatrix}, \tag{2.12}$$

with h a real scalar field. After choosing a convenient $SU(2)_L$ gauge transformation to cancel the three ξ_i fields, the expression of ϕ is inserted in the Lagrangian in Equation 2.9. The expansion will give rise to the masses of the gauge bosons (terms in v^2 of the form $m^2 B_\mu B^\mu$) and the Higgs self-interaction (terms in h^2, h^3 and h^4). However the W_μ^k and B_μ fields are no longer mass eigenstates. They can be redefined in order to make the mass matrix diagonal:

$$W_\mu^\pm = \frac{1}{\sqrt{2}}(W_\mu^1 \mp iW_\mu^2) \qquad Z_\mu = \frac{gW_\mu^3 - g'B_\mu}{\sqrt{g^2 + g'^2}} \qquad A_\mu = \frac{gW_\mu^3 + g'B_\mu}{\sqrt{g^2 + g'^2}}. \tag{2.13}$$

---

[4] The Higgs field potential is often pictured – in a two-dimensional representation – as a Mexican-hat: the center has a local maximum causing meta-stability whereas the ground states are in the circular dip in the brim of the hat.

A convenient parameterisation of the Z_μ and A_μ mixing is:

$$Z_\mu = W^3_\mu \cos\theta_W - B_\mu \sin\theta_W \qquad A_\mu = W^3_\mu \cos\theta_W + B_\mu \sin\theta_W, \tag{2.14}$$

where θ_W is the weak mixing angle (Weinberg angle) defined as $\theta_W = \tan^{-1} g'/g$.

W^1_μ and W^2_μ mix and form the massive W^+_μ and W^-_μ boson fields. W^3_μ and B_μ mix to form the massive Z field and a massless A_μ field, identified with the photon. Hence three of the four degrees of freedom of the Higgs field are "eaten" by the W^+, W^- and Z bosons. Each of these three particles acquires a longitudinal degree of freedom that renders them massive. The remaining degree of freedom corresponds to the scalar field of the massive Higgs boson.

Through this mechanism known as electroweak symmetry breaking (EWSB), the Higgs field ϕ broke the Standard Model $SU(3)_C \times SU(2)_L \times U(1)_Y$ symmetry down to a low-energy $SU(3)_C \times U(1)_{\mathrm{EM}}$ invariance. Here the $U(1)_{\mathrm{EM}}$ leaves the vacuum ϕ^0 invariant and corresponds to the conservation of the electric charge Q. This interaction, electromagnetism, is mediated by the massless field A_μ, represented by the photon γ.

Lastly, fermions acquire mass through terms of the form $\bar{\psi_L}\phi\psi_R$, which are now $SU(2)_L \times U(1)_Y$ invariant. These are known as Yukawa interactions between the scalar fields ϕ and the fermions fields, which are $SU(2)_L$ doublets ψ_L and singlets ψ_R. The associated Lagrangian (shortened here to one generation) is:

$$\mathcal{L}_{\mathrm{Yukawa}} = -i \left(y^\ell \, \bar{\psi}^\ell_L \, \phi \, \psi^\ell_R \; + \; y^d \, \bar{\psi}^q_L \, \phi \, \psi^d_R \; + \; y^u \, \bar{\psi}^q_L \, \tilde{\phi} \, \psi^u_R \right) \; \text{with } \tilde{\phi} = \begin{pmatrix} \phi^{0*} \\ \phi^{+*} \end{pmatrix} \tag{2.15}$$

where $\tilde{\phi}$ has a hypercharge $Y = -1$ such that the total hypercharge of each term equals zero. The ℓ, q, u and d superscripts refer to the lepton, quark doublet, up-type and down-type quark singlets respectively. After EWSB, these Yukawa interactions provide mass terms to all fermions.

Figure 2.1 offers a schematic summary of the Standard Model, before and after EWSB. The colour code in each fermion cell indicates which bosons from the third column are interacting with the considered fermion.

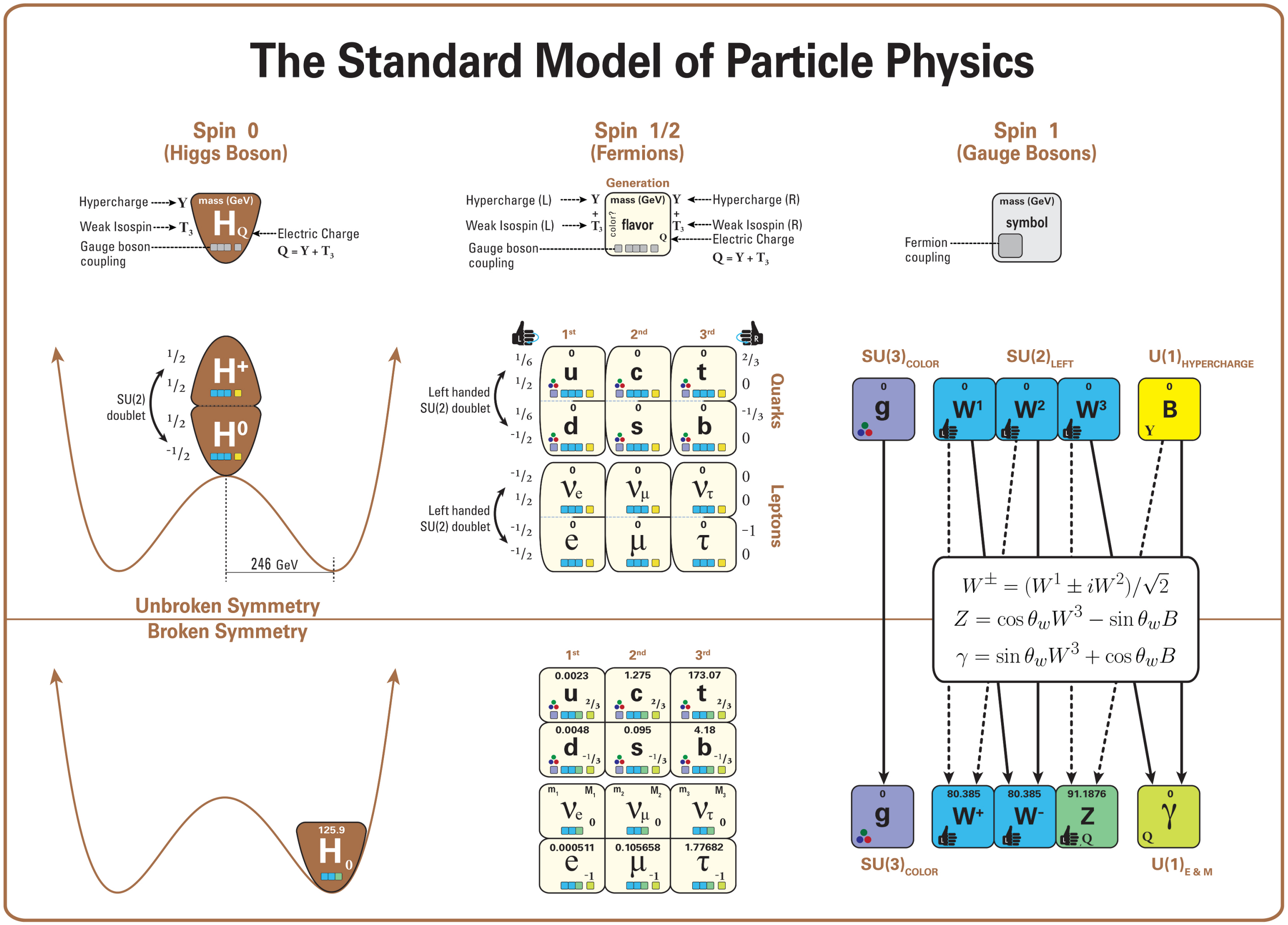

Figure 2.1: Structure of the Standard Model of particle physics with the fields arranged in columns according to their spin value. Properties and interactions of the elementary particles are shown before (top row) and after (bottom row) EWSB, where the Higgs doublet "falls" into the minimum value of the potential (at $v = 246$ GeV), breaking $SU(3)_C \times SU(2)_L \times U(1)_Y$ symmetry down to $SU(3)_C \times U(1)_{\text{EM}}$ [8].

2.1.4 Limitations of the Standard Model

The Standard Model unifies three fundamental forces in an elegant and compact formalism. Many SM predictions of particles and fields have been successfully tested at the per mille level over a large energy range. However, the SM is not a complete theory and leaves many open questions. Those that are most relevant to the present analysis are now presented.

The hierarchy problem

The Higgs vev at 246 GeV defines the electroweak scale Λ_{EM}, the energy at which electroweak processes are described. The SM itself cannot explain the value of this parameter, in particular why it is much smaller than the Planck mass.[5] There is a lack of understanding of the huge discrepancy between the electroweak scale and the Planck scale. This is an aspect of the hierarchy problem.

Another side of the hierarchy problem is related to the mass of the Higgs boson [9]. If the Higgs mechanism shows how the elementary particles acquired their mass, it does not explain why these masses span several orders of magnitude: from the neutrinos[6] in the eV range to the top quark, in the order of hundred of GeV. More problematic are the large radiative corrections on the Higgs mass coming from loop diagrams. At first order, they are of the form:

$$\delta m_h^2 \;\propto\; \mathcal{O}\left(\frac{\alpha}{\pi}\right)\Lambda^2, \tag{2.16}$$

where the energy cutoff Λ is used to regulate the loop integral. The quantum corrections are quadratically divergent in Λ. If the current theory is extended up to the Planck scale, then nothing prevents scalar particles in the Standard Model to receive very large corrections. To keep m_h at its measured experimental value of 125 GeV, very precise cancellations must occur. This “fine-tuning” of the Higgs mass, whose parameters require very precise values on 30 orders of magnitude, seems aesthetically unsatisfying. Physicists are rather guided by naturalness: models likely to be true are not requiring parameters of arbitrary and incredibly specific values.

---

[5] The planck mass $M_{\mathrm{Planck}} \approx 1.22 \times 10^{19}$ GeV is the energy where gravitational effects are no longer negligible in describing subatomic physics.

[6] Although conclusive experimental results confirmed neutrino oscillations, which requires them to have a mass, the exact nature of neutrinos is not yet established and is an active area of research.

Dark matter

Astronomical observations, such as the rotation speed of galaxies and gravitational lensing as well as the latest measurements of the Cosmic Microwave Background, all suggest the existence of another type of distributed matter that is non-luminous but massive and electrically neutral [10–12]. These mysterious constituents are roughly five times more abundant than the ordinary baryonic matter described by the Standard Model, which accounts for only 5% of the content of the Universe (against 26% for dark matter).

Theoretical deficiencies

There are other open questions on the Standard Model. Its formalism, albeit phenomenally accurate when compared to experimental measurements, still remains theoretically unsatisfying. Why is it governed by the product of the $SU(3)_C \times SU(2)_L \times U(1)_Y$ gauge groups? Why is one symmetry chiral $SU(2)$ and the others not? On top of the Higgs fine-tuning, some features seem to be *ad hoc*: the number of independent parameters, the minimal implementation of the Higgs mechanism, the arbitrary scalar potential of the Higgs in $\lambda\phi^4$. Moreover, the SM fails to account for the matter-antimatter asymmetry in the visible universe.

All of these arguments give a strong push to go “beyond the Standard Model” in order to find new physics able to address the current theory’s shortcomings.

2.2 Supersymmetry

Important theoretical efforts have been invested to address the shortcomings of the Standard Model. Supersymmetry (SUSY) [13–20], developed in the early 1970s, is one of the favoured candidate theory to extend the Standard Model. It postulates the existence of a higher level of symmetry that connects fermions with bosons. SUSY exhibits attractive features in particular regarding its elegant solution of the hierarchy problem, as well as the possible merging of all three fundamental forces at high energy scale (known as the unification problem). Its experimental discovery – or exclusion – is one of the main components of the LHC program.

2.2.1 General presentation

A higher symmetry

There are distinct elements in the Standard Model that may suggest an underlying unified scheme. Bosons and fermions form separate families and obey different statistics. The SM also contains two types of symmetries: spacetime and internal symmetries. Progress in modern theoretical physics has often been achieved while encompassing various phenomena into a simpler and more compact formalism. This motivates the search for a more general symmetry that would encompass spin and the conserved quantum numbers. Unfortunately, several no-go results – in particular the Coleman and Mandula theorem [21] – forbid to the combination of spacetime and internal symmetries. This is true if one considers only the generators that obey commutation relations in the SM, called bosonic generators. In QFT another class of operators exists, the anticommuting generators, which change the spin by half a unit. These are referred to as fermionic. Haag, Lopuskanski and Sohnius [22] circumvented the limitations of the Coleman and Mandula theorem by introducting these fermionic operators. This is the main idea behind SUSY: Supersymmetry transformations are generated by quantum operators Q, which change the fermionic states into bosonic ones and vice versa:

$$Q|\text{fermion}\rangle = |\text{boson}\rangle \qquad ; \qquad Q|\text{boson}\rangle = |\text{fermion}\rangle. \tag{2.17}$$

Allowing anticommuting generators (fermionic) as well as commuting ones (bosonic) leads to the possibility of Supersymmetry. Furthermore: it has been shown that in the context of relativistic theories, the favoured models which can lead to a solution of the unification problem without an awkward fine-tuning are supersymmetric theories (*i.e.* the models are invariant under operations mixing fermionic and bosonic states).

Key concepts in SUSY formalism

The drastic change in SUSY theories is the introduction of fermionic generators which carry spin angular momentum 1/2. The notation used for the SUSY generators are the complex, anticommuting Weyl spinors Q_α and its Hermitian conjugate $Q^\dagger_{\dot\alpha}$. The undotted (dotted) indices $\alpha = 1, 2$ ($\dot\alpha = 1, 2$) are used to differentially refer to the left-handed (right-handed) Weyl spinor. The fundamental properties of SUSY algebra are:

$$\left\{Q_\alpha\,,\,Q^\dagger_{\dot\alpha}\right\} = 2\,(\sigma_{\alpha\dot\alpha})^\mu\,P_\mu \qquad \left\{Q_\alpha\,,\,Q_\beta\right\} = \left\{Q^\dagger_{\dot\alpha}\,,\,Q^\dagger_{\dot\beta}\right\} \qquad = 0 \tag{2.18}$$

$$\left[P_\mu\,,\,Q_\alpha\right] = \left[P_\mu\,,\,Q^\dagger_{\dot\alpha}\right] \qquad = 0\,, \tag{2.19}$$

where P_μ is the four-momentum generator of spacetime translations and $\sigma^\mu = (\mathbb{1}, \boldsymbol{\sigma})$, with $\boldsymbol{\sigma}$ being the vector of Pauli matrices σ^i.

The irreducible representations of SUSY algebra are called *supermultiplets* [9]. A supermultiplet is a set of quantum states that can be transformed into one another by one or more supersymmetric operations. Each supermultiplet thus contains both fermion and boson states, which are commonly known as superpartners of each other. This predicts a fairly large amount of particles to be discovered! However, inserting in the SM Lagrangian the axioms of Supersymmetry produces several “miracles” that make SUSY one of the most plausible extension of the SM (see Section 2.2.3).

SUSY is broken (softly)

From the translational invariance in Equation 2.19, Q does not change the momentum and thus commutes with $-P^2$. Hence the pair of states in the same irreducible supermultiplet must have equal masses. As many experiments sensitive to the superpartner masses have not found any of the Standard Model “twins”, it follows that Supersymmetry must be broken.

It is still possible to add Supersymmetry-breaking terms to the total Lagrangian $\mathcal{L}$ of a SUSY model:

$$\mathcal{L} = \mathcal{L}_{\text{SUSY}} + \mathcal{L}_{\text{Soft}}, \tag{2.20}$$

where $\mathcal{L}_{\text{SUSY}}$ is the Standard Model Lagrangian augmented with superpartners and $\mathcal{L}_{\text{Soft}}$ refers to the Supersymmetry-breaking piece. The latter term lifts off the mass degeneracy between SM and SUSY particle content by making the latter heavier. It is “soft” as it should not reintroduce any unwanted quadratic divergences seen in the Standard Model [23]. Indeed the superpartner masses can not be too huge – they should be of order of the electroweak scale, $\mathcal{O}(1\ \text{TeV})$ – otherwise the corrections to the Higgs mass would be unnaturally large, leading to a fine-tuning which was meant to be avoided in the first place. The origin of Supersymmetry-breaking remains unknown and $\mathcal{L}_{\text{Soft}}$ has its share of arbitrariness. However it is important to mention here the possibility of maintaining the attractive aspects of SUSY while increasing the masses of its predicted superpartners. It gives some explanation as to why no SUSY particles have been seen yet in detectors and offers exciting prospects of discovering some of them at the LHC.

2.2.2 Minimal Supersymmetric Standard Model

Particle content

The Minimal Supersymmetric Standard Model (MSSM) [24] represents the supersymmetrisation of the Standard Model with the smallest increase in field content. Apart from pairing SM particle with a supersymmetric partner, no additional field is added (except in the Higgs sector, reviewed in the next section). Its construction – not detailed here as it is beyond the scope of this thesis – starts from the $SU(3)_C \times SU(2)_L \times U(1)_Y$ invariance and SM field content. Table 2.3 lists the chiral and gauge supermultiplets of the MSSM.

The superpartners of the SM fermions are named with a prepended "s" and the SUSY counterparts of SM bosons receive an Italian suffix in "ino". SUSY particles are written with a tilde on their symbol.

The mirroring of SM particles into supersymmetric ones is not fully... symmetric! The superpartners are not necessarily the mass eigenstates. This is due to some mixing occuring after electroweak symmetry breaking and supersymmetry breaking. This is especially the case in the third fermion generation (not pictured in Table 2.3 because it is not relevant here) and in the Higgs sector.

The Higgs sector

The MSSM necessitates two complex Higgs doublets: $H_u = (H_u^+, H_u^0)$ and $H_d = (H_d^0, H_d^-)$. The former (latter) will generate the masses to the up-type (down-type) quarks. This is imposed by the form of the superpotential in the SUSY Lagrangian, which does not simultaneously allow the presence of a scalar field and its complex conjugate. Moreover gauge anomalies arising from triangular diagrams are not cancelled anymore while extending the SM to SUSY. This destroys gauge invariance and hence renormalizability. Adding a second doublet of opposite hypercharge $Y = -1$ nicely cancels these anomalies.

The eight degrees of freedom from the two Higgs doublets are re-arranged after EWSB. Three are absorbed into $W^\pm$ and Z to provide them mass. The remaining

Table 2.3: Content of the SM and MSSM multiplets with name, symbol and spin. The fermions in the quarks and leptons are summarized with the index $i = 1, 2, 3$. In the electroweak and Higgs sector, gauge and mass eigenstates are shown separately when they differ due to mixing after symmetry breaking (more information in the text).

Particles (SM)	Spin	Fields SM		Fields MSSM			Spin	Sparticles
Quarks q^i	$\frac{1}{2}$	$\begin{pmatrix} u_L^i \\ d_L^i \end{pmatrix}$		$\begin{pmatrix} \widetilde{u}_L^i \\ \widetilde{d}_L^i \end{pmatrix}$			0	Squarks $\widetilde{q}^i$
		u_R^i		$\widetilde{u}_R^i$				
		d_R^i		$\widetilde{d}_R^i$				
Leptons ℓ^i	$\frac{1}{2}$	$\begin{pmatrix} \nu_L^i \\ \ell_L^i \end{pmatrix}$		$\begin{pmatrix} \widetilde{\nu}_L^i \\ \widetilde{\ell}_L^i \end{pmatrix}$			0	Sleptons $\widetilde{\ell}^i$
		ℓ_R^i		$\widetilde{\ell}_R^i$				
Gluons g	1	g		$\widetilde{g}$			$\frac{1}{2}$	Gluinos $\widetilde{g}$
Electroweak gauge bosons	1	W^1	W^+	$\widetilde{W}^+$	$\widetilde{\chi}_1^+$	Charginos	$\frac{1}{2}$	Gauginos
		W^2	W^-	$\widetilde{W}^-$	$\widetilde{\chi}_1^-$			
		W^3	Z^0	$\widetilde{W}$	$\widetilde{\chi}_2^+$			
		B^0	γ	$\widetilde{B}$	$\widetilde{\chi}_2^-$			
Higgs bosons	0	$\begin{pmatrix} H_u^+ \\ H_u^0 \end{pmatrix}$	h^0	$\begin{pmatrix} \widetilde{H}_u^+ \\ \widetilde{H}_u^0 \end{pmatrix}$	$\widetilde{\chi}_1^0$	Neutralinos	$\frac{1}{2}$	Higgsinos
			H^0		$\widetilde{\chi}_2^0$			
		$\begin{pmatrix} H_d^0 \\ H_d^- \end{pmatrix}$	A^0	$\begin{pmatrix} \widetilde{H}_d^0 \\ \widetilde{H}_d^- \end{pmatrix}$	$\widetilde{\chi}_3^0$			
			H^+, H^-		$\widetilde{\chi}_4^0$			

five lead to two neutral scalar fields h^0, H^0, a pseudoscalar field A^0 and two charged bosons H^+ and H^-. By definition, h^0 is the lightest neutral Higgs boson and the upper bound on its mass – after radiative corrections – is $m_{h^0} \lesssim 135$ GeV. This is one of the reasons why h^0 is referred to as the "Standard Model-like" Higgs. Nothing prevents the observed resonance at the LHC – confirmed to be *a* Higgs boson compatible with the SM – from being in fact the lightest Higgs scalar field of the MSSM.

The fermionic superpartners of the Higgs are the Higgsinos $\widetilde{H}_u = (\widetilde{H}_u^+, \widetilde{H}_u^0)$ and $\widetilde{H}_d = (\widetilde{H}_d^0, \widetilde{H}_d^-)$. After electroweak symmetry breaking in the MSSM, the Higgsinos mix with the winos $\widetilde{W}^\pm$, $\widetilde{W}^0$ and bino $\widetilde{B}$, the superpartners of the electroweak gauge bosons. The neutral wino $\widetilde{W}^0$ and the bino $\widetilde{B}$ mix with the Higgsinos $\widetilde{H}_d^0$ and $\widetilde{H}_u^0$ to give 4 observable Majorana fermionic neutral eigenstates called *neutralinos*, with masses conventionally arranged as:

$$m_{\widetilde{\chi}_1^0} \leqslant m_{\widetilde{\chi}_2^0} \leqslant m_{\widetilde{\chi}_3^0} \leqslant m_{\widetilde{\chi}_4^0}. \tag{2.21}$$

The charged winos $\widetilde{W}^\pm$ mix with the charged higgsinos $\widetilde{H}_d^-$ and $\widetilde{H}_u^+$ to give 2 observable Dirac fermionic charged eigenstates called *charginos* $\widetilde{\chi}_1^\pm$ and $\widetilde{\chi}_2^\pm$.

From parity to LSP

Terms violating baryonic (B) and leptonic (L) numbers can be added in the MSSM Lagrangian. However this would lead to forbidden decays, conflicting with measurements (such as the proton's lifetime). These terms are suppressed by requiring an additional symmetry. A new quantum number, defined for each field, is postulated. The R-parity is given by:

$$P_R = (-1)^{3(B-L)+2S}, \tag{2.22}$$

with S the spin of the particle. Standard Model particles have $P_R = 1$ and the superpartner are assigned $P_R = -1$.

R-parity conservation eliminates the possibility of B and L violating terms in the renormalizable superpotential. It also leads to interesting consequences. First, it implies that sparticles may only be produced or annihilated by pairs. Moreover, superpartners decay cascades will inevitably lead to the production of the lightest supersymmetric particle (LSP). As it has no lighter entity to decay into, the LSP is stable.

2.2.3 Attractive features of Supersymmetry

The beauty of SUSY resides in its simple design, generalizing space-time transformations. The theory has gained popularity due to its rich phenomenological consequences, which provide elements of answer to various open questions in physics and cosmology. Above addressing the hierarchy problem, SUSY offers two other main attractive features, which are detailed below.

Stabilization of the Higgs mass

One of the main motivations for the MSSM is its natural solution to eliminate the quadratic divergences on the Higgs boson mass.

Each radiative correction from closed fermion loops is compensated by the corresponding contribution of the bosonic superpartner, as the two diagrams have a relative minus sign. Schematically, a fermionic field ψ_f coupling with the Higgs field ϕ_h with a Lagrangian term $-\lambda_f \overline{\psi_f} \phi_h \psi_f$ gives 1-loop contribution to Higgs boson mass of $-\frac{|\lambda_f|^2}{8\pi^2}\Lambda^2$, where λ_f is the Yukawa coupling. Its scalar superpartner $\phi_{\tilde{f}}$ has an interaction term in $\lambda_{\tilde{f}}|\phi_h|^2|\phi_{\tilde{f}}|^2$ and the 1-loop correction on the Higgs boson mass is $\frac{\lambda_{\tilde{f}}}{8\pi^2}\Lambda^2$. Requiring fermionic-bosonic multiplet symmetry, that is to say $\lambda_{\tilde{f}} = |\lambda_f|^2$, the total correction for a 1-loop contribution on the Higgs boson mass becomes:

$$\delta m_h^2 = \frac{\lambda_{\tilde{f}}}{8\pi^2}\Lambda^2 - \frac{|\lambda_{\tilde{f}}|^2}{8\pi^2}\Lambda^2 + ... = \frac{\Lambda^2}{8\pi^2}(\lambda_{\tilde{f}} - |\lambda_f|^2) + ... = 0 + (\text{finite terms}) \qquad (2.23)$$

The correction terms remain bounded to all orders of perturbation theory. Supersymmetry hence naturally stabilizes the vacuum, through intrinsic cancellations, without any fine-tuning needed. The soft SUSY breaking terms reintroduce a logarithmic sensitivity to the cutoff, but no quadratic divergences arise. Hence the vacuum remains stable in the case of soft SUSY breaking, provided the difference of masses between fermions and their superpartners are of the order of the electroweak scale.

Gauge unification

The coupling constants g_s, g and g' – sometimes labelled with the Greek letter α – are associated to $SU(3)_C$, $SU(2)_L$ and $U(1)_Y$ respectively. They are usually referred to as "running coupling constants" as their value is defined only for a given energy scale. While extrapolating their measured values from the electroweak scale to very high energies, the progression suggests the constants will converge. In the Standard

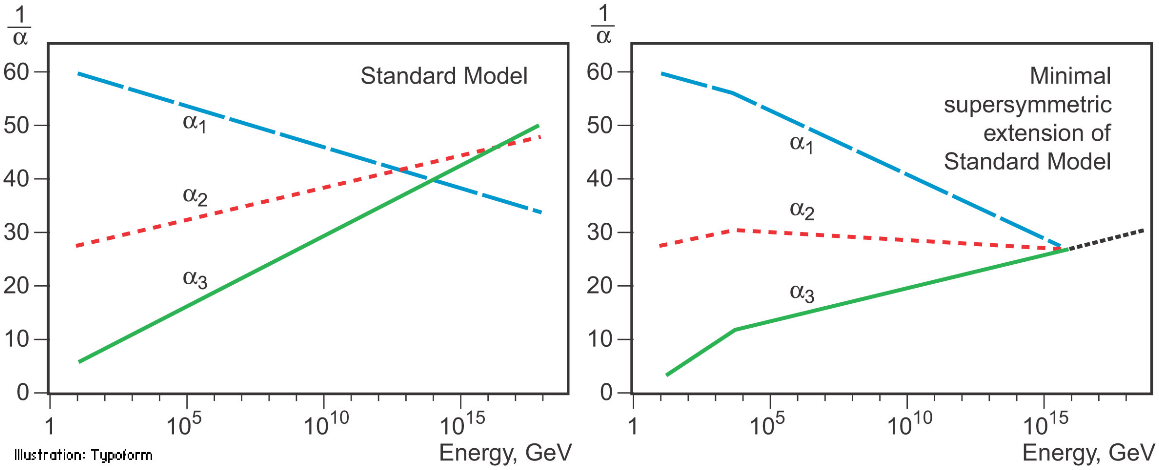

Figure 2.2: Evolution of the inverse of the coupling constants associated with the electromagnetic (α_1), the weak (α_2) and the strong (α_3) forces in the Standard Model only case (left) and in the context of the MSSM (right) [25].

Model, they do not converge: the three lines do not meet at a unique point, as illustrated in Figure 2.2. With the MSSM however, the convergence is nearly perfect. This remarkable result clearly hints that the three interactions are low-energy manifestations of a single force lying around the energy $10^{15} - 10^{16}$ GeV, known as the "Grand Unification" (GUT) scale.

Dark matter candidate

The R-parity conservation – an *ad hoc* assumption to suppress forbidden decays – ensures that the lightest supersymmetric particle (LSP) is stable.[7] This leads to a surprising consequence in cosmology. If the LSP is massive and does not carry any $U(1)_{\mathrm{EM}}$ nor colour charges, it would interact with regular matter only through gravitation and the weak force. This qualifies it as a Weakly Interacting Massive Particle (WIMP), a class of hypothetized constituents of the Universe non visible content. Thus, Supersymmetry provides an excellent candidate for a dark matter particle. The lightest neutralino – with a mass starting around 100 GeV – is the favoured possibility as its small interaction cross section can match the current estimated abundance of dark matter in the Universe [26].

---

[7] In this thesis, the LSP is assumed to be the lightest neutralino $\tilde{\chi}_1^0$.

2.2.4 The phenomenological Minimum Supersymmetric Standard Model

The MSSM possesses 124 independent parameters. This renders any experimental scan very impractical. The phenomenological MSSM (pMSSM) has been introduced to facilitate the exploration of MSSM phenomena. The following assumptions are made based on experimental data and theoretical simplicity:

***R*-Parity is exactly conserved.**

No new sources of CP-violation in the sparticle sector is achieved by requiring the soft parameters to be real.

Minimal flavor violation is imposed at the electroweak scale. In other words, parameters that would give rise to additional (non observed experimentally) flavour-changing neutral currents are absent.

The first two generations of sfermions are degenerate as experimental observations severely limit the mass splitting between the two generations of squarks and sleptons.

The LSP is assumed to be the neutralino that can be identified as a dark matter candidate.

After applying these constraints, the number of free parameters at the TeV scale decreases to 19 (more details on these parameters will be given in Chapters 5 and 9). The pMSSM has the advantage of being agnostic regarding the mechanism of SUSY-breaking and the sparticle content at energy scales higher than the TeV. The analysis in this dissertation is interpreted in the context of the pMSSM, first using a specific parameterization sensitive to the decay channel in question (Chapter 5) and subsequently scanning numerous sets of these 19 parameters as part of a summary paper (Chapter 9).

Chapter 3

The ATLAS detector at the Large Hadron Collider

In experimental particle physics, very high energy collisions are used to lift the veil on the laws of nature that govern the smallest constituents of matter. These collisions are achieved by giant machines such as the Large Hadron Collider (LHC). The LHC has its share of superlatives; among others it is the most powerful particle collider as well as the largest experimental facility ever developed. It also ranks among the greatest human endeavours, bringing more than 10,000 scientists and engineers together from over 100 countries.

For conciseness only a brief summary of the accelerator complex will be stated[1], as the focus will be on one of the main detectors operating on the LHC ring: the ATLAS experiment. After detailing this multi-purpose detector, the dataset of proton-proton collisions it collected from 2010 to 2012 will be described.

3.1 The Large Hadron Collider

Synchrotron Particle Accelerator

The LHC [28] is a 27 km long circular accelerator lying in a tunnel 50 to 175 m beneath the Franco-Swiss border near Geneva, Switzerland. It was built and is operated by the European Organization for Nuclear Research (CERN). The LHC accelerates

---

[1] A captivating narrative on the construction and technological challenges of the LHC can be found in Reference [27].

in separate pipes two beams of hadrons (either protons or heavy ions[2]) circulating in opposite directions. The LHC is a synchroton, bringing particles to higher kinetic energies using sixteen radio-frequency cavities while 1232 dipole magnets are *synchronized* to maintain the accelerated beams into their circular orbit. An additional 392 quadrupole magnets are used to keep the beams focused.

CERN uses state-of-the-art superconducting dipoles made of niobium-titanium (NbTi) alloy. An unprecedented cryogenic system cools these magnets at a temperature of 1.9 K (lower than outer space!), where helium becomes superfluid and very effectively conducts heat out of the dipoles. At this temperature, the magnets can sustain a 11,850 A current, needed to create a high magnetic field up to 8.33 T that bends the particle beam.

Protons are extracted from a hydrogen gas bottle and are gradually boosted in a series of linear and circular accelerators as shown in Figure 3.1. The protons group together in bunches during the acceleration process. In 2012 the LHC circulated per beam approximately 1380 bunches containing 1.7×10^{11} protons each, with a bunch crossing of 50 ns. The stored energy per proton in each beam was 4 Tera electronvolt (TeV)[3], which corresponds to 143 MJ [30]. Two beams of protons with four-momenta $p_1 = (E, \vec{p})$ and $p_2 = (E, -\vec{p})$ colliding head on will give $s = (p_1 + p_2)^2 = 4E^2$, so a centre-of-mass energy $\sqrt{s} = 2E$. The 2012 dataset used in this analysis has been collected with $\sqrt{s} = 8$ TeV.

Luminosity

Accelerator performance is characterized by its instantaneous luminosity L. It relates the event production rate $\mathrm{d}N/\mathrm{d}t$ of a given physics process with the cross section σ of this process:

$$\frac{\mathrm{d}N}{\mathrm{d}t} = L\,\sigma\,. \tag{3.1}$$

The instantaneous luminosity is expressed in units of $\mathrm{cm}^{-2}\ \mathrm{s}^{-1}$. It is usually indicated as $\mathrm{b}^{-1}\ \mathrm{s}^{-1}$, where b is a Barn, a unit of area defined as $1\ \mathrm{b} = 10^{-28}\ \mathrm{m}^{-2}$. The luminosity is computed using beam specific characteristics, such as the area at the collision point, the numbers of bunches per beam and protons per bunch. The 2012 dataset delivered by the LHC had a peak instantaneous luminosity of 7.73×10^{33} $\mathrm{cm}^{-2}\ \mathrm{s}^{-1}$ [31], close to the design value of $10^{34}\ \mathrm{cm}^{-2}\ \mathrm{s}^{-1}$ [30].

---

[2] The remaining of this thesis will solely focus on proton–proton collisions.

[3] The machine is designed to operate at 7 TeV per beam.

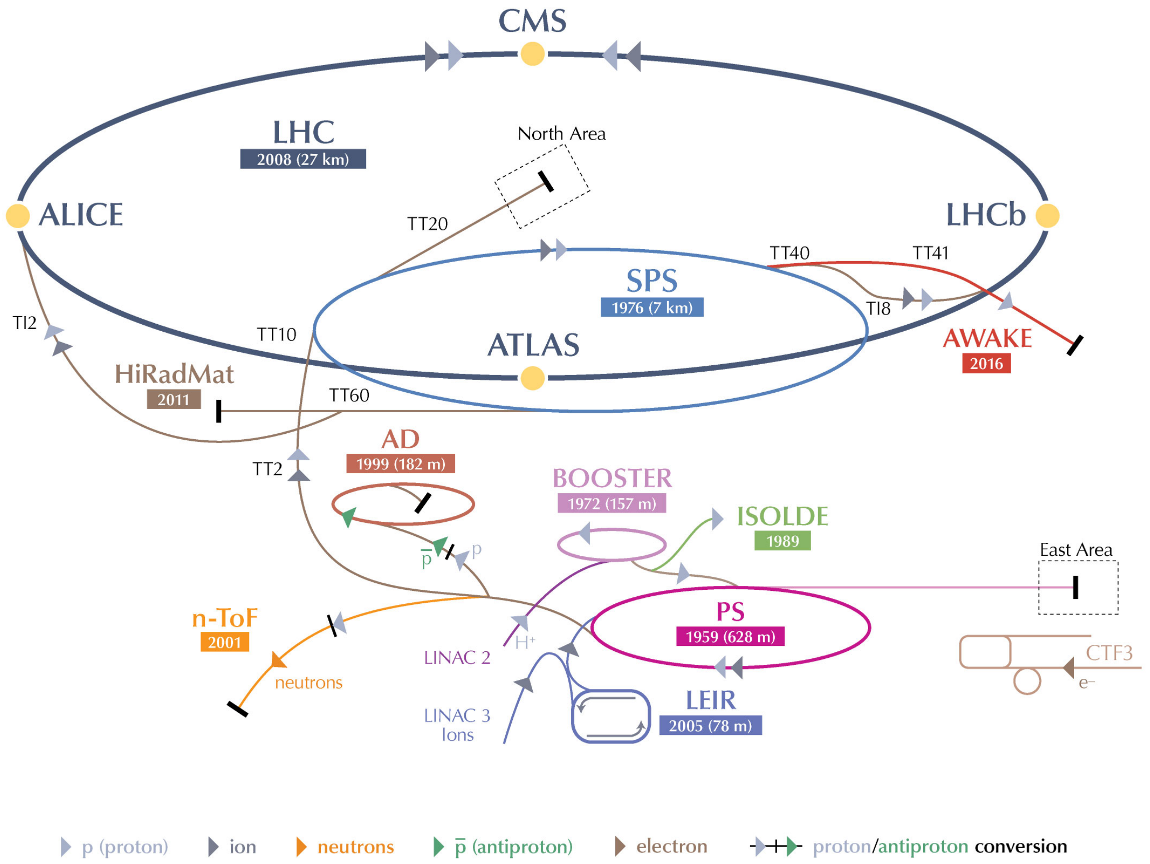

Figure 3.1: Schematic view of CERN accelerator complex. The LHC injection chain for protons starts with LINAC2, continues with the Proton Synchrotron Booster (Booster), Proton Synchrotron (PS) and finishes at the Super Proton Synchrotron (SPS), where 450 GeV protons are eventually injected into the LHC main ring [29].

The integral of the delivered luminosity over time, $\int L\,\mathrm{d}t$, is called integrated luminosity $\mathcal{L}$, expressed in inverse femtobarns, fb^{-1}. It is a measure of the collected data size, independently on the type of process. More details on the dataset of this thesis will be given in Section 3.3.

LHC Experiments

Four major detectors reside at the LHC interaction points, labelled in Figure 3.1. ALICE is specialized in analysing lead-ion collisions. LHCb studies the matter–antimatter asymmetry using hadrons containing b quark. CMS is one of the two multi-purpose detectors of the LHC, famous for his high mass of 14,000 tons. ATLAS is the other general apparatus and is described in detail in the next section. Designed with different detector philosophies, ATLAS and CMS share similar physics goals: they aim at performing precision measurements of Standard Model processes and discovering new particles predicted by candidates theories, in particular Supersymmetry.

3.2 The ATLAS Detector

The ATLAS detector [32] derives its name from a weird acronym, “A Toroidal LHC ApparatuS”, which at least hints on his titanic size. It measures 44 m in length and has a diameter of 25 m, making it the largest collider detector ever constructed.

Detector Design

ATLAS nearly covers 4π in solid angle, with the exception of two cones of $0.2°$ allowing the entry of the LHC beams. This hermetic design is key to accurately reconstruct the missing transverse momentum, a crucial observable in most supersymmetric searches.

ATLAS is composed of specialized sub-systems operating independently and complementing each others for particle identification. These sub-detectors are built in nested cylindrical layers, centered on the IP and aligned along the beam axis. Each are divided into three regions: the cylindrical centre “barrel” and two closing disks called “end-caps” at the extremities. Figure 3.2 shows a cutaway view of the entire detector with the trackers near the centre, surrounded by the calorimeters and closed by the muon spectrometers. These three sub-systems will be described in the next sections, after first defining the conventional coordinate system and the commonly encountered notation.

Coordinate System

ATLAS uses a right-handed coordinate system with its origin at the nominal interaction point (IP) in the centre of the detector and the z-axis along the beam line. The anti-clockwise beam direction defines the positive z-axis, with the x-axis pointing to the center of the LHC ring and the y-axis upwards.

The anzimutal angle ϕ in cylindrical coordinates is measured in the transverse plane (x–y) and defined as $\phi = \tan y/x$. The polar angle θ is defined as $\tan\theta = \sqrt{x^2 + y^2}/z$.

Particles reconstructed in ATLAS are generally characterized by their outward four-momentum $p = (E, p_x, p_y, p_z)$. In the context of high-energy hadronic collisions,

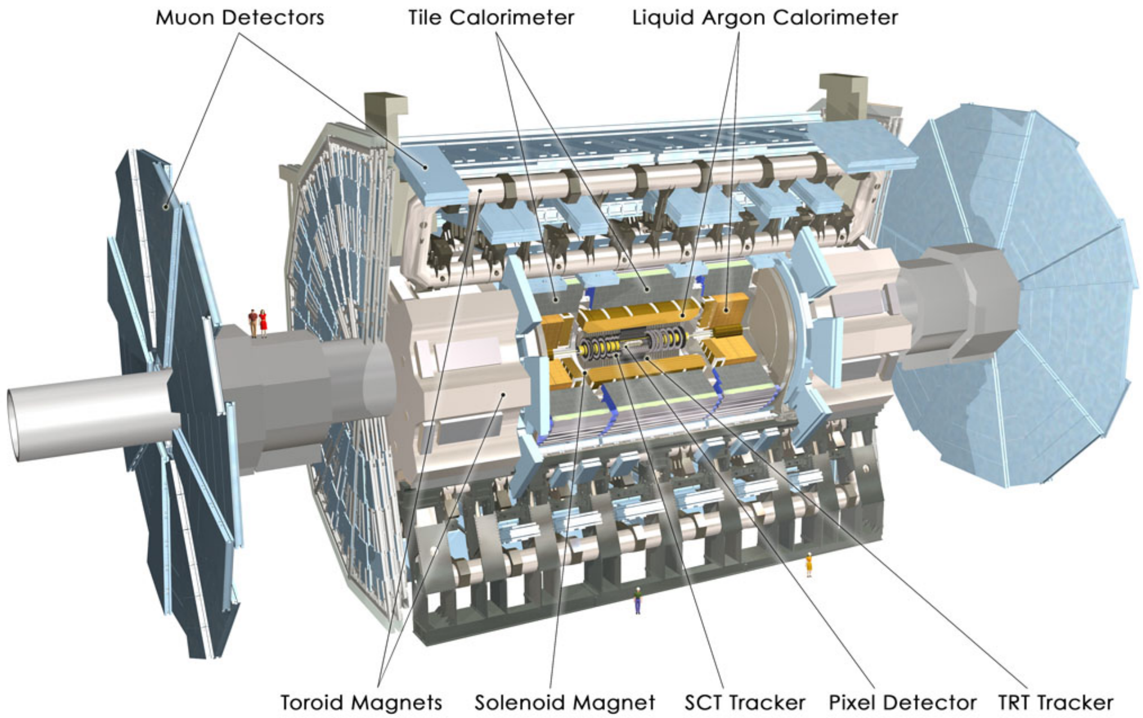

Figure 3.2: Cutaway view of the ATLAS detector and its sub-systems, with humans (not supposed to be on the beam pipe) shown to scale. Credit: CERN.

the longitudinal boost along the beam direction is *a priori* unknown, as the hard scattering partons share a fraction of the proton momentum. However their energy contribution along the x and y components is negligible and thus momentum conservation is expected in the transverse plane. Hence the key quantity, commonly used in lieu of absolute momentum, is the transverse momentum $p_{\mathrm{T}} = \sqrt{p_x^2 + p_y^2}$. The pseudorapidity η, defined as:

$$\eta = -\ln\tan\frac{\theta}{2}\,, \tag{3.2}$$

is preferentially used in place of θ as differences of pseudorapidity are invariant under Lorentz boosts along the beam axis z.

The angular separation between two reconstructed particle objects is assessed using $\Delta R = \sqrt{\Delta\phi^2 + \Delta\eta^2}$, unless stated otherwise.

3.2.1 Tracking subdetectors

The central tracker, referred to as the Inner Detector (ID), is responsible for the position and momentum measurement of charged particles emanating from the primary

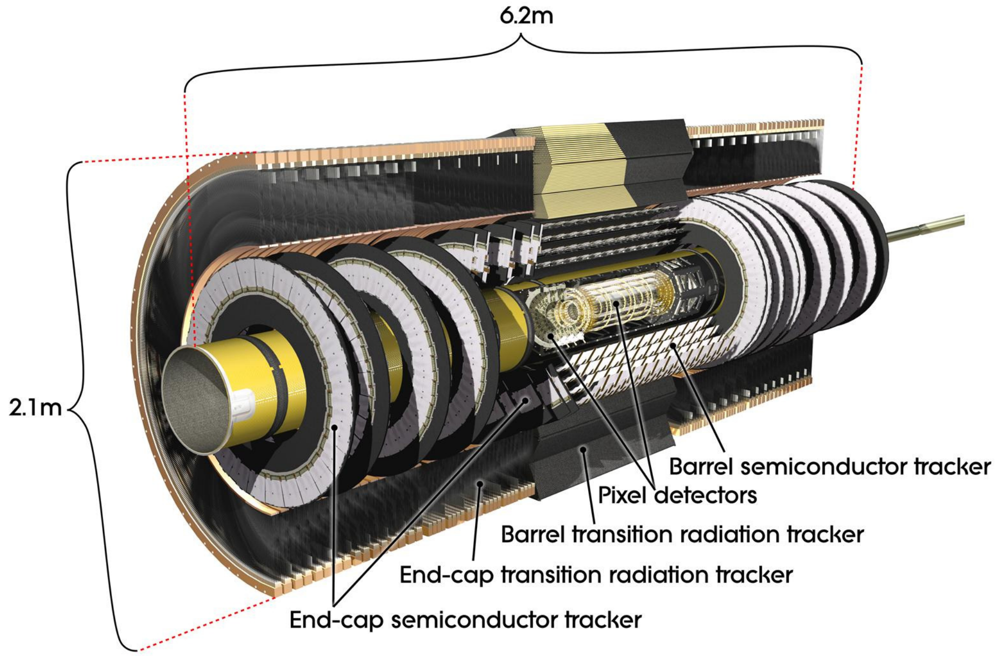

Figure 3.3: Cutaway view of the inner detector and labelled sub-systems. Credit: CERN.

pp interactions. To do so, a superconducting solenoid magnet envelopes the ID and creates a 2 T magnetic field parallel to the beam pipe. The trajectories of passing charged particles, which are bent by the magnetic field, are reconstructed using the signals (or “hits”) recorded in the layered sensors of the ID. The charge and momentum of each particle can be deduced from the curvature of the measured track. The ID is composed of three independent and complementary sub-systems, covering the range $|\eta| < 2.5$. Figure 3.3 shows the entire inner tracker and its sub-detectors, which are described as follow, from the closest to the furthest of the interaction point.

The Pixel Detector is the innermost device in ATLAS and has the challenging mission of reconstructing vertices (coordinate of the points where tracks merge) in a high radiation environment. For this, a very high granularity is required to allow for precision track measurements. This is achieved by using radiation-tolerant silicon sensors (“pixels”) of nominal size $r\text{–}\phi \times z = 50 \times 400\ \mu\text{m}^2$. They are grouped into 1744 modules arranged over three concentric cylindrical barrels and six end-cap disks. The pixel detector has more than 80 millions readout channels and reaches resolutions of $r\text{–}\phi \times z = 50 \times 115\ \mu\text{m}$.

The Semiconductor Tracker (SCT) is key for particle momentum determination. It consists of four barrel layers and nine wheels in each endcap, all instrumented on both sides with 12 cm long silicon micro-strips. This covers a larger volume of the SCT compared to the Pixel detector. There are in total 6.3 million readout channels, significantly less than in the Pixel detector. By pairing sensors at a small angle (one strip is aligned parallel to the beam axis and the other is offset by 40 mrad), it is possible to determine the z coordinate in each module traversed by a charged particle. A particle track generally leaves eight hits in the SCT. The 80 μm strip pitch allows a resolution of 17 μm in r–ϕ and 580 μm in z (R) for the barrel (endcap) modules.

The Transition Radiation Tracker (TRT) is made of 4 mm drift tubes, referred to as straws, filled with a gas mixture of mostly xenon and embedded in a matrix of polypropylene fibres as radiator material[4]. The straws are 144 cm (37 cm) long and disposed parallel to the beam line (radially) in the barrel (endcaps). Charged particles passing through a straw ionize the xenon and a high voltage between the cathode (straw wall) and the anode (gold-plated tungsten wire on the longitudinal straw axis) will drift electrons and ions appart, generating a current proportional to the energy loss of the incoming particle. With its geometry and volume, the TRT improves track measurements thanks to its high number of close ionizations pulses or “hits”, on average 32 per track, with an accuracy of 130 μm per straw. Between the straws, the radiator material (polypropylene fibres) cause ultra-relativistic charged particles to produce transition radiation. The associated signal is proportional to the relativistic boost γ of the charged particle: electrons, which are light, produce large energy depositions around 10 keV, whereas minimum-ionizing particles such as pions, which are heavier, deposit about 2 keV. The TRT thus contributes to electron identification.

3.2.2 The calorimeters

ATLAS’ calorimeters measure the energy of the many particles emerging from the interaction. Particle physics calorimeters employ a destructive method consisting of stopping the incoming particle in a dense medium. The incident particle interacts

---

[4] A charged particle crossing two media with different dielectric constants emits so-called transition radiation.

with the material and initiates a decay cascade – known as a particle shower – of lower energy particles, which eventually get absorbed by the material. The energy released in the detector material by the shower's constituents, mainly through ionization and excitation, is proportional to the energy of the incident particle.

The key features of calorimeters are their thickness in radiation lengths and hermeticity. The former ensures the full cascade is contained in the apparatus and does not escape beyond the calorimeter, which would underestimate the energy of the incident particle. The latter is crucial to cover all showers created in an event and therefore to accurately measure the sum of momenta in the transverse plane. The presence of momentum imbalance, or missing transverse momentum, is a typical signature of a new physics scenario where *e.g.* supersymmetric particles leave ATLAS undetected.

There are two types of showers: the electromagnetic and the hadronic showers. They are of different shape and length, therefore the ATLAS calorimeters are divided into two nested apparatuses: one electromagnetic and one hadronic. In both cases, the devices are sampling calorimeters: they are made of alternating thin layers of inactive dense material (the absorber) to favour showering and active layers (the sampler) equipped with read-out sensors to measure the energy deposition.

The Liquid Argon Electromagnetic Calorimeter

The electromagnetic (EM) calorimeter measures the energy of electrons, positrons and photons. As seen in Figure 3.4, the EM calorimeter is composed of a barrel (targeting the central region $|\eta| < 1.475$) and two end-caps (covering the range $1.375 < |\eta| < 3.2$), all surrounding the inner detector. Both barrel and end-caps are constructed with successive layers of 1–2 mm thick lead plates alternating with honey-comb spacers filled with liquid argon. Particles from the shower ionize the liquid argon, the created pairs of electrons–ions drift apart in the presence of an electric field and they are collected on the electrodes installed in the samplers.

The hallmark of the ATLAS electromagnetic calorimeter is its accordion geometry, as shown in Figure 3.5. This design was chosen to ensure high azimuthal uniformity, a regular liquid argon ionization gap thickness, and a constant sampling fraction within a given detector region.

Over the region devoted to precision physics ($|\eta| < 2.5$), the EM calorimeter is radially segmented in three layers. From the innermost to uppermost layers, the gran-

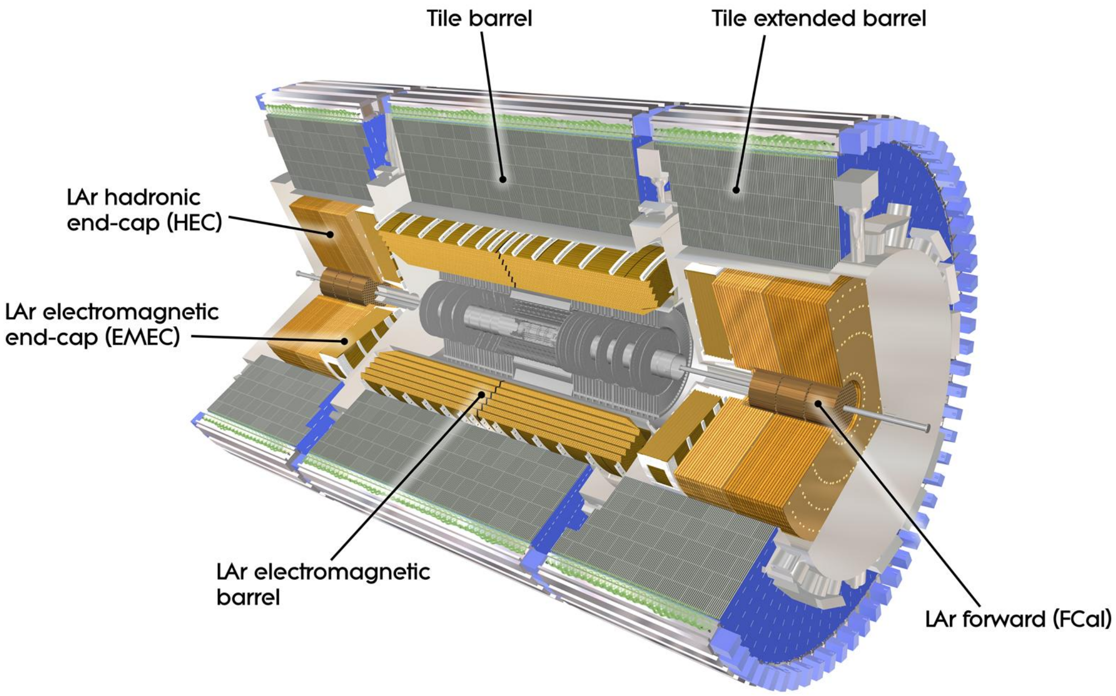

Figure 3.4: Cutaway view of the ATLAS calorimeters. Credit: CERN.

ularity in η and ϕ becomes coarser, as the shower laterally spreads. The middle layer, with a thickness of 16 radiation lengths[5] (X_0), absorbs most of the electromagnetic shower.

In the region of $|\eta| < 1.8$, a presampler detector is used to correct for the energy lost by electrons and photons upstream of the calorimeter. The presampler consists of an active LAr layer of thickness 1.1 cm (0.5 cm) in the barrel (end-cap) region.

The relative energy resolution of the EM LAr calorimeter is given by the following quadratic sum:

$$\frac{\sigma(E)}{E} = \frac{10\%}{\sqrt{E}} \oplus 0.7\% \,. \tag{3.3}$$

The constant noise term of 0.7% meets the calorimeter design performance goals. The main aspects of the LAr online monitoring are discussed in appendix A.

---

[5] The radiation length X_0 is the average distance travelled by an electron before its looses 63% $(1 - 1/e)$ of its energy.

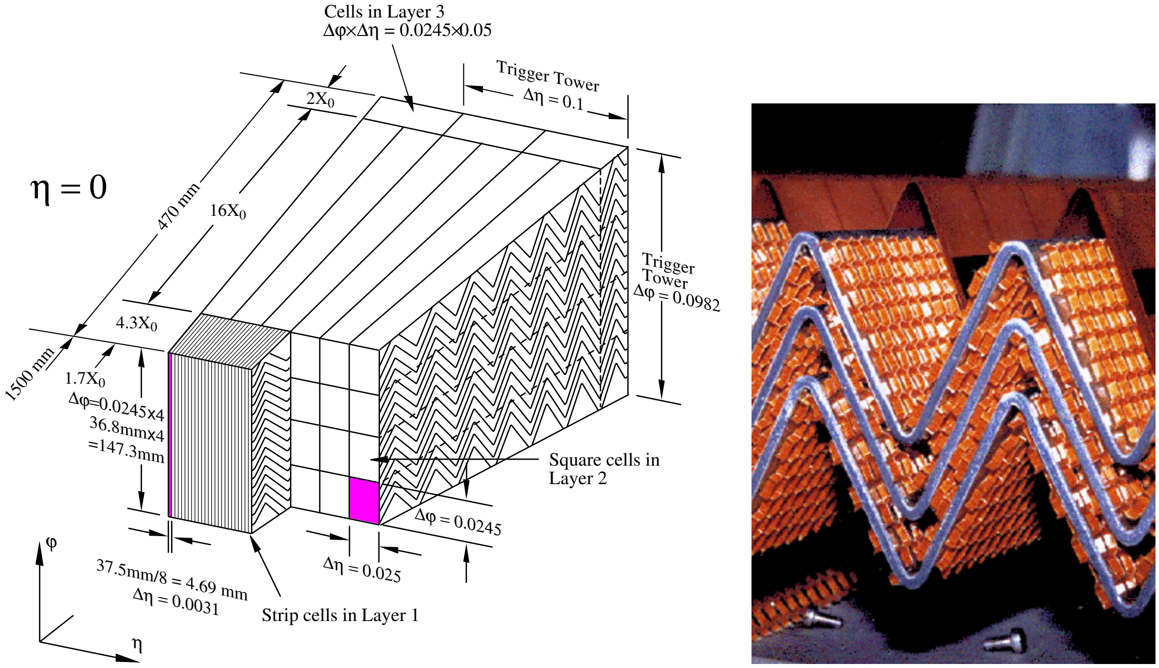

(a) (b)

Figure 3.5: (a) Sketch of a barrel module with the visible three layers and their accordion geometry. (b) The photography offers a magnified view of the accordion readout and sampling design showing the honeycomb electrode spacers that form the ionization gap [32].

The Hadronic Calorimeter

The hadronic calorimeter measures the energy of charged and neutral hadrons. Hadronic showers are far more complex than electromagnetic ones. They are initiated by a high energy incident hadron but contain both strongly and electromagnetically interacting particles in fluctuating ratios. Moreover, the interactions of hadrons with nuclei leave an invisible non-EM contributions and some of the shower products like muons and neutrinos will escape the calorimeter. Shower development scales with nuclear absorption length λ_a (equivalent to X_0 in a hadronic context). Compared to EM showers, hadronic showers take longer to form and end up being thicker. For this reason, the hadronic calorimeter extends up to ten interaction lengths λ_a at $\eta = 0$. With an inner radius of 2.28 m to an outer radius of 4.25 m and 11 m in length, the hadronic calorimeter's large dimensions ensure very few hadrons will escape the apparatus.

The hadronic calorimeter is composed of the TileCal (barrel) and two hadronic end-caps (HEC). The TileCal covers the range $|\eta| < 1.0$ and has extensions in $0.8 <$

$|\eta| < 1.7$. It is made of steel absorbers alternating with scintillating plastic tile samplers. These scintillator glow at the passage of a shower and the produced photons are brought via optic fibers to photomultipliers. The energy resolution of the TileCal is $\sigma(E)/E = 56.4\%/\sqrt{E} \oplus 5.5\%$, measured with test beam data [32]. The HEC is composed of two independent wheels made of 32 identical wedge-shaped modules with two segments each, copper plates act as absorber with interleaved liquid argon as sampler. The resolution of the HEC is $\sigma(E)/E = 50\%/\sqrt{E} \oplus 3\%$ [32].

The LAr Forward Calorimeter

To provide hermicity as well as to shield the muon spectrometer from radiations background, a special calorimeter is placed in the forward regions, between the inner detector and the hadronic end-caps. It is performing both electromagnetic and hadronic calorimetry measurements. The former is ensured in the first layer using copper as absorber, while hadronic energy estimations are done in the two outer layers using tungsten as absorber. The sampler material is liquid argon for both shower types. The forward calorimeter extends the covarge up to $|\eta| < 4.9$ and its design resolution, limited by its high-radiation operating environment, is $\sigma(E)/E = 100\%/\sqrt{E} \oplus 10\%$ [32].

3.2.3 Muon Spectrometers and Toroidal Magnets

The muon spectrometer (MS) of ATLAS represents a cornerstone of the detector's design, extending outwards 6.5 metres from the end of the hadronic calorimeter. While most particles from the interaction points are absorbed by the calorimeters, the muons are low-ionizing and therefore escape without much energy loss. To allow for momentum determination, the trajectories of passing energetic muons need to be bent by a strong magnetic field. This is done with ATLAS' toroidal magnets, which consist of a barrel toroid made of eight-superconducting air-core coils encased in individual racetrack-shaped vessels and two identical end-caps with eight coils as in the barrel but smaller in size (see Figure 3.6).

The magnets can produce a field of approximately 0.5 T in the barrel and 1 T in the end-caps. The most important numbers for track momentum measurements are the field integrals over the track length inside the tracking volume. The toroidal magnetic field provides for typical bending powers of 3 Tm in the barrel and 6 Tm in the end-cap regions.

Precision tracking is accomplished by more than a thousand chambers, arranged

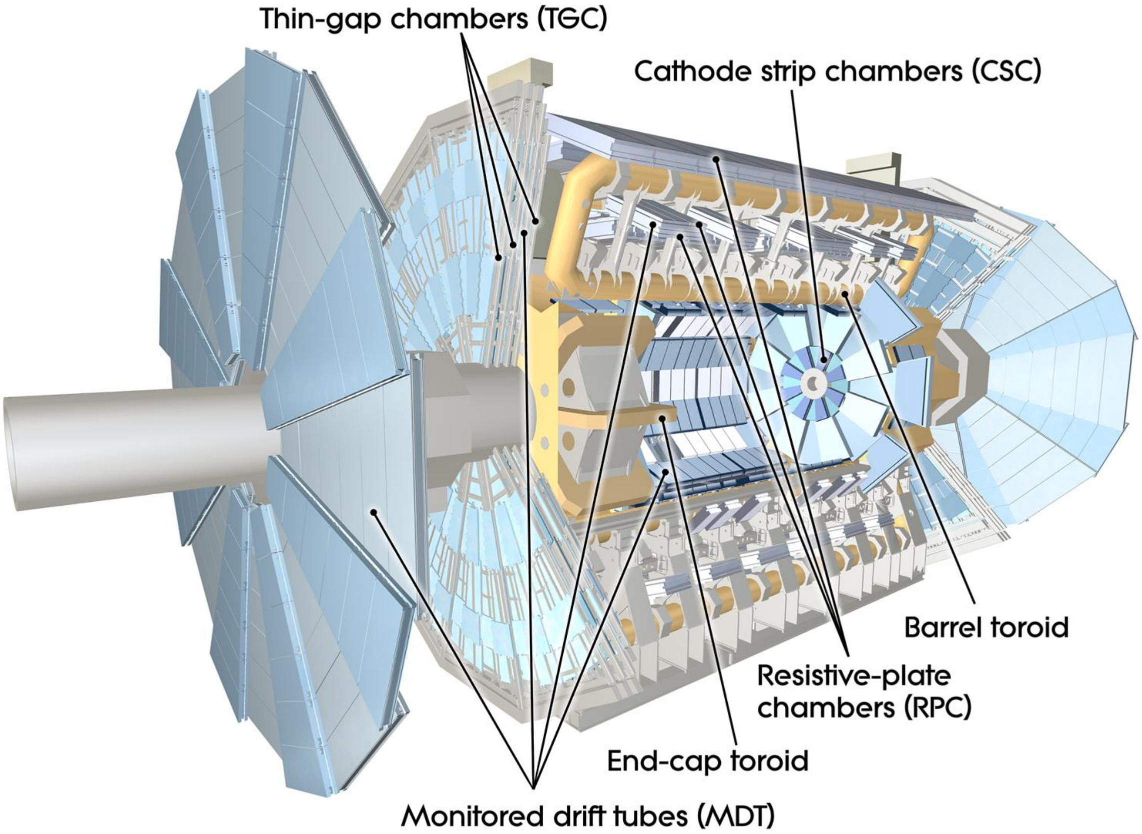

Figure 3.6: Overview of the ATLAS muon spectrometer components and toroidal magnet system. Credit: CERN.

in three concentric cylindrical shells in the barrel and present in trapezoidal form on the end-cap, giving ATLAS its characteristic shape (see Figure 3.6). Two technologies are used:

Monitored Drift Tubes (MDTs) chambers are filled with several layers of tubes, similar to the TRT straws but larger in diameter. The MDTs cover the central region ($|\eta| < 2.7$) and reaches, per chamber, a resolution of 35 μm on the bending plane r–z.

Cathode-Strip Chambers (CSCs) are multi-wire proportional chambers designed to extend the MDT coverage in the forward region ($2.0 < |\eta| < 2.7$) with their higher rate capability. CSCs have a 40 μm (5 mm) resolution in the bending plane r–z (transverse plane r–ϕ).

The precision trackers permit transverse momentum precision of approximately 10% for 1 TeV tracks.

Two other sub-systems are designed to provide fast, robust readout for use in the online trigger and data acquisition (further detailed in the next section). In the barrel central region ($|\eta| < 1.05$), Resistive Plate Chambers (RPCs) give a precision of 10 mm within only 1.5 ns. Thin Gap Chambers (TGCs) reach the forward regions ($1.05 < |\eta| < 2.4$) to measure the muon coordinate with a radial (transverse) resolution of 2–6 mm (3–7 mm) within 4 ns[6].

3.2.4 Online trigger for data acquisition

To discover new particles such as supersymmetric partners with small production cross sections, a very large number of collision events is required. In 2012 the LHC bunch crossing rate was mostly 20 MHz, half of its design value of 40 MHz [30]. Storing the information of all collision events is impractical given the limited disk storage capacity, the time response of some ATLAS sub-systems and, last but not least, the output bandwidth limitation of 400 Hz. Moreover, as the processes of interest for exploring new physics are extremely rare, the vast majority of pp interactions are irrelevant for most ATLAS analyses and can safely be discarded. The event filtering is performed on the fly by the ATLAS trigger system [32]. It is organized into three consecutive levels, each level refining the decisions made at the previous stage by using more information about the event (at a longer time cost in the decision making):

---

[6] This is well below 50 ns, the time between two bunch crossings in 2012 data.

Level One (L1) trigger is hardware based. Custom electronics receive signals from the muon trigger chambers and coarse data from the calorimeter to define "regions of interest" (RoI), which are the η and ϕ coordinates where the L1 trigger sees a potential high-p_{T} muon, electron, photon, jets or large $E_{\mathrm{T}}^{\mathrm{miss}}$. The L1 trigger has less than 2.5 μs to decide if the event contains no RoI and therefore needs to be vetoed. If the event exhibits RoIs, it is sent as input to L2. At that stage, the event rate is reduced from 20 MHz to 75 kHz.

Level Two (L2) is software-based and performs a simplified event reconstruction in 40 ms from the information of all ATLAS sub-detector but limited near the RoI. This step brings the rate of events down to approximately 1 kHz.

Event Filter (EF) employs sophisticated algorithms, similar to the offline software, to fully reconstruct the event in 4 s. This is done using a large farm of CPUs installed near the detector. The final decision of the EF selects the events, at the required rate of 400 Hz, that are recorded for subsequent offline analysis.

3.3 Data quality and integrated luminosity in 2012 dataset

The search for SUSY presented in this dissertation uses the full dataset of proton–proton collisions recorded at $\sqrt{s} = 8$ TeV. During this year of data taking, the LHC delivered an integrated luminosity of 22.8 fb^{-1}, out of which 21.3 fb^{-1} were successfully recorded by the ATLAS detector [31].

The quality of the data is verified as being recorded, as part of the "online monitoring" procedures. Potentially flawed data are flagged *e.g.* if there is the presence of unphysical detector artifacts or bugs in the reconstruction software. In 2012, an integrated luminosity of 20.3 fb^{-1}(more than 95% of the data recorded by ATLAS) passed the online quality requirements and was deemed "good for physics", as shown in Figure 3.7. This illustrates the excellent performance of all ATLAS sub-systems, on both hardware and software levels.

By selecting events containing one or several hard objects (as seen in Section 3.2.4), the ATLAS trigger records hard scattering processes, which are the probes for new physics. However in the same bunch crossing, additional unrelated proton–proton interactions can occur. These interactions, referred to as pile-up, are recorded in the

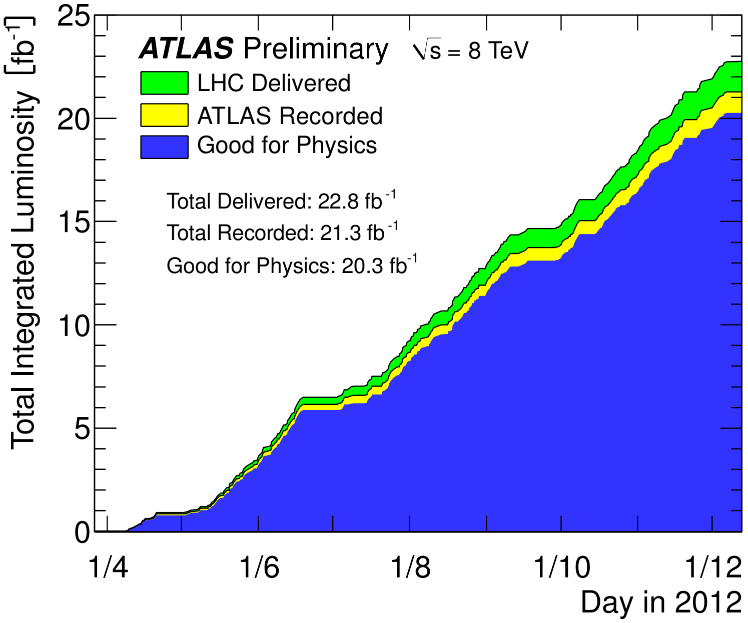

Figure 3.7: Cumulative luminosity versus time delivered by the LHC (green), recorded by ATLAS (yellow), and certified to be good quality data (blue) for the 2012 pp collisions at $\sqrt{s} = 8$ TeV [31].

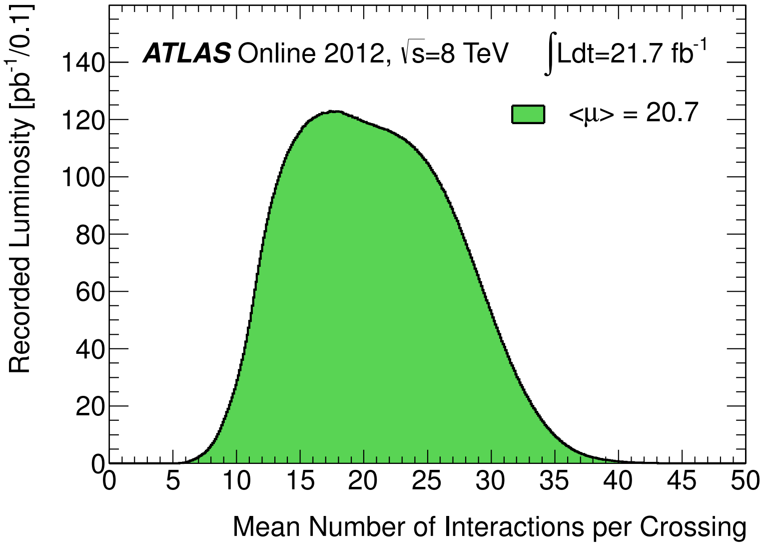

Figure 3.8: Luminosity-weighted distribution of the mean number of interactions per crossing for the full 2012 pp collisions dataset [31].

same event. Several corrections are applied to remove the pile-up while defining reconstructed physics objects. These noise suppression methods generally use the averaged number of interactions per bunch crossing, μ, whose luminosity-weighted distribution is shown in Figure 3.8 for the full 2012 dataset. This real number μ corresponds to the mean of the Poisson distribution on the number of interactions per crossing for each bunch. It serves as a good estimator for pile-up, and subsequently ensures a noise-free reconstruction of the offline physics objects, which are now detailed in the next chapter.

Chapter 4

Object reconstruction

By combining information of the different hardware components previously described, the ATLAS detector is able to reconstruct and identify the passage of four particles: photons, electrons, muons and hadrons. The objects of interest in this thesis are electrons and muons as well as hadron jets coming from a pair of bottom and anti-bottom quarks. After describing their reconstruction and identification techniques, the specifications from the SUSY ATLAS Working Group will be presented. The computation of the missing transverse momentum will be reviewed in this chapter, which ends with a list of the event cleaning cuts designed to ensure high-quality data.

4.1 Lepton identification and isolation

Events containing isolated leptons[1] – mainly coming from the decays of the W and Z bosons – are rarely produced in a hadronic environment such as the LHC. Yet many of the new physics processes have a signature involving one or more isolated leptons. Their identification thus plays a key role in probing new phenomena at the electroweak scale.

4.1.1 Electron reconstruction and identification

Electron reconstruction

The electron reconstruction is the process that establishes if the signals left by a particle in the ATLAS sub-detectors are consistent with the passage of an electron,

---

[1] Throughout this thesis, the term lepton indicates electron $e^{\pm}$ or muon $\mu^{\pm}$.

and computes its four-momentum components.

In the central region ($|\eta| < 2.5$) covered by the inner detectors, the reconstruction technique combines calorimetric and tracking information. First, energy deposits (clusters) in the electromagnetic calorimeter are identified using a "sliding-window" algorithm [33]. A fixed-size window of 3×5 units in η, ϕ is moved accross the electromagnetic calorimeter in steps of one unit $\Delta\eta \times \Delta\phi = 0.025 \times 0.025$. This corresponds to the granularity of the middle layer of the electromagnetic calorimeter, where most of the electron energy deposition occurs. The position of the window is adjusted so that its contained transverse energy is at a local maximum. The efficiency of the initial cluster reconstruction is almost 100% for electrons with $E_{\mathrm{T}} > 20$ GeV [34]. In a second step, the tracks are extrapolated from their last measured point in the ID to the middle layer of the electromagnetic calorimeter in order to check their proximity to the pre-selected clusters. Once a cluster is associated to a track, the electron total energy is determined by correcting the deposited energy observed in the cluster for the estimated fraction of energy measured by the sampling calorimeter. Three other contributions related to the estimated amount of energy losses – in front of the electromagnetic calorimeter, in neighboring cells, and beyond the electromagnetic calorimeter – are added. The four-momentum is derived by combining the tracking and cluster direction and energy measurements.

Outside of the tracking acceptance, another algorithm using only the calorimetric information reconstructs the forward electrons ($2.5 < |\eta| < 4.9$), but these are not used in this thesis.

Electron identification

All reconstructed electrons are further analyzed to discriminate between those of interest for the signal and the background electrons. The former should come from the primary vertex and be "hard" – *i.e.* of high p_{T} – while the latter are mostly misidentified hadrons as electrons, non-isolated electrons and electrons from photon conversion. The identification process in ATLAS employs three hierarchical working points with increasing background-rejection power at some cost to the identification efficiency: *loose*, *medium*, and *tight*. Each level is a cut-based selection on several variables exploiting the shower shape in the cluster, the track quality, the closeness of the tracks to the cluster and the presence of high threshold hits in the TRT. Higher purity is achieved by adding variables and tightening the cuts from the previous level,

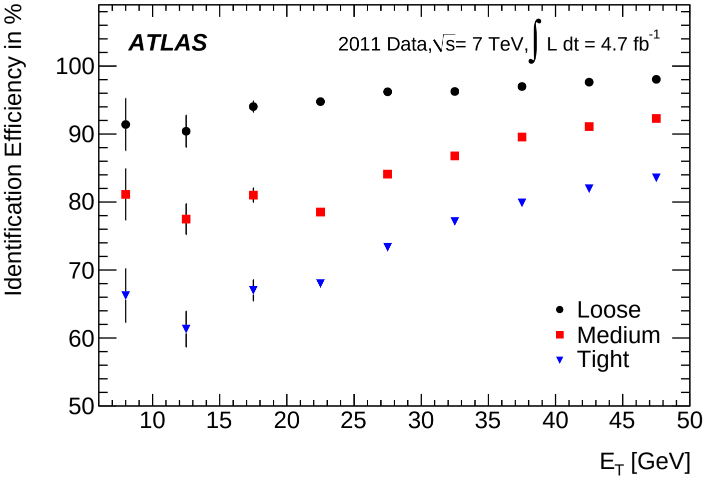

Figure 4.1: Identification efficiencies of central electrons with respect to their transverse energy for the *loose*, *medium* and *tight* working points using 2011 data. Error bars correspond to the total uncertainties [34].

as fully detailed in Reference [34]. The analysis in this thesis uses central electrons that are *medium* and *tight*. Their identification efficiencies range from 80% at 7 GeV to 90% at 50 GeV for the *medium* criteria and from about 65% at 7 GeV to 80% at 50 GeV for the *tight* criteria, as illustrated in Figure 4.1.

4.1.2 Muon reconstruction and identification

The muons produced in ATLAS have energies in the GeV range and are thus minimum ionizing particles [4]. They go through the calorimeters without significant showering and can escape the ATLAS detector. This is when the Muon Spectrometer (MS) enters into action. Ionization signals produced by muons can be used to construct a muon track and determine its momentum using the deflection of the magnetic field from the superconducting toroid magnets. Tracks in the MS are reconstructed in two steps: the hits from the chambers in individual stations are first used to form track segments, then the segments are combined to form a track.

ATLAS reconstruction distinguishes four types of muons, depending on the information available in the different subsystems [35].

Standalone muons are reconstructed entirely from the MS: the measured track is extrapolated to the interaction point.

Combined (CB) muon is the main type of reconstructed muon. Its reconstruction is achieved by spatially matching the independently measured tracks of the MS to the ones from the ID. This type of muon has the highest purity, however they are only reconstructed within the acceptance of the ID, *i.e.* $|\eta| < 2.5$.

Segment-tagged (ST) muons are defined when an extrapolated track from the ID is matched to a track segment in the MS. This recovers the muons failing to leave a full track in the MS.

Calorimeter muons (CaloTag), used only for performance studies, are built by matching an ID track to mimimum ionization clusters from the electromagnetic calorimeter.

The ATLAS Collaboration developed independent reconstruction chains, each having its own algorithm for each category of muon. Analyses in the SUSY Working Group use combined and segment-tagged muons reconstructed with the "chain 1" or *Staco* (statistical combination) [35]. Figure 4.2 shows the muon reconstruction efficiencies for this chain as a function of η as measured from $Z \to \mu\mu$ events in 2012 data. The muon reconstruction efficiency is close to 99% over most of the pseudorapidity range of $|\eta| < 2.5$, except in the regions $|\eta| \approx 0$ and $|\eta| \approx 1.2$ which are partially equipped with muon chambers (due to space required for service and uninstalled chambers). Similarly to electrons, muons have three quality criteria: *loose*, *medium* and *tight* [35]. This analysis makes use of *loose* muons, along with a set of additional identification cuts common for supersymmetric searches (see Section 4.4).

4.2 Jet reconstruction and flavour-tagging

4.2.1 What is a jet?

Unlike electrons and muons, partons (quarks, anti-quarks and gluons) engage in the strong interaction, described by quantum chromodynamics (QCD). When high-energy partons are moving apart, the strong force between them increases with distance up to a breaking point when it is more energetically favourable for a quark-antiquark pair to be created. The direct consequence of confinement is that free quarks and gluons are never observed experimentally. Instead, an outgoing parton generates a cascade of quark-antiquark pairs. These quarks and antiquarks cluster into colour-neutral particles such as pions, kaons and nucleons, all travelling in approximately the same direction as the original parton. This shower of collimated hadrons (accompanied

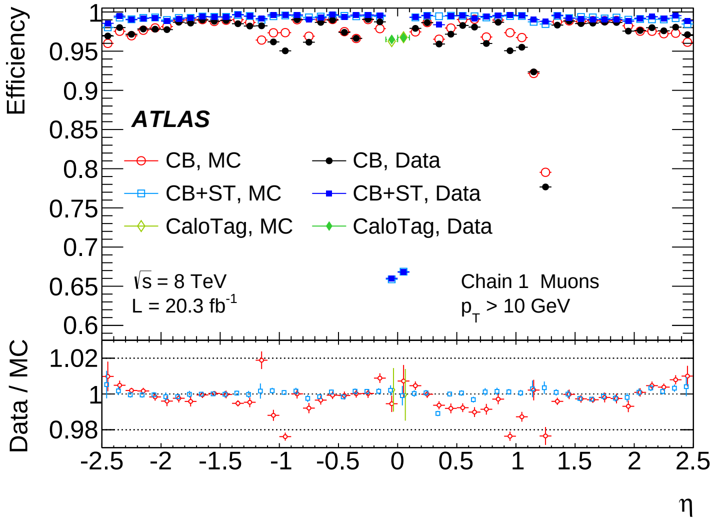

Figure 4.2: η-dependence of the ATLAS muon reconstruction efficiency as measured in $Z \to \mu\mu$ events in 2012 data. The bottom panel shows the ratio between the measured and predicted efficiencies, where errors bars include statistical and systematic uncertainties [35].

also by photons and leptons) is called a "jet"; it is the experimental signature of a quark or a gluon.

A jet can be easily recognized in ATLAS by looking at grouped energy deposits in the calorimeter and a dense spray of tracks in the inner detector (Figure 4.3). However a proper "jet-finding" procedure is required to define a jet. This involves a reconstruction algorithm specifying which signal entity measured in ATLAS should be associated to a jet, as well as a scheme to combine the four-momenta of the jet constituents. Retracing the energy-momentum of the initial parton is not trivial and for this matter, a complex calibration procedure is needed.

4.2.2 Reconstruction algorithm

Calorimeter inputs

The input signals used to reconstruct jets are the "topo-clusters". These are groups of cells in the calorimeter which have received significant energy deposits. The significance is measured as the signal-to-noise ratio |S/N|. A topo-cluster is built iteratively, starting from a seed cell where |S/N| > 4, adding neighboring cells if they verify |S/N| > 2, finally gathering their own neighboring cells, regardless of their |S/N|. The final topo-cluster is treated as a massless pseudo-particle: its energy is

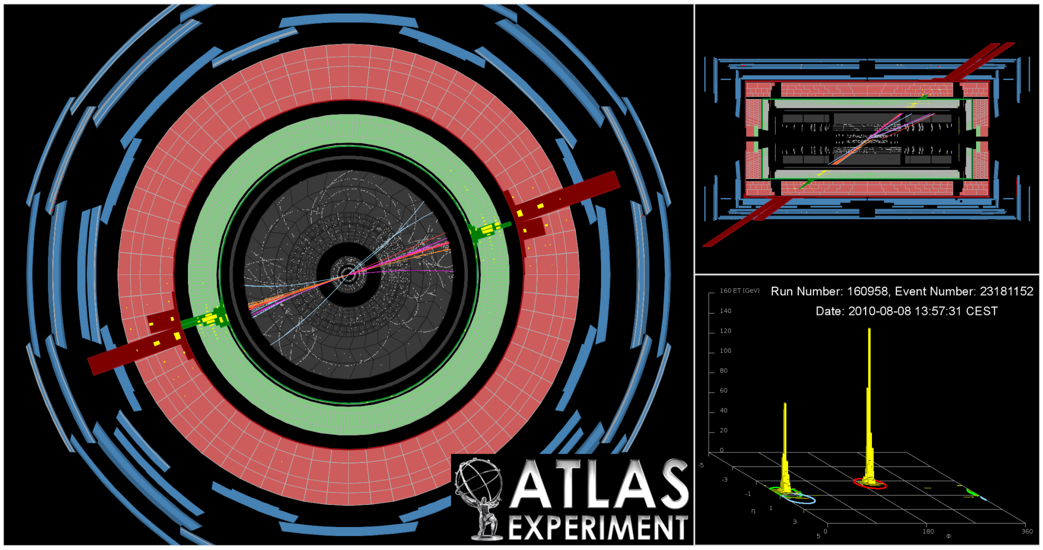

Figure 4.3: Event display of a high-mass di-jet event in the ATLAS detector. The tracks in the inner detector (in grey) align with the energy deposits in the electromagnetic (in green) and hadronic (in red) calorimeters. Muon chambers are shown in blue.

defined as the energy sum of all the included calorimeter cells, its mass is zero and its reconstructed direction is calculated from the pseudorapidities and azimuthal angles of the constituent cells.

Anti-k_t algorithm

The jet reconstruction method commonly used in ATLAS is the anti-k_t algorithm. This sequential recombination procedure compares for all possible pairs of objects (in our case the topo-clusters, but it can be reconstructed particles) the distance d_{ij} between two entities i and j with the distance d_{iB} between the entity i and the beam, defined as:

$$d_{ij} = \min(\frac{1}{k_{t,i}^2}, \frac{1}{k_{t,j}^2})\frac{\Delta R_{ij}}{R^2} \qquad d_{iB} = \frac{1}{k_{t,i}^2}\ , \tag{4.1}$$

where k_t is the transverse momentum of the considered entity, $\Delta R_{ij} = \sqrt{\Delta y^2 + \Delta\phi^2}$ the spatial distance between the two objects i and j in the $y - \phi$ plane and R is the parameter of the algorithm controlling the size of the output jet. If the minimum between all d_{ij} and d_{iB} is d_{ij}, objects i and j will be combined into a new object by adding their four-momenta. If however the minimum is d_{iB}, object i is considered as a jet and is removed from the list of objects at the next iteration. The distances are recalculated and the procedure repeated until no entities are left.

This algorithm satisfies theoretical requirements (order independence, collinear and infrared safety [36]) and has a fast computation. Moreover, by clustering first the entities with highest momentum, soft particles will tend to cluster with hard ones long before they cluster among themselves. As seen in Figure 4.4, the anti-k_t jets are conical with a regular edge. This known shape is experimentally useful to facilitate calibration and remove pile-up noise.

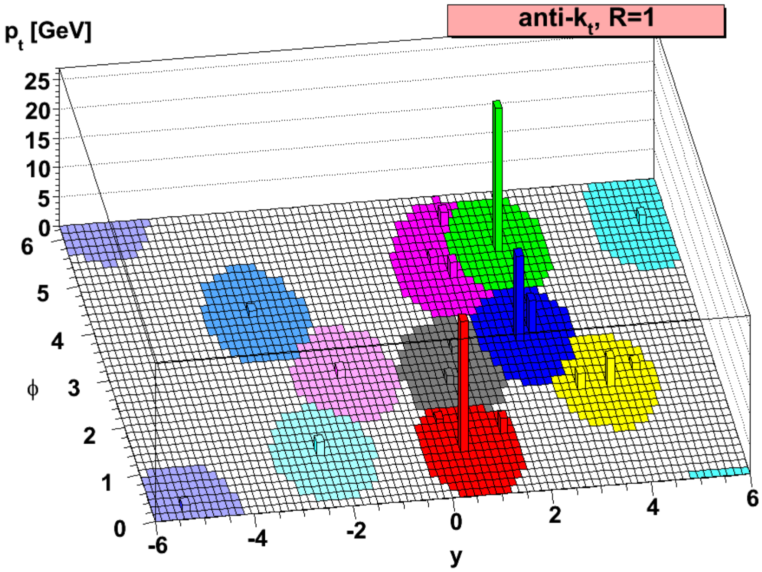

Figure 4.4: Illustration of hard and randomly generated soft "ghost" particles clustered into jets using the anti-k_t algorithm. The resulting hard jets (highest p_{T} peaks) are circular with a radius $R = 1$ as seen in the projected circles on the $\phi - y$ plane [37].

4.2.3 Jet calibration

ATLAS calorimeters are non-compensating: the energy response to hadrons is lower than the response of electrons and photons of the same energy. A calibration procedure is therefore necessary to retrieve the true energy of the jets by restoring the final hadronic energy scale. The method also corrects for detector effects that affect the energy measurement, such as:

Dead material: energy losses in the inactive regions of the detector.

Leakage: energy of particles reaching outside the calorimeters.

Out-of-cone: energy not collected in the jet reconstruction (*e.g.* low momentum particles deflected by the magnetic field).

Particle reconstruction efficiency: signal losses in the calorimeter clustering and jet reconstruction.

ATLAS developed several calibration schemes. The simplest being a p_{T}- and η-dependent correction (detailed later) on the jet energy scale (JES) applied to each jet, which are by default reconstructed at the electromagnetic scale (EM) [38]. A more sophisticated scheme called Local Cluster Weighting (LCW) improves the jet energy resolution by first calibrating the topo-clusters individually before performing the jet finding [39].

Local Cluster Weighting

The topo-clusters are classified as mainly electromagnetic or hadronic depending on the cluster shape properties, in particular the energy density and the longitudinal shower depth. Weights are applied to correct the non-compensating hadronic response. These corrections are derived from the Monte Carlo simulations for single charged and neutral pions. Additional adjustments account for the signal losses outside the topo-clusters and in dead material. The procedure is designated as “local” because it operates on each topo-cluster one-by-one, independently of the jets to be reconstructed.

Jet Energy Scale

Once the jets are reconstructed using topo-clusters calibrated via the local cluster weighting (LCW) method, the calibration scheme referred to as LCW+JES restores the jet energy scale by correcting the jet four-momentum [38, 39]. It proceeds in four subsequent steps:

Step 1: Pile-up offset correction In a recorded event triggered by a hard scattering process, additional unrelated proton–proton interactions can occur. This effect, known as pile-up, includes contributions from within the event bunch crossing (in-time pile-up) and from adjacent bunch crossings (out-of-time pile-up). The energy of the jets are over-estimated due to pile-up noise. A correction is performed by estimating the amount of transverse momentum generated by the pile-up, and substract this offset from the reconstructed jet p_{T}. This adjustment is derived from MC simulations; the number of reconstructed primary vertices N_{PV} is used to estimate the in-time pile-up contribution and the expected average number of interactions per bunch crossing, μ, helps in characterizing the out-of-time pile-up.

Step 2: Origin correction Jets are reconstructed using the centre of the ATLAS detector. A correction to the calorimeter jet direction is applied that makes the jet pointing back to the primary event vertex. The primary vertex of an event is identified as the vertex with the largest $\sum p_{\mathrm{T}}^2$ of the associated tracks.

Step 3: Energy and η calibration The jet energy and pseudorapidity are adjusted using calibration factors derived from simulated Monte Carlo QCD events. The correction is based on the jet energy response $\mathcal{R}^{\mathrm{jet}}$, defined as the ratio of the reconstructed jet energy E_{reco}, measured with the ATLAS calorimeter topo-clusters, and the energy E_{truth} of reference jets, also called "truth jets". The truth jets are built using the same algorithm as the reconstructed jets, but using as inputs the four-momenta of final state particles simulated by the Monte Carlo generator. First, reconstructed and truth jets are matched if they are each isolated (no other jet of the same type is found within a given ΔR) and their angular separation is small: $\Delta R < 0.3$. The average jet energy response $\langle \mathcal{R}^{\mathrm{jet}} \rangle$ is computed for each pair of matched jets in bins of E_{truth} and reconstructed jet pseudorapidity η^{det} (before the origin correction). The jet energy calibration function is the inverse of the average jet response, for a given (E_{truth}, η^{det})-bin. After the jet origin and energy corrections, the jet pseudorapidity is further adjusted, based on the average difference $\Delta\eta = \eta_{\mathrm{truth}} - \eta_{\mathrm{origin}}$. The change is small ($\Delta\eta < 0.01$), except in the poorly instrumented transition regions where topo-cluster energies are underestimated, therefore causing a bias in the jet direction.

Step 4: Residual in situ corrections A residual correction derived in situ is applied as a last step to jets reconstructed in data.

Figure 4.5 shows the average energy response for various jet energies as a function of the jet pseudorapidity η^{det} measured in the detector frame of reference.

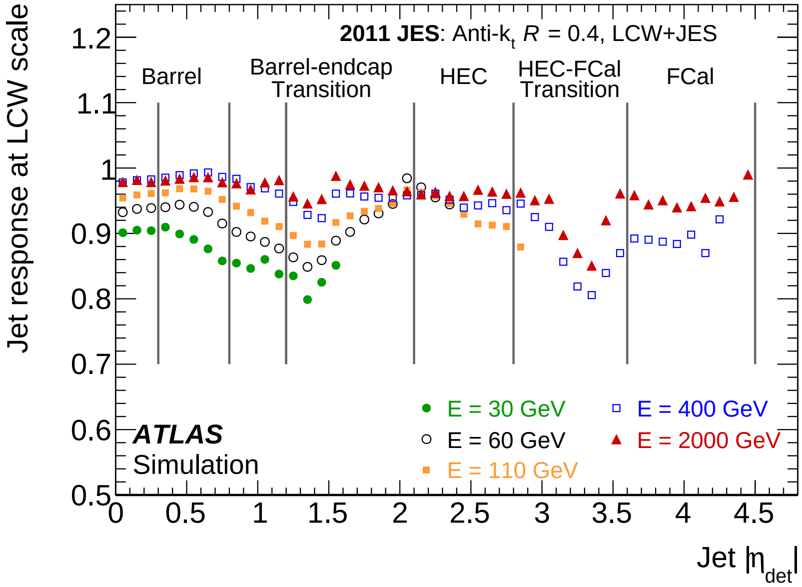

Figure 4.5: Average response of simulated jets formed from topo-clusters calibrated using the LCW scheme for various truth-jet energies as function of the uncorrected (detector) jet pseudorapidity η^{det}. Also indicated are the different calorimeter regions. The inverse of the jet response corresponds to the average jet energy scale correction in each η^{det} bin [39].

Jet Energy Resolution

The jet energy resolution (JER) has been measured with two different in situ methods using 2010 data at $\sqrt{s} = 7$ TeV with an integrated luminosity of 35 pb^{-1} [40]. Adding the tracking information to the calorimeter-based jets improves the jet energy resolution by 10% (5%) at low (high) p_{T} for the jets calibrated using the LCW+JES scheme. For the subpopulation of these jets falling in the central region where $|\eta| < 0.8$, the JER is below 15% for jets with $p_{\mathrm{T}} = 30$ GeV and goes below 10% for jets with $p_{\mathrm{T}} > 100$ GeV. The Monte Carlo simulation of the jet energy resolution has been compared with data and the agreement is within 10% overall.

4.2.4 Flavour identification

The correct calibration of the complex objects known as jets is a milestone on its own. The ATLAS Collaboration has gone one step further by developing algorithms capable of identifying the flavour of the quark initiating the jet. The ability to identify jets originating from b-quark fragmentation (b-tagging) is of crucial importance within the scope of the LHC program: b-quarks are the primary decay products of the top quark, the Standard Model Higgs boson main decay mode is $h \to b\bar{b}$ and several supersymmetric theories favour b-quark production via the decays of third generation superpartners.

The flight of the b-hadron

Bottom quarks fragment into bound states referred to as b-hadrons. The b-hadrons usually take 70% of the initial b-quark momentum [41], thus conserving most of the direction and energy information of the initial b-quark. The key feature of b-hadrons is their relatively long lifetime, of the order of the picosecond. A b-hadron created in a high-energy collision can therefore travel several millimeters away from the collision point before decaying. Such a decay gives rise to a secondary vertex, significantly displaced with respect to the primary vertex. This characteristic signature of "displaced vertices" inside b-jets can be reconstructed in the ATLAS detector, thanks to the precision of its tracking systems.

The idea behind all b-tagging methods is to build a discriminating variable, called jet weight, that would separate the b-jets from the lighter jets. A jet having a weight above a certain cut value is then tagged as b-jet. The b-tagging algorithms have become more and more complex; the tool used in the analysis of this thesis combines three taggers developed at the earlier stage of jet flavour identification [42]. These taggers are introduced below.

Impact parameter-based algorithms

The track impact parameter is the distance of closest approach between the extrapolation of the track and the primary vertex, as illustrated in Figure 4.6. The z coordinate at this point of closest approach is referred to as the longitudinal impact parameter z_0 and the distance in the $r\phi$ projection is the transverse impact parameter d_0. The latter entity is signed: it is defined as positive if the extrapolated track crosses the jet direction in front of the primary vertex, and negative otherwise. As the b-hadron must lie along its flight path, tracks from a b-hadron decay tend to have large and positive d_0, while tracks not coming from a displaced vertex have a d_0 distribution centered around zero. This asymmetry towards positive values for b-jets can be seen in Figure 4.7, showing the signed significance $d_0/\sigma(d_0)$, where $\sigma(d_0)$ is the experimental uncertainty on the transverse impact parameter. This ratio gives more weight to precisely measured tracks. The high-performance IP3D algorithm uses a likelihood ratio technique, comparing the impact parameter of tracks associated to the jet with two-dimensional normalized and smoothed reference distributions of $d_0/\sigma(d_0)$ and $z_0/\sigma(z_0)$, generated using Monte Carlo for both b- and light jet hypotheses.

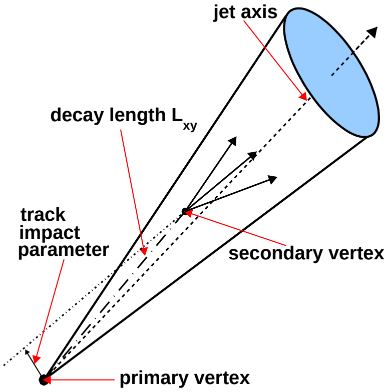

Figure 4.6: Schematic view of a displaced vertex inside a jet, with three charged particles tracks. One track is extrapolated near the primary vertex, where its impact parameter is shown [43].

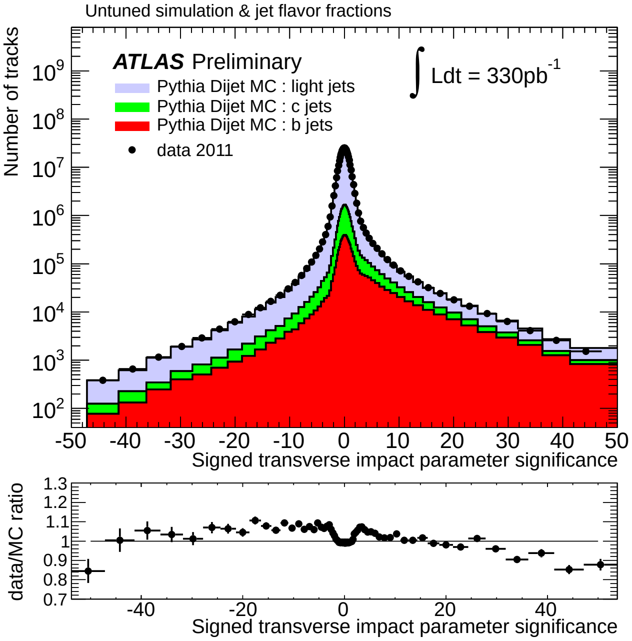

Figure 4.7: Distributions of the signed significance transverse impact parameter in data and MC simulations for b-, c- and light jets [42].

Secondary vertex-based algorithms

The "SV" taggers reconstruct the secondary vertex by combining tracks associated to the jet that are sufficiently away from the primary vertex [42]. An iterative procedure removes the least compatible tracks until the χ^2 fit of the candidate vertex becomes satisfying. The key discriminating variable here is the signed decay length significance $L/\sigma(L)$, measured in 3D. The SV1 tagger adds other criteria to increase discriminating power, such as the vertex invariant mass, the energy fraction of the tracks associated to the vertex with respect to all tracks in the jets, the angle between the jet axis and the line formed by the primary and secondary vertices. The SV1 algorithm combines these variable using a likelihood ratio technique.

JetFitter

The presence of a b-hadron implies its delayed decay into a charm-quark forming a d-hadron, thus creating another displaced, third vertex in a *b*-jet. However the secondary vertex finders introduced above fit all displaced tracks to one inclusive vertex. The JetFiller algorithm [44] performs a multi-vertex fit with the assumption that the primary vertex is aligned with both the *b*- and *d*-hadron decay vertices, as depicted in Figure 4.8. A single charge particle track can thus be reconstructed as a vertex at the track intersection with the b-hadron flight axis. The discrimination between *b*-, *c*- and light jets is based on a likelihood using similar variables as in the SV1 tagger.

Combined tagger MV1

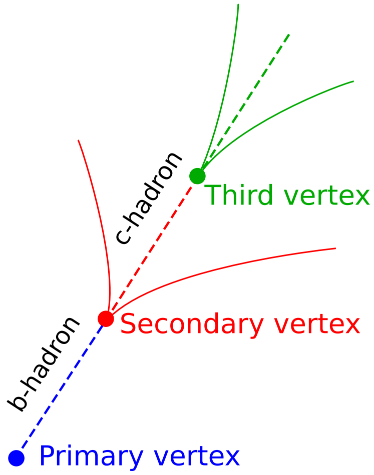

Figure 4.8: Schematic view of the primary, secondary and third vertices within a jet, the two latters issued from the b- and d- hadron decays respectively. JetFitter algorithm is based on the hypothesis of their alignment [44].

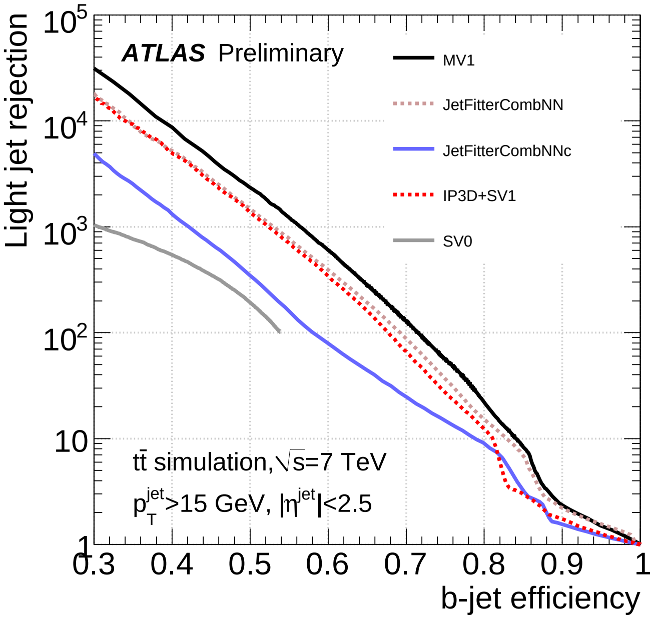

Figure 4.9: Light-jet rejection as a function of the *b*-tag efficiency for several *b*-tagging algorithms in a sample of simulated $t\bar{t}$ events at $\sqrt{s} = 7$ TeV. [45].

More sophisticated *b*-tagging algorithms achieve a higher separation power by combining taggers, thus taking the correlations of the various input quantities into account. This is generally done using an Artifical Neural Network (ANN), a computational model structured schematically in a similar way as a human brain, where layers of interconnected processing elements (the artifical neurons) work in unison to solve specific problems. In the context of jet classification, the question is to determine the jet flavour. JetFitterCombNN combines the taggers IP3D and JetFitter in an ANN, where the response of each neurone in the last layer is a probability of the jet to have a given flavour. The final jet weight is built using a likelihood ratio from these probabilities. The JetFitterCombNNc algorithm is identical to JetFitterCombNN with the exception that the neural network is trained to reject c-jets rather than light-flavour jets.

The b-tagging algorithm used in this thesis is MV1, which employs an artifical neural network based on IP3D, SV1 and JetFitterCombNN. It is trained with b-jets as signal and light-flavour jets as background, and computes a tag weight w_{MV1} for each jet. All jets having a MV1 weight above a certain cut value are then tagged as b-jets. To each cut value of MV1 weight is associated a given b-tagging efficiency (ϵ_b), defined as the fraction of true b-jets that are tagged as b-jets. The true jet flavour is determined in Monte Carlo by spatially matching the truth jets (defined in Section 4.2.3) with the Monte Carlo quarks from the particle-level collection. If a b-quark is within $\Delta R < 0.3$ of the truth jet axis, the truth jet is labelled truth b-jets; if not, the same check is performed with c-quark, τ-lepton and in the remaining case the jet is label as light truth jet.

The performance of b-tagging algorithms is characterised by the b-tagging efficiency ϵ_b and the rejection rate of light-jets R_u, defined as the inverse of the fraction of true light-jets that are falsely tagged as b-jets.

Figure 4.9 shows the performance curves of several taggers, plotting the $R_u - \epsilon_b$ correspondance. Going at higher efficiency has a price: the light jet rejection rate decreases, thus increasing the light jet contamination in the tagged population. MV1 performs well, achieving the highest light jet rejection rate compared to the other taggers for all the efficiency range.

4.3 Missing Transverse Momentum

In hadron-hadron collisions, the longitudinal boost of the initial state is not known; colliding partons share a variable fraction of the proton momentum. However, in the transverse plane, momentum conservation is expected unless some particles not detectable by ATLAS carry part of the energy. These unseen objects can be neutrinos or perhaps weakly-interacting stable supersymmetric partners. Using the ATLAS hermetic design, it is possible to measure the momentum[2] imbalance $E_{\mathrm{T}}^{\mathrm{miss}}$, obtained from the negative vector sum of the momenta of all particles detected:

$$\boldsymbol{E}_{\mathrm{T}}^{\mathrm{miss}} = -\sum \boldsymbol{p}_{\mathrm{T}}^{\mathrm{visible}}. \tag{4.2}$$

This variable plays a key role in most searches for SUSY. Its computation requires care to avoid double-countings, while suppressing pile-up contamination.

4.3.1 Calculation

The core of the missing transverse momentum computation happens in the calorimeter. The $E_{\mathrm{T}}^{\mathrm{miss}}$ algorithm is object-based: instead of adding all calorimeter energy deposits independently, the $E_{\mathrm{T}}^{\mathrm{miss}}$ calculation uses reconstructed physics objects. This allows proper calibration of the calorimeter cells according to which physics object they are associated to. The association of calorimeter cells with a reconstructed and identified high-p_{T} parent object follows a specific order to avoid double-counting contributions, as the same cell can be used by different reconstruction algorithms [46]. First cells corresponding to *medium* electron clusters are taken, then those of photons ($p_{\mathrm{T}} > 10$ GeV), soft-jets (built using anti-k_t with $\Delta R = 0.6$ and of $7 < p_{\mathrm{T}} < 20$ GeV), jets (anti-k_t with $\Delta R = 0.4$, $p_{\mathrm{T}} > 20$ GeV) and finally muons. Cells outside any reconstructed objects (`CellOut` term below) are added in the $E_{\mathrm{T}}^{\mathrm{miss}}$ calculation, to account for soft hadronic activity not resolved into jets. The missing transverse momentum is thus given by:

$$E_{\mathrm{x\ (y)}}^{\mathrm{miss}} = E_{\mathrm{x\ (y)}}^{\mathrm{miss,\ electrons}} + E_{\mathrm{x\ (y)}}^{\mathrm{miss,\ photons}} + E_{\mathrm{x\ (y)}}^{\mathrm{miss,\ jets}} + E_{\mathrm{x\ (y)}}^{\mathrm{miss,\ softjets}} + E_{\mathrm{x\ (y)}}^{\mathrm{miss,}\ \mu} + E_{\mathrm{x\ (y)}}^{\mathrm{miss,\ CellOut}}$$

where each term is calculated as the negative sum of the calibrated reconstructed objects, projected onto the x and y directions.

The muon contribution $E_{\mathrm{x\ (y)}}^{\mathrm{miss,}\ \mu}$ has two components: $E_{\mathrm{x\ (y)}}^{\mathrm{miss,}\ \mu\text{-tracks}}$ and $E_{\mathrm{x\ (y)}}^{\mathrm{miss,}\ \mu\text{-calo}}$. $E_{\mathrm{x\ (y)}}^{\mathrm{miss,}\ \mu\text{-tracks}}$ is built from the negative sum of the transverse momenta of muon tracks from the spectrometer, using matched inner detector tracks if available. $E_{\mathrm{x\ (y)}}^{\mathrm{miss,}\ \mu\text{-calo}}$ corresponds to the energy loss by muons in the calorimeter. This term is added into the $E_{\mathrm{T}}^{\mathrm{miss}}$ calculation only if the muon falls within a jet or is outside tracker acceptance. For isolated muons, the momentum computation already accounts for their energy

---

[2] In the ultra-relativistic approximation where $E \sim p$, the vectors $\boldsymbol{E}_{\mathrm{T}}^{\mathrm{miss}}$, $\boldsymbol{p}_{\mathrm{T}}^{\mathrm{miss}}$ and their magnitudes $E_{\mathrm{T}}^{\mathrm{miss}}$, $p_{\mathrm{T}}^{\mathrm{miss}}$ are used interchangeably.

loss in the calorimeter, therefore $E_{\mathrm{x\,(y)}}^{\mathrm{miss},\ \mu\text{-calo}}$ is not added to avoid double-counting of energy in the total $E_{\mathrm{T}}^{\mathrm{miss}}$ estimation.

To improve the calculation of the $E_{\mathrm{x\,(y)}}^{\mathrm{miss,\ CellOut}}$ term, low-p_{T} tracks are added and topo-clusters are matched to ID tracks when possible. The track momentum is preferentially used instead of the topo-cluster energy to benefit from the better tracker resolution at low momentum [46].

The missing transverse momentum is very sensitive to pile-up, which distorts the reconstructed jet momenta and creates additional undesired jets. Several methods have been developed to mitigate the impact of pile-up. The jet momentum is corrected using the jet-area method [47]. It assumes that the pile-up activity in an event can be quantified using the median p_T density ρ^{event} measured in the event and that the susceptibility of a jet to pile-up scales with its area A^{jet}. The corrected jet $p_{\mathrm{T}}^{\mathrm{corr}}$ is calculated as $p_{\mathrm{T}}^{\mathrm{jet}} - \rho^{\mathrm{event}} \times A^{\mathrm{jet}}$. To suppress the additional jets originating from pile-up, a cut is applied based on the jet vertex fraction JVF, defined in Section 4.4.3.

4.3.2 Performance

The performance of the missing transverse momentum computation has been assessed in both Monte Carlo simulation and 2012 data. A very good agreement between the two is observed in the $E_{\mathrm{T}}^{\mathrm{miss}}$ distributions in $Z \to \mu\mu$ decays, as illustrated in Figure 4.10 (left). The $E_{\mathrm{T}}^{\mathrm{miss}}$ resolution is rapidly degraded due to pile-up – by a factor two when the number of reconstructed vertices in the event goes from 5 to 20 – but after pile-up suppression this dependence is greatly reduced, as shown by the flatter red curve in Figure 4.10 (right).

4.4 SUSY Working Group object definitions

In addition to the standard ATLAS criteria described in the previous sections, a set of recommendations is used within the SUSY Working Group to facilitate comparison across analyses. The common SUSY objects are first predefined as "baseline". Then potential overlaps are removed. Lastly, isolation criteria are applied on surviving objects, which are deemed as "signal" and enter the final selection.

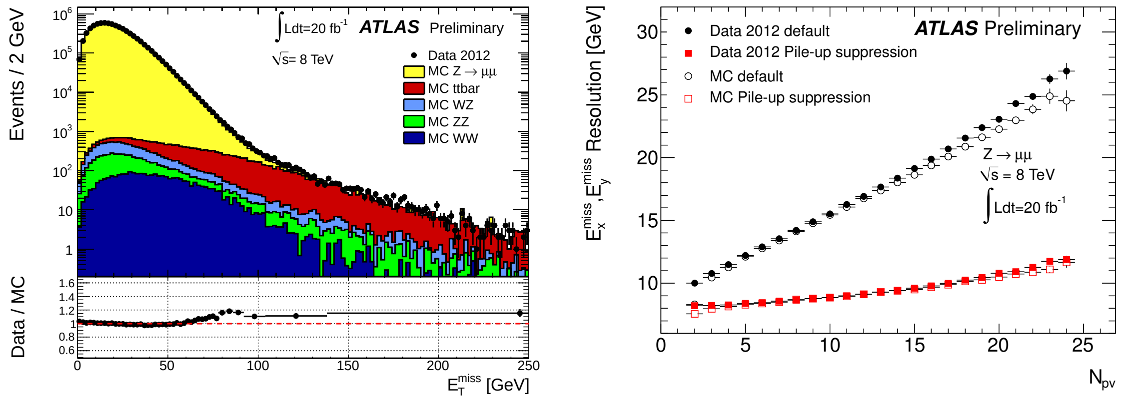

Figure 4.10: Left: $E_{\mathrm{T}}^{\mathrm{miss}}$ distributions in MC simulation (weighted by cross section and stacked) and 2012 data (overlaid). Right: $E_{\mathrm{T}}^{\mathrm{miss}}$ resolution before (black dots) and after pile-up supression (red dots) with respect to the number of reconstructed vertices in the event. Both measurements are performed in $Z \to \mu\mu$ events using 2012 data. Sources: [46–48].

4.4.1 Baseline objects

Baseline electrons must satisfy the *medium*++ identification criteria, a modified working point reoptimised to account for the high trigger rates and the pile-up due to the increased instantaneous luminosity of the 2012 data. Baseline muons are identified using the *loose* working point [35]. A cut on the transverse energy $E_{\mathrm{T}} > 10$ GeV is applied for both leptons. The acceptance in η for electron is $|\eta| < 2.47$ to select only central electrons, which are reconstructed using an algorithm optimised for high p_{T}. Muons are required to have a pseudorapidity $|\eta| < 2.4$. If electrons pass through regions of the electromagnetic calorimeter where the signal is not read out, mostly due to dead optical transmitters, these electrons are discarded. Regarding the muons, quality criteria of the track in the ID need to be sufficient to remove fake backgrounds and achieve an optimal energy resolution. This is done by requiring a minimum number of signal hits and maximum number of holes (*i.e.* missing expected measurement) in the pixel tracker and SCT. The multiplicity of TRT outliers – isolated straw pulses or TRT tracks which do not spatially match a track from the pixel and SCT – is also constrained.

Baseline jets must have a transverse momentum $p_{\mathrm{T}} > 20$ GeV and be within $|\eta| < 4.5$. Because electron clusters may be simultaneously reconstructed as jets (the reconstruction algorithms operate independently), baseline jets are subject to the electron-jet overlap removal step (see next section) after passing the p_{T} cut. If the jets are not removed during this overlap removal, they are deemed baseline provided they do not fall in the "bad" jet category, as explained in Section 4.4.4.

4.4.2 Overlap removal

One single baseline object can fall in more than one category, being therefore effectively double-counted. For example, one isolated electron is typically reconstructed both as an electron and as a jet. To mitigate any duplication between reconstructed leptons or between leptons and jets, a procedure to remove overlaps between final state objects is therefore used as follows:

Step 1 If any two baseline electrons (e_1 and e_2) lie within a distance $\Delta R(e_1, e_2) < 0.1$ of each other, the electron with the lowest cluster E_{T} is rejected.

Step 2 If a baseline jet j and a baseline electron e surviving Step 1 lie within a distance $\Delta R(j, e) < 0.2$ of each other, the baseline jet is rejected.

Step 3 If a baseline jet j and a baseline electron e surviving Step 2 lie within a distance $\Delta R(j, e) < 0.4$ of each other, the baseline electron is rejected.

Step 4 If a baseline jet j and a baseline muon μ lie within a distance $\Delta R(j, \mu) < 0.4$ of each other, the baseline muon is rejected.

4.4.3 Signal objects

After undergoing the overlap removal scheme, baseline objects receive stricter signal criteria, such as higher p_{T}, increased thresholds on object quality, isolation and impact parameter.

Signal lepton candidates should have $p_{\mathrm{T}} > 25$ GeV. Signal electrons need to pass the *tight*++ requirements, a revisited algorithm deriving from the *tight* working point, which was initially designed for the startup of LHC in low-luminosity conditions [34]. Signal muons have to satisfy the *loose* [35] criterium.

Non-prompt leptons are removed with cuts on the track parameters: the significance of the transverse impact parameter d_0[3] is required to satisfy $|d_0|/\sigma_{d_0} < 5$

---

[3] A track in ATLAS is parametrized at the perigee, the point of closest approach with respect to the primary vertex of the event. The transverse impact parameter d_0 is the radial distance from the perigee to the primary vertex.

(3) for the electron (muon) and the longitudinal impact parameter z_0[4] must satisfy $|z_0 \sin\theta| < 0.4$ mm for both lepton types, where θ is the polar angle of the track with respect to the z-axis.

For assessing the lepton isolation, the variables used are the scalar sum of the p_{T} of the tracks associated with the primary vertex and within a cone $\Delta R = 0.3$ of the lepton track ($p_{\mathrm{T}}^{\mathrm{cone}\,0.3}$), and the scalar sum of the transverse energies E_{T} of the calorimeter cell clusters within $\Delta R = 0.3$ of the signal lepton candidate ($E_{\mathrm{T}}^{\mathrm{cone}\,0.3}$). The latter receives a correction to account for the pile-up. The contribution due to the object itself is not included in either sum. Signal electrons should have the sum $p_{\mathrm{T}}^{\mathrm{cone}\,0.3}$ ($E_{\mathrm{T}}^{\mathrm{cone}\,0.3}$) lower than 16% (18%) of the electron transverse energy. For muons, both sums $p_{\mathrm{T}}^{\mathrm{cone}\,0.3}$ and $E_{\mathrm{T}}^{\mathrm{cone}\,0.3}$ should be lower than 12% of the muon transverse energy. In all these cuts, E_{T} is capped at 30 GeV, making the isolation requirement absolute rather than relative at high E_{T}. This option reduces the lepton fake rate at high p_{T}.

The signal jets consist of the sum of two subcategories: central and forward jets. Central jets are baseline jets satisfying $|\eta| < 2.4$, $p_{\mathrm{T}} > 25$ GeV and $|\mathrm{JVF}| > 0.5$ for jets with $p_{\mathrm{T}} < 50$ GeV. The JVF stands for Jet Vertex Fraction and is defined as the p_{T}-weighted fraction of tracks matched to the jet which are associated with the hard scattering vertex:

$$\mathrm{JVF} \;=\; \sum_{\text{jet tracks} \to \text{HS}} p_{\mathrm{T}} \;/ \sum_{\text{jet tracks}} p_{\mathrm{T}} \tag{4.3}$$

where the “jet tracks” are the tracks matched to the jet and the numerator sums the jet-tracks associated to the hard scatter HS. Jets with no associated tracks are assigned JVF $= -1$. Ensuring $|\mathrm{JVF}| > 0.5$ means that at least half of the jet’s track p_{T} must be traceable to the hard scatter, which is useful for pile-up suppression. The robustness against pile-up in the jets has been checked in 2012 data by looking at the correlation between the number of jets and the average number of pile-up interactions per bunch crossing μ. The check is performed for events passing the selection of the “QCD validation” region – enriched in jets – defined in Section 5.5.1. Figure 4.11 shows the distributions of baseline jets (before the JVF cut is applied) as function of μ, for electron and muon selections separately. Each data-taking period is weighted by its luminosity. Figures 4.12 show the same distributions after applying the JVF cut, which exhibits a much flatter shape, as expected for selection not affected by pile-up.

---

[4] The longitudinal impact parameter z_0 is the z-coordinate of the track’s perigee with respect to the primary vertex.

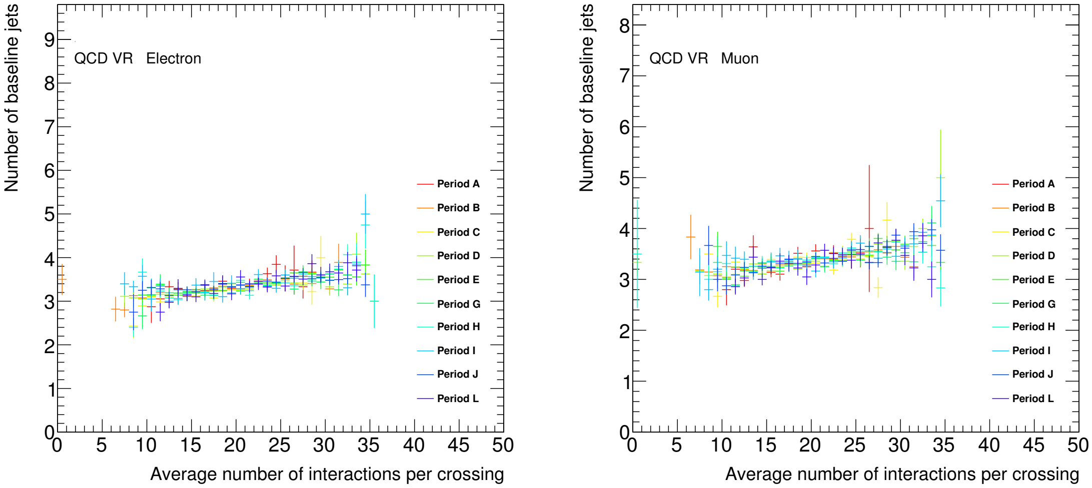

Figure 4.11: Luminosity-weighted yields of number of baseline jets as a function of $\langle\mu\rangle$, the average number of interactions per bunch crossing, for the electron selections (left) and the muon selections (right).

Forward jets are of higher transverse momentum $p_{\mathrm{T}} > 30$ GeV satisfying $2.4 < |\eta| < 4.9$.

The b-jets are tagged using the MV1 algorithm. As the b-tagging algorithm requires the tracks from the ID, only central jets (of acceptance $|\eta| < 2.4$) can be candidates for b-jets.

4.4.4 Event cleaning

Some events can contain undesired instrumental effects or corrupted data. In order to not compromise physics results, events failing a number of quality cuts, which are specified by the standard SUSY event cleaning criteria, are discarded. This procedure reduces the event yields by 1 to 5%.

Data-quality Data acquisition runs when the LHC delivered stable beams and the ATLAS detector was operating properly, with both the solenoid and toroid fields running at nomimal conditions, are recorded on a “Good Run List”. Only events from the “good” runs are selected for data analysis.

Primary vertex Vertices compatible with the proton-proton interactions are reconstructed using tracks from the inner detector. Events are analysed if the primary vertex has five or more tracks, each with transverse momentum $p_{\mathrm{T}} > 400$ MeV.

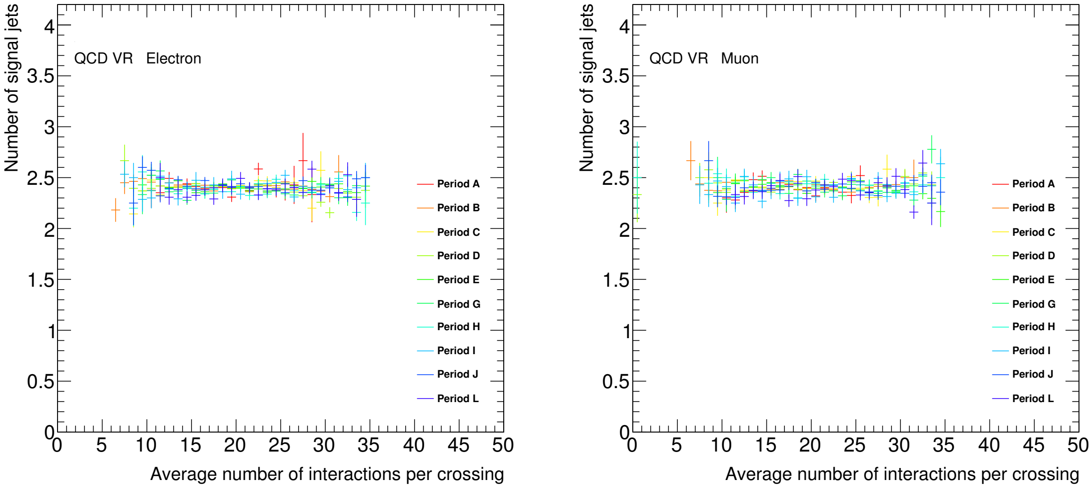

Figure 4.12: Luminosity-weighted yields of number of signal jets as a function of $\langle\mu\rangle$, the average number of interactions per bunch crossing, for the electron selections (left) and the muon selections (right).

Data corruption A problem in the Timing, Trigger and Control (TTC) caused incomplete events to be written to the buffer. Also the liquid argon and tile calorimeters were affected with noise burst, non-operational cells leading to a fake source of missing energy. These events received error flags due to corrupted data and are removed.

Cosmic muons Cosmic rays that hit the Earth's atmosphere can also produce muons that can enter the detector and occasionally mimic the trajectory of a muon from a beam collision. To suppress this cosmic muon background, event are rejected if they contain a muon having transverse impact parameter with respect to the primary vertex $|d_0| > 0.2$ mm or longitudinal impact parameter with respect to the primary vertex $|z_0| > 1$ mm.

Bad muons Events containing muons with $\frac{\sigma_{q/p}}{|q/p|} \geq 0.2$ (charge over momentum and its associated uncertainty $\sigma_{q/p}$) are excluded from the analysis selection to veto events with potentially mismeasured muons. Such fake muons are a potential source of fake $E_{\mathrm{T}}^{\mathrm{miss}}$. This cleaning cut is applied before overlap removal (Section 4.4.2).

Bad jet event veto Fake (or "bad") jets are jets not associated to real energy deposits in the calorimeters. A set of cuts having a high rejection against fake jets while preserving an efficiency close to 100% for signal jets has been designed. Bad jets arise from various sources, ranging from hardware problems, LHC beam background and cosmic-ray showers. The selection criteria are based on the quality of the fit on the calorimeter pulse shape, on the fraction of jet energy belonging to specific calorimeter samples and on the amount of jet charged energy fraction as measured in the inner detector. The selections are summarized here [49]. Events are rejected if any of the jets with $p_{\mathrm{T}} > 20$ GeV satisfies the `VeryLooseBad` jet definition. This is done after Step 1 of the overlap removal procedure detailed in Section 4.4.2.

Chapter 5

Search for Supersymmetry in final states with one lepton, two b-jets consistent with a Higgs boson, and missing transverse momentum

The search for supersymmetric particles is among the primary goals of the LHC physics program. As mentioned in the introduction, Supersymmetry constitutes an elegant theoretical framework addressing several of the Standard Model's shortcomings. The strategy in the ATLAS SUSY group has been to explore as much of the broad SUSY parameter space as possible to include the maximum number of scenarios. After the LHC results put stringent limits on the masses of gluinos and squarks [50], electroweak (EW) SUSY – which refers to the direct production of the Standard Model electroweak superpartners – could be the dominant process observable in the full LHC Run 1 data [51]. The work of this thesis is motivated by an ATLAS search for directly pair-produced electroweakinos (chargino and neutralino), leading to the presence of a lepton, two bottom-tagged jets originating from a SM-like Higgs boson and transverse missing energy in the final states. For the first time a Higgs boson was included in the possible cascade, probing its couplings to both SUSY particles and fermions. This chapter contextualizes the search, describes the signal models considered and the simulated samples used. The optimization strategy and resulting signal regions will be detailed before focusing on the background estimation techniques. The analysis is reported in an internal ATLAS supporting note [52]. It has been published [53] with two other searches probing the Higgs decay modes $\gamma\gamma$ and $WW \to q\bar{q}\ell\nu$.

5.1 Context of the search

Within a large class of SUSY models, it is expected that pair production of strongly interacting sparticles – gluinos $\tilde{g}$ and squarks $\tilde{q}$ – constitutes the dominant SUSY production cross sections. The main production modes are:

$$pp \to \tilde{q}\tilde{q},\ \tilde{q}\tilde{g},\ \tilde{g}\tilde{g} + X \tag{5.1}$$

together with the charge conjugated processes, with the X representing the different final states, mostly energetic jets, significant transverse missing energy and possible leptons. Electroweak production of sleptons $\tilde{\ell}^{\pm}$, charginos $\tilde{\chi}^{\pm}$ and neutralinos $\tilde{\chi}^{0}$, through the modes:

$$pp \to \tilde{\chi}_1^{\pm}\tilde{\chi}_1^{\mp},\ \tilde{\chi}_1^{\pm}\tilde{\chi}_i^{0},\ \tilde{\chi}_1^{\pm}\tilde{\chi}_j^{0},\ \tilde{\chi}_i^{0}\tilde{\chi}_i^{0},\ \tilde{\ell}\tilde{\ell} \tag{5.2}$$

have cross sections several orders of magnitude lower than the ones of colourful superpartners. This is illustrated in Figure 5.1. Searches for gluinos and squarks were

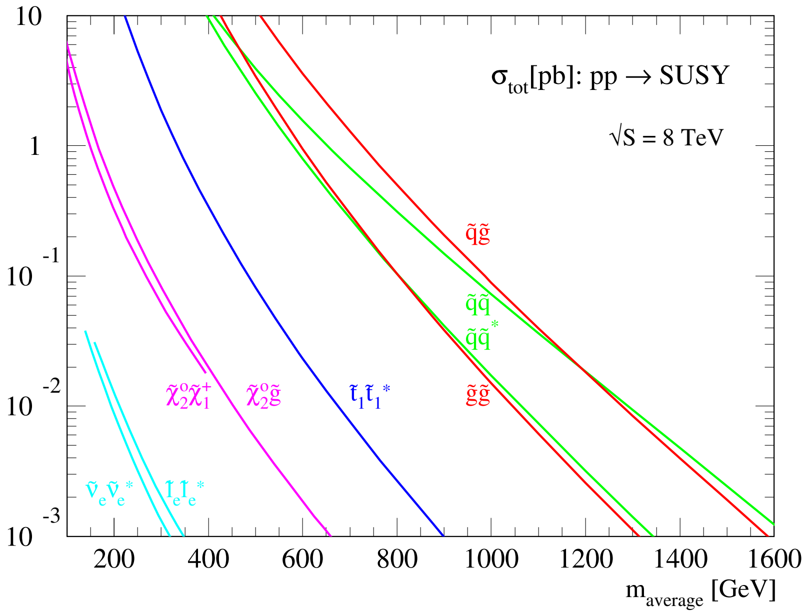

Figure 5.1: Hierarchy of production cross sections of supersymmetric partners in proton-proton collisions at $\sqrt{s} = 8$ TeV, calculated using Prospino2 [54].

performed with the ATLAS detector using the full LHC Run 1 data set of 20.3 fb^{-1} of proton-proton collisions at $\sqrt{s} = 8$ TeV [50]. As no significant excess over the Standard Model expectation was observed, limits at 95% CL were derived. Depending on the simplified model considered, the limits are able to exclude gluino masses up to 1330 GeV and squark masses up to 850 GeV. These significantly reduce the parameter space. Higher mass gluinos cannot be observed at the LHC as the $\tilde{g}\tilde{g}$ subprocess cross sections with parton distribution functions (PDFs) requires sampling higher and higher values of parton fractional momentum x_F. For such high values of x_F, the parton-parton luminosity is sharply falling.

If first and second generations of squarks have masses above 1 TeV and are not significantly lighter than the gluino, then the electroweak production becomes the dominant process for electroweakino masses of hundreds of GeV. The third generation squarks (stop and sbottom) have a special status. Due to the strong Yukawa coupling of the top ($m_t \approx 173$ GeV), the most important radiative corrections stabilizing the Higgs potential depend on the stop mass. To preserve naturalness and hence be able to solve the hierarchy problem, the stop should remain at or below the TeV scale. Also directly coupling to the Higgs sector, electroweakino masses are expected to be in the order of hundreds of GeV. This is within the reach of the Large Hadron Collider and the integrated luminosity of the full 2012 dataset would allow observation of such sparticles. In this thesis, the search focuses on the pair-production of a chargino $\tilde{\chi}_1^{\pm}$ and a next-to-lightest neutralino $\tilde{\chi}_2^0$ via a Higgs boson:

$$\tilde{\chi}_2^0 \rightarrow h\, \tilde{\chi}_1^0 \tag{5.3}$$

In the hypothesis that the discovered Higgs boson in 2012 is the lightest MSSM Higgs, this new object allows the probing of SUSY in the electroweak sector. It would confirm the couplings with both superpartners and Standard Model fermions. The Standard Model Higgs most frequently decays through the $h \rightarrow b\bar{b}$ channel (with a branching ratio of 58%) and ATLAS can tag jets originating from a bottom or antibottom quark. This offers a rare feature among supersymmetric signals: the presence of a resonance in the di-jet invariant mass spectrum. Beside this potentially visible peak, the chargino can decay to a W boson that, in turn, can decay leptonically:

$$\tilde{\chi}_1^{\pm} \rightarrow W^{\pm}\, \tilde{\chi}_1^0 \tag{5.4}$$

The presence of a lepton – electron or muon – provides a very clear experimental signature in the detector, helping the extraction of the signal from the background. The missing transverse momentum is caused by the neutrino, and mostly by the two lightest neutralinos $\tilde{\chi}_1^0$. Figure 5.2 shows the decay cascade considered for the search.

5.2 Simulated samples

A discovery in this analysis would manifest itself as an excess of data collision events with a di-jet invariant mass near 125 GeV, the SM-like Higgs boson mass. This excess needs to be compared to the theoretical prediction. For this, simulations of collision events are used to compute the expected yields of all background Standard Model processes as well as the predicted signal contribution of a given SUSY model. These simulations are done with Monte Carlo (MC) techniques. The SUSY signal models and the background contributions will be presented along with the MC generators used for their evaluation.

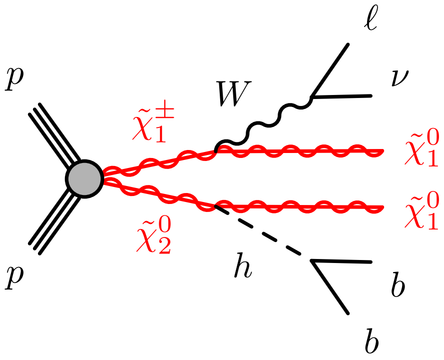

Figure 5.2: Feynman diagram for the production mechanism and the decay mode of the studied signal.

5.2.1 Monte Carlo production chain in ATLAS

To simulate high energy physics in ATLAS, the Monte Carlo sample production is generally divided into four steps:

Event generation A large number of simulated collision events, each consisting of a list of final-state particles and their energy-momentum four-vectors, is produced using MC generators. These programs use parton distribution functions, model the parton cascade and the subsequent fragmentation. The produced primary hadrons, most of which are unstable, eventually decay to observable particles.

Simulation The MC generated events are passed to a program that computes the particle interactions with the ATLAS sub-detectors, providing a realistic estimate of their response to collision events. This is done through the GEANT4 [55] toolkit (full simulation) or fast simulation ATLFAST II [56].

Digitization The simulated energy deposits are converted into digital signals; additional events from in-time and out-of-time pile-up are overlaid. The format of the output of this stage is identical to the format of the raw data coming from the ATLAS detector.

Reconstruction The digital signals are interpreted as analysis objects such as energy clusters, jets, electrons, muons, etc. Both the simulated and real data from the detector are run through the same ATLAS trigger and reconstruction packages.

Unlike real data, MC samples need to be adjusted to match the integrated luminosity recorded in ATLAS. Other corrections intervene to better mimic the data, in the form of weights applied event-by-event. Starting with a given sample with N generated events, the MC prediction N^{expected} is given by:

$$N^{\text{expected}} = \frac{\mathcal{L}^{\text{Data}}}{\mathcal{L}^{\text{MC}}} N^{\text{weighted}} \tag{5.5}$$

where $\mathcal{L}^{\text{Data}}$ and $\mathcal{L}^{\text{MC}}$ are the integrated luminosities for real data and Monte Carlo respectively. The later is calculated as follow:

$$\mathcal{L}^{\text{MC}} = \frac{1}{\sigma\, k} \sum_{i=1}^{N} w_i^{\text{MC}} \tag{5.6}$$

where σ is the cross section of the simulated process in the MC sample, with the k-factor bringing Next-to-Leading-Order (NLO) corrections. The numerator computes the initial prediction on the number of events for the generated MC sample, given by the sum of all “MC event weights” w_i^{MC}. Often all these weights are set to unity and the sum matches the raw number of events. However there may be negative event weights due to the interference between the tree and one-loop amplitudes in the $2 \to 2$ subprocesses. This is specific to NLO generators. The N^{weighted} in Equation 5.5 is the sum of the product of several weights, or scale-factors, applied for each event i to correct the simulated MC samples:

$$N^{\text{weighted}} = \sum_{i=1}^{N} \left(w_i^{\text{MC}} \times w_i^{\text{pile-up}} \times w_i^{\text{lepton trigger}} \times w_i^{\text{lepton identification}} \times w_i^{b\text{-tagging}} \right) \quad (5.7)$$

These are explained as follows:

- $\boldsymbol{w}^{\textbf{MC}}$ is given by the MC generator tuning events with respect to the differencial cross section and interferences at NLO, as mentioned above.
- $\boldsymbol{w}^{\textbf{pile-up}}$ accounts for the pile-up (additional noise due to several hard scattering events in the same and adjacent bunch crossings). Each MC event is weighted so that the distribution of the number of collisions per event matches the experimental distribution in the data.
- $\boldsymbol{w}^{\textbf{lepton trigger}}$ is derived using the efficiency of the lepton trigger on real data and MC, then taking the ratio of these efficiencies.
- $\boldsymbol{w}^{\textbf{lepton identification}}$ is derived using the efficiency of the lepton identification.
- $\boldsymbol{w}^{\boldsymbol{b}\textbf{-tagging}}$ for the b-jet pair tagging algorithm efficiency.

By multiplying all these weights for each event and then summing over all simulated collision events, the MC sample becomes compatible with real data, which always serve as the reference.

5.2.2 SUSY signal samples

Simplified model grid

Supersymmetry has too many variables to allow for a complete scan of its parameter space. The use of simplified models is an approach in which one tests for specific new particles and decays rather than full particle physics theories. In the context of $\tilde{\chi}_1^{\pm}\tilde{\chi}_2^0$ production, several assumptions are made to reduce the number of free parameters:

- Slepton and squark masses are effectively decoupled and play no role in the physics. Their masses are arbitrarily fixed to 3 TeV.
- The branching ratios for the chargino and neutralino decays are set to 1:

$$\text{BR}(\tilde{\chi}_1^{\pm} \to W^{\pm}\,\tilde{\chi}_1^0) = 1 \quad (5.8)$$

$$\text{BR}(\tilde{\chi}_2^0 \to h\,\tilde{\chi}_1^0) = 1 \quad (5.9)$$

The choice of this maximum value allows the reinterpretation of the analysis result *a posteriori* via multiplying factors.

- The considered Higgs boson has the properties of the Standard Model Higgs, with a mass of $m_h = 125$ GeV and same branching ratio for the decay to bottom and anti-bottom quarks as in the SM: $\mathrm{BR}(h \to b\bar{b}) = 0.58$
- To further reduce the number of parameters, the pair-produced supersymmetric electroweakinos are assumed to be mass degenerate: $m_{\tilde{\chi}_1^\pm} = m_{\tilde{\chi}_2^0}$
- Only the case $\Delta m = m(\tilde{\chi}_1^\pm \tilde{\chi}_2^0) - m(\tilde{\chi}_1^0) > 125$ GeV is considered, to make sure the Higgs boson is produced on-shell.

The $\tilde{\chi}_1^\pm \tilde{\chi}_2^0$ production is thus entirely characterized by two variables, the $\tilde{\chi}_2^0$ and the $\tilde{\chi}_1^0$ masses. The parameter space of this simplified model is shown in Figure 5.3, along with the excluded, kinematically disfavoured and allowed regions. A signal point

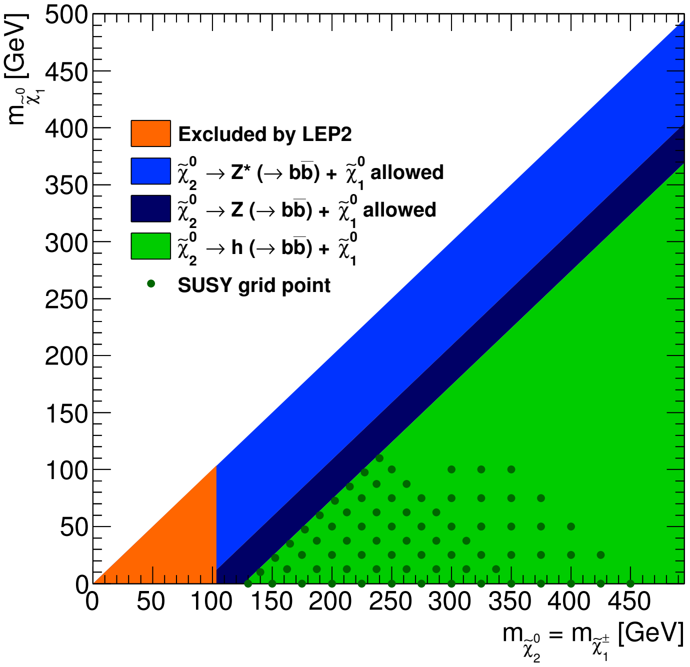

Figure 5.3: Parameter space of the simplified model, with $\tilde{\chi}_1^0$ on the y-axis and $\tilde{\chi}_1^\pm/\tilde{\chi}_2^0$ on the x-axis. In the regions were the mass splitting $\Delta m = m(\tilde{\chi}_1^\pm, \tilde{\chi}_2^0) - m(\tilde{\chi}_1^0)$ is less than the Standard Model Higgs mass $m_h = 125$ GeV, the production of an off-shell ($\Delta m < 90$ GeV, blue band) or on-shell ($90 < \Delta m < 125$ GeV, dark blue band) Z boson is dominant. The production of an on-shell Higgs boson is kinematically favoured in the green region where $\Delta m > 125$ GeV. The green dots correspond to the generated signal points.

is defined by a given choice of $m(\tilde{\chi}_1^\pm \tilde{\chi}_2^0)$ and $m(\tilde{\chi}_1^0)$. Due to the production cross sections rapidly falling when the created particle masses increase (see Table 5.1), the grid has upper limits at 450 GeV for $\tilde{\chi}_1^\pm/\tilde{\chi}_2^0$ and 100 GeV for $\tilde{\chi}_1^0$ masses. The electroweakino pair production is divided into two modes depending on the sign of the chargino: positive ($\tilde{\chi}_1^+ \tilde{\chi}_2^0$) and negative ($\tilde{\chi}_1^- \tilde{\chi}_2^0$). For this analysis a total of eight million simulated collision events have been generated in 150 samples (75 with positive chargino and 75 with negative chargino) using HERWIG++ [57]. Cross sections have been calculated at the Next-to-Leading Order with PROSPINO2 [54].

Table 5.1: Cross sections for the $\tilde{\chi}_1^\pm \tilde{\chi}_2^0$ production for several values of $m(\tilde{\chi}_1^\pm \tilde{\chi}_2^0)$.

$m(\tilde{\chi}_1^\pm \tilde{\chi}_2^0)$ [GeV]	130	150	200	250	300	350	400	450
Cross section σ [pb]	4.24	2.45	0.80	0.32	0.15	0.074	0.04	0.022

Phenomenological MSSM grid

An alternative way to analyze the large SUSY parameter space is through the phenomenological Minimal Supersymmetric Standard Model (pMSSM), as seen in Section 2.2.4. In this approach, the parameter space is reduced to a manageable subspace by imposing conditions that are motivated by experimental constraints, but are unrelated to any theoretical assumptions about the mechanism of SUSY breaking. In the electroweak sector, the pMSSM is characterized by only five parameters:

- M_1: the U(1) gaugino mass
- M_2: the SU(2) gaugino mass
- μ: the higgsino mass
- $\tan\beta$: the ratio of the vacuum expectation values of the two Higgs field doublets
- m_A: the mass parameters of the left and right handed sleptons and the mass parameter of the CP-odd Higgs

The masses M_1 and M_2 are defined at the EWSB scale. The pMSSM grid considered here was produced by varying the M_2 and μ parameters for a fixed value of $M_1 =$ 50 GeV and $\tan\beta = 10$. The $\tan\beta$ value is constrained with the radiative corrections to the mass m_h, which depend logarithmically on the SUSY scale[1] M_S: one cannot

---

[1] The SUSY scale M_S corresponds to the energy level above which supersymmetric effects become relevant.

Table 5.2: Simulated samples used for background estimates. "Tune" refers to the choice of parameters used for the underlying-event generation.

Process	Generator	Cross section	Tune	PDF set
Single top, t-channel	AcerMC [59]+Pythia6 [60]	NNLO+NNLL [61]	AUET2B [62]	CTEQ6L1 [63]
Single top, s-channel	Powheg [64,65]+Pythia6	NNLO+NNLL [66]	Perugia2011C [67]	CT10 [68]
Single top, tW-channel	Powheg+Pythia6	NNLO+NNLL [69]	Perugia2011C	CT10
$t\bar{t}$	Powheg+Pythia6	NNLO+NNLL [70–75]	Perugia2011C	CT10
$t\bar{t}W$, $t\bar{t}Z$	MadGraph [76]+Pythia6	NLO	AUET2B	CTEQ6L1
W, Z	Sherpa [77]	NLO	–	CT10
WW, WZ, ZZ	Sherpa	NLO	–	CT10
Wh, Zh	Pythia8 [78]	NNLO(QCD)+NLO(EW) [79]	AU2 [80]	CTEQ6L1

obtain a value $m_h \approx 125$ GeV for $\tan\beta \lesssim 3 - 5$ in the MSSM, even if one favourably tunes the other SUSY parameters [58]. The mass of the CP-odd Higgs (m_A) is set to 1 TeV while the other mass parameters to 3 TeV. The mass of the SM-like Higgs (m_h) is tuned to 125 GeV with mixing in the stop sector. Since all slepton masses are set to 3 TeV, the electroweakino decays via W, Z and Higgs bosons dominate. Each of the 59 signal points in the pMSSM grid has 10000 simulated collision events. The simplified model was generated using Herwig++.

5.2.3 Background samples

It is crucial to understand and correctly model the background processes leading to the signal final states under study. In this section, the relevant nominal background samples are listed in Table 5.2. More details can be found in [52]. The estimation of the background contributions will be detailed in section 5.5.

5.3 Data samples and trigger chains

After performing an event selection following the object definitions detailed in Chapter 4, additional cuts pertaining to data-quality, trigger and detector performance are required.

5.3.1 Data samples

This analysis uses the Run 1 dataset of pp collisions at $\sqrt{s} = 8$ TeV recorded by the ATLAS experiment at the LHC in 2012. Data are written to inclusive data streams based on the trigger type. This analysis uses the `Egamma` (electron triggered) and `Muon`

Table 5.3: Trigger chains used in this analysis with their properties.

Lepton flavor	Chain name	Reco. Quality	Isolation	Acceptance
Electron	`EF_e24vhi_medium1`	`medium`	yes	$p_T > 24$ GeV, $\lvert\eta\rvert < 2.5$
	`EF_e60_medium1`	`medium`	no	$p_T > 60$ GeV, $\lvert\eta\rvert < 2.4$
Muon	`EF_mu24i_tight`	`tight`	yes	$p_T > 24$ GeV, $\lvert\eta\rvert < 2.4$
	`EF_mu36_tight`	`tight`	no	$p_T > 36$ GeV, $\lvert\eta\rvert < 2.4$

streams. After applying beam, detector and data-quality requirements (detailed in Section 4.4.4), the dataset corresponds to an integrated luminosity of 20.3 fb^{-1}.

5.3.2 Triggers

Events are recorded with a combination of single-lepton triggers listed in Table 5.3. A selected event must pass at least one of these trigger chains. The "EF" stands for Event Filter, the numbers refer to the minimum allowed p_T (in GeV) of the reconstructed object and the "i" indicates if isolation criteria are applied. The p_T thresholds ensure that the leptons are in the high efficiency (80-100%) "plateau" region of the turn-on curve for that particular trigger chain.

5.4 Signal region definition

After preselecting the events consistent with the weak production of charginos and neutralinos resulting in a final state with one lepton and two b-jets, specific kinematic variables are used to further discriminate the signal over the background. In the final step of the optimization, the discovery potential of the analysis is maximized, leading to the final sets of cuts that define the signal regions.

5.4.1 Event Preselection

After defining the objects (Chapter 4) and applying the cleaning cuts (Section 4.4.4), the selected events must contain the objects corresponding of the final states of the analysis: one lepton and two b-jets.

There should be one unique baseline lepton that is also the signal lepton. This isolated lepton should be the lepton that activated the ATLAS L1 trigger. This check is called trigger-matching. The offline reconstruction of electron or muon is matched to the online trigger lepton if both objects lie in a cone of $\Delta R < 0.15$ and have a transverse momentum $p_{\mathrm{T}} > 25$ GeV.

To avoid any ambiguities, events with two overlapping leptons are vetoed. This procedure is performed with baseline leptons surviving the overlap removal explained in Section 4.4.2 (that are discarding objects only):

Step 1 If a baseline electron (e) or baseline muon (μ) lie within $\Delta R(e, \mu) < 0.1$ of each other, the event is rejected.

Step 2 If two baseline muons μ_1 and μ_2 lie within $\Delta R(\mu_1, \mu_2) < 0.1$ of each other, the event is rejected.

The quark gluon radiation in the initial or final state can lead to topologies with additional jets. To increase the acceptance of the signal, a third central or forward jet may be present in the event. Events containing four or more jets (among the central and forward collections) are rejected because it would be largely dominated by semi-leptonic $t\bar{t}$ background. Only a small fraction of the signal falls into this category. The signal selection requires the presence of two central jets that are tagged as b-jets using the MV1 tagging algorithm. A jet is b-tagged if its MV1 weight is $w_{\mathrm{MV1}} > 0.7892$; this chosen operating point identifies b-jets in simulated $t\bar{t}$ events with an efficiency of 70%, it misidentifies charm 20% of the time and light-flavour (including gluon-induced) jets less than 1% of the time. In addition, the two b-tagged jets must be the leading jets in the events, *i.e.* they must be the highest-p_{T} central jets.

5.4.2 Discriminating variables

To further separate the signal from SM backgrounds, four discriminating variables are used: the missing transverse momentum $E_{\mathrm{T}}^{\mathrm{miss}}$, the invariant mass of the two b-jets m_{bb}, the contransverse mass m_{CT} and the transverse mass m_{T}.

The first variable used in the analysis is the missing transverse momentum $E_{\mathrm{T}}^{\mathrm{miss}}$, presented in Section 4.3. The disintegration of the $\tilde{\chi}_1^{\pm}\tilde{\chi}_2^0$ pair via a W and a Higgs bosons gives three invisible particles in the detector: a neutrino and two LSP $\tilde{\chi}_1^0$. In most topologies, this will result in a transverse missing energy greater than in most Standard Model processes.

A feature of this analysis is the existence of a resonance from the Higgs decay, here into a bottom and anti-bottom quark pair. In the Standard Model, only two processes exhibit such a $b\bar{b}$ resonance that is accompanied with one lepton:

$$pp \to W\,(\to \ell\nu)\; Z\,(\to b\bar{b}) \tag{5.10}$$

$$pp \to W\,(\to \ell\nu)\; h\,(\to b\bar{b}) \tag{5.11}$$

The Z resonance peaks at $m_Z = 91.2$ GeV, with a branching ratio $\mathrm{BR}(Z \to b\bar{b}) = 15\%$. The Standard Model Higgs mostly decays into $b\bar{b}$ – 58% of the time – but this background can be severely reduced with a high transverse missing energy cut. The invariant mass m_{bb} of the two b-jets is the key variable of this analysis; it is the fitted kinematic variable leading to the final results (Chapter 8). Shown in Fig. 5.4 are the normalized distributions for $E_{\mathrm{T}}^{\mathrm{miss}}$ and m_{bb} after baseline selection. The distributions of two signal points from the simplified model are overlaid to compare with the background stacked ones. One of the benchmark points has a small Δm, with $m(\tilde{\chi}_1^{\pm}\tilde{\chi}_2^0) = 130$ GeV and $m(\tilde{\chi}_1^0) = 0$ GeV, whereas the second has a large Δm, with $m(\tilde{\chi}_1^{\pm}\tilde{\chi}_2^0) = 250$ GeV and $m(\tilde{\chi}_1^0) = 0$ GeV. It can be seen that the shapes of signal and background show significant differences, especially in the high $E_{\mathrm{T}}^{\mathrm{miss}}$ tail and around the Higgs invariant mass hypothesis.

After the requirement of $E_{\mathrm{T}}^{\mathrm{miss}} > 100$ GeV, only three background contributions remain: the top quark pair production $t\bar{t}$, followed by $W+$jets and single-top Wt production (detailed later in Section 5.5).

The contransverse mass m_{CT} is extremely effective at removing a large fraction of $t\bar{t}$ events [81]. This variable was originally designed to measure the mass of pair produced heavy particles which decay identically and semi-invisibly. The contransverse mass m_{CT} is defined as:

$$m_{\mathrm{CT}}(v_1, v_2) = \sqrt{(E_{\mathrm{T}}^{v_1} + E_{\mathrm{T}}^{v_2})^2 - |\vec{p}_{\mathrm{T}}^{\,v_1} - \vec{p}_{\mathrm{T}}^{\,v_2}|^2}, \tag{5.12}$$

where $E_{\mathrm{T}}^{v_i}$ and $\vec{p}_{\mathrm{T}}^{\,v_i}$ are the transverse energy and momentum of the visible particles or particle aggregates v_i. In our case, v_1 and v_2 are the b-quarks from the Higgs boson decay and are treated as massless. Therefore, this formula reduces to

$$m_{\mathrm{CT}}(b_1, b_2) \approx \sqrt{2\, p_{\mathrm{T}}^{b_1} p_{\mathrm{T}}^{b_2} (1 + \cos\,(\vec{p}_{\mathrm{T}}^{\,b_1}, \vec{p}_{\mathrm{T}}^{\,b_2}))} \tag{5.13}$$

A main feature justifying the use of the contranverse mass is its kinematic endpoint,

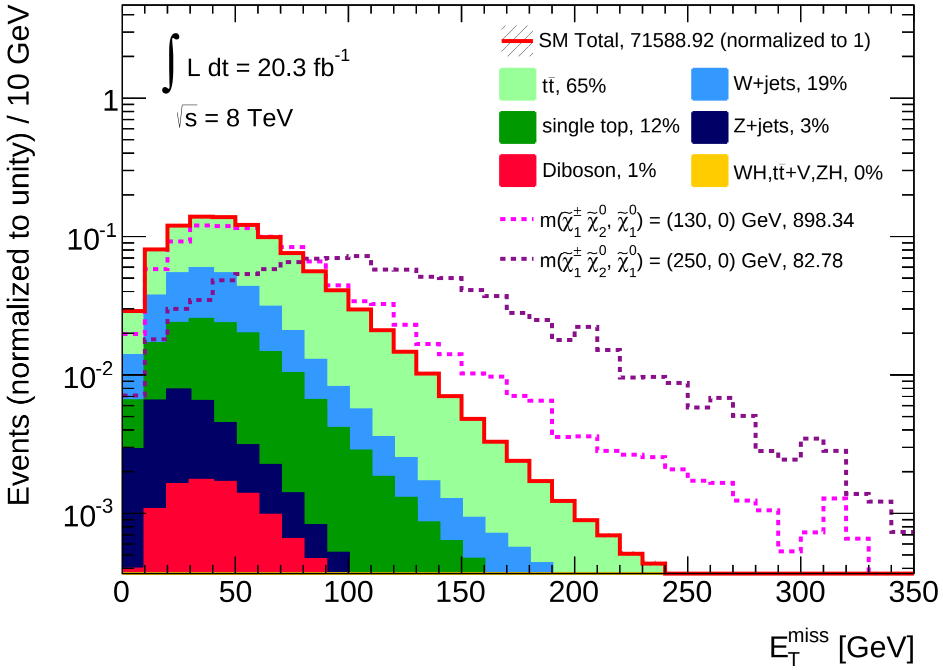

(a) Normalized $E_{\mathrm{T}}^{\mathrm{miss}}$.

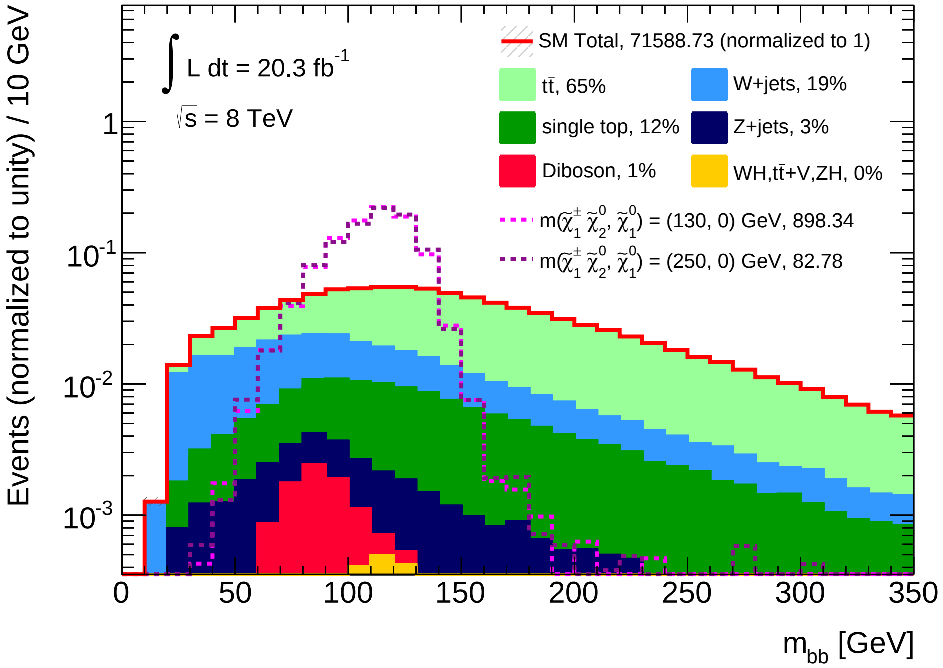

(b) Normalized m_{bb}.

Figure 5.4: $E_{\mathrm{T}}^{\mathrm{miss}}$ and m_{bb} distributions normalized to unit area after baseline selection.

given by:

$$m_{\mathrm{CT}}^{\max} \approx \frac{m_{heavy}^2 - m_{invis}^2}{m_{heavy}} \tag{5.14}$$

Adapting the $t\bar{t}$ background to this kinematic topology gives $m_{heavy} = m_t$, the two visible particles are the two b-tagged jets, and $m_{invis} = m_W$, the remainder of the top decay. With this identification, Eq. 5.14 implies that $t\bar{t}$ should have an endpoint at $\approx$ 135 GeV. Initial- and final-state radiations (ISR and FSR) can smear this endpoint considerably, and only partial corrections are possible. This analysis uses a boost-corrected m_{CT}, which corrects for collinear boosts of the $t\bar{t}$ system in the transverse plane [82].

In addition to m_{CT}, the transverse mass m_{T} reconstructs the mass of a particle decaying in one visible daughter particle and one invisible daughter particle. The variable m_{T} can describe W candidates in background events, where the visible particle is the lepton and the invisible one is the neutrino, whose presence is only inferred from the missing energy. It is defined as

$$m_{\mathrm{T}} = \sqrt{2\, E_{\mathrm{T}}^{\ell} E_{\mathrm{T}}^{\mathrm{miss}} - 2\, \vec{p}_{\mathrm{T}}^{\,\ell} \cdot \vec{p}_{\mathrm{T}}^{\,\mathrm{miss}}}, \tag{5.15}$$

where E_{T}^{ℓ} is the transverse energy of the lepton and $\vec{p}_{\mathrm{T}}^{\,\ell}$ its transverse momentum. Assuming no outside sources of $E_{\mathrm{T}}^{\mathrm{miss}}$ are present in the event, the transverse mass has an endpoint at the mass of the semi-leptonically decaying particle. In the case of the W boson, this endpoint is m_W at around 80 GeV, though the tail extends much farther due to off-shell W bosons and experimental effects. Requiring $m_{\mathrm{T}} > 100$ GeV efficiently suppresses the $W+$jets background of the present analysis.

Shown in Figure 5.5 are the normalized distributions for m_{CT} and m_{T} after baseline selection. The shapes of the signal and background significantly differ in the high m_{CT} and m_{T} regions, where the background is sharply falling after passing the endpoints of 135 GeV and 100 GeV for m_{CT} and m_{T} respectively. Other kinematic and angular variables have been studied and did not provide enough discrimation power for this search. Table 5.4 summarizes the analysis variables and the purpose of each cut.

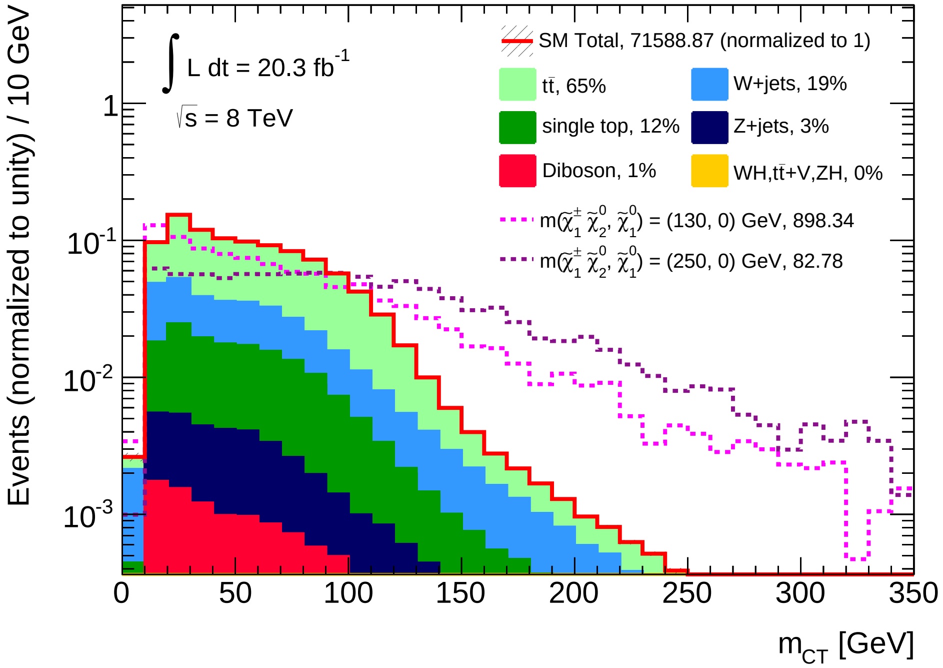

(a) Normalized m_{CT}.

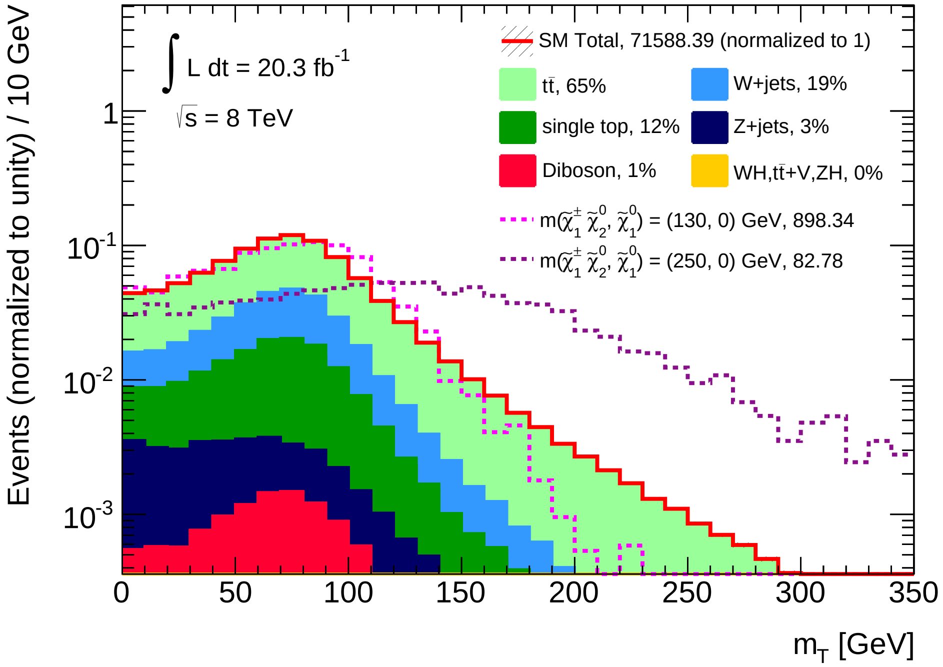

(b) Normalized m_{T}.

Figure 5.5: m_{CT} and m_{T} distributions normalized to unit area after baseline selection.

Table 5.4: Summary of analysis cuts and variables with the SM background they are designed to reduce.

Cuts	Description
$E_{\mathrm{T}}^{\mathrm{miss}}$	Reduce all backgrounds, particularly QCD and $t\bar{t}$
Exactly 2 b-tagged jets	Reduce W+jets
Leading b-tagged jets	Reduce $t\bar{t}$
Additional-lepton veto	Reduce dileptonic $t\bar{t}$
Fourth jet veto	Reduce fully hadronic and semi-leptonic $t\bar{t}$
m_{CT}	Reduce $t\bar{t}$ (missed W)
m_{T}	Reduce all leptonic W backgrounds
105 GeV $< m_{bb} <$ 135 GeV	Reduce non-Higgs $b\bar{b}$ backgrounds

5.4.3 Signal region optimization

Di-jet mass signal bin

The key variable of this analysis – m_{bb} – is fitted for all simplified model signal points using a Crystal Ball function [83]. This function, commonly used in high-energy physics processes, comprises a Gaussian and a power law below a certain threshold. It offers a good modelling of the resonance shape and the energy loss by radiation emission in the final state. The adjusted curve peaks at $m_{bb} \approx 120$ GeV and a half width at half maximum of $\sigma_{bb} \approx 15$ GeV. These values have been estimated for all simplified model points and remain stable throughout the whole signal grid. The fitted m_{bb} lineshape motivates the division of the distribution into five bins. Four side-bands ("sb") border the Higgs sensitive ("h") bin:

- 45 GeV $< m_{bb} <$ 75 GeV: side-band
- 75 GeV $< m_{bb} <$ 105 GeV: side-band
- 105 GeV $< m_{bb} <$ 135 GeV: Higgs sensitive bin
- 135 GeV $< m_{bb} <$ 165 GeV: side-band
- 165 GeV $< m_{bb} <$ 195 GeV: side-band

Figure 5.6 displays an example of the fitted m_{bb} distribution on a simplified model signal sample. The vertical dashed lines delimit the five bins.

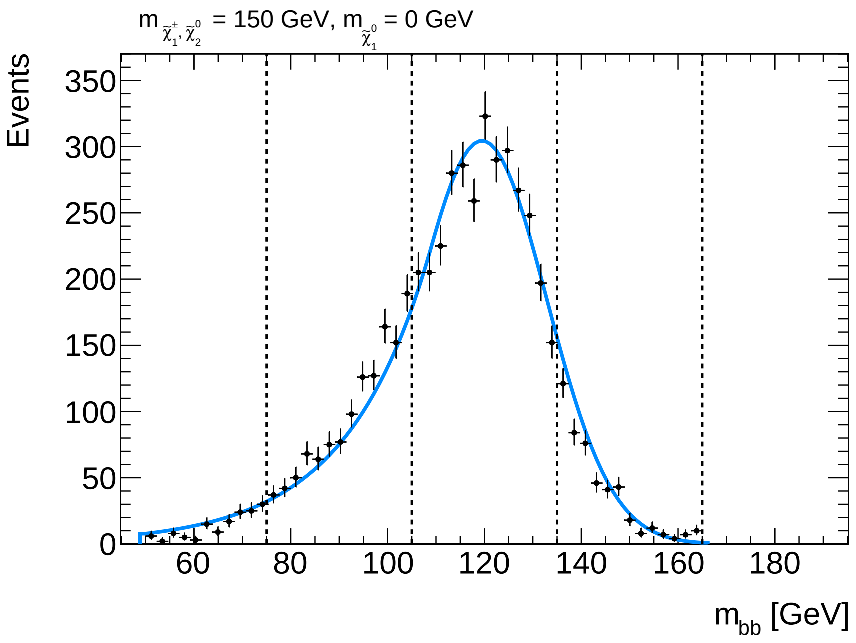

Figure 5.6: Invariant mass m_{bb} distribution for a Monte Carlo simulated signal sample (black data points with statistical errors) fitted with a Crystal Ball function (blue curve) in a region with exactly 2 b-tagged jets and no additional jets, $E_{\mathrm{T}}^{\mathrm{miss}} > 100$ GeV and $m_{\mathrm{T}} > 40$ GeV.

Strategy

The strategy in the optimization stage of an analysis is to obtain a series of cuts which will reduce the predicted background while keeping most of the signal events. The bigger the separation between the signal s and background b yields, the higher the discovery potential. The statistical tools used to quantify this discovery potential are actually computing the rareness – or incompatibility – of observing a number of events in the data under the hypothesis that the observed data sample contains only Standard Model background events (null hypothesis). Rejecting the null hypothesis is a conservative and safe approach before establishing any claims on the presence of new physics, here Supersymmetry. The usual way of quantifying the level of incompatibility – therefore being able to state a discovery – is to compute a p-value. The discovery p-value states how frequent an excess of events (or greater excess) would occur in a set of repeated identical experiments, assuming this excess is only due to background fluctuations (null hypothesis). This will be fully explained in Chapter 8, dedicated to the statistical methods. At this stage of optimization, the real data are not available and N^{observed} is simply taken as $s + b$, which relates to a discovery scenario (excess of signal events on top of the background prediction). The sensitivity of the analysis is assessed through a commonly used figure of merit: the significance Z_N. It corresponds to the number of standard deviations $Z_N \times \sigma$ at which a Gaussian random variable of zero mean and standard deviation σ would give a one-sided tail area equal to the p-value[2]. For the purpose of benchmarking, a reasonable uncertainty assumption of 30% on the background prediction is conventionally assumed. The greater the significance, the more sensitive the analysis is to the presence of physics beyond the Standard Model. Optimal cuts on each object multiplicity or variables are obtained by locally maximizing the approximate Z_N, as shown in the next subsection.

Two orthogonal signal regions

The simplified model grid contains a number of points with a wide range of mass splittings between the $\tilde{\chi}_2^0$ and $\tilde{\chi}_1^0$ particles. As a consequence, the kinematic configurations will differ for low and high mass splitting regions. Therefore, during optimization the grid was divided into two broad regions, low and high mass splitting – each optimized separately to accommodate different kinematic properties. The low (high) mass splitting region is called SRA (SRB) and is defined to be where $m(\tilde{\chi}_2^0) - m(\tilde{\chi}_1^0)$ is below (above) 175 GeV.

During the optimization studies, the signal regions are constrained to the central bin "h" where $105 < m_{bb} < 135$ GeV and are denoted SRAh/SRBh (in the limit setting presented in Chapter 8, the signal regions are extended to the five m_{bb} intervals to better constrain peaking backgrounds such as WZ and WH). For m_{CT} and $E_{\mathrm{T}}^{\mathrm{miss}}$ the optimal cuts in both regions to mitigate background while keeping reasonable statistics were found to be $m_{\mathrm{CT}} > 160$ GeV and $E_{\mathrm{T}}^{\mathrm{miss}} > 100$ GeV. The highest sensitivity is obtained in SRAh with an m_{T} window of 100 GeV $< m_{\mathrm{T}} <$ 130 GeV. In SRBh, a lower cut $m_{\mathrm{T}} > 130$ GeV maximizes the significance and ensures the two regions are orthogonal. Figures 5.7 and 5.8 show the $E_{\mathrm{T}}^{\mathrm{miss}}$, m_{CT} and m_{T} "N-1" distributions (in the N cut-space, all cuts are applied except the cut on plotted variable) and their corresponding Z_N significance as a function of the cut value in SRA and SRB respectively. For m_{T} distributions, neither lower and upper cuts are applied.

---

[2] The N index refers to the normal distribution, taken as convention.

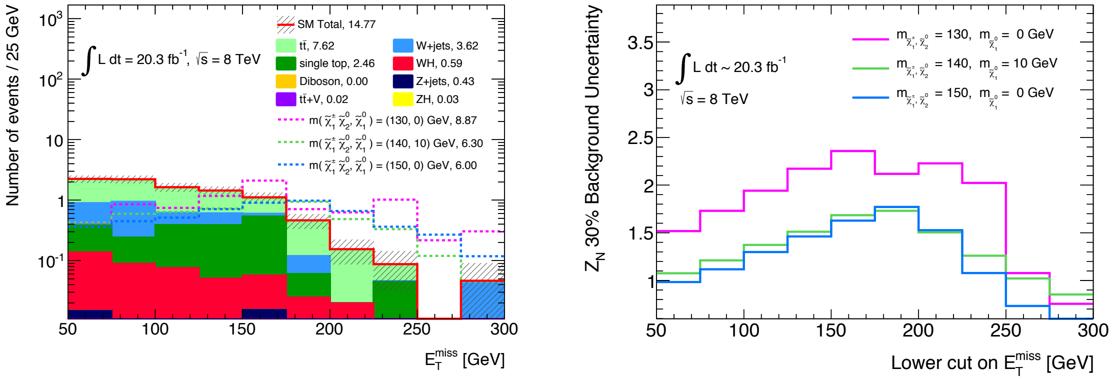

(a) $E_{\mathrm{T}}^{\mathrm{miss}}$ N-1 distribution (b) $E_{\mathrm{T}}^{\mathrm{miss}}$ N-1 significance

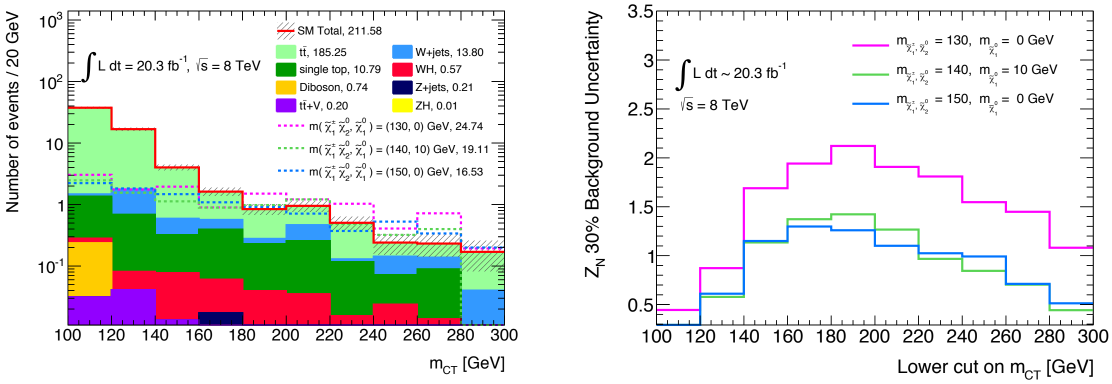

(c) m_{CT} N-1 distribution (d) m_{CT} N-1 significance

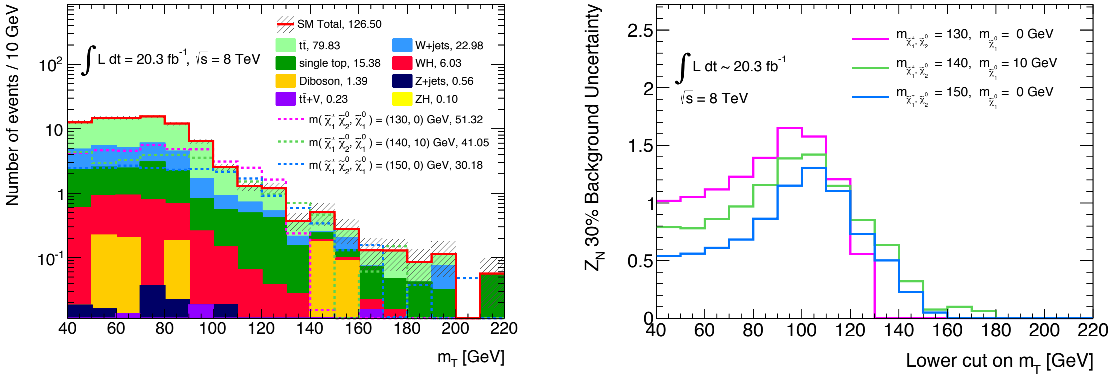

(e) m_{T} N-1 distribution (f) m_{T} N-1 significance

Figure 5.7: N-1 signal+background distributions (left) of $E_{\mathrm{T}}^{\mathrm{miss}}$, m_{CT} and m_{T} with corresponding Z_N significance (right) as a function of cut value in SRA.

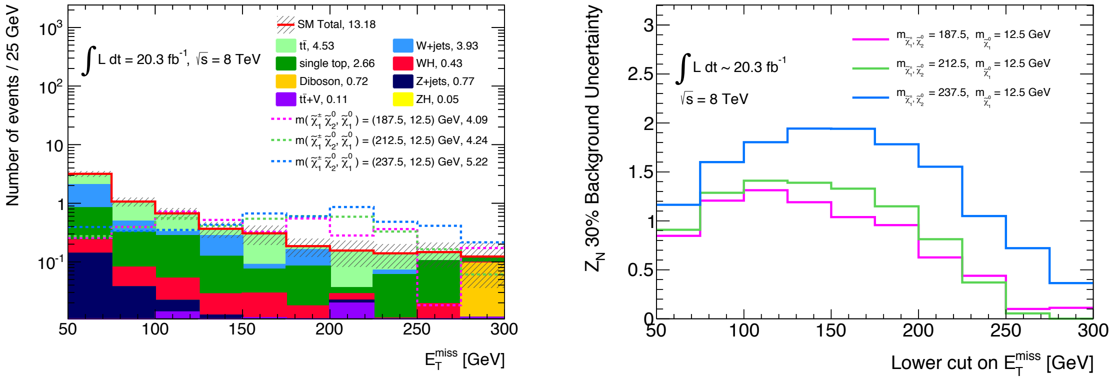

(a) $E_{\mathrm{T}}^{\mathrm{miss}}$ N-1 distribution (b) $E_{\mathrm{T}}^{\mathrm{miss}}$ N-1 significance

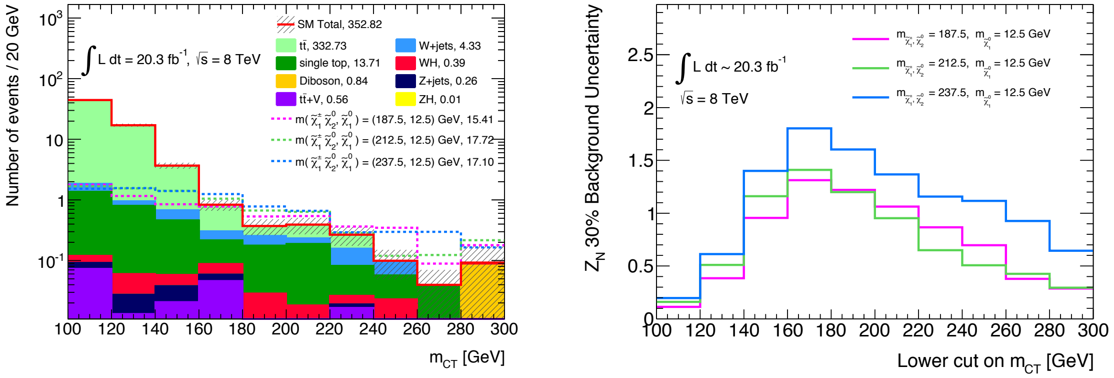

(c) m_{CT} N-1 distribution (d) m_{CT} N-1 significance

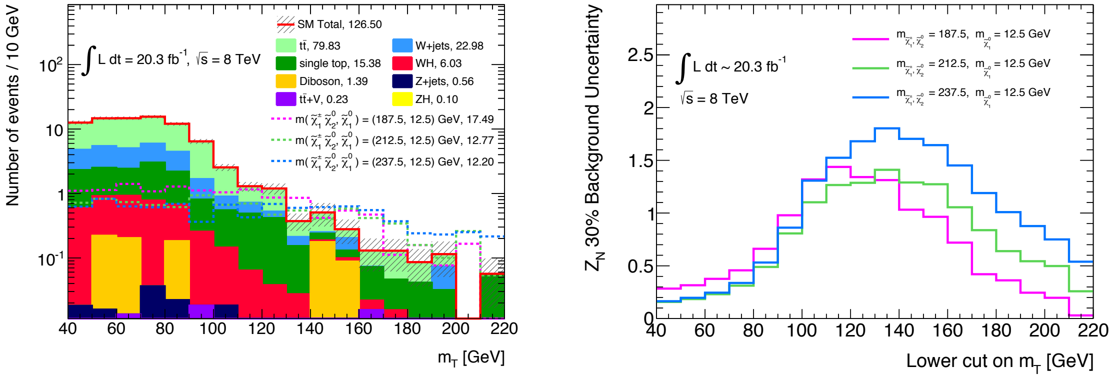

(e) m_{T} N-1 distribution (f) m_{T} N-1 significance

Figure 5.8: N-1 signal+background distributions (left) of $E_{\mathrm{T}}^{\mathrm{miss}}$, m_{CT} and m_{T} with corresponding Z$_N$ significance (right) as a function of cut value in SRB.

5.4.4 Sensitivity maps

For each signal region, the analysis was optimized using three benchmark signal points representative of the kinematics of the considered region. It is essential to see how the significance, maximized for these points only, vary throughout the full signal grid. Figures 5.9 and 5.10 show the expected discovery significance for all points of the simplified model and pMSSM grids respectively. The model points that have the highest discovery potential, *i.e.* with the highest Z_N, are the first to be excluded in the absence of an excess in the data over the summed background yields. The exclusion at the 95% confidence level (CL) is analoguous to a p-value of 0.05, which correspond to a $Z_N^{\text{excluded}} \approx 1.64$ (see Chapter 8). The black contour in the sensitivity maps outlines the Z_N^{excluded} line. In absence of an excess, models below the line are potentially excluded whereas no conclusion can be drawn for the models above the line as the analysis is not sensitive enough.

5.5 Background estimation

Several known Standard Model processes can mimic a SUSY signal with 1 lepton, 2 b-tagged jets and missing energy. Reducible and irreducible backgrounds are described along with the methodologies to estimate them. The latter will be normalized to data in dedicated "control" regions. To verify the accuracy of the background modeling, "validation" regions are defined at the end of this section.

5.5.1 Reducible background

The LHC, as any high-energy hadronic collider, is a jet factory: QCD processes dominate. These multi-jet events only contribute to the signal selection if the reconstructed $E_{\mathrm{T}}^{\mathrm{miss}}$ is sufficiently large and a "fake" lepton is erroneously reconstructed as a signal lepton. Fake leptons can originate from a misidentified jet, semileptonic decays of heavy quarks (b and c) or photon conversion. As all other background processes in this analysis feature a "real" or "prompt" lepton coming from a boson decay, it is possible to estimate the number of events with a non-prompt lepton to quantify the QCD multi-jet reducible background.

This is done using a data-driven technique called the "matrix method" [84]. The matrix method exploits correlations between tight (T)/loose (L) and real (R)/fake (F) leptons through a series of linear equations. Loose leptons are baseline leptons

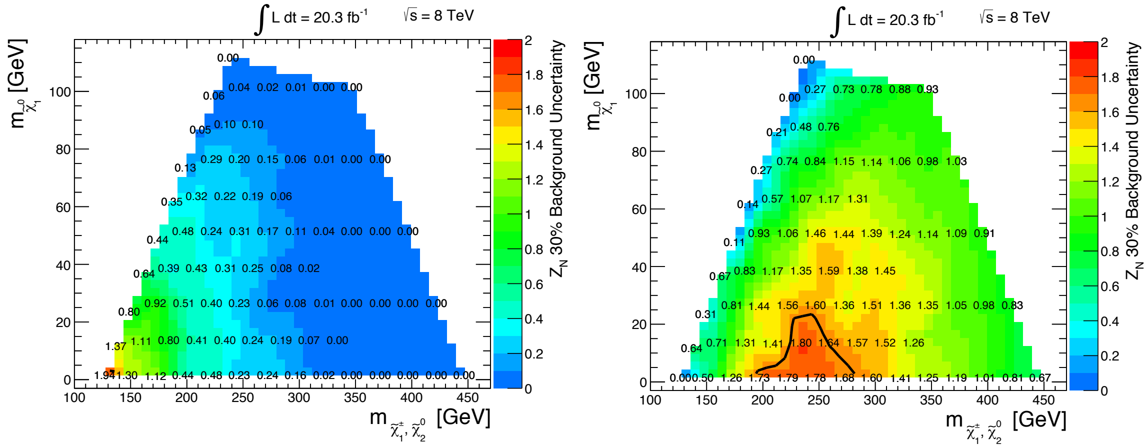

(a) SRAh

(b) SRBh

Figure 5.9: Expected discovery significance for the simplified model grid in the two signal regions SRAh and SRBh. The black line in Figure 5.9b marks the exclusion potential at 95% CL. All yields have been scaled to the integrated luminosity of 20.3 fb^{-1}.

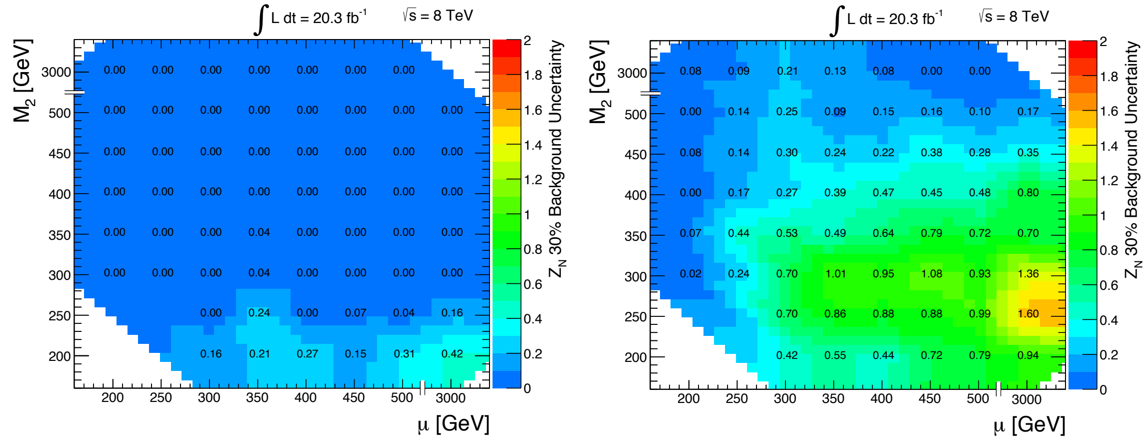

(a) SRAh

(b) SRBh

Figure 5.10: Expected discovery significance for the pMSSM grid in the two signal regions SRAh and SRBh. All yields have been scaled to the integrated luminosity of 20.3 fb^{-1}.

while tight leptons are signal leptons (defined in Section 4.1). For a final state with one lepton, the system of equations of the matrix method is:

$$\begin{pmatrix} N_T \\ N_L \end{pmatrix} = \begin{pmatrix} \epsilon & f \\ (1-\epsilon) & (1-f) \end{pmatrix} \cdot \begin{pmatrix} N_R \\ N_F \end{pmatrix}, \tag{5.16}$$

where ϵ is the probability that a real lepton is tagged as a tight lepton and f is the probability of reconstructing a fake lepton as tight, also referred as "fake rate". The number of fake leptons passing the tight quality criteria is then given by:

$$N_{F\to T} = \left(\frac{f}{\epsilon - f}\right)(\epsilon \times N_L - N_T + \epsilon \times N_T) \tag{5.17}$$

The electron and muon identification efficiencies are derived from $Z \to \ell\ell$ events both in data and MC simulations. The efficiencies used here were measured by analyses searching for supersymmetric particles in the QCD sector [50] and are largely sample-independent. The fake rates, however, depend strongly on the heavy flavor content of the selection considered and should be tailored to the specific analysis in question. The region used to derive the fake rates should be kinematically representative of the signal region: it contains 2 b-tagged jets but allows one or more baseline (loose) lepton. To enrich the region in QCD events, the cuts on kinematic variables are reversed: $E_{\mathrm{T}}^{\mathrm{miss}} < 25$ GeV, $m_{\mathrm{T}} < 40$ GeV. The fake rates are calculated by counting loose and tight electrons and muons in bins of p_{T} and η in both data and Monte Carlo simulation with real (prompt) leptons. The real lepton yields are then subtracted from the data yields, and the remainder is assumed to be of fake origin. The ratio of tight to loose in a given bin is the fake rate. Consequently, the number of fake lepton passing the tight selection can be deduced and thereafter the QCD multi-jet background contribution.

It has been found that, in this validation region, QCD processes remain a small background compared to the dominant ones (presented in the next section) and is not expected to significantly contribute to our selections where $E_{\mathrm{T}}^{\mathrm{miss}} > 100$ GeV is requested. In the control and validation regions that will be defined later in this chapter, the contribution of multi-jet production is found to be less than 3% of the total background and is thus neglected.

5.5.2 MC-modelled backgrounds

Irreducible backgrounds refer to the Standard Model processes generating events indistinguishable from the signal, namely in this analysis one "real" signal lepton and 2 b-jets. The three major backgrounds for this search are top pair production $t\bar{t}$, $W+$jets and single top. Smaller contributions arise from diboson (WW, WZ, ZZ) and Wh processes. Figure 5.11 shows example Feynman diagrams of the main processes, detailed as follow:

Top pair production $t\bar{t}$ events produce two on-shell – *i.e.* close to the nominal mass of the particle – top quarks, each decaying into a b-jet and a W boson. Dilepton $t\bar{t}$ – both W bosons decay leptonically – can enter the selection if one of the leptons failed the reconstruction. $t\bar{t}$ events have, in addition to the b-jets pair, two high p_{T} jets. By choosing events where the b-jets are leading and no more than three jets are present, the $t\bar{t}$ contribution can be reduced but it remains the largest background in this analysis.

$W+$jets W boson production in association with hard jets from ISR, in conjunction with a leptonic decay, can generate large $p_{\mathrm{T}}^{\mathrm{miss}}$ from a highly boosted neutrino. The $Wb\bar{b}$ subprocess directly reproduces the analysis signature whereas the Wjj, $Wc\bar{c}$ and Wcj subprocesses, where j refers to a light jet, enter the data when jets are misidentified as b-jets.

Single top At hadron colliders, there are three single top quark production modes: the s-, the t- and Wt-channels. The former two exchange a virtual W boson. The Wt production produces an on-shell W boson in association with a top quark and has its own s- and t-channel submodes (Figures 5.11c and 5.11d). The Wt production is contributing the most in this analysis, as it can result in one lepton, one b-jet (from the top decay) and, if the W decays hadronically, additional jets that can be identified as b-jets.

Diboson WW and WZ each has a similar signature as the signal when one W decays to $\ell\nu$ while the other boson decays to quarks. ZZ events might mimic our signal when one Z decays to two jets and the other to two leptons of which one is not reconstructed. However, the cross sections for these processes are small, diboson events are hence not a major background for this search.

Wh The associated production of a Standard Model Higgs and W bosons can lead to the final states of the analysis if the W boson decays leptonically $W \to \ell\nu$ and the Higgs boson gives a $b\bar{b}$ pair. The transverse missing energy would be then carried by the neutrino, hence a high $E_{\mathrm{T}}^{\mathrm{miss}}$ cut suppresses most of this background.

Table 5.5 list the main production cross sections of the background mentioned above, calculated at NLO and Next-to-Next-to-Leading-Order (NNLO) for the top pair and single productions.

Table 5.5: NLO production cross sections for some Standard Model processes at $\sqrt{s} = 8$ TeV at the LHC. Note that for $W+$jets and diboson, only the subprocess leading to the exact final states of the analysis is quoted here: $W \to \ell b\bar{b}$ for $W+$jets and $WW \to \ell\nu qq$ or $WZ \to \ell\nu qq$ for diboson. There are more samples contributing to the cross section through misidentified or non-reconstructed objects that are not present on this table, whose aim is to show the relative importance of the backgrounds.

Background	$t\bar{t}$	$W+$jets	Single top			Diboson		Wh
			t	Wt	s	WW	WZ	
σ [pb]	253	12.1×10^3	87.8	22.4	5.61	7.72	2.00	0.13

5.5.3 Construction of control and validation regions

Beside signal regions, control regions are enriched in a specific Standard Model process and serve to constrain the normalization of this background contribution. Validation regions are defined orthogonal to both signal and control regions but should remain kinematically close to the signal. They aim at validating the quality of the extrapolation from the control to the signal regions. The model validation will be detailed in Chapter 8 after describing studies to improve the sensitivity of this analysis (Chapter 6) and reviewing the sources of uncertainties (Chapter 7). This section lists the control and validation regions; all regions – including the signal ones – are summarized in Table 5.6.

CRT: this region is enriched in $t\bar{t}$ events by inverting the cut $m_{\mathrm{CT}} > 160$ GeV, which successfully suppresses $t\bar{t}$ background in the signal regions. To stay kinematically close to the signal region, a $m_{\mathrm{CT}} > 100$ GeV cut is applied. According to the MC simulation, this region exhibits a very high purity in $t\bar{t}$ of 93.5% with 2.5% of $W+$jets only.

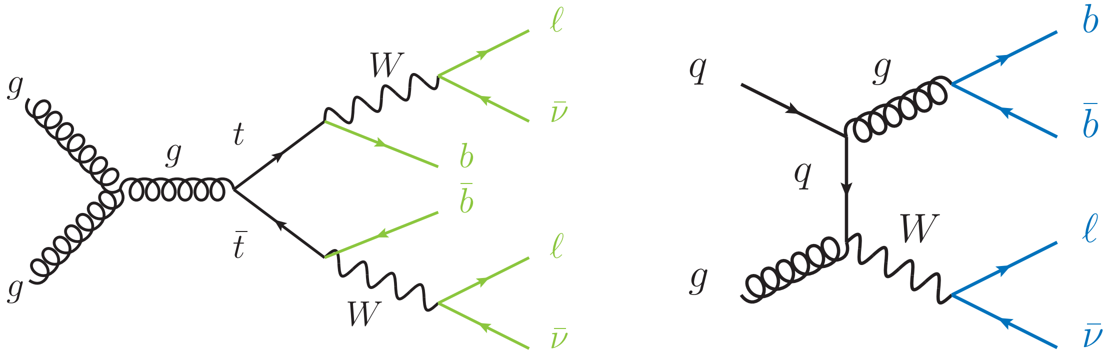

(a) Top pair production.

(b) W+jets production.

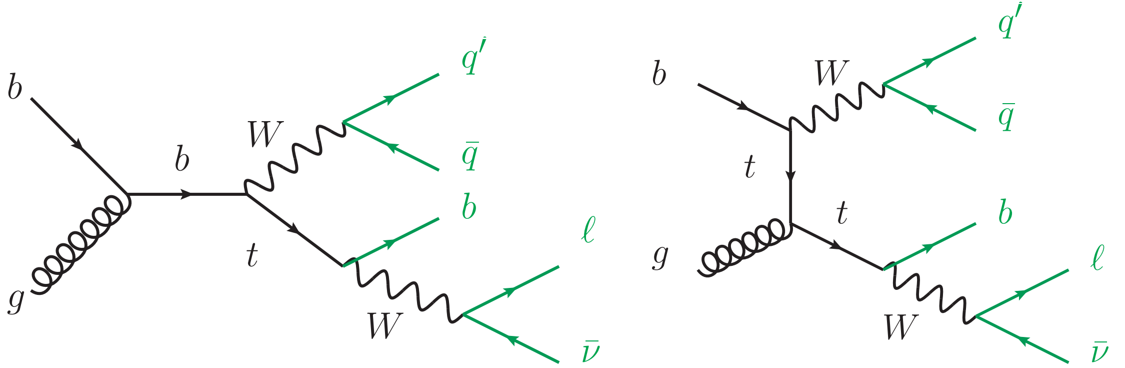

(c) Single top Wt production (s-channel)

(d) Single top Wt production (t-channel)

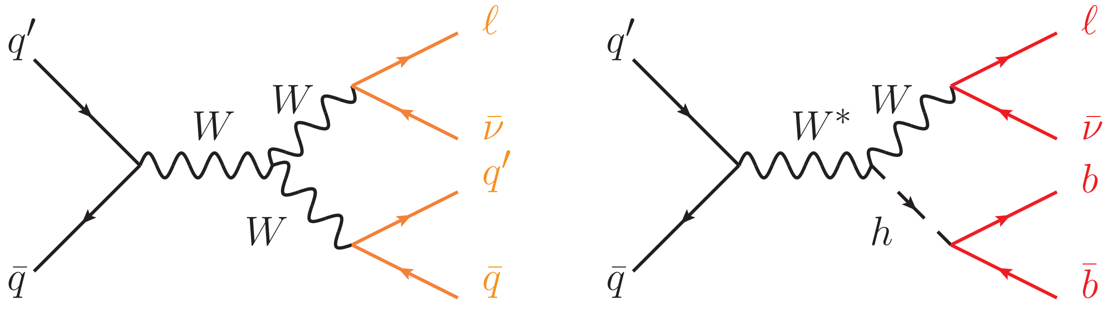

(e) Diboson production.

(f) Standard Model Higgs production associated with a W boson.

Figure 5.11: Representative diagrams for the main background processes modelled with MC.

CRW: this region contains a high percentage of $W+$jets. It is defined with the same m_{CT} cut as in the signal ($m_{\mathrm{CT}} > 160$ GeV). Contrary to all the other regions, CRW requires only one b-tagged jet to target $W+$jets decays and exactly two signal jets to reduce the $t\bar{t}$ contamination. A loosened m_{T} cut $40 < m_{\mathrm{T}} < 100$ GeV increases the acceptance in order to obtain high statistics. The $W+$jets events amount to 51.7% with $t\bar{t}$ processes reduced to 37.1%.

VRA: this validation region is identical to CRT but requires $40 < m_{\mathrm{T}} < 100$ GeV.

VRB: is defined like the signal regions (with $m_{\mathrm{CT}} > 160$ GeV) but remains orthogonal to them by imposing $40 < m_{\mathrm{T}} < 100$ GeV.

SRAsb and SRBsb: the side bands in the signal regions are obtained from SRA and SRB by restricting the m_{bb} di-jet mass spectrum – divided in five bins around the Higgs mass (see Section 5.4.3) – to the four non signal bins, *i.e.* $45 < m_{bb} < 105$ GeV and $135 < m_{bb} < 195$. The data in these regions are never blinded and always used as a constraint in the fit (detailed in Chapter 8), as a result these regions act as control regions.

The schematics in Figure 5.12 depicts the control (CR), validation (VR) and signal (SR) regions – emphasizing their orthogonality – as a function of m_{T}, m_{CT}, and the signal- and b-tagged jet multiplicities.

Table 5.6: Selection requirements for the signal, control and validation regions of the analysis. The number of jets and b-jets is labelled with n_{jet}, and $n_{b\text{-jet}}$ respectively.

	SRA	SRB	CRT	CRW	VRA	VRB
n_{jet}	2–3	2–3	2–3	2	2–3	2–3
$n_{b\text{-jet}}$	2	2	2	1	2	2
$E_{\mathrm{T}}^{\mathrm{miss}}$ [GeV]	> 100	> 100	> 100	> 100	> 100	> 100
m_{CT} [GeV]	> 160	> 160	100–160	> 160	100–160	> 160
m_{T} [GeV]	100–130	> 130	> 100	> 40	40–100	40–100

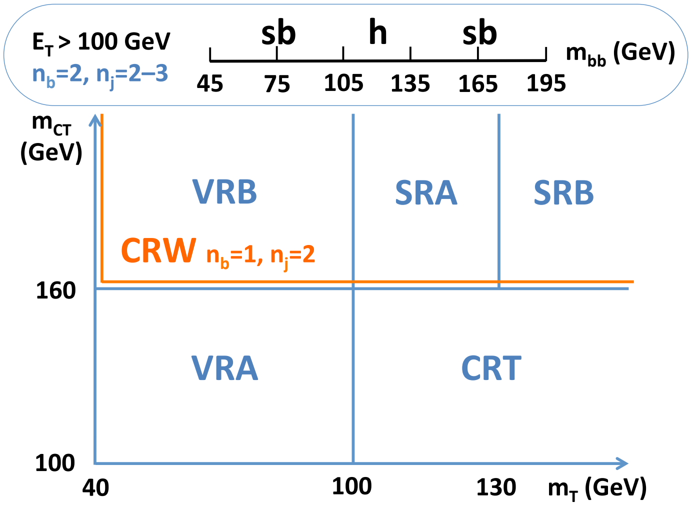

Figure 5.12: Control (CR), validation (VR) and signal (SR) regions as a function of m_{T}, m_{CT}, the signal jet and b-tagged jet multiplicities. Each region is split into the five m_{bb} bins as shown in the top bar. The comparison of data and simulated yields occurs in SRAh and SRBh, which are defined as SRA and SRB with the requirement $105 < m_{bb} < 135$ GeV. The side-bands SRAsb and SRBsb act as other control regions.

Chapter 6

Improvements of the analysis sensitivity

The event selection detailed in the previous chapter corresponds to the analysis optimization published in Reference [53]. Several investigations have been performed by the author in an attempt to increase the sensitivity of the search. Two of these studies are reported in the present chapter.

6.1 The *deconstructed* transverse mass

6.1.1 Motivation

The search of this dissertation uses, among other discriminating variables, the transverse mass, m_{T}, in order to separate the signal from SM backgrounds. The reader is reminded of its definition here:

$$m_{\mathrm{T}} = \sqrt{2\,E_{\mathrm{T}}^{\ell} E_{\mathrm{T}}^{\mathrm{miss}} - 2\,\vec{p}_{\mathrm{T}}^{\,\ell} \cdot \vec{p}_{\mathrm{T}}^{\,\mathrm{miss}}}, \tag{6.1}$$

where E_{T}^{ℓ} is the transverse energy of the lepton and $\vec{p}_{\mathrm{T}}^{\,\ell}$ its transverse momentum. This variable is defined to reconstruct the mass, in the transverse plane, of the W boson m_W that decays into one lepton and one neutrino, assuming no other source of missing transverse momentum. The presence of invisible particles such as neutralinos in the final state leads to additional missing transverse momentum. Hence signal-like events exhibit larger values of m_{T}. These events are thus extracted from the SM backgrounds by applying a strict cut m_{T}^{0} on the transverse mass: $m_{\mathrm{T}} > m_{\mathrm{T}}^{0} > m_W$.

Given Equation 6.1, a uniform cut on the transverse mass can discard information about the transverse missing energy, $E_{\mathrm{T}}^{\mathrm{miss}}$, and its vector, $\vec{p}_{\mathrm{T}}^{\,\mathrm{miss}}$. To preserve the correlations on the norm and direction of the missing energy, the transverse mass m_{T} is rewritten as:

$$1 - \frac{m_{\mathrm{T}}^2}{2\,E_{\mathrm{T}}^{\ell} E_{\mathrm{T}}^{\mathrm{miss}}} = \cos\phi \quad \text{with} \quad \cos\phi = \frac{\vec{p}_{\mathrm{T}}^{\,\ell} \cdot \vec{p}_{\mathrm{T}}^{\,\mathrm{miss}}}{p_{\mathrm{T}}^{\ell}\, p_{\mathrm{T}}^{\mathrm{miss}}}, \tag{6.2}$$

where ϕ – sometimes also written as $\Delta\phi(\vec{p}_{\mathrm{T}}^{\,\ell}, \vec{p}_{\mathrm{T}}^{\,\mathrm{miss}})$ – is the transverse angle between the lepton p_{T} and the missing transverse momentum. Defining Q as

$$Q \equiv 1 - \frac{(m_{\mathrm{T}}^0)^2}{2\,E_{\mathrm{T}}^{\ell} E_{\mathrm{T}}^{\mathrm{miss}}}, \tag{6.3}$$

the transverse mass is therefore "deconstructed" into two independent variables, one angular component $\cos\phi$ and one dimensionless magnitude component Q [85]. The correlations between the two become apparent when plotting the event distributions in the $\cos\phi - Q$ plane. It is possible to refine the signal and background separation by choosing a contour on that plane that maximizes the signal and contains the fewest number of background events. Such an attempt to gain sensitivity has been investigated in the context of the $1\ell + 2b$-jets + $E_{\mathrm{T}}^{\mathrm{miss}}$ SUSY search detailed in Chapter 5. The following section reports on this study.

6.1.2 Event distributions in the $\cos\phi - Q$ plane

The two-dimensional event distributions of the variables Q and $\cos\phi$ are shown in Figures 6.1a and 6.1b for the $t\bar{t}$ background and the simplified model signal point $m(\tilde{\chi}_1^{\pm}\tilde{\chi}_2^0, \tilde{\chi}_1^0)$ = (130,0) GeV respectively. These distributions are obtained from a region requiring events with exactly 2 b-jets and where the cuts common to all regions described in Section 5.5.3 are applied: $m_{\mathrm{CT}} > 100$ GeV, $E_{\mathrm{T}}^{\mathrm{miss}} > 100$ GeV, $m_{\mathrm{T}} > 40$ GeV and $45 < m_{bb} < 195$ GeV.

The sum of the signal regions presented in Chapter 5 are defined with a uniform cut $m_{\mathrm{T}} > 100$ GeV. This graphically translates into taking the region above the black diagonal line defined by $Q = \cos\phi$. Looking at the distributions of Figures 6.1a and 6.1b, most of the signal events are actually located towards values of Q and $\cos\phi$ approaching one, but below this diagonal. They are therefore removed by the cut, which was designed to select signal-like events in the first place. Moreover,

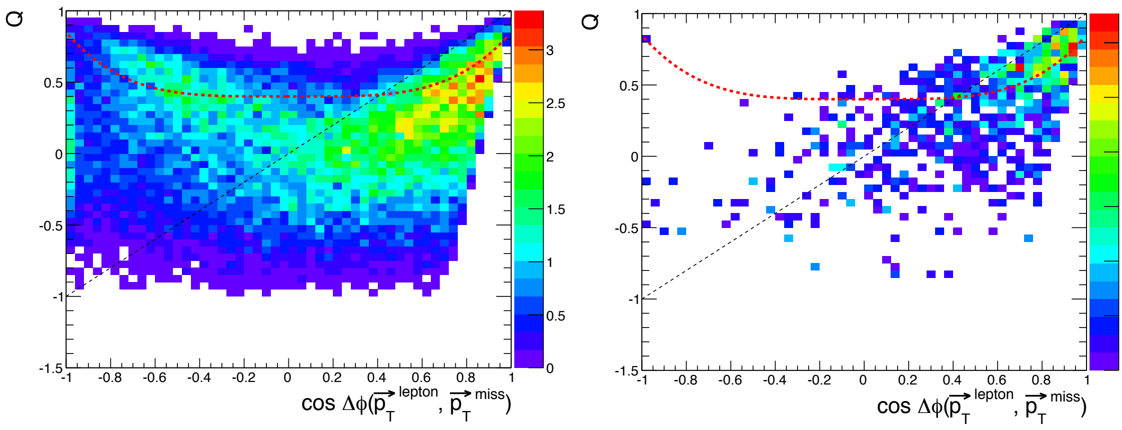

(a) $t\bar{t}$ background.

(b) Simplified model signal point defined by $m(\tilde{\chi}_1^{\pm}\tilde{\chi}_2^0, \tilde{\chi}_1^0)$ = (130,0) GeV.

Figure 6.1: Deconstructed transverse mass shown as event distributions in the $\cos\phi - Q$ plane for $t\bar{t}$ background (left) and a signal point (right) from the simplified model grid. The upper region above the black diagonal line defined by $Q = \cos\phi$ corresponds to selecting events where $m_{\mathrm{T}} > m_{\mathrm{T}}^0 = 100$ GeV. The red contour describes an alternative region that attempts to collect more signal events while removing a larger portion of the $t\bar{t}$ background (more information in text).

the diagonal cut with a fixed[1] m_{T} is not doing a good job at removing most of the background events, especially when $\cos\phi$ tends to -1.

In order to maximize the signal over background ratio, different contours have been investigated using the event distributions in the $\cos\phi - Q$ plane for several signal points. It is important to mention that m_{T}^0 is an arbitrary, fixed number. The chosen value for this optimization study is $m_{\mathrm{T}}^0 = 100$ GeV; below this threshold, the background contribution is too important and above it, the signal sensitivity is decreasing. The signal points that serve for benchmarking are those from the simplified model grid, $m(\tilde{\chi}_1^{\pm}\tilde{\chi}_2^0, \tilde{\chi}_1^0)$ = (130,0) GeV and $m(\tilde{\chi}_1^{\pm}\tilde{\chi}_2^0, \tilde{\chi}_1^0)$ = (250,0) GeV, which are mostly sensitive in SRAh and SRBh regions respectively. For conciseness, only one example of contour is drawn in Figures 6.1a and 6.1b: the dashed red curve is defined as a polynomial function of degree four: $Q = \alpha(\cos\phi)^4 + \alpha$, with $\alpha = 0.4$. To quantitatively assess the sensitivity, the significance Z_N is computed in the new selection that corresponds to taking events in the upper region above the red contour.

---

[1] Here the diagonal corresponds to $m_{\mathrm{T}}^0 = 100$ GeV but the statement still holds for m_{T}^0 values within 100±20 GeV.

6.1.3 Impact on the sensitivity

One-sided significances, as introduced in Section 5.4.3, are calculated for the different contours studied with all signal points of the simplified model grid. The uncertainty on the background prediction is assumed to be 30%. For comparison, the expected discovery significance for all points of the simplified model grid are shown in Figure 6.2a for the union of SRAh and SRBh, as defined in Chapter 5: 2 b-jets, $m_{\mathrm{CT}} > 100$ GeV, $E_{\mathrm{T}}^{\mathrm{miss}} > 100$ GeV, $m_{\mathrm{T}} > 100$ GeV and $45 < m_{bb} < 195$ GeV. Figure 6.2b shows the significances for the same signal grid in a modified region using the same cuts as above except the constraint on m_{T}, which is replaced by: $Q > \alpha(\cos\phi)^4 + \alpha$, with $\alpha = 0.4$.

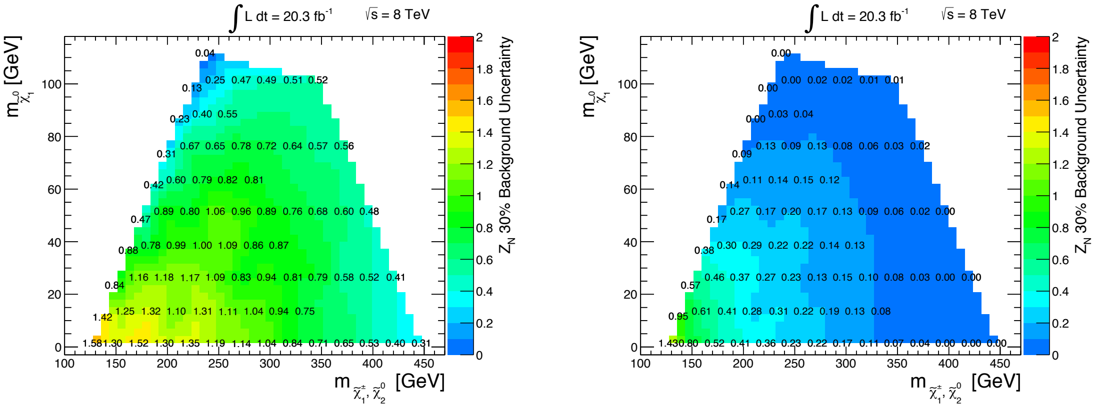

(a) Standard m_{T} cut.

(b) Deconstructed m_{T} cut (quartic contour).

Figure 6.2: Significance maps for the simplified model grid in the union of SRAh and SRBh as defined in Chapter 5. One the right, the cut $m_{\mathrm{T}} > 100$ GeV is replaced by the deconstructed transverse mass cut: $Q > \alpha(\cos\phi)^4 + \alpha$, with $\alpha = 0.4$.

It turns out that the new contour fails to improve the significance and unfortunately worsens the sensitivity. The other contours are giving similar unsatisfying results. This is partly understandable as the analysis after optimization is severely constraint by low statistics in the signal regions. More importantly, the method used here is a simple attempt to refine signal and background separation based on guessing a contour. This contour is adjusted "by hand" after looking at several event distributions in the $\cos\phi - Q$ plane for the main backgrounds and signal points. A more rigorous procedure would have been to implement a proper multi-variate analysis (such as a Boosted Decision Trees), which the timeline of this thesis did not allow.

6.2 Correction of b-jet momentum

A more successful investigation has been performed on the analysis to gain sensitivity. It uses the technique developed by the ATLAS group searching for the SM Higgs boson decaying into a pair of b-jets [86]. This method corrects the four momentum of the selected signal b-jets in order to improve the resolution of the di-jet mass resonance; a well reconstructed resonance mass acts as a powerful discriminant against the – mostly non-resonant – main backgrounds.

6.2.1 The "muon-in-jet" correction

As seen in Chapter 4, jets are a collection of particles. Pions produced by the hadronization of the b-quarks can decay leptonically, thus muons can be found in jets. Sometimes a muon near the edge of a jet can be mistakenly reconstructed as a separate lepton. The overlap removal procedure described in Section 4.4.2 suppresses the muons that are falling within an angular distance $\Delta R < 0.4$ of the jet axis; these can not be considered as signal isolated leptons.

However the information about the energy of these deleted muons, which are likely to be part of the jet due to their closeness, is lost. The "muon-in-jet" correction consists of adding the 4-vector of baseline muons that satisfy $\Delta R(\mu, \text{jet}) < 0.4$ back into the jet 4-vector. To avoid double-counting of energy, the muon's energy deposits in the calorimeter (which are already included in the reconstructed jet) are substracted from the muon's 4-vector beforehand. If two in-jet muons are found, the closer of the two to the jet is taken.

This procedure increases the energy of the considered jets, which are more likely to pass the selection cuts (*e.g.* on p_{T} threshold). Their momentum is more accurately reconstructed, leading to a possible improvement of the di-jet mass resolution.

6.2.2 Implementation in the SUSY search

The muon-in-jet correction has been implemented in the $1\ell + 2b\text{-jets} + E_{\mathrm{T}}^{\mathrm{miss}}$ SUSY search. For all signal and background events, the baseline muons before overlap removal are saved. The two leading jets[2] are inspected. If a muon is found within $\Delta R(\mu, \text{jet}) < 0.4$ of the leading or sub-leading jet, the muon 4-vector is added to the jet 4-vector after removing the energy deposited by the muon in the calorimeter.

---

[2] Reminder: the two b-jets should be the leading jets in the signal regions.

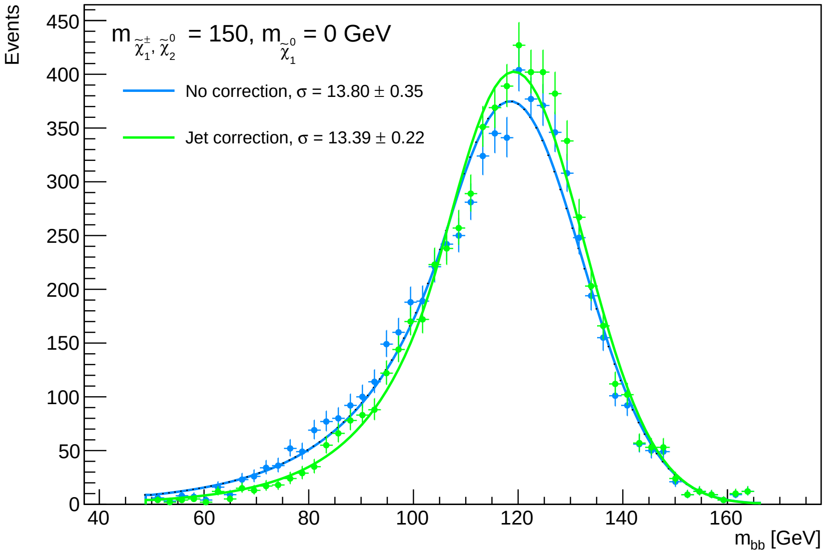

Figure 6.3: Fitted distributions of the di-jet invariant mass m_{bb} (blue) and its correction m_{bb}^{corr} (green) after applying the muon-in-jet correction in a region with exactly two leading b-jets. Tthe legend indicates the fit results on the σ parameter of the Crystal Ball function.

The increase in p_{T} of the corrected jets is around 30%. Jets free of muons have their 4-vector unchanged. The di-jet mass computed after the jet correction is noted m_{bb}^{corr}. As m_{CT} also depends on the jet p_{T}, the discriminating variable is also re-calculated: $m_{\mathrm{CT}}^{\mathrm{corr}}$. To quantify the improvement in the resolution on the signal, distributions of m_{bb}^{corr} are fitted using a Crystal Ball function as it has been performed in Section 5.4.3. The simplified model point $m(\tilde{\chi}_1^{\pm}\tilde{\chi}_2^0, \tilde{\chi}_1^0)$ = (150,0) GeV, which has been produced with enhanced statistics, is used for illustration. Figure 6.3 shows the overlaid fitted distributions of m_{bb} and m_{bb}^{corr}.

For this signal point, the corrected peak is slightly sharper, with the σ parameter of the Crystal Ball function decreasing by 3%. Looking at the resonance maximum, the corrected di-jet mass distribution contains more events in the signal bin defined by $105 < m_{bb} < 135$ GeV (see Section 8.1.1). These increased statistics in the m_{bb} window positively affect the signal yields. What remains to know now is the change of the corrected di-jet distribution for the backgrounds – the main ones being non-resonant around the Higgs mass – to finally get an estimate of the new significance $S/\sqrt{B}$. More precisely, the figure of merit to assess the sensitivity is again the one-sided significance Z_N.

6.2.3 Impact on the sensitivity

In the previous section, the one-sided significances Z_N have been computed in the union of the signal region SRAh and SRBh, in order to compare with the deconstructed transverse mass cut, which could be applied with only one value of m_{T}. As the two signal regions SRAh and SRBh have been independently optimized to address different kinematic configurations, it is more relevant to compute the significance in each region and add them in quadrature. This computation has been done using the regions presented in Section 5.4 and using the same cuts on the modified variables m_{bb}^{corr} and $m_{\mathrm{CT}}^{\mathrm{corr}}$. Figure 6.4 displays the total significance,

$$Z_{N,\mathrm{tot}} = \sqrt{\left(Z_{N,\mathrm{SRAh}}\right)^2 + \left(Z_{N,\mathrm{SRBh}}\right)^2}, \tag{6.4}$$

for all model points of the simplified model grid before and after the muon-in-jet correction. It can be seen on the right figure that the exclusion line at 95% CL, which corresponds to $Z_N \approx 1.64$ (more details in Chapter 8), is pushed to higher values of chargino and neutralino masses. There is thus a significant increase in the exclusion potential for the search. This gain in sensitivity can also be seen, to a lesser extent, on the pMSSM grid in Figure 6.5. New signal regions using a shifted signal bin defined as $110 < m_{bb}^{\mathrm{corr}} < 140$ GeV have been investigated but the expected sensitivity

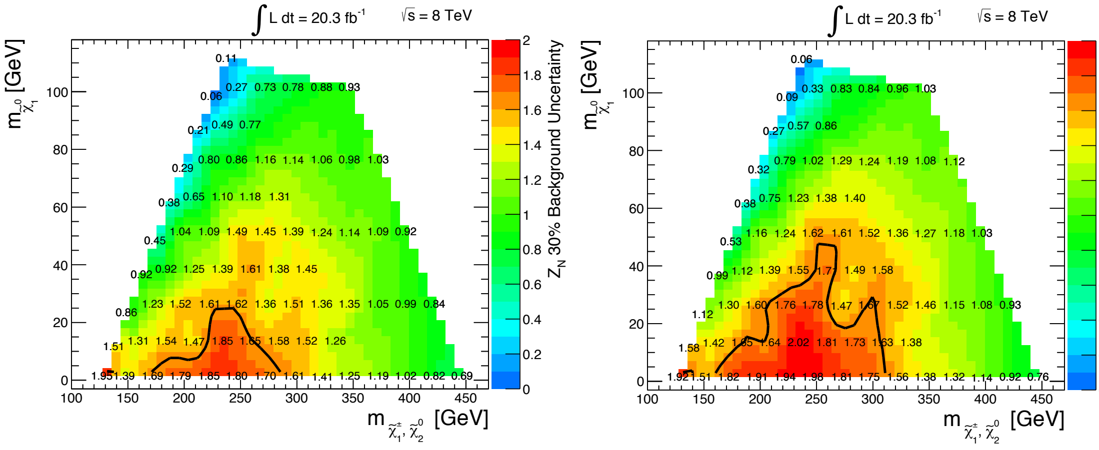

(a) Before correction.

(b) After muon-in-jet correction.

Figure 6.4: Total one-sided significances $Z_{N,\mathrm{tot}}$ (Equation 6.4) for the simplified model grid before (left) and after (right) applying the muon-in-jet correction on the variables m_{bb}^{corr} and $m_{\mathrm{CT}}^{\mathrm{corr}}$.

gave similar results with respect to the current bin at $105 < m_{bb}^{\mathrm{corr}} < 135$ GeV.

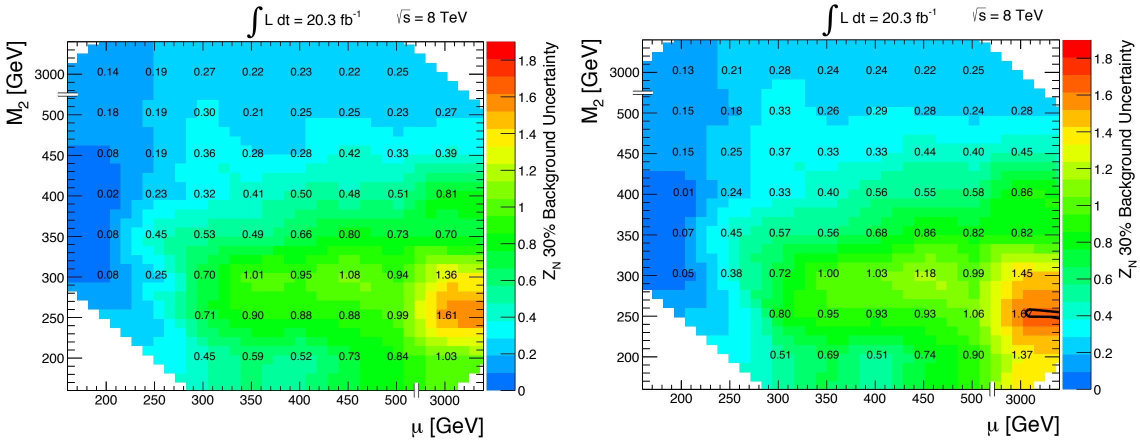

(a) Before correction.

(b) After muon-in-jet correction.

Figure 6.5: Total one-sided significances $Z_{N,\mathrm{tot}}$ (Equation 6.4) for the pMSSM grid before (left) and after (right) applying the muon-in-jet correction on the variables m_{bb}^{corr} and $m_{\mathrm{CT}}^{\mathrm{corr}}$.

The muon-in-jet correction successfully improves the expected sensitivity of the $1\ell + 2b$-jets $+ E_{\mathrm{T}}^{\mathrm{miss}}$ SUSY search. This investigation uses so far predicted yields from simulated Monte Carlo. The final outcome of this study on the observed exclusion limits using ATLAS data will be presented in Chapter 8.

Chapter 7

Systematic uncertainties

Experimental physics results live or die by systematics. While statistical uncertainties are the result of random and uncorrelated fluctuations based on a finite sample, systematic uncertainties, however, are reproducible inaccuracies linked with the measurement apparatus or the imperfect modelling of analysis observables. In the extraction of the final results by the profile likelihood fit described in the next chapter, the background predictions are allowed to vary within the size of the systematic uncertainties and are further constrained by data. The fitting procedure also incorporates the correlations between systematics, which helps reducing their impact while extrapolating the background expectation from the control to the signal regions. This present chapter introduces the systematic uncertainties relevant in the search of this dissertation, categorized into those related to the Monte Carlo modelling (theoretical uncertainties) and those caused by the detector measurements (experimental uncertainties). A summary table for both theoretical and experimental uncertainties lists the variations and their percentage with respect to the nominal yield in the region considered for their estimation.

7.1 Theoretical uncertainties

7.1.1 Variations of Monte Carlo parameters

Monte Carlo programs, albeit very powerful to estimate the background and signal yields, have limitations. These programs need several input parameters, *e.g.* the parton showering algorithm, the strength of initial and final state radiation or the parton distribution functions. The resulting number of simulated events[1], will depend on the choice of these input parameters. The theoretical systematic uncertainties are obtained by varying these parameters and studying their influence on the resulting number of events with respect to the nominal yield. These parameters are:

Generator

Some Monte Carlo generators are better suited for describing a given physics process. Yet their performance may not be the same in all regions of the phase space. That is why it is important to compare the outputs from different generators. The convention used to estimate the uncertainty on generator modelling is to take the difference in yields with two Monte Carlo generators:

$$\sigma^{\text{ generator}} = \sqrt{|S_1 - S_2|^2 + (\sigma_2^{\text{stat}})^2}, \tag{7.1}$$

where S_1 is the event yield taken as the nominal value, S_2 the event yield using a different generator and σ^{stat} is the statistical uncertainty of this other generator. The systematic is symmetrized: the uncertainty is $\pm\sigma^{\text{ generator}}$ around the nominal value S_1.

Parton shower

The initial partons and those produced in the hard scatter are particles with colour charge and therefore radiate virtual gluons, which can in turn create quark-antiquark pairs or gluons. This cascade of parton emissions is referred to as the parton shower (PS). An uncertainty on the choice of the showering algorithm is computed by comparing different shower Monte Carlo programs, applied on the same generated events. As above, the full difference in yields between the nominal S_1 and the variation S_2 is evaluated and symmetrized: $\sigma^{\text{parton shower}} = |S_1 - S_2|$. In this case however, no statistical uncertainty is added since the two samples use the same input events.

Initial and final state radiation

The emission of additional partons in the initial or final states is referred to initial and final state radiation (ISR and FSR), respectively. The related uncertain-

---

[1] At this stage this predicted number of events comes from the theoretical modelling of proton-proton collisions and is independent of the detector efficiency and acceptance.

ties are assessed using dedicated samples produced with Monte Carlo generator AcerMC. In these samples labelled "MorePS" and "LessPS", the parameters that control the amount of initial and final radiation are changed to produce more ISR/FSR or less ISR/FSR, respectively. The nominal value is the mean of the two yields: $S^{\text{Nom}} = (S^{\text{MorePS}} + S^{\text{LessPS}})/2$. The systematic uncertainty is half the difference and is symmetrized:

$$\sigma^{\text{ ISR/FSR}} = \frac{\left|S^{\text{MorePS}} - S^{\text{LessPS}}\right|}{2}. \tag{7.2}$$

Finite number of partons

The background contributions involving the production of W and/or Z bosons are generated by subprocess (*e.g.* $Wb\bar{b}$, $Wb\bar{b}$, $Wc\bar{c}$, $W\ell\nu\ell\nu$, $W\ell\nu qq$), each divided with a fixed number of extra partons N_p in the final state ($N_p = 0, 1, 2, 3...$). To account for the impact from the use of finite number of additional partons in the nominal samples, an uncertainty is evaluated by comparing samples generated with different numbers of partons (*e.g.* for diboson, nominal samples contain up to 2 extra partons and are compared with samples containing up to 3 additional partons). The systematic is the full difference of yields, symmetrized.

Scale variation

All Monte Carlo events are generated using a specific scale, which is process-dependent. The renormalization scale imposes a short-distance cutoff to absorb the ultraviolet infinities. Factorization acts in the same way at the opposite end of the energy range of perturbative QCD, isolating the infrared singularities of long-distance physics. A measurable cross section – leading to an event yield – should not be dependent on this regularization of infrared or ultraviolet divergences. To estimate the impact of the scale choice, the renormalization and factorization scales are conventionally varied by half and twice the nominal scales. This is done using specific Monte Carlo samples labelled ×0.5 and ×2 for each scale. The uncertainty is taken as the full difference of yields $S^{\times 0.5}_{\text{fac, ren}} - S^{\times 2}_{\text{fac, ren}}$, symmetrized around the nominal value $S^{\text{nom}}_{\text{fac, ren}} = (S^{\times 0.5}_{\text{fac, ren}} + S^{\times 2}_{\text{fac, ren}})/2$.

Matching scheme

Interfacing the outputs of a hard process from a Monte Carlo generator to an external showering package can lead to double counting of some portions of the phase space (*e.g.* the parton shower can generate additional jets in phase space regions already covered at the event generation level). The matching refers to the procedure aiming at removing those double-countings. Some background samples use the CKKW scheme, which chooses a scale at which to separate the parton shower description and the matrix element description. As for the renormalization and factorization scales, the comparison of yields from different CKKW scales (usually 10 GeV and 30 GeV) emulates the uncertainty associated with this procedure.

PDF sets

When the two high-energy beams of protons meet in the center of ATLAS, the created collision involves the partons, each carrying a fraction x of the longitudinal momentum of the proton. Pardon Distribution Functions (PDFs) represent the probability densities to find a given parton (among the gluon and the six quark flavors) carrying a momentum fraction x at the energy scale Q^2 of the hard interaction. PDFs are obtained through fits on experimental data. The results are extrapolated to higher values of Q^2 that match the LHC energy scale. PDF fits contain inherent uncertainties due to the fitting procedure and therefore each nominal PDF set produced by a given collaboration is accompanied by error PDF sets. The variations are assessed by changing one by one the independent parameters, which are called “eigenvectors”. In this analysis, most background samples use the PDF set CT10 which contains 52 additional error sets. An uncertainty is derived by reweighting each event and taking the maximum/minimum differences between the nominal PDF yield.

7.1.2 Prescription for deriving theoretical uncertainties

The SUSY Working Group provides recommendations on how to derive the uncertainties for all processes simulated with Monte Carlo. These technical prescriptions are detailed in Appendix B. Table 7.1 lists the theoretical systematic uncertainties of the major and secondary backgrounds, expressed in per cent of the total considered background yield in each control, validation and signal regions. The dominant theoretical uncertainties for this analysis are related to the generator and parton shower for the $t\bar{t}$ background and to the generator+interference and parton shower for the single-top Wt-channel contribution.

Concerning the signal, all the theoretical uncertainties on a given signal point are merged into an uncertainty on the predicted cross section, as it will be further explained in the next chapter.

Table 7.1: Theoretical systematic uncertainties of the main backgrounds expressed in percentage with respect to the nominal yield of the considered background and variation. The W+jets background has uncertainties associated with the parton shower, factorization, renormalization, scale variations and heavy flavor removal, which are all negligible except for the factorization variation. The uncertainty on $t\bar{t}$ (W+jets) cross section is contained in the uncertainty of the normalization parameter $\mu_{t\bar{t}}$ ($\mu_{W\text{+jets}}$), obtained through a fitting procedure to adjust the floated backgrounds $t\bar{t}$ and W+jets to the data (see Chapter 8).

	Variation	CRT	CRW	VRA	VRB	SRA	SRB
$t\bar{t}$	Generator	7.33	6.67	7.14	12.89	45.49	70.29
	Parton shower	14.81	10.08	1.27	9.33	9.57	15.37
	ISR/FSR	5.22	3.43	1.44	1.06	11.50	11.31
	Factorization	0.10	0.06	2.15	0.18	14.30	13.90
	Renormalization	0.21	0.12	3.42	0.70	9.42	3.82
	PDFs	$^{+5.68}_{-5.11}$	$^{+7.51}_{-6.84}$	$^{+5.69}_{-5.14}$	$^{+8.20}_{-7.24}$	$^{+8.13}_{-7.42}$	$^{+8.39}_{-7.34}$
W+jets	Factorization	5.39	0.08	5.40	7.71	6.35	7.30
	PDFs	$^{+2.99}_{-3.23}$	$^{+3.22}_{-2.70}$	$^{+2.45}_{-2.54}$	$^{+3.03}_{-3.40}$	$^{+3.23}_{-3.76}$	5.58
Single-top	Gen. & interference (Wt)	10.56	6.75	6.19	7.71	27.05	51.61
	Parton shower (Wt)	14.92	9.26	1.32	8.00	12.29	1.28
	ISR/FSR	11 (t-channel), 7 (s-channel)					
	Cross section t-channel	$^{+3.92}_{-2.18}$					
	Cross section t-channel	3.92					
	Cross section t-channel	6.80					
Diboson	Factorization		18.56	derived in			
	Renormalization		2.33	inclusive region			
	CKKW-matching		6.08	(see Appendix B)			
	Cross section	5 (WW and ZZ), 7 (WZ)					

7.2 Experimental uncertainties

Each entity measured in ATLAS, such as the particle momentum or the object identification efficiency, is accompanied by a systematic error on its assessment. Experimental systematic uncertainties are common to all samples, signal and background. Two methods are used to obtain the up/down variation of a systematic: the variation is either stored as an up/down weight applied event-by-event or the variation is applied to the properties of an object, leading to a separate event selection that gives the varied up/down yield. The different classes of experimental systematic uncertainties considered in this analysis are briefly explained below.

7.2.1 Pile-up uncertainty

The nominal value of the pileup weight is determined by scaling the average number of interactions per crossing μ in the Monte Carlo by 0.9 (this is based on a data/MC comparison of the number of vertices as a function of μ). The lower- and upper-variations are derived with 1.05 and 1.13 scaling on the average number of interactions per crossing, respectively.

7.2.2 Luminosity uncertainty

The luminosity measurement is performed by the ATLAS detector. An uncertainty of 2.8% on the integrated luminosity (20.3 fb^{-1}) is assumed, derived following the methodology detailed in Reference [87].

7.2.3 Jet uncertainties

Jet energy scale

The calibration procedure to correct the jets to the proper energy scale generates the highest source of experimental uncertainty in most analyses with jets as final state objects. The JES uncertainty is estimated by comparing transverse momentum balance between the jet and a reference object [39]. It is split into 18 components that cover the various sources of uncertainty, such as the pile-up contamination, the calorimeter response, the in-situ and MC-based calibration techniques in different p_{T}/η ranges, the jet flavor composition and the presence of close-by jets. For each component, the jet four-momentum receives a p_{T}- and η-dependent modification; the event selection is then performed on the modified jet properties, leading to a different event yield. The total JES uncertainty is given by the quadratic sum of all 18 contributions, however in this search all parameters are propagated through the analysis separately in order to maintain the full information on correlations.

Jet energy resolution

An extra p_{T} smearing is added to the jets based on their p_{T} and η to account for a possible underestimate of the jet energy resolution value in the MC simulation [40].

Jet vertex fraction

This pile-up suppression cut is applied in this analysis only on the central jets with $p_{\mathrm{T}} < 50$ GeV. The jet vertex fraction (JVF) cut is afflicted with a systematic uncertainty: the jets are defined either as hard-scatter or pile-up jets based on an angular matching between truth and reconstructed jets. Depending on the category the jet falls into, a separate up/down JFV cut is applied as a function of p_{T} and η.

Flavor tagging

The b-tagging uncertainty is evaluated by varying the η-, p_{T}-, operating point, and flavor-dependent scale factors applied to each jet within a range that reflects the systematic uncertainty on the measured tagging efficiency and mistag rates. These variations are applied separately to b-jets, c-jets and light jets, leading to three uncorrelated systematic uncertainties.

7.2.4 Lepton uncertainties

Lepton reconstruction and trigger efficiencies

For every selected lepton in MC, a multiplicative scale factor is applied to account for data/MC differences in the lepton reconstruction and trigger efficiencies. Each scale factor is varied within its $\pm 1\sigma$ errors to assess the two systematic uncertainties on the lepton reconstruction and trigger efficiencies.

Lepton energy scale and momentum resolution

For all selected leptons, the correction factor on the energy scale is fluctuated up and down by its 1σ uncertainties. There are separate uncertainties for the $Z \to e^+e^-$ measurements used for calibration, the presampler scale, material, and low-p_{T} electrons, all of which are treated as uncorrelated [88]. The uncertainty on the electron energy resolution is derived using $Z \to e^+e^-$ events [88]. Two uncertainties, one related to the ID and the other to the MS, account for the muon momentum resolution assessed by smearing the muon momentum to match it with the dimuon invariant mass resolution in $Z \to \mu^+\mu^-$ events [89].

7.2.5 Uncertainty on the missing transverse momentum

The $E_{\mathrm{T}}^{\mathrm{miss}}$, as defined in Section 4.3, is the sum built from the properties of the objects listed above. Therefore the effects from the jet and lepton scale and resolution uncertainties are for the most part already taken into account. Yet an additional systematic uncertainty needs be derived for the last term of the $E_{\mathrm{T}}^{\mathrm{miss}}$ sum (`CellOut`), as this entity incorporates the calorimeter clusters outside any reconstructed objects. It is found to be negligible compared to the total $E_{\mathrm{T}}^{\mathrm{miss}}$ uncertainty.

7.2.6 Summary on experimental uncertainties

Now that the experimental systematic uncertainties have been introduced, it is of importance to know which ones are contributing the most and which variations are small with respect to the nominal yields. Table 7.2 lists the experimental uncertainties calculated on all samples in this analysis, with their relative percentage with respect to the nominal yield of the total background. It can be seen from this table that the JES and the b-tagging uncertainties are dominant, as this is generally the case for analyses with flavor tagged jets in the final states. The lepton uncertainties are small ($< 3\%$) and have been merged. The 18 JES components are groupped for better readability, however in the extraction of final results, they are treated separately to account for all correlations. This fitting procedure is presented in the following chapter.

Table 7.2: Breakdown of the experimental systematic uncertainties on background estimates expressed in percentages relative to the total expected background (except the top three rows expressed in total event yields). Here the uncertainties on the Jet Energy Scale have been grouped together for better readability, as well as these on the electron and muon reconstruction, which are small. The total uncertainties are obtained by summing the individual ones in quadrature but it is not the case after the fitting procedure due to the correlations.

Uncertainty	CRT	CRW	VRA	VRB	SRAsb	SRBsb	SRAh	SRBh
Total background expectation	547.96	1703.17	830.35	241.95	11.23	7.79	4.98	2.24
Total statistical ($\sqrt{N_{\mathrm{exp}}}$)	±23.41	±41.27	±28.82	±15.55	±3.35	±2.79	±2.23	±1.50
Total background systematic	±101.78	±90.93	±71.49	±25.62	±3.27	±2.00	±1.69	±0.94
Total relative uncertainty (in %)	18.57	5.34	8.61	10.59	29.12	25.72	33.92	42.04
Pile-up	0.11	0.07	0.32	0.23	2.05	1.28	2.81	2.68
Luminosity	0.11	0.31	0.30	0.47	0.53	1.28	0.80	1.34
Jet Energy Scale	8.68	2.17	4.85	1.25	6.86	4.49	11.85	20.09
Jet Energy Resolution	0.23	0.00	0.43	0.95	1.69	0.39	2.21	8.04
Jet Vertex Fraction	1.14	0.59	0.43	0.08	0.80	0.26	0.60	0.89
Jet b-tagging efficiency	2.20	0.46	2.27	0.91	1.51	3.34	1.41	2.68
Jet c-tagging efficiency	0.04	0.36	1.96	5.62	5.08	2.95	5.82	4.02
Electron reconstruction	0.52	0.18	0.43	0.48	1.34	1.41	3.21	3.13
Muon reconstruction	0.14	0.09	0.11	0.14	0.62	1.67	1.20	0.89
$E_{\mathrm{T}}^{\mathrm{miss}}$ Soft Scale	0.36	0.49	0.23	0.76	3.29	1.80	3.61	3.13
$E_{\mathrm{T}}^{\mathrm{miss}}$ Resolution	0.02	0.04	0.16	0.17	1.42	0.51	2.41	2.68

Chapter 8

Test statistic and interpretation of results

To conclude whether the supersymmetric scenario postulated in this search is likely to occur in nature or not, the observed data are compared to the background and signal predictions. The level of compatibility between the observed data and a hypothesis — the absence or presence of SUSY signal — is quantified; results are derived through several fitting procedures as part of a frequentist likelihood-based approach. This chapter first introduces the statistical method used by ATLAS SUSY searches. The results of the background-only fit, which adjusts the main Monte Carlo backgrounds to the data, are disclosed. Then the model-independent and model-dependent interpretations of the results obtained from exclusion fits are presented. The exclusion contours of the published analysis (Chapter 5) are compared with the ones produced using the corrected di-jet mass m_{bb}^{corr} (Chapter 6). Finally the results from the combination with the analyses targeting the other decay modes of the Higgs boson, $h \to \gamma\gamma$ and $h \to WW$, will be given and discussed.

8.1 Statistical analysis

The goal of a statistical analysis is to state, from a dataset, the likelihood on its outcome given a model. In a *frequentist* approach, the key variable is the p-value.

The p-value measures the significance of a deviation between the predicted yields and the observed event count from the data, always under a given hypothesis. This deviation can be an excess of data events above the background prediction (possible discovery) or insufficient data events reaching the background+signal yields (possible signal model exclusion). In other words, it states how *frequent* such a deviation in the observed data from the prediction would occur if there were a collection of ATLAS detectors repeating the same experiment, assuming only the background (or the background+signal in a context of signal exclusion) contributes to the predicted yields.

The computation of a p-value requires several steps that are listed in the next subsections.

8.1.1 Parametrization of inputs

The input ingredients that serve to parametrize the dataset are event yields, usually presented as histograms of a kinematic variable. In the context of the $1\ell + 2b$-jets + $E_{\mathrm{T}}^{\mathrm{miss}}$ search, these histograms are the distributions of the discriminating variable m_{bb}. These distributions are each divided into bins of equal width $\Delta m_{bb} = 30$ GeV (as explained in Section). In total the distributions form a collection of 18 bins in the control regions (five in CRT, five in CRW, four in SRAsb and four in SRBsb) and two single-bin signal regions (SRAh and SRBh). For each bin i, the information available is:

- the observed event count n_i^{obs} in the data,
- the expected number of signal events s_i,
- the total expected number of events b_{tot} from all background sub-processes,
- the systematics uncertainties on the signal and the background, $\boldsymbol{\theta}_s$ and $\boldsymbol{\theta}_b$, respectively. They are represented as a vector of all the different theoretical and experimental systematics that can be applied on either the signal, the background or both.

For each bin i, the expected number of events n_i^{exp} can be parametrized in the following way (ignoring the systematics contribution for now):

$$n_i^{\mathrm{exp}} = \mu s_i + b_i, \tag{8.1}$$

where μ is the parameter of interest. It represents the signal strength: $\mu = 0$ corresponds to the null hypothesis where the signal is absent, whereas $\mu = 1$ refers to the hypothesis of the presence of the considered signal at the expected cross section.

Equation 8.1 gives the mean number of events for only one bin. The information on the shape of the histograms, that is to say the correlations across bins in the m_{bb} distributions, is modelled through a probability density function:

$$s_i = s_{\text{tot}} \int_{\text{bin } i} f_s(x;\boldsymbol{\theta}_s)\,dx \qquad\qquad b_i = b_{\text{tot}} \int_{\text{bin } i} f_b(x;\boldsymbol{\theta}_b)\,dx, \tag{8.2}$$

where $f_s(x;\boldsymbol{\theta}_s)$ and $f_b(x;\boldsymbol{\theta}_b)$ are the probability density functions of the variable m_{bb} (written x here for more readability) for the signal and the background, respectively. The quantities s_{tot} and b_{tot} are the total expected mean numbers of signal and background events. The parameters $\boldsymbol{\theta}_s$ and $\boldsymbol{\theta}_b$ characterize the shapes of the probability density functions.

The number of events for background and signal predictions is assumed to follow Poisson statistics. The probability of observing, in the bin i, n_i^{obs} events given the model prediction $n_i^{\text{exp}}(\mu)$ is $\text{Pois}\left(n_i^{\text{obs}}|n_i^{\text{exp}}(\mu)\right)$.

8.1.2 Likelihood function

The numerous input parameters are encapsulated in a function summarizing in a single value all available information about the dataset: the likelihood function $L(\mu,\boldsymbol{\theta})$. It is the probability of the observed data, given the model parameters (that are here the assumed signal strength μ and $\boldsymbol{\theta}$). The general form of the likelihood function, conditioned by the set of observed event counts $\boldsymbol{n}^{\text{obs}}$ in the N bins, is a product of Poisson probabilities:

$$L(\mu,\boldsymbol{\theta}|\boldsymbol{n}^{\text{obs}}) = \prod_{i}^{N} \text{Pois}(\,n_i^{\text{obs}}\,|\,n_i^{\text{exp}}(\mu,\boldsymbol{\theta}))\;\times\; C_{\text{syst}}(\boldsymbol{\theta}^0,\boldsymbol{\theta}) \tag{8.3}$$

where $\boldsymbol{\theta} = (\boldsymbol{\theta}_s, \boldsymbol{\theta}_b, b_{\text{tot}})$ includes the expected number of background events and all the systematics that impact the total predicted number of events n_i^{exp}. The left product runs over all regions of the phase-space (here all the N bins), while the right term relates to the modelling of the systematics, which is clarified in the next subsection.

8.1.3 Treatment of systematic uncertainties

Each systematic uncertainty u is described as a nuisance parameter θ_u. The values of each θ_u are allowed to vary around the corresponding measured values θ_u^0. These central values θ_u^0 are obtained by subsidiary measurements, detailed in Chapter 7. The probability density function for the nuisance parameters are typically modelled by Gaussians of unit width, such that $\theta_u = \pm 1$ translates to a variation of $\pm 1\sigma$ around the central value θ_u^0. $C_{\mathrm{syst}}(\boldsymbol{\theta}^0, \boldsymbol{\theta})$ represents the probability that the nuisance parameters take on particular value $\boldsymbol{\theta}$. Assuming the nuisance parameters are independent, $C_{\mathrm{syst}}(\boldsymbol{\theta}^0, \boldsymbol{\theta})$ is simply the product of the individual probability distributions – obtained by the auxiliary measurements – of the N_u considered systematic uncertainties:

$$C_{\mathrm{syst}}(\boldsymbol{\theta}^0, \boldsymbol{\theta}) = \prod_u^{N_u} G(\theta_u^0 - \theta_u). \tag{8.4}$$

These probabilities are included in the product of the likelihood function, constraining the nuisance parameters in the likelihood maximization procedure, which is presented in the next section. With this formulation, if the measurements do not match the Monte Carlo predictions, the background normalization factor b_{tot} as well as the systematic uncertainties $\boldsymbol{\theta}$ can accommodate the deviations.

8.1.4 The CL$_s$ method

The likelihood function conveniently encapsulates in one number the agreement between data and the predicted yields, for a hypothesized value of μ. It can actually serve as a test statistic. The prescription followed by ATLAS and CMS is a test based on a profile log-likelihood ratio (LLR) [90]. A general formulation[1] of the test statistic for one hypothesized signal strength μ is defined as:

$$q_\mu = -2 \ln \frac{L(\,\mu, \hat{\hat{\boldsymbol{\theta}}}(\mu)\,)}{L(\,\hat{\mu}, \hat{\boldsymbol{\theta}}(\mu)\,)}, \tag{8.5}$$

where $\hat{\mu}$ and $\hat{\boldsymbol{\theta}}$ maximize the likelihood function in the denominator, and $\hat{\hat{\boldsymbol{\theta}}}(\mu)$ maximizes L for the specified value of μ. This ratio thus tests a hypothesized μ against $\hat{\mu}$, the maximum likelihood estimator of μ. If the tested μ is very different from $\hat{\mu}$, *i.e.* the data are incompatible with the hypothesis, then q_μ will take large values, as the denominator gets much greater than the numerator from the maximization of $L(\,\hat{\mu}, \hat{\boldsymbol{\theta}}(\mu)\,)$.

---

[1] A more detailed definition of this test depending on the ranges of μ and $\hat{\mu}$ will be given in Section 8.3.1.

The p-value is calculated using a distribution of the test statistic: $f(q_\mu|\mu, \boldsymbol{\theta}(\mu))$. The evaluation of this probability density function is reviewed later in Section 8.3.1. From this test statistic, two p-values are defined. The p-value of the signal+background $s+b$ hypothesis[2] is defined as the probability to find a value of q_{s+b} with equal or greater than (*i.e.* with equal or lesser compatibility with) the $s+b$ model relative to q^{obs}:

$$p_{s+b} = \mathbb{P}(q \geqslant q^{\text{obs}}\,|s+b) = \int_{q^{\text{obs}}}^{\infty} f(q|s+b)dq, \tag{8.6}$$

where q^{obs} is the observed value obtained from the experimental data. The p_b for the alternate background-only hypothesis is:

$$p_b = \mathbb{P}(q \leqslant q^{\text{obs}}\,|b) = \int_{-\infty}^{q^{\text{obs}}} f(q|b)dq = 1 - \int_{q^{\text{obs}}}^{\infty} f(q|b)dq. \tag{8.7}$$

To exclude a signal model, the ATLAS Collaboration follows the CL_s method [91], which uses a modified version of the p-value:

$$\text{CL}_s = \frac{p_{s+b}}{1-p_b} = \frac{\text{CL}_{s+b}}{\text{CL}_b}, \tag{8.8}$$

where CL_{s+b} and CL_b are the confidence levels for the signal+background and background hypotheses, respectively. A signal model is regarded as excluded at a confidence level (CL) of $1-\alpha$ if one finds $\text{CL}_s < \alpha$, where α is usually set to 5%.

This definition prevents the spurious exclusion of signal for which the analysis has no sensitivity (when $s \ll b$). In the case of a downward fluctuation of the data where $n^{\text{obs}} < b$, there is greater incompatibility with respect to the signal+background hypothesis, hence p_{s+b} becomes small. The model could be erroneously excluded if only p_{s+b} was assessed. This is avoided with the CL_s method because, in this situation, the denominator $1-p_b$ becomes small to penalize p_{s+b} and thus the final value of CL_s is increased.

---

[2] The signal+background hypothesis corresponds to the case $\mu = 1$ while the background-only hypothesis is for $\mu = 0$. The reason behind this change of writing is to comply with usual notation in the literature, as well as not to confuse p_b with p_0, the former being assessed in an exclusion fit configuration while the latter commonly refers to a discovery p-value, established with a different test statistic [90].

8.2 Background validation

As a first step, the predictions of the simulated background processes are adjusted to the data.

8.2.1 Background-only fit

The signal component is removed from the likelihood function in Equation 8.3 and a “background-only” fit is performed. The free parameters of the fit are the normalization factors $\mu_{t\bar{t}}$ and $\mu_{W\text{+jets}}$ of the main backgrounds $t\bar{t}$ and $W+$jets, respectively. They are constrained by the number of observed events in the control regions (CRs) and signal region (SR) sidebands.[3] The nuisance parameters $\boldsymbol{\theta}$ are also varied such as to maximize the likelihood function.

The normalization factors of $\mu_{t\bar{t}}$ and $\mu_{W\text{+jets}}$ given by the fit serve to coherently extrapolate the background predictions from the CRs to the VRs and then to the SRs. The modelling of systematic uncertainties in the likelihood leads to an error propagation that takes into account the correlations between the different systematic uncertainties.

The background-only fit, as well as the limit-setting procedure, is performed using the HistFitter package [92].

8.2.2 Results

The results of the blinded fit are presented in Table 8.1: the estimated Monte Carlo predictions and fitted yields are shown for the main backgrounds, along with the extrapolated predictions in the SRAh and SRBh bins.

---

[3] At first, only the eight m_{bb} sideband bins of the SRs and the ten m_{bb} bins of the CRs are considered, as part of a “blinded” fit configuration. Once a satisfactory agreement is found between the normalized background predictions and the observed data in the validation regions, the background predictions are further extrapolated to the SRs and an “unblinded” fit is performed including the two remaining bins of the signal regions SRAh and SRBh.

Table 8.1: Expected yields from the Monte Carlo simulation before and after the blinded background-only fit. "Single top" merges the contributions of s-, t- and Wt-channels. Negligible backgrounds are grouped into "Others" and include Z+jets, ZH and WH. The errors shown are the quadratic sum of the statistical and systematic uncertainties.

Yields in regions	**CRT**	**CRW**	**SRAsb**	**SRBsb**	**VRA**	**VRB**	**SRAh**	**SRBh**
Observed events	651	1547	14	10	885	235	4	3
MC yields after fit	642.0 ± 24.9	1558.0 ± 38.7	13.1 ± 2.4	8.8 ± 1.7	880.4 ± 85.5	245.2 ± 17.2	6.0 ± 1.3	2.8 ± 0.8
$t\bar{t}$	607.3 ± 25.3	676.6 ± 56.9	8.0 ± 2.4	3.1 ± 1.4	684.8 ± 85.6	141.0 ± 17.9	3.8 ± 1.2	1.4 ± 0.7
W+jets	11.1 ± 1.6	693.8 ± 59.8	2.7 ± 0.5	1.7 ± 0.3	99.2 ± 11.9	62.2 ± 8.4	0.6 ± 0.3	0.2 ± 0.1
Single top	19.5 ± 3.5	111.5 ± 13.8	1.9 ± 0.6	2.5 ± 1.1	80.0 ± 9.6	27.2 ± 3.8	1.3 ± 0.4	0.7 ± 0.4
Diboson	2.3 ± 0.4	64.4 ± 7.7	0.3 ± 0.1	1.1 ± 0.2	10.2 ± 1.5	9.0 ± 1.0	0.0 ± 0.0	0.2 ± 0.0
Others	1.8 ± 0.3	11.7 ± 1.0	0.2 ± 0.0	0.4 ± 0.1	6.3 ± 0.6	5.8 ± 0.5	0.3 ± 0.0	0.2 ± 0.1
MC yields before fit	548.0 ± 101.8	1703.2 ± 90.9	11.2 ± 3.3	7.8 ± 2.0	830.4 ± 71.5	242.0 ± 25.6	5.0 ± 1.7	2.2 ± 0.9
$t\bar{t}$	511.7 ± 101.0	636.6 ± 93.5	5.8 ± 3.1	2.0 ± 1.6	617.2 ± 61.0	124.9 ± 23.8	2.8 ± 1.5	0.9 ± 0.8
W+jets	13.7 ± 1.6	880.5 ± 2.6	3.2 ± 0.6	2.2 ± 0.4	123.0 ± 9.2	76.6 ± 7.7	0.7 ± 0.4	0.3 ± 0.2
Single top	18.7 ± 3.8	111.6 ± 15.1	1.7 ± 0.6	2.1 ± 1.1	74.9 ± 13.8	26.2 ± 4.1	1.2 ± 0.4	0.6 ± 0.4
Diboson	2.1 ± 0.5	62.8 ± 8.7	0.4 ± 0.2	1.1 ± 0.2	9.4 ± 2.0	8.7 ± 1.2	0.0 ± 0.0	0.2 ± 0.1
Others	1.9 ± 0.3	11.6 ± 1.2	0.2 ± 0.1	0.4 ± 0.1	6.0 ± 0.7	5.6 ± 0.6	0.3 ± 0.1	0.2 ± 0.1

The normalization factors are found to be 1.03 ± 0.15 for $t\bar{t}$ and 0.79 ± 0.07 for $W+$jets, where the errors include statistical and systematic uncertainties. These factors are negatively correlated due to the CRs' composition: while CRT is highly dominated by $t\bar{t}$ events, CRW is evenly populated by $t\bar{t}$ and $W+$jets events. If the normalization of $t\bar{t}$ increases, the normalization of $W+$jets thus decreases, and inversely. As a consequence, the uncertainties on individual background sources do not add up quadratically to the uncertainty on the total SM expectation.

The $W+$jets normalization factor differs from unity and this can be explained by the limited accuracy of the Monte Carlo generator, which only includes NLO contributions. However the shapes of the $W+$jets distributions agree well with data in the validation regions.

As a reminder and for better visualization, the map of CRs, VRs, and SRs in the m_{T}–m_{CT} plane shown in Chapter 5 is displayed here in Figure 8.1. Table 8.2 lists the combination of regions used to validate the extrapolation, *i.e.* where the resulting region covers the full range of the considered variable. Figures 8.2, 8.3, 8.4 and 8.5 show the event distributions of the main kinematic variables, which are extrapolated in these merged regions.

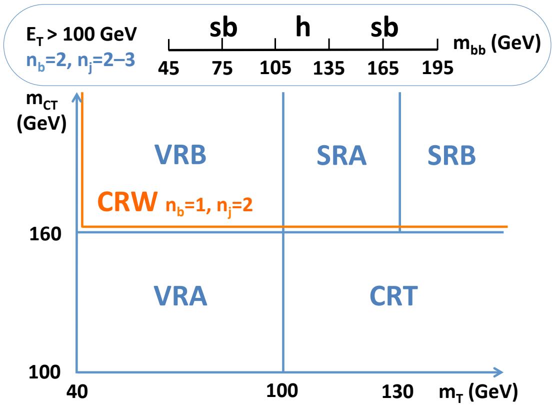

Figure 8.1: Control, validation and signal regions as a function of m_{T}, m_{CT}, the signal jet and b-tagged jet multiplicities. More information in text and in Section 5.5.3.

Table 8.2: Extrapolation regions for each kinematic variables defining the CRs, VRs and SRs.

Variable	**Regions of extrapolation**
m_{CT}	VRA+VRB CRT+SRAsb+SRBsb CRT+SRAh+SRBh
m_{T}	VRA+CRT VRB+SRAsb+SRBsb VRB+SRAh+SRBh
m_{bb}	VRA+VRB SRA+SRB
$n^{b\text{-jet}}$	SRA*+SRB* * without the cut: $n^{b\text{-jet}} = 2$.

Additional tables and figures with more details on the blinded and unblinded background-only fits are provided in Appendix C.

The same procedure has been performed on the analysis with the corrected di-jet

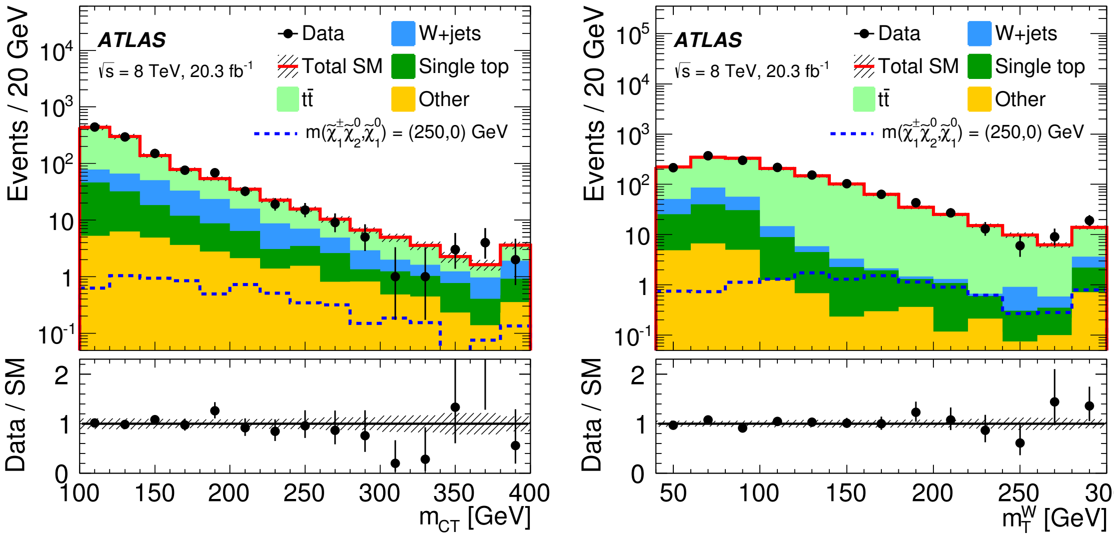

(a) m_{CT} distribution in VRA+VRB.

(b) m_{T} distribution in VRA+CRT.

Figure 8.2: Distributions of m_{CT} (left) and m_{T} (right) in VRA+VRB and VRA+CRT respectively after the background-only fit. The rightmost bin includes overflow. The hashed areas accounts for all MC uncertainties. The distribution of the signal point $m(\tilde{\chi}_1^{\pm}\tilde{\chi}_2^0, \tilde{\chi}_1^0) = (250{,}0)$ GeV from the simplified model grid is overlaid on the background histograms (not stacked).

mass m_{bb}^{corr} that includes the energy of removed in-jet muons (Chapter 6). The fit results are comparable to the published version of the search. The normalization factors calculated using m_{bb}^{corr} as discriminating variable[4] are $\mu_{t\bar{t}}^{\mathrm{corr}} = 1.03 \pm 0.15$ and $\mu_{W\text{+jets}}^{\mathrm{corr}} = 0.84 \pm 0.07$. The yield tables, event distributions and further information about the background-only fit using m_{bb}^{corr} can be found in Appendix C. In both scenarios, with m_{bb} or m_{bb}^{corr}, the numbers of observed event count in the data agree with the fitted background yields in the signal regions. As no excess above the Standard Model prediction is found in the data, exclusion limits are derived, as presented in the next section.

---

[4] When m_{bb}^{corr} is used as discriminating variable, the regions are defined using m_{bb}^{corr} and $m_{\mathrm{CT}}^{\mathrm{corr}}$ instead of m_{bb} and m_{CT}.

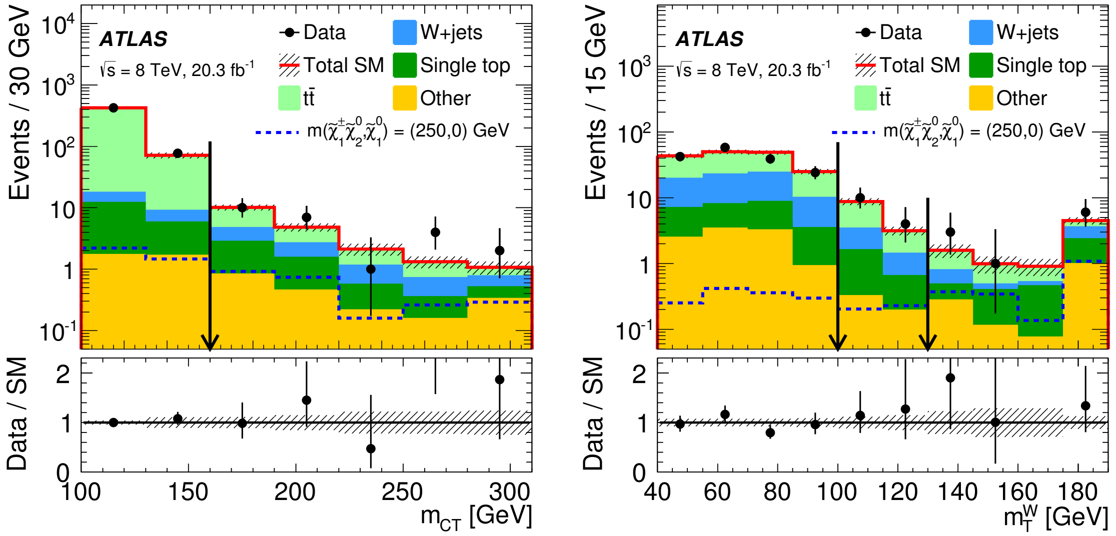

(a) m_{CT} distribution in CRT+SRAsb+SRBsb. (b) m_{T} distribution in VRB+SRAsb+SRBsb.

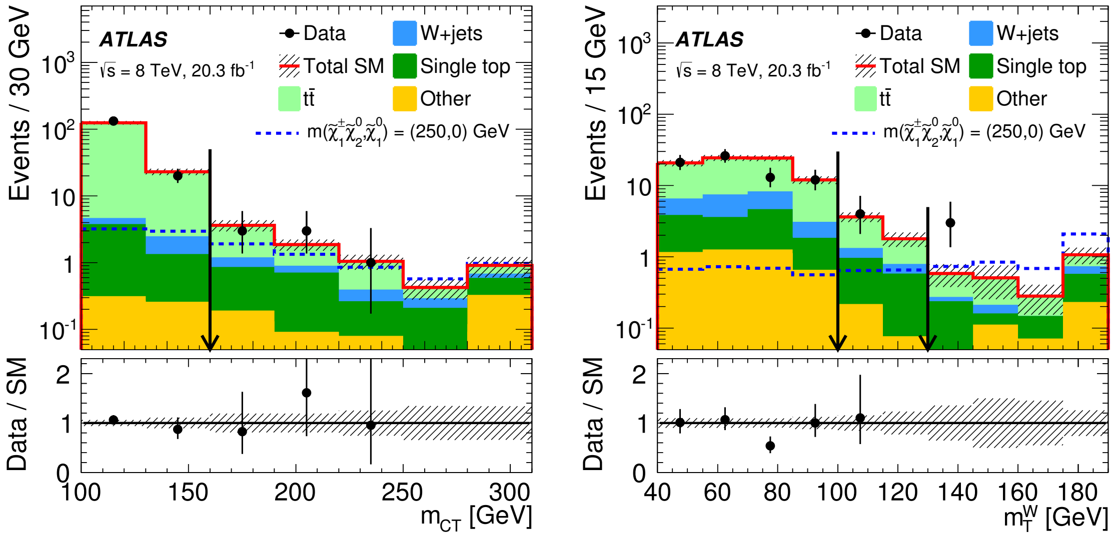

(c) m_{CT} distribution in CRT+SRAh+SRBh. (d) m_{T} distribution in VRB+SRAh+SRBh.

Figure 8.3: Distributions after the background-only fit of m_{CT} (left) and m_{T} (right) extrapolated from the CRs/VRs to the SRs in merged regions defined in Table 8.2. The rightmost bin includes overflow. The hashed areas accounts for all MC uncertainties. The distribution of the signal point $m(\tilde{\chi}_1^{\pm}\tilde{\chi}_2^0, \tilde{\chi}_1^0) = (250{,}0)$ GeV from the simplified model grid is overlaid on the background histograms (not stacked). The vertical black arrows indicate the boundaries of the signal regions.

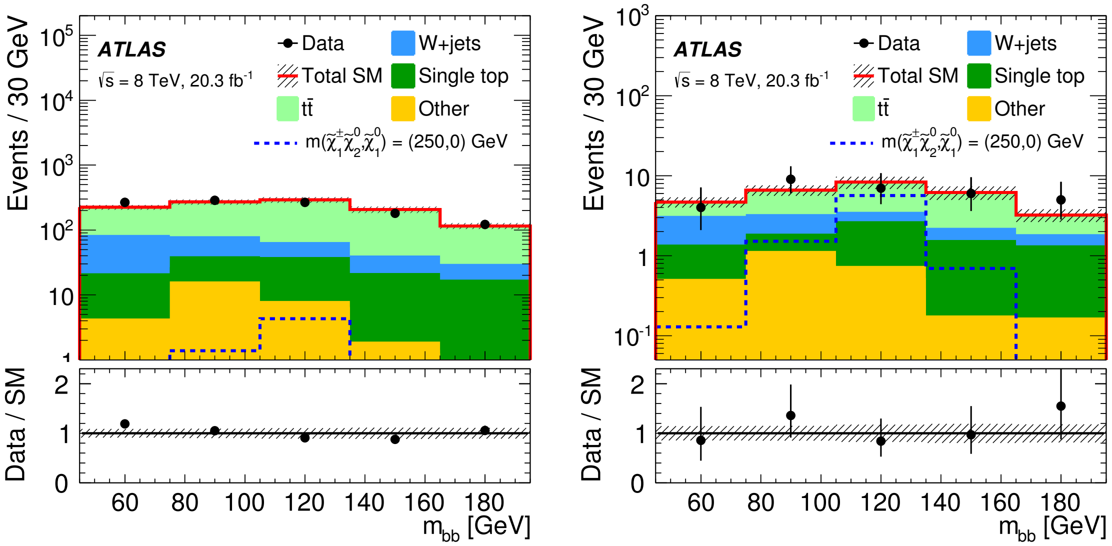

(a) m_{bb} distribution in VRA+VRB.

(b) m_{bb} distribution in SRA+SRB.

Figure 8.4: Distributions of m_{bb} after the background-only fit in the unions of validation regions VRA+VRB and signal region SRA+SRB for the sideband and signal bins. The distribution of the signal point $m(\tilde{\chi}_1^{\pm}\tilde{\chi}_2^0, \tilde{\chi}_1^0)$ = (250,0) GeV from the simplified model grid is overlaid on the background histograms (not stacked).

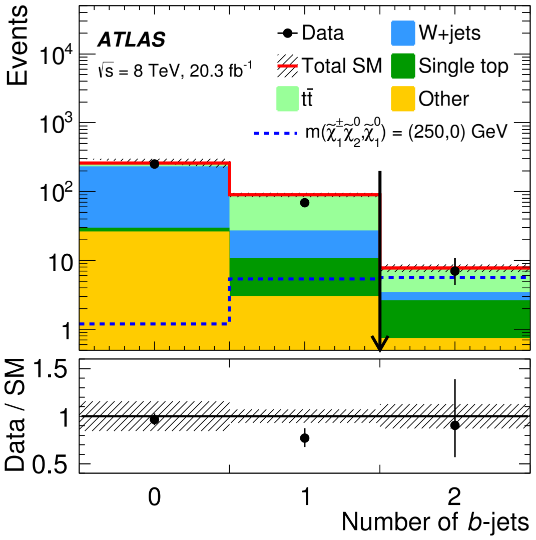

Figure 8.5: Distribution of the b-jet multiplicity after the background-only fit in a region defined by the union of SRAh+SRBh but without the b-jet multiplicity requirement applied. The rightmost bin after the arrow corresponds to the actual definition of SRAh+SRBh with $n^{b\text{-jet}} = 2$.

8.3 Result interpretation of the $1\boldsymbol{\ell} + 2\boldsymbol{b}$-jets + $\boldsymbol{E}_{\mathrm{T}}^{\mathrm{miss}}$ SUSY search

If the observed data are compatible with the Standard Model predictions, the expected signal from a given SUSY scenario is likely to be excluded. It is then possible to extract information from the dataset to set limits. These limits are split into two types. Model-independent limits assess the maximum signal strength of a non-excludable hypothetical signal, which can be any scenario beyond-the-Standard Model. Model-dependent limits establish an upper limit on the visible signal cross section and can restrict the parameter space of a given signal grid by excluding the masses of the corresponding excluded model points.

8.3.1 Test statistic for exclusion

Definition

To set exclusion limits, the SUSY searches in ATLAS use a profile log-likelihood ratio as a test statistic. Its expression is given by:

$$q_\mu = \begin{cases} -2\ln\dfrac{L(\,\mu, \hat{\hat{\boldsymbol{\theta}}}(\mu)\,)}{L(\,0, \hat{\boldsymbol{\theta}}(0)\,)} & \hat{\mu} < 0, \\ -2\ln\dfrac{L(\,\mu, \hat{\hat{\boldsymbol{\theta}}}(\mu)\,)}{L(\,\hat{\mu}, \hat{\boldsymbol{\theta}}(\mu)\,)} & 0 \leq \hat{\mu} \leq \mu, \\ 0 & \hat{\mu} > \mu. \end{cases} \tag{8.9}$$

As it was stated in Section 8.1.4, the variable q_μ measures the incompatibility between the observed data and the hypothesis of a signal of strength μ. Since there cannot be any interference between the Standard Model and the new physics states, the presence of a signal would translate into an excess of data events above the background prediction in an experiment such as ATLAS. Thus, a negative parameter $\hat{\mu}$ would not be physical here. If $\hat{\mu}$ is found to be below zero while maximizing $L(\,\hat{\mu}, \hat{\boldsymbol{\theta}}(\mu)\,)$, its value is truncated to zero in the denominator of the likelihood ratio. In case of an upward fluctuation of the observed event count such that $n^{\mathrm{obs}} > b + \mu s$, the data becomes then compatible with the signal hypothesis. For setting exclusion limits, this configuration is not considered — since q_μ is defined to measure incompatibility with the signal hypothesis — therefore q_μ is set to zero.

The remaining subsections detail the two different types of upper limits and their derivation methods.

Upper limits on the number of beyond-the-SM signal events

ATLAS searches typically set an upper limit on the number of events beyond the expected SM prediction in each signal region. The purpose is to calculate, using several values of q_μ, the largest value of μ for which $\mathrm{CL}_s \geq 0.05$, *i.e.* the largest possible signal strength μ that, given the data, would not be excluded at 95% CL. The fitting procedure is often referred to as a model-independent fit because no assumption, apart from the free parameter μ, is made on the signal.

Exclusion limits on model parameters

The same test statistic defined in Equation 8.9 is performed on each model point of a specific signal grid, assuming the $\mu = 1$ hypothesis. Exclusion regions in the parameter space of the signal grid can be defined if some model points become excluded. It is also possible to set upper limits on the signal cross section of the model for a given range of superpartner masses.

Upper limits evaluation

To evaluate these limits, the distribution $f(q_\mu|\mu)$ needs to be determined for $\mu = 0$, $\mu = 1$ and other tested values of μ. None of these are known analytically. To build the probability density functions of $f(q_\mu|\mu)$, a first possibility is to generate with random numbers Monte Carlo "pseudo-experiments". A pseudo-experiment represents an expected possible outcome if the experiment were repeated. As the maximization of the profile log-likelihood ratio involves numerous fitting procedures to find $\hat{\mu}$, $\hat{\boldsymbol{\theta}}$ and $\hat{\hat{\boldsymbol{\theta}}}$, the computation of q_μ for each pseudo-experiment is very CPU intensive.

A second possibility is to use the asymptotic behaviour of the log-likelihood ratio. The test statistics are cleverly constructed to be approximated with known distributions when the data sample size is large: in the asymptotic regime, the log-likelihood ratio follows a Gaussian whose parameters can be extracted using the covariance matrix of the $\boldsymbol{\theta}$ estimators. The probability density function $f(q_\mu|\mu)$ becomes then a non-central χ^2 distribution. With this important results [93, 94], pseudo-experiments are no more needed to compute the p-values. Nevertheless, the limits derived with the asymptotic approximation are usually validated by comparing with the results obtained using a limited number of pseudo-experiments.

8.3.2 Model-independent upper limits

The upper limits are calculated for each signal region SRAh and SRBh independently. Since a multi-bin signal region supposes the knowledge of the signal shape spreading over these bins, the signal regions considered for this *model-independent* fit are constructed as single-bin regions. The fit uses all the CRs, which are considered free of signal contamination. The parameter μ of this fit corresponds to a "dummy signal" prediction.

The fit result gives the largest signal strength μ for which $\mathrm{CL}_s \geq 0.05$ using the CL_s prescription. This is interpreted as the 95% CL upper limit on the number of beyond-the-SM signal events, written S^{95}_{obs}. In other words, it is the maximum yield of a hypothetical signal that, given the data and the background prediction from the SM, would not be excluded.

It is sometimes more convenient to present results in terms of cross section. The yield S^{95}_{obs} can be translated into a visible cross section, $\langle\sigma_{\mathrm{vis}}\rangle^{95}_{\mathrm{obs}}$, by dividing it by the integrated luminosity. It is called visible cross section because it is estimated from a yield *a posteriori*. For a signal model with a cross section σ, only a fraction A, the acceptance,[5] of the predicted events will pass the fiducial cuts of the model. The remaining event number is further reduced by the ATLAS detector reconstruction and trigger efficiencies, ϵ. The visible cross section, $\langle\sigma_{\mathrm{vis}}\rangle^{95}_{\mathrm{obs}} = \sigma \times A \times \epsilon$, thus includes these event losses. The ATLAS Collaboration provides, for each published analysis, the acceptances and efficiencies for the tested signal grids, in order to help theorists reinterpreting the data with their models.

Table 8.3 summarizes, for SRAh and SRBh, the expected and observed numbers of events along with the associated upper limits, calculated with 10 000 pseudo-experiments and the asymptotic approximation. It lists the observed 95% CL upper limits $\langle\sigma_{\mathrm{vis}}\rangle^{95}_{\mathrm{obs}}$ and S^{95}_{obs} on the visible cross section and number of signal events, respectively. It also gives the expected upper limit S^{95}_{exp}, which is the limit that would have been obtained if the number of observed events was exactly matching the background prediction. This quantity represents the expected performance of the analysis.

---

[5] The acceptance is defined as the fraction of events passing the geometric and kinematic selections at particle level.

The value is given with the ±1σ excursions of the expectation. The ATLAS Collaboration also provides the observed confidence level of the background, CL$_b$, in the context of exclusion and the discovery p-value, p_0, obtained using a discovery test statistic [90].

Table 8.3: Expected (N_{exp}) and observed (N_{obs}) number of events in each signal bin SRAh and SRBh, 95% CL upper limits on the number of expected (S^{95}_{exp}) and observed signal events (S^{95}_{obs}), and the visible cross section $\langle\sigma_{\text{vis}}\rangle^{95}_{\text{obs}}$. The confidence level observed for the background-only hypothesis (CL$_b$) and the discovery p-value (p_0), truncated at 0.5 are also provided [53].

SR	N_{exp}	N_{obs}	Method	S^{95}_{exp}	S^{95}_{obs}	$\langle\sigma_{\text{vis}}\rangle^{95}_{\text{obs}}$ [fb]	CL$_b$	p_0
SRAh	5.69 ± 1.10	4	Pseudo-exp.	$6.3^{+2.6}_{-1.3}$	5.6	0.27	0.27	0.50
			Asymptotics	$6.3^{+3.4}_{-2.0}$	5.3	0.26	0.28	0.50
SRBh	2.67 ± 0.69	3	Pseudo-exp.	$5.1^{+2.2}_{-1.2}$	5.6	0.28	0.61	0.43
			Asymptotics	$5.1^{+2.6}_{-1.4}$	5.5	0.27	0.56	0.43

8.3.3 Model-dependent limits

This section presents the exclusion limits for the two signal grids considered in the $1\ell + 2b$-jets + $E_{\text{T}}^{\text{miss}}$ SUSY search. A model-dependent fit is carried out for each of the 75 signal points of the simplified model grid. The same procedure is repeated on each of the 59 signal points of the pMSSM grid as well.

The fit is performed in the CRs and SRs simultaneously. The signal contribution of the tested model point is taken into account in all regions, including the signal contamination in the CRs. In this strategy, the signal strength is fixed at $\mu = 1$, as the parameter of interest here is the resulting CL$_s$. If CL$_s < 0.05$, the signal point is excluded at 95% CL.

It is advantageous to have multiple signal regions in the fit, provided they are mutually exclusive. This is the case in this analysis: SRA ($m_{\text{T}} \in [100, 130]$ GeV) and SRB ($m_{\text{T}} > 130$ GeV) do not overlap. Better exclusion sensitivity can be obtained by performing the model-dependent signal fit on the statistical combination of the regions.

The results are usually visualized graphically as an exclusion region on a two-dimensional plot, where the axes are relevant model parameters. Figure 8.6a shows the excluded region for the simplified model, where the two free parameters are the masses of the electroweakinos $\tilde{\chi}_1^{\pm}$, $\tilde{\chi}_2^0$ — assumed to be mass degenerate — and the LSP $\tilde{\chi}_1^0$. The solid red line, visible for the lowest mass values, indicates the 95% CL observed limit. Its associated uncertainty bands are the dotted red lines, which are obtained by performing the same fit with the uncertainties on the theoretical cross sections varied by $\pm 1\sigma_{\text{theory}}^{\text{SUSY}}$. The blue dashed line corrresponds to the 95% CL expected limit, whose uncertainty bands in yellow accounts for the experimental uncertainties $\pm 1\sigma_{\text{exp}}$ (all uncertainties listed in Chapter 7 except the ones on the signal cross section). Both up and down variations are computed.

For electroweakino masses $m(\tilde{\chi}_1^{\pm}\tilde{\chi}_2^0)$ above 180 GeV, an upper fluctuation of the data event count in SRh puts the expected limit above the observed one. In the region around $m(\tilde{\chi}_1^{\pm}\tilde{\chi}_2^0) = 240$ GeV, the expected exclusion is driven by SRBh, which targets large mass splittings between $\tilde{\chi}_1^{\pm}/\tilde{\chi}_2^0$ and the LSP $\tilde{\chi}_1^0$. At low electroweakino masses, where $m(\tilde{\chi}_1^{\pm}\tilde{\chi}_2^0)$ is below 140 GeV, the presence of an observed exclusion contour is mostly due to the sensitivity in SRAh, which addresses scenarios with small mass splittings. The published analysis is able to exclude one signal point in this region, $m(\tilde{\chi}_1^{\pm}\tilde{\chi}_2^0, \tilde{\chi}_1^0) =$ (130,0) GeV, the observed CL$_s$ being 0.025. Figure 8.7a shows the upper limits on the signal cross section normalized by the simplified model prediction, $\sigma/\sigma^{\text{SUSY}}$, for several values of $m(\tilde{\chi}_1^{\pm}\tilde{\chi}_2^0)$ and a massless LSP.

Figure 8.6b is the new exclusion region obtained using the b-jet momentum correction, detailed in Chapter 6. The fit is performed as in the published version, but the CRs and SRs are defined with the discriminating variables m_{bb}^{corr} and $m_{\text{CT}}^{\text{corr}}$, the former being the fitted variable. The signal maps displaying the discovery significances in Figure 6.4 showed an increase of the expected exclusion potential, with respect to the Z_N values of the analysis done without the b-jet momentum correction. One would expect a greater exclusion zone; however the observed exclusion contour is reduced in Figure 8.6b. The expected limit is slightly enhanced, but its uncertainty upper band is also larger. The absence of improvement is partly explained by the final configuration used in the model-dependent fit. Originally, only the central bin of each signal region was considered, the sidebands SRAsb and SRBsb acted as control regions. Due to the lack of sensitivity, these sidebands were added as signal regions, the fit being performed using SRA and SRB with the full m_{bb} range (45 to 195 GeV). Also, the large bin width of 30 GeV increases the risk of having extra data events caused by an upper fluctuation. Nevertheless, the exclusion range is similar to the one of the published analysis; the version with m_{bb}^{corr} excludes the signal point $m(\tilde{\chi}_1^{\pm}\tilde{\chi}_2^0, \tilde{\chi}_1^0)$ = (130,0) GeV. Additional plots showing the exclusion contours are shown in Appendix C; the corresponding expected and observed CL$_s$ values are displayed for each signal point.

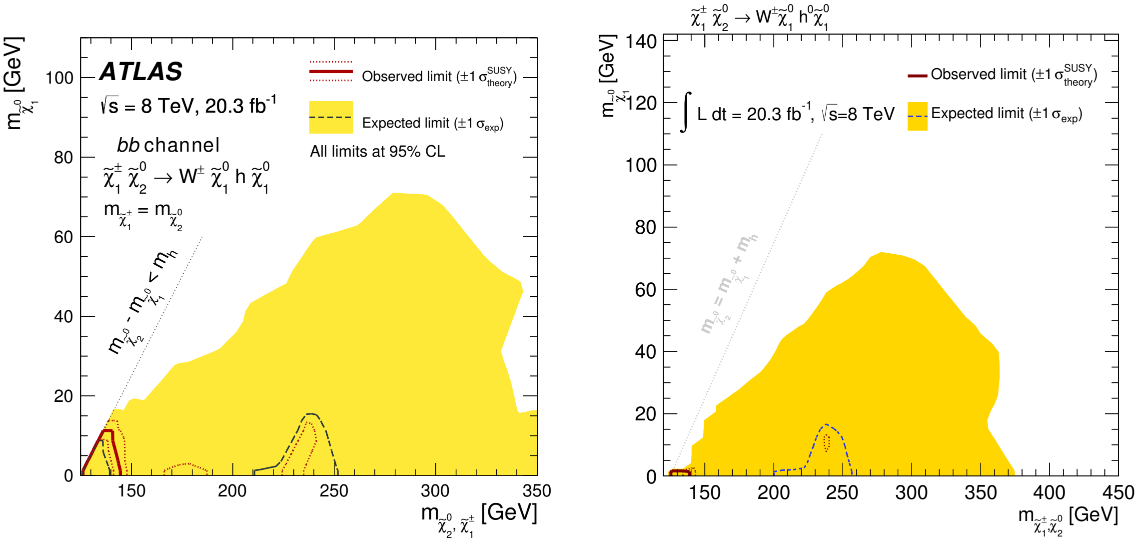

(a) Fit performed with m_{bb} (published version).

(b) Fit performed with m_{bb}^{corr}.

Figure 8.6: Exclusion regions in the $m(\tilde{\chi}_1^{\pm}, \tilde{\chi}_2^0) - m(\tilde{\chi}_1^0)$ plane in the simplified model for the published analysis and the version with corrected di-jet mass m_{bb}^{corr}. The 95% CL observed limit is given by the solid red line. The dotted red lines indicate the observed limits that would have be obtained after varying the theoretical signal cross sections by $\pm 1\sigma_{\text{theory}}^{\text{SUSY}}$. The 95% CL expected limit is shown as a blue dashed line and the yellow bands around it mark the $\pm 1\sigma_{\text{exp}}$ uncertainty, which account for all uncertainties except the ones on signal cross section.

Limits in the context of the pMSSM have also been derived. The pMSSM signal grid considered was presented in Section 5.2.2, with fixed parameters $\tan\beta = 10$ and $M_1 = 50$ GeV. Figure 8.8a shows the model-dependent fit results in the $\mu - M_2$ plane. Very similar results are obtained with the search using m_{bb}^{corr}; the corresponding exclusion region is shown in Appendix C, along with additional plots where the observed and expected CL$_s$ are indicated.

Figure 8.7b shows the upper limits on the normalized signal cross section $\sigma/\sigma^{\text{SUSY}}$ for several values of M_2 and a fixed pMSSM parameter $\mu = 3000$ GeV. The analysis has sensitivity when $|\mu| \gg M_2, M_1$. The chargino $\tilde{\chi}_1^{\pm}$ and neutralino $\tilde{\chi}_2^0$ are thus wino-like and quasi-degenerate, while $\tilde{\chi}_1^0$ is mostly bino-like. This corresponds to the

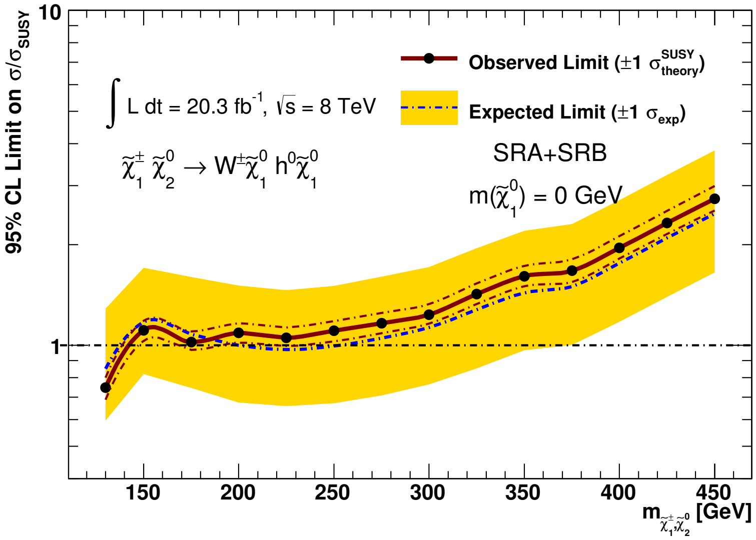

(a) Projection in the simplified model for a massless LSP, $\tilde{\chi}_1^0 = 0$.

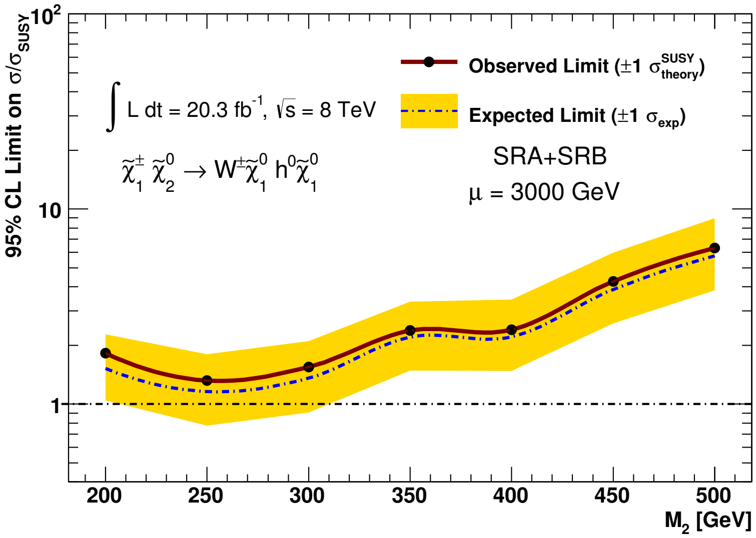

(b) Projection in the pMSSM for $\mu = 3000$ GeV.

Figure 8.7: Upper limits on the signal cross section normalized to the SUSY model prediction, $\sigma/\sigma^{\mathrm{SUSY}}$ in the simplified model (top) and pMSSM (bottom). The 95% CL observed limit is given by the solid red line. The dotted red lines indicate the observed limits that would have be obtained after varying the theoretical signal cross sections by $\pm1\sigma^{\mathrm{SUSY}}$. The 95% CL expected limit is shown as a blue dashed line and the yellow uncertainty bands account for all experimental uncertainties except the ones on signal cross section.

scenario considered in the simplified model. In this region of the parameter space, the decay $\tilde{\chi}_2^0 \to h\tilde{\chi}_1^0$ is enhanced, with a large branching ratio of 97%.

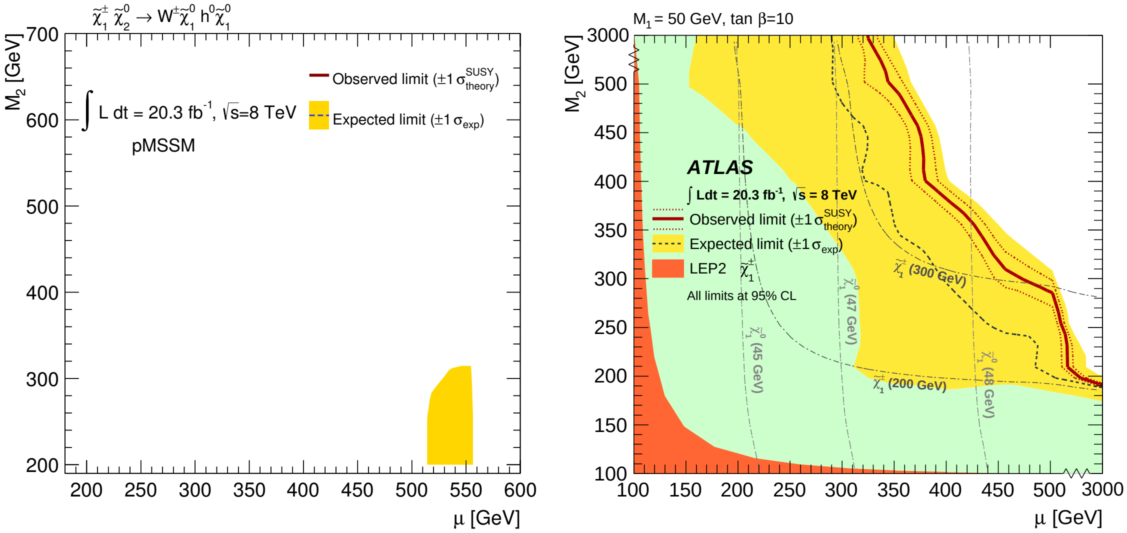

(a) Exclusion region (expected) of the $1\ell+2b$-jets $+E_{\mathrm{T}}^{\mathrm{miss}}$ analysis.

(b) Exclusion regions of the combined 2- and 3-lepton searches.

Figure 8.8: Exclusion regions of the $1\ell+2b$-jets$+E_{\mathrm{T}}^{\mathrm{miss}}$ search (left) and the combined searches for 2- and 3-leptons (right) for the same pMSSM model grid.

The search is not able to exclude any point in the pMSSM grid. This is not surprising given the high value of M_1 (50 GeV), leading to $\tilde{\chi}_1^0$ masses of the same order; the analysis was optimized for the simplified model with a massless LSP. However the expected exclusion region in Figure 8.8a nicely completes the 2-lepton [95] and 3-lepton [96] searches for large μ. The combined exclusion limits of these two analyses for the same pMSSM grid are shown in Figure 8.8b.

8.4 Results of the combined search

The present analysis looks for direct pair production of $\tilde{\chi}_1^{\pm}$ and $\tilde{\chi}_2^0$ decaying to the 125 GeV Higgs boson via the $b\bar{b}$ channel only. Two parallel ATLAS searches target the Higgs boson decay modes $h \to \gamma\gamma$ and $h \to WW$. The latter scenario refers to a search with two same sign leptons ($\ell^{\pm}\ell^{\pm}$) in the final states, with main signal contribution due to $h \to WW$. A third analysis, looking for electroweakino pair-production processes leading to three leptons in the final states [96], includes a Wh-mediated simplified model in its results interpretation (3ℓ-Wh). Figure 8.9 shows the diagrams of the Wh-mediated SUSY decay cascades corresponding to these searches.

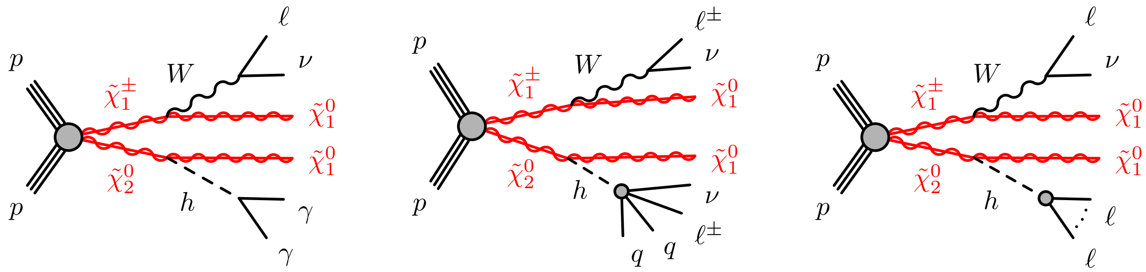

(a) $\ell\gamma\gamma$ channel. (b) $\ell^{\pm}\ell^{\pm}$ channel. (c) 3ℓ-Wh channel.

Figure 8.9: Diagrams of the scenarios targeted by three other electroweak SUSY searches in ATLAS: the one lepton and two photon channel ($\ell\gamma\gamma$), the same-sign dilepton channel ($\ell^{\pm}\ell^{\pm}$) and the Wh-mediated trilepton channel (3ℓ-Wh).

The signal regions of the four analyses (ℓbb, $\ell\gamma\gamma$, $\ell^{\pm}\ell^{\pm}$ and 3ℓ-Wh) are mutually exclusive; no signal event is present in more than one SR. These SRs are all fitted simultaneously, taking into account correlated experimental and theoretical systematic uncertainties as common nuisance parameters across analyses. Figure 8.10 shows the 95% CL upper limits on the signal cross section σ, normalized by the simplified model prediction σ^{SUSY}, assuming the LSP is massless, $m(\tilde{\chi}_1^0) = 0$.

The ℓbb channel represents the Higgs most frequent decay mode, with a branching ratio of 58%. Yet this analysis alone excludes only a small range of the $\tilde{\chi}_1^{\pm}\tilde{\chi}_2^0$ masses in the context of the simplified model. However Figure 8.10 indicates that for masses of $\tilde{\chi}_1^{\pm}\tilde{\chi}_2^0$ greater than 180 GeV, the ℓbb channel is the most sensitive analysis, predominantly contributing to the global exclusion. With the four analyses combined, degenerate electroweakino masses $m(\tilde{\chi}_1^{\pm}, \tilde{\chi}_2^0)$ up to 250 GeV are excluded at 95% CL for a massless $\tilde{\chi}_1^0$.

Figure 8.11 shows the observed exclusion contour for all individual analyses and the combined exclusion region, with the observed and expected 95% CL limits of the combination.

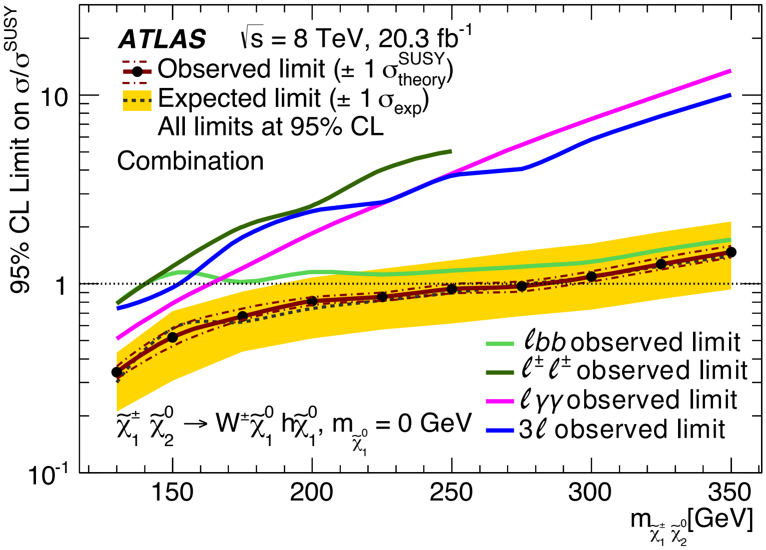

Figure 8.10: Observed 95% CL upper limits on the signal cross section σ, normalized by the simplified model prediction σ^{SUSY}, for the individual analyses ℓbb, $\ell\gamma\gamma$, $\ell^{\pm}\ell^{\pm}$ and 3ℓ-Wh, as a function of $m(\tilde{\chi}_1^{\pm}\tilde{\chi}_2^0)$, for $m(\tilde{\chi}_1^0) = 0$. The observed (solid red line) and expected (dashed blue line) 95% CL upper limits correspond to the combination of the results from the four analyses. The dash-dotted red lines are the up and down observed limit if the SUSY signal cross sections were varied by their theoretical $\pm 1\sigma_{\mathrm{theory}}^{\mathrm{SUSY}}$ uncertainties. The yellow bands are the experimental uncertainties σ_{exp} (theoretical cross section uncertainties are removed) associated with the expected limit.

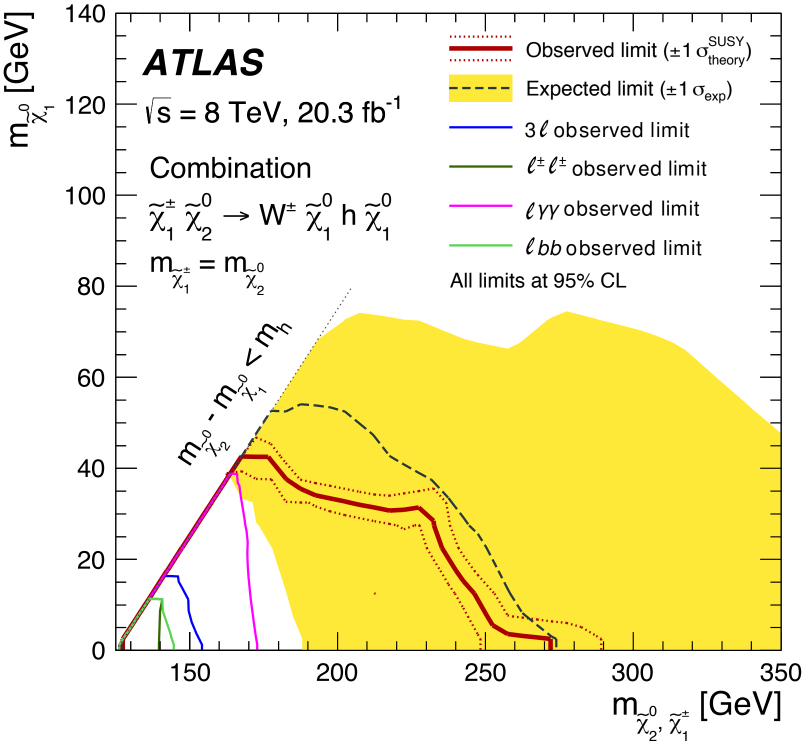

Figure 8.11: Exclusion regions in the $m(\tilde{\chi}_1^\pm, \tilde{\chi}_2^0) - m(\tilde{\chi}_1^0)$ plane in the simplified model after combination of the analysis results in the ℓbb, $\ell\gamma\gamma$, $\ell^\pm\ell^\pm$ and 3ℓ channels. The 95% CL observed limit is given by the solid red line. The dotted red lines indicate the observed limits that would be obtained after varying the theoretical signal cross sections by $\pm 1\sigma^{\rm SUSY}_{\rm theory}$. The 95% CL expected limit is shown as a blue dashed line and the yellow bands around it mark the $\pm 1\sigma_{\rm exp}$ uncertainty, which account for all uncertainties except the ones on signal cross section.

Chapter 9

Interpretations in phenomenological MSSM

The analysis described in this dissertation has been reinterpreted, along with 22 other ATLAS Supersymmetry searches, in the context of many possible SUSY scenarios coming from a large scan of the phenomenological Minimal Supersymmetric Standard Model (pMSSM). This chapter presents this summary work, whose resulting publication [97] offers the most comprehensive assessment of the ATLAS constraints on Supersymmetry models to date.

9.1 Context

9.1.1 Goals

After the LHC Run 1 data collection, the ATLAS experiment performed more than fifty searches for Supersymmetry. As no significant excess has been observed, exclusion limits on the masses of the sought superpartners have been derived. Most of the results have been interpreted using simplified models, which represent the ideal scenario where the relevant SUSY production and decay chain are fixed. More realistic models were considered, such as the pMSSM. However, a very restricted subset of its parameter space was explored, since only two or three parameters were varied and all others were fixed in order to favour the SUSY process in question. To see the full impact of ATLAS searches on R-parity-conserving Supersymmetry, 22 analyses have been reinterpreted using a large set of more than 300,000 pMSSM model points.[1] On top of exploring the sensitivity of the combined set of ATLAS SUSY searches, this summary work demonstrates the overlap and complementarity between different analyses and shows how light the various SUSY particles can be outside simplified models. After detailing the sampling procedure, the strategy to categorize all model points will be reviewed, before concluding on the effects of the ATLAS searches on the scanned pMSSM.

9.1.2 ATLAS searches

The 22 ATLAS analyses used for this summary project are classified into four broad categories, depending on the targeted scenario.

- **Inclusive** searches are those primarily targeting decays, including cascade decays, initiated by production of squarks of the first two generations or gluinos.
- **Third-generation** searches are those targeted particularly at the production of top squarks $\tilde{t}$ and bottom squarks $\tilde{b}$.
- **Electroweak** SUSY targets the direct production of electroweakinos and sleptons.
- **"Others"** refers to the searches of heavy, long-lived particles and heavy Higgs bosons.

This categorisation helps interpreting the type of sparticles a given analysis might be sensitive to. In total, almost 200 distinct signal regions are considered. The analysis of this dissertation belongs to the electroweak group and is referred to as ℓh in the publication and in this chapter as well for consistency. The ℓ refers to the sought lepton (electron or muon) in the final states and h designates the lightest supersymmetric Higgs boson produced in the SUSY decay cascade.

9.2 Sampling the pMSSM parameter space

This section explains the generation of the pMSSM model points and their selection, which depends on theoretical, experimental and indirect constraints.

---

[1] A specific set of the 19 parameters of the pMSSM is referred to as a model point in parameter space.

Table 9.1: Scan ranges used for each of the 19 pMSSM parameters. Where the parameter is written with a modulus sign both the positive and negative values are permitted. LH and RH refers to as left-handed and right-handed respectively.

Parameter	Definition	Min value	Max value
$m_{\widetilde{\nu}_L^{1,2}} = m_{\widetilde{\ell}_L^{1,2}}$	LH slepton masses of first two generations	90 GeV	4 TeV
$m_{\widetilde{\ell}_R^{1,2}}$	RH slepton masses of first two generations	90 GeV	4 TeV
$m_{\widetilde{\nu}_L^{3}} = m_{\widetilde{\ell}_L^{3}}$	LH slepton masses of third generation	90 GeV	4 TeV
$m_{\widetilde{\ell}_R^{3}}$	RH slepton masses of third generation	90 GeV	4 TeV
$m_{\widetilde{u}_L^{1,2}} = m_{\widetilde{d}_L^{1,2}}$	LH squark masses of first two generations	200 GeV	4 TeV
$m_{\widetilde{u}_R^{1,2}}$	RH up-type squark masses of first two generations	200 GeV	4 TeV
$m_{\widetilde{d}_R^{1,2}}$	RH down-type squark masses of first two generations	200 GeV	4 TeV
$m_{\widetilde{u}_L^{3}} = m_{\widetilde{d}_L^{3}}$	LH squark masses of third generation	200 GeV	4 TeV
$m_{\widetilde{u}_R^{3}}$	RH up-type squark masses of third generation	200 GeV	4 TeV
$m_{\widetilde{d}_R^{3}}$	RH down-type squark masses of third generation	200 GeV	4 TeV
$\lvert M_1 \rvert$	Bino mass parameter	0 GeV	4 TeV
$\lvert M_2 \rvert$	Wino mass parameter	70 GeV	4 TeV
$\lvert \mu \rvert$	Bilinear Higgs mass parameter	80 GeV	4 TeV
$\lvert M_3 \rvert$	Gluino mass parameter	200 GeV	4 TeV
$\lvert A_t \rvert$	Trilinear top coupling	0 GeV	8 TeV
$\lvert A_b \rvert$	Trilinear bottom coupling	0 GeV	4 TeV
$\lvert A_\tau \rvert$	Trilinear tau lepton coupling	0 GeV	4 TeV
$\lvert M_A \rvert$	Pseudoscalar Higgs boson mass	100 GeV	4 TeV
$\tan\beta$	Ratio of the Higgs vacuum expectation values	1	60

9.2.1 Model point generation

The pMSSM studied in this work verifies the assumptions listed in Chapter 2 and hence has 19 parameters. This reduced dimensionality is still too large to allow for a grid sampling technique at regular intervals. The parameter space is therefore sampled by taking random values for each parameter, chosen from a flat probability distribution. The lower and upper bounds of each parameters are given in Table 9.1. The lower bounds are defined to avoid experimental constraints whereas the upper limits are all[2] set at 4 TeV. This maximum value ensures a high density of model points where all states are kinematically accessible at the LHC. Once the 19 parameters are chosen, software packages calculate the mass spectrum (`SoftSUSY`) and the sparticle decays (`SUSY-HIT`).

---

[2] A larger range is permitted for $|A_t|$ as it increases the fraction of model points having the mass of the lightest Higgs boson close to the measured value.

9.2.2 Indirect constraints

The theoretically consistent models are further required to satisfy experimental constraints summarized as follow:

Precision electroweak and flavor constraints

Among the calculated model properties are the relevant observables in precision electroweak and flavor physics, such as the $\Delta\rho$ parameter, the branching ratios BR($b \to s\gamma$), BR($B_s \to \mu^+\mu^-$) and the SUSY contribution to the anomalous magnetic moment of the muon $\Delta(g-2)_\mu$. Models are discarded if the computed values does not fall within an interval – or union of intervals – around the theoretical prediction and the experimental measurement(s) (usually 2σ).

Dark matter constraints

Since R-parity is conserved, the LSP is stable and therefore has a non-zero cosmological abundance. Albeit a good candidate for dark matter, it may not be its sole constituent. Hence the LSP abundance should remain under the observed central value plus 2σ of the total dark matter abundance, measured by the Planck collaboration.

Dark matter direct detection experiments provide upper limits on the spin-independent and spin-dependent cross sections for the interaction of a neutralino with a nucleus. These upper limits assume the LSP makes up all the dark matter. As stated before, the LSP can contribute partially to the dark matter density. These cross sections are thus scaled down by the ratio of the LSP abundance to the total dark matter abundance.

Collider constraints

The combined LEP searches assign constraints on the Z boson width ($<$ 2 MeV) and on sparticle's minimum mass ($>$ 200 GeV for 1^{st} and 2^{nd} generation squarks, $>$ 100 GeV for all others). The lightest Higgs boson mass is required to lie in the range 124 to 128 GeV. It has been shown that the sensitivity of the SUSY searches does not depend measurably on the value of the Higgs mass inside this interval.

9.2.3 Importance of sampling by LSP type

As seen in Chapter 2, the neutralinos are mass eigenstates coming from the mixture of the wino $\widetilde{W}$, the Higgsinos $\widetilde{H}$ and the bino $\widetilde{B}$. The LSP, assumed to be the lightest neutralino $\tilde{\chi}_1^0$, is said to be bino-like, wino-like or Higgsino-like if the corresponding component in the mixing matrix is dominant. The produced models assume that R-parity is conserved, thus the LSP is stable and its cosmological abundance is bounded by the dark matter relic density. However the dark matter annihilation strongly depends on the nature of the LSP. For wino-like and Higgsino-like LSPs, effective mechanisms of coannihilation reduce the abundance of dark matter. Model points with a bino-like LSP tend to overproduce dark matter and are therefore more likely to be discarded during the random scan of parameters. To remedy this undersampling of bino-like LSP models, the selection has been performed in such a way that approximately equal numbers are obtained for each LSP category. The phenomenology of each LSP type can be then explored separately thanks to the large number of model points in each category.

9.2.4 Properties of model points

In total 500 million model points are sampled randomly within the ranges listed in Table 9.1. The first 20 million sets, which had a wino-like or Higgsino-like LSP, yield to 206,917 models verifying the theoretical and experimental constraints stated above. With a bino-like LSP, the remaining 480 million model points are ultimately giving 103,410 viable models. The numbers of sampled and simulated models, along with the relative percentage for each LSP category, are listed in Table 9.2.

Figure 9.1 shows the mass distributions for each type of LSP. It can be seen that there is a large amount of selected model points with $m(\tilde{\chi}_1^0) \lesssim 100$ GeV, to which the ℓh analysis detailed in this dissertation can potentially show sensitivity, as the LSP is assumed to be dominantly bino-like. The high concentration of viable pMSSM model points in this low-mass range is explained by the possibility to obtain the correct dark matter relic density through a enhanced pair annihilation via the Z or Higgs boson poles (called "funnels", at half the mass of the two gauge bosons). These resonances can been seen in the inset to Figure 9.1.

Table 9.2: Categorization of the 310,327 model points from the scanned pMSSM, according to the nature of the LSP, with the corresponding percentage of models for each LSP type.

LSP type	**Sampled**	**Simulated**
Bino-like	480×10^6	103,410 (35%)
Wino-like	20×10^6	80,233 (26%)
Higgsino-like		126,684 (39%)
Total	500×10^6	310,327

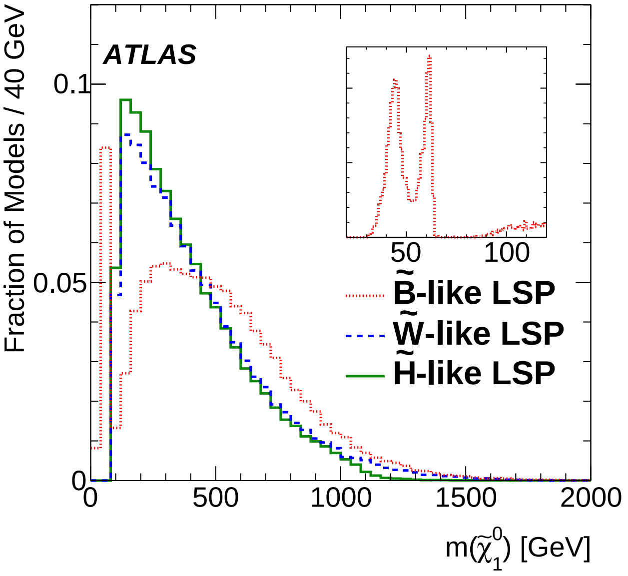

Figure 9.1: Distributions of the LSP masses for the three LSP types, normalised to unit area. The bino-like curve is scaled by $\frac{1}{24}$.

9.3 Methodology of model evaluation

The goal here is to determine now the sensitivity of the ATLAS searches on each point, in other words if a given model can be excluded or not for a given analysis. Simulating, reconstructing all the 310,327 model points and then running the full set of considered ATLAS searches on each of them would be extremely time and CPU consuming. A more resource efficient methodology is followed, where the models are successively preselected, through three consecutive steps, according to their exclusion potentiality. Only the models that are most likely to be excluded ultimately undergo the full ATLAS simulated and reconstruction.

9.3.1 Model evaluation steps

Cross section evaluation

The cross section for the different SUSY particle production is computed at LO and at NLO only if the LO result is above 0.25 fb. As the ATLAS searches exhibit very different sensitivity depending on the sparticle production, the SUSY processes are split in four groups: strong, mixed, electroweak and slepton pair productions. If the total cross section for a group (or more) is higher than specific thresholds (*e.g.* 7.5 fb for electroweak) and if the LSP is lighter than 1 TeV, the corresponding model is kept for the next step. If not, the model is marked as not excluded.

Truth-level evaluation

A large sample of Monte Carlo events is generated for each of the passing production mode(s) of the selected models. MadGraph is used for the sparticle pair production while the other sparticle decays and the showering are done by Pythia6. The events are generated at particle-level. This allows for a first estimation of the expected signal event yield $N_{\text{truth}}^{\text{SR}}$, for each model point and in each signal region SR of a given analysis. By comparing $N_{\text{truth}}^{\text{SR}}$ to the observed model-independent upper limit in each analysis signature paper, the models are divided into three categories depending on their exclusion potentiality: the ones that "certainly will not be excluded", "certainly will be excluded" and "potentially excludable" (more details in Section 9.3.2).

Reconstructed-level analysis

Models entering the category "potentially excludable" are simulated at reconstructed-level (*i.e.* detector-level) using ATLFAST II. Signal events are generated corresponding to four times the integrated luminosity recorded (*i.e.* 81.2 fb^{-1}). Exclusion limits are derived on these inconclusive model points following the CLs method, as previously done in the original analyses. The results of the exclusion fits give the final status of the model: excluded or not-excluded.

9.3.2 Categorization of models

The categorization of models is performed at particle-level. For each model point, the analyses run their event selection and estimate the expected signal event yield $N_{\text{truth}}^{\text{SR}}$ in each signal region SR. This truth-level prediction, by definition, lacks the inefficiencies coming from the detector-level reconstruction. A single efficiency factor ϵ^{SR}, computed using the simulated signal grids previously used for interpretations, corrects the ideal truth prediction. The resulting expected signal event yield $N_{\text{truth}}^{\text{SR}} \times \epsilon^{\text{SR}}$ is compared to the observed model-independent upper limit, S_{obs}^{95}, published in

Table 9.3: Classification of the pMSSM models according to their exclusion potentiality. The r_1^{SR} and r_3^{SR} are model and analysis dependent.

Category 1	Category 2	Category 3
$r^{\mathrm{SR}} \leq r_1^{\mathrm{SR}}$	$r_1^{\mathrm{SR}} < r^{\mathrm{SR}} \leq r_3^{\mathrm{SR}}$	$r^{\mathrm{SR}} > r_3^{\mathrm{SR}}$
"Very likely not to be excluded"	"Potentially excluded"	"Almost certainly excluded"

the individual signature papers. The following ratio is calculated:

$$r^{\mathrm{SR}} = \frac{N_{\mathrm{truth}}^{\mathrm{SR}} \times \langle \epsilon^{\mathrm{SR}} \rangle}{N_{\mathrm{UL}}^{\mathrm{SR}}}. \tag{9.1}$$

Ideally, a signal region should be excluding a given model at 95% CL if $r^{\mathrm{SR}} \geq 1$. However the accuracy with which the particle-level evaluation reproduces the results of a full simulation may significantly vary depending on the model. The classification is therefore loosened using two bounds r_1^{SR} and r_3^{SR} that define three categories, as shown in Table 9.3. In most analyses, r_1^{SR} and r_3^{SR} are set to 0.5 and 2 respectively, allowing the truth prediction to be a factor 2 off. Yet these values are analysis and signal region dependent, as it will be seen in the following section, dedicated to the ℓh reinterpretation.

9.4 Reinterpretation of ℓh analysis

The analysis ℓh considered in the summary work corresponds to the 1ℓ+$2b$-jets+$E_{\mathrm{T}}^{\mathrm{miss}}$ search[3] detailed throughout this dissertation. Nothing is changed in the event selection and signal region definitions with respect to the analysis optimization described in Chapter 5. This section explains the implementation of the truth-level selection, its validation towards the assessment of the analysis sensitivity to the model points, which are subsequently categorized, the potentially excludable model points being eventually processed at reconstructed-level.

9.4.1 Truth object definition

At particle level, the selection is performed using the following truth object definitions.

---

[3] The search has been published [53] with two other searches probing the Higgs decay modes $\gamma\gamma$ and $WW \to q\bar{q}\ell\nu$ but only the $2b$-jets decay channel is considered here.

Leptons Electrons and muons are identified based on their identification number in the Monte Carlo particle numbering scheme [4] and should originate from either a top quark, a SUSY particle, a τ, a W or a Z boson decay. For the three latter cases, leptons originating from virtual τ, W or Z bosons coming from heavy flavor decays are vetoed. Truth lepton identification and trigger scale factors are set to 100%.

Jets Truth jets are built using the `AntiKt` algorithm that is applied on the final state hadron quadrivectors. The b-tagging efficiencies are all set to 1.

$E_{\mathrm{T}}^{\mathrm{miss}}$ The missing transverse momentum is calculated using the vector sum of non-interacting stable final-state particles (neutrinos, sneutrinos, and neutralinos), accessible directly in the truth collection. The overlap removal procedure as well as the truth object requirements on their p_{T}, $|\eta|$ and multiplicity are performed in the same manner as for the reconstructed objects. The kinematic variables and selections are applied identically to the reconstructed analysis.

9.4.2 Signal region efficiencies

The simplified model was used to extract the average signal efficiencies for each signal region. For this two ingredients are needed: $N^{\mathrm{SR}}_{\mathrm{fiducial,truth}}$ and $N^{\mathrm{SR}}_{\mathrm{fiducial,reco}}$. The former is the number of raw[4] events passing the selection at truth-level, which is related to the acceptance, an important entity assessing the sensitivity of an analysis. The latter is the number of weighted events passing the selection at reconstructed-level, where the weights account for the detector efficiencies/inefficiencies and resolution effect but not the luminosity rescaling. The acceptance A^{SR} and the efficiency ϵ^{SR} are defined as follow:

$$A^{\mathrm{SR}} = \frac{N^{\mathrm{SR}}_{\mathrm{fiducial,\ truth}}}{N_{\mathrm{total\ events}}} \qquad \epsilon^{\mathrm{SR}} = \frac{N^{\mathrm{SR}}_{\mathrm{fiducial,\ reco}}}{N^{\mathrm{SR}}_{\mathrm{fiducial,\ truth}}}, \tag{9.2}$$

where $N_{\mathrm{total\ events}}$ is the total number of generated (raw) events in the considered signal sample.

Figures 9.2 show the efficiency of each point from the grid as well as the average efficiency for all points in each signal region. In the analysis, b-jets were identified

---

[4] In these signal samples, events are all generated with the same Monte Carlo weights, all set to one. A "raw" event means that no detector-related weights are applied.

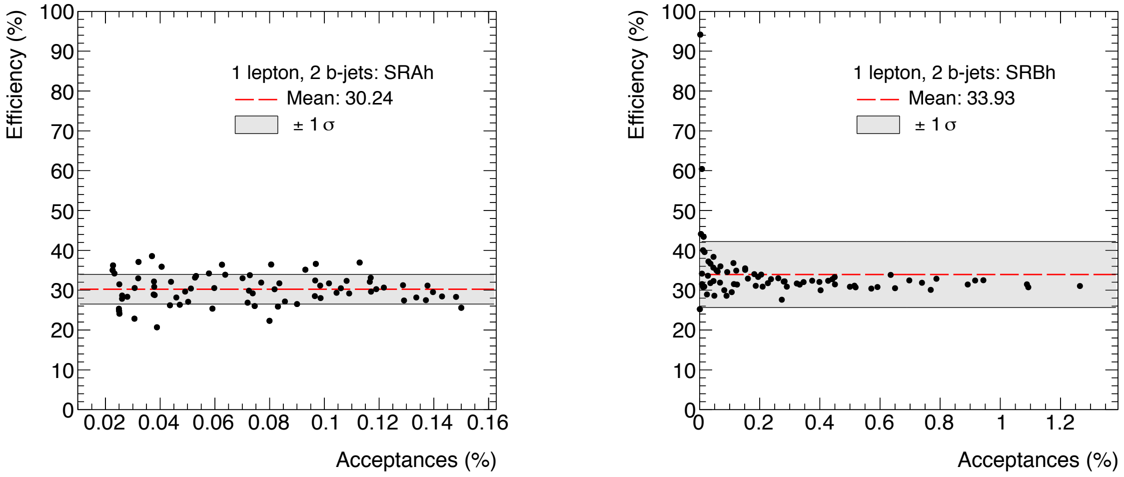

Figure 9.2: Efficiency vs acceptance for the simplified model of the ℓh analysis in the two signal regions SRAh (left) and SRBh (right). The average efficiency for each signal region is shown by the red dashed line. The $\pm 1\,\sigma$ band covers approximately 68% of points in all cases. Points with low acceptance ($< 0.05\%$) have a large spread of efficiencies.

using the MV1 algorithm at the 70% working point. Therefore, to correctly tag two b-jets, one expects to have an efficiency of around 0.49%. The simplified model has a generator level filter[5] that vetoes events with hadronic taus and requires a lepton satisfying $p_{\mathrm{T}} > 15$ GeV, $|\eta| < 2.7$; this reduces the average efficiency to 30.24% (SRAh) and 33.93% (SRBh).

9.4.3 Truth- vs reconstructed-level comparison

The average efficiencies serve to simulate, at truth-level, what the predicted yield will be with the ATLAS detector (reconstructed-level). However it is important to check beforehand if the truth selection is reproducing the analysis at reconstructed-level. The validation is done using a signal point from the simplified model grid. Figure 9.3 shows the histograms of the variables $E_{\mathrm{T}}^{\mathrm{miss}}$, m_{CT}, m_{T} and m_{bb}. These distributions are produced after the pre-selection cuts in a loose region, where events are required to have 2 leading b-jets, no more than 3 jets in total, $E_{\mathrm{T}}^{\mathrm{miss}} > 100$ GeV, $m_{\mathrm{CT}} > 100$ GeV, $m_{\mathrm{T}} > 40$ GeV and $45 < m_{bb} < 195$ GeV. The cleaning cuts are applied at reconstructed-level only. The truth histograms are scaled with the efficiency calculated as described above but in the considered pre-selection loose region. The shapes

---

[5] This filter has an efficiency of approximately 70%.

of the $E_{\mathrm{T}}^{\mathrm{miss}}$, m_{CT} and m_{T} distributions between truth and reconstruction levels are in very good agreement. The m_{bb} is more problematic, as it is often the case in an analysis with b-tagged jets in the final states. The truth distribution shows a narrow peak sharply falling at around 120 GeV, whereas the reconstructed distribution exhibits a smeared resonance shifted towards higher values of m_{bb} (maximum at ∼125 GeV). One can however see that the area within the signal bin of $105 < m_{bb} < 195$ GeV is roughly the same as the two different shapes compensate each other.

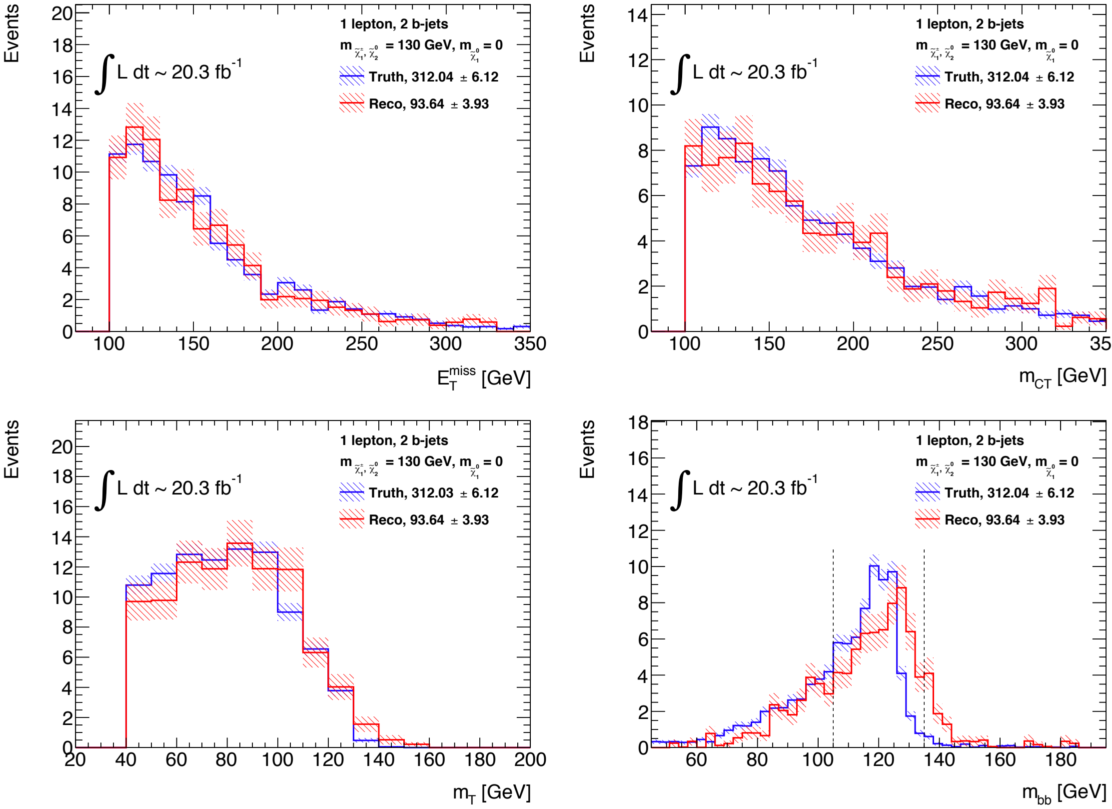

Figure 9.3: Comparisons of distributions at truth- (times efficiency) and reconstructed-levels, for the simplified model point $m(\tilde{\chi}_2^0, \tilde{\chi}_1^{\pm}) = 130$ GeV, $m(\tilde{\chi}_1^0) = 0$, of $E_{\mathrm{T}}^{\mathrm{miss}}$ (top left), m_{CT} (top right), m_{T} (bottom left) and m_{bb} (bottom right). On the latter distribution, the region between the two vertical dashed lines corresponds to the signal bin of $105 < m_{bb} < 195$ GeV. The numbers in the legend indicate the expected yields at truth- (without the efficiency rescale) and reconstructed-levels.

9.4.4 Categorization of pMSSM model points

After validating the truth-level selection, the sensitivity is assessed for each model point. The expected signal event yield $N_{\text{truth}}^{\text{SR}}$ is obtained for each model point in each signal region SR by:

$$N_{\text{truth}}^{\text{SR}} = \mathcal{L}^{\text{SR}} \sum_{\text{process } i} A_i^{\text{SR}} \times \sigma_i, \tag{9.3}$$

where $\mathcal{L}^{\text{SR}}$ is the integrated luminosity, A_i^{SR} the signal region acceptance for a given process i and σ_i the corresponding cross section[6]. It is now possible to compute the r-value for each signal region in order to categorize the model. As electroweak searches lack sensitivity compared to the analyses of strongly produced particle, a loosened r_1^{SR} value of 0.15 is chosen. Thus if $r^{\text{SR}} \leq r_1^{\text{SR}}$, the model point falls in category 1, *i.e.* “very likely not to be excluded”. If $r_1^{\text{SR}} < r^{\text{SR}} \leq r_3^{\text{SR}}$, the model point belongs to the category 2, *i.e.* “potentially excluded”. The upper boundary r_3^{SR} was first set to 2. It will be seen later that all the pMSSM model points have r-values much lower than r_3^{SR}, hence the category 3, “almost certainly excluded”, has not been considered for the ℓh analysis.

A test of this categorization is displayed in Figure 9.4, where r-values have been calculated for the simplified model grid. As reco-level MC is available for these points, it is known if the points have been excluded by the electroweak ℓh analysis. The excluded (non-excluded) signal points are shown in green (black). The hatched band in Figure 9.4 corresponds to category 2. We can see no excluded points are present in the category 1 and the non-excluded ones sit below the $r = 1$ mark.

The pMSSM model points belonging to the category 2 undergo full ATLAS simulation and reconstruction.

9.4.5 Validation and results of $\boldsymbol{\ell h}$ analysis

A first pre-selection among all pMSSM models was done using the number of events entering the signal regions at truth-level, N_{truth}, with a cutoff of $N_{\text{truth}} > 2.8$ for all signal regions. The cutoff value is obtained using the model-independent limit on the number of signal events $N_{\text{UL}}^{\text{SR}} = 5.6$. With an average efficiency $\langle \epsilon^{\text{SR}} \rangle \sim 30\%$, this limit translates into ~18.7 truth events, and the lowered r_1^{SR} bound at 15% yields a

---

[6] Unlike simplified models, which restricted the sparticle production to a unique process (*e.g.* $\tilde{\chi}_1^{\pm}\tilde{\chi}_2^0$ for this analysis), a pMSSM model point consider all possible production modes, weighted by their corresponding rate σ_i.

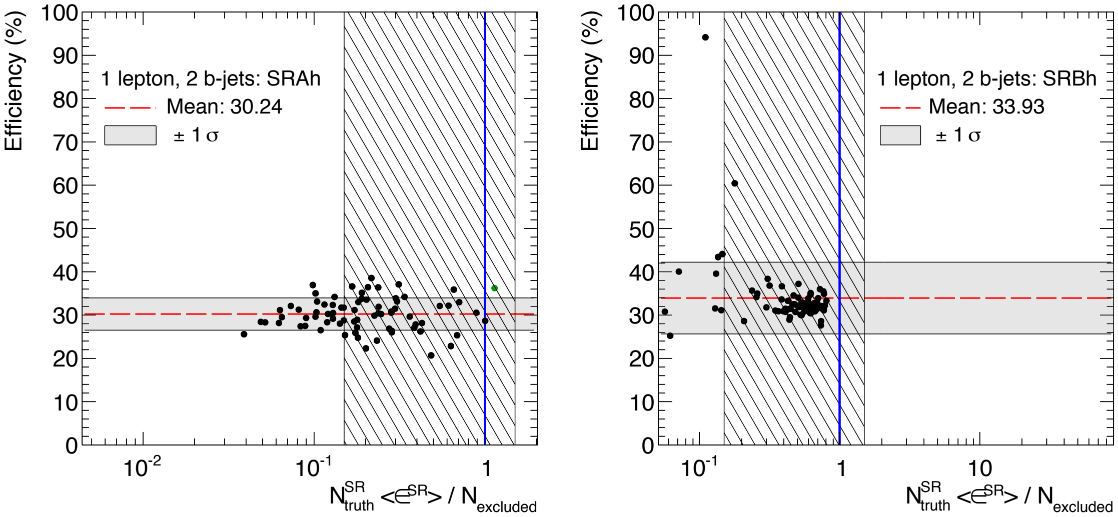

Figure 9.4: r-values for the simplified model grid points in SRAh (left) and SRBh (right) signal regions. The dot in green refers to the signal point that has been excluded by the ℓh analysis. To the left and within the vertical hatched region are the category 1 (*i.e.* not excluded) and category 2 (*i.e.* potentially excludable) respectively. Note that there are no excluded (green) points in the category 1 region.

final threshold of 2.8 events at truth-level.

A total of 64 models (1 from wino- and 63 from bino-like LSP) were fully simulated, reconstructed and analyzed. Figure 9.5 compares the number of events that enter each signal region from both reconstructed- and truth-level Monte Carlo. The averaged efficiencies computed using the simplified model points are applied to the truth-level yields only. The spread of the efficiencies due to the low yields at reconstructed-level justify the choice of a very small r_1 value of 0.15 for this analysis. If the method to predict the number of observed events using only truth information is correct, the model points should be aligned along the dashed purple line $N_{\text{reco}} = N_{\text{truth}}\langle\epsilon^{\text{SR}}\rangle$. This is the case in SRBh, confirming that the truth prediction are reflecting the yields at reconstructed level. In SRAh, the absence of alignment is mostly due to the very low statistics.

Exclusion limits are derived for each of the 64 analyzed model points. The p_0 and CLs values extracted from the fits are listed in Appendix D. As it can be read from Tables D.1 and D.2, no CLs is below 0.05, thus the ℓh analysis does not exclude any model points. It is in fact the only search that yields zero exclusion; Table D.3 from Appendix D lists the percentage of model points excluded for each analysis and ℓh has a line of zeroes. The lack of sensitivity for that analysis is not unexpected

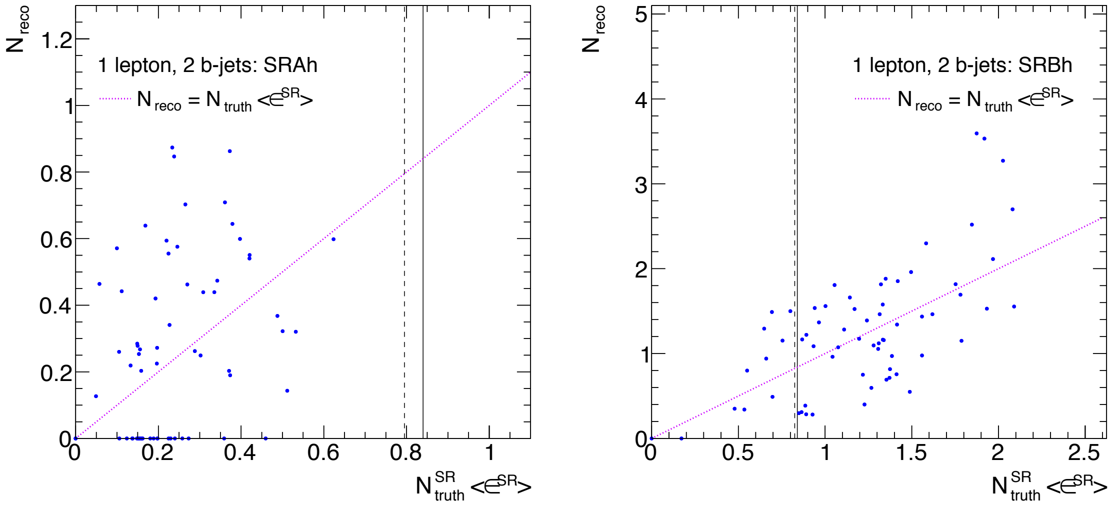

Figure 9.5: Comparison of the number of events entering each of the ℓh analysis signal region for both truth- and reconstructed-level MC. Note all relevant scaling and weighting factors have been applied, including the averaged signal region efficiencies in the truth-MC case. Each blue point represents one of the 64 pMSSM models considered. The vertical lines show the $r_1 \times S^{95}_{\mathrm{obs}}$ values, where S^{95}_{obs} is the 95% observed upper limit calculated with MC pseudo-experiments (solid line) and asymptotic calculator (dashed line). Models on the left (right) of r_1 are in the category 1 (2).

since the excluded points in the simplified model interpretation have very light LSPs. An inspection of the models with the lowest CLs ($\mathrm{CLs}^{\mathrm{obs}} \lesssim 0.18$) reveals that the sparticles masses are similar to the configuration of the pMSSM grid used in the signature paper: the $\tilde{\chi}^0_2$ and $\tilde{\chi}^{\pm}_1$ masses are around 300 GeV while the LSP is indeed light at around 60 GeV. The branching ratio $\mathrm{BR}(\tilde{\chi}^0_2 \rightarrow \tilde{\chi}^0_1\, h)$ is favoured as it reaches 80%.

Perhaps more sensitivity could have been obtained by adding the results of the searches probing the other Higgs decay modes $\gamma\gamma$ and $WW \rightarrow q\bar{q}\ell\nu$; however, the timescale of the publication did not allow for the combinaison of analyses. With only the $b\bar{b}$ channel, the ℓh analysis is unable to constrain the pMSSM set with the luminosity available. Whether it forsees a future excess or it simply shows the limitation in sensitivity of electroweak analyses at 8 TeV LHC, some speculation remains regarding the ℓh scenario at the LHC Run 2.

9.5 Results

More than 20 direct ATLAS searches for SUSY have been reinterpreted within the pMSSM framework, cleverly scanned into viable model points. This offers a unique generalized view on the sensitivity of ATLAS analyses after the LHC Run 1 and the constraints they bring on various theoretical aspects. This section summarizes the results relevant in the context of this dissertation, such as the impact on sparticle masses and dark matter. Other outcomes are briefly mentioned and can be found in more details in the publication [97].

9.5.1 Impact of ATLAS searches on sparticle masses

A useful representation that shows the global effects of the ATLAS searches on the pMSSM is to display the fraction of excluded models, projected onto a two-dimensional plane of sparticle masses. The analyses originally interpreted their results in the context of simplified models; the observed limits from the most constraining analysis of the associated simplified model are overlaid on each map for comparison. Although the fraction of excluded models can depend on requirements external to the analyses (*i.e.* scan ranges and non-collider constraints), the region of excluded pMSSM points generally matches the exclusion limits determined previously in the context of simplified models. This fact is mostly verified for the searches of strongly interacting sparticles, which robustly constrain the gluino masses (completely excluded up to 1 TeV for neutralino masses less than 400 GeV) and to a lesser extent the third generation squarks.[7] The electroweak searches fail to place lower bound on sleptons[8], charginos and neutralinos. Figures 9.6a and 9.6b show the fraction of models excluded by only the electroweak searches projected on the $\tilde{\chi}_2^0 - \tilde{\chi}_1^0$ and $\tilde{\chi}_1^\pm - \tilde{\chi}_1^0$ planes respectively. The dominant exclusion mechanism at large $m(\tilde{\chi}_2^0)$ values in Figure 9.6a is due to the Disappearing Track analysis, which features long-live charginos decaying in a wino-like LSP. If the ℓh analysis had excluded some pMSSM model points, it would have been likely to happen in the low LSP mass regions ($m(\tilde{\chi}_1^0) \lesssim 50$ GeV), as models away from the diagonal $m(\tilde{\chi}_2^0, \tilde{\chi}_1^\pm) = m(\tilde{\chi}_1^0)$ mostly have bino-like LSPs.

---

[7] Corresponding figures are in the publication [97].

[8] Slectrons, muons and their sneutrino counterparts.

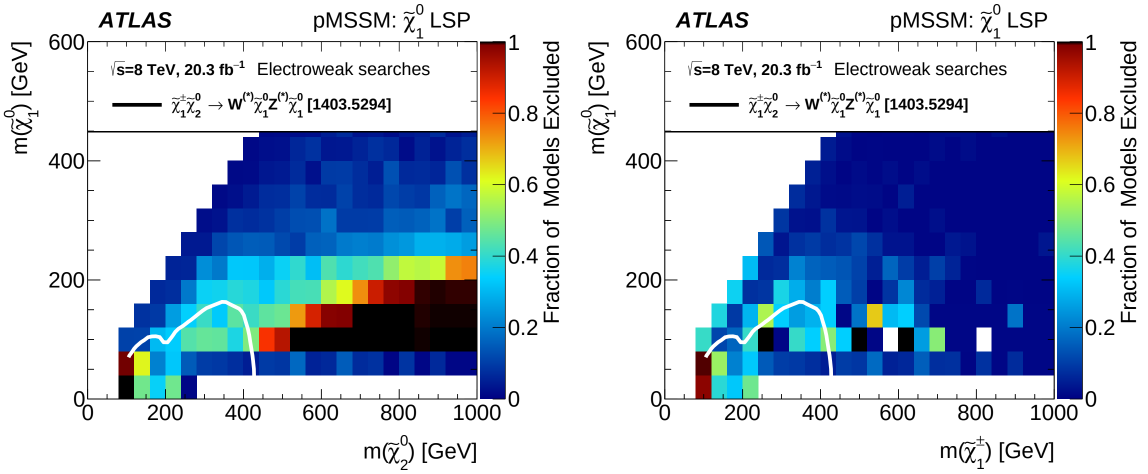

(a) Projection in the $\tilde{\chi}_2^0 - \tilde{\chi}_1^0$ plane.

(b) Projection in the $\tilde{\chi}_1^{\pm} - \tilde{\chi}_1^0$ plane.

Figure 9.6: Impact of electroweak searches on the $\tilde{\chi}_2^0 - \tilde{\chi}_1^0$ (a) and $\tilde{\chi}_1^{\pm} - \tilde{\chi}_1^0$ (b) planes. The black squares are indicating that 100% of model points have been excluded. The white solid curve shows the 95% CL observed exclusion limit from Reference [98] where the production $\tilde{\chi}_1^{\pm} + \tilde{\chi}_2^0$ is assumed to be purely wino-like (as it is the case in the simplified model used in the ℓh interpretation).

9.5.2 Impact of ATLAS searches on dark matter

As explained in Sections 9.2.3 and 9.2.4, the constraints on dark matter strongly depend on the nature of the LSP. For models with bino-like LSP – the scenario considered for the ℓh analysis – the ATLAS searches are sensitive up to $m(\tilde{\chi}_1^0) \lesssim 800$ GeV. At low bino mass, about two-thirds of the model points are excluded through the Z- and Higgs-funnel regions. This can be seen by plotting the density of viable pMSSM model points in the plane of the $\tilde{\chi}_1^0$ relic density $\Omega(\tilde{\chi}_1^0)h^2$, where h is the dimensionless Hubble parameter, versus the mass of the $\tilde{\chi}_1^0$ before (Figure 9.7a) and after (Figure 9.7b) applying the constraints from the ATLAS SUSY searches. The colour code indicates the dark matter annihilation mechanism. The ATLAS analyses are particularly sensitive to model points with light-flavor[9] squark or gluino coannihilators.

Regarding the complementarity of ATLAS constraints with the dark matter direct detection limits, the ATLAS searches can stretch to regions with cross sections several orders of magnitude below those of the current best direct detection experiments.

---

[9] Squarks from the first two generations.

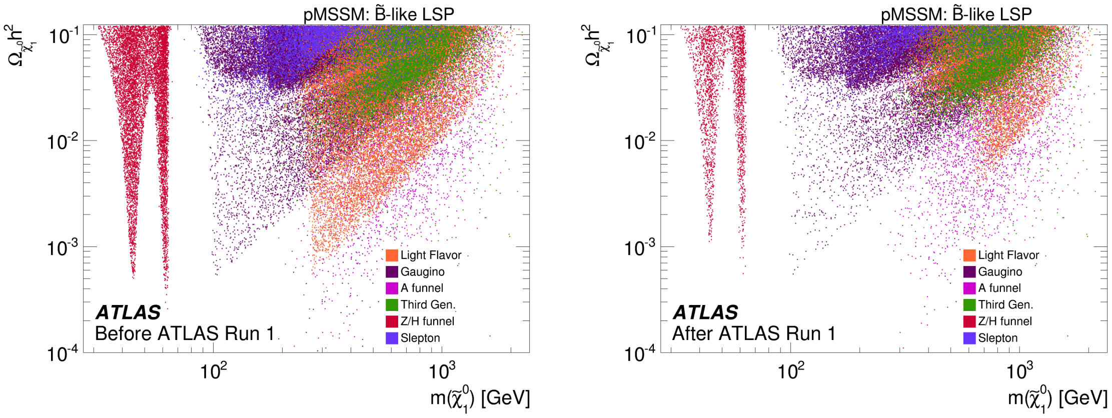

(a) Before ATLAS Run 1.

(b) After ATLAS Run 1.

Figure 9.7: Density of non-excluded pMSSM points on the plane of the relic density versus the (bino-like) LSP mass, before and after the ATLAS constraints. The colour code refers to the dark matter annihilation mechanism.

9.5.3 Other results

The results of the direct SUSY searches are completemented by ATLAS measurements on the Higgs boson coupling (in particular the coupling of the Higgs field to the b-quarks, κ_b) and decay rates. The current ATLAS observed fitted value for κ_b disfavours only 3.1% of all pMSSM points.

The branching ratio BR($h \to \tilde{\chi}^0_1\tilde{\chi}^0_1$) can be enhanced if the LSPs are sufficiently light. Only bino models can have sufficiently light LSP and still satisfy pre-ATLAS Run 1 constraints. The disfavoured pMSSM model points by the invisible branching ratio fit represent only 6.6% of the pMSSM points with bino-like LSP and 0.0056% of all surviving models.

In general, ATLAS Run 1 searches exclude model points uniformly across the range of precision observables, demonstrating the complementarity of analyses. These precision variables depend on sparticles such as the smuon and gauginos masses, which are not as constraints as the sparticle masses in the strongly interesting sector of the pMSSM.

Naturalness is not part of the requirements during the model selection. Yet it is interesting to see that the ATLAS Run 1 searches exclude pMSSM points with a wide range of different fine-tuning values. The surviving models with the lowest fine-tuning have wino-like LSP. They also have relatively light top squarks, which indicates they would be expected to produce observable signal at LHC Run 2.

Chapter 10

Conclusion

The analysis presented in this dissertation belongs to the set of Supersymmetry searches performed at the Large Hadron Collider during the Run 1 data period. It uses 20.3 fb^{-1} of proton–proton data collision at $\sqrt{s} = 8$ TeV recorded in 2012 with the ATLAS detector. The analysis focuses on the electroweak sector of Supersymmetry, looking for the direct pair production of a chargino one $\tilde{\chi}_1^{\pm}$ and neutralino two $\tilde{\chi}_2^0$, decaying into a W and a Higgs boson. It is the first LHC search to exploit the presence of a SM-like Higgs boson in the supersymmetric decay chain.

The selected events contain as final states one lepton (from the W), a pair of b-jets (from the Higgs boson) and missing transverse momentum. The reconstruction of these objects requires a good understanding of the complementary information received by the ATLAS subdetectors. The electromagnetic and hadronic calorimeters play a particular role in this analysis, mostly in the precise measurement of the missing transverse momentum and the momentum determination of jets. The ATLAS calorimeters are required to be functioning well for this analysis to ensure flawless recordings of events and accurate measurements.

Complex flavor tagging algorithms are used to identify jets originating from b-quarks. The Higgs resonance can thus be reconstructed through the $b\bar{b}$ channel. In this thesis, a slight improvement of the di-jet mass resolution is obtained after correcting the b-jets: the energy from muons within a b-jet is added to the energy of the b-jets.

As no significant excess is observed with respect to the prediction from SM processes, exclusion limits are derived. In the context of the considered simplified model, degenerate $\tilde{\chi}_1^{\pm}$ and $\tilde{\chi}_2^0$ masses are excluded up to 150 GeV for $m(\tilde{\chi}_1^0) = 0$. The improved di-jet mass resolution, enhancing the expected exclusion potential, does not increase the observed exclusion contour.

Three other searches have addressed the Higgs diphoton and WW decay modes in the same simplified model scenario. When combining the results, common masses of $\tilde{\chi}_1^\pm$ and $\tilde{\chi}_2^0$ are excluded up to 250 GeV for a massless $\tilde{\chi}_1^0$. The analysis presented in this dissertation – the ℓbb channel – contributes for the most part to the global exclusion for electroweakino masses greater than 180 GeV. For comparison, the CMS Collaboration released a similar search [99] in which the observed limit $m(\tilde{\chi}_1^\mp\tilde{\chi}_2^0)$ is 210 GeV for $(\tilde{\chi}_1^0) = 0$.

In the context of the pMSSM, the analysis shows sensitivity for large values of the Higgsino mass, in a pMSSM parametrization where slepton masses are decoupled. Although no exclusion can be claimed, the analysis completes a gap in the sensitivity reach from two other ATLAS electroweak searches [53] for the same pMSSM grid.

The analysis in this thesis has been reinterpreted, along with 21 other ATLAS searches, in the context of the pMSSM. More than three million viable R-parity-conserving models, with neutralino as LSP, were tested. About 40% of them were found to be ruled out by the current ATLAS searches, severely reducing the plausible SUSY candidates for dark matter particles. This summary work, well received in the community of theorists, has been featured in CERN Courier [100]. It represents the most comprehensive assessment of the ATLAS constraints on Supersymmetry models to date.

Additional work could be done to improve the sensitivity of the present analysis. A continuous b-tagging procedure, instead of a single operating point, could enhance the b-tagging efficiency. More advanced flavor taggers, such as MV3, have become available to better identify b-jets. This analysis has been optimized using a cut-based approach. Multivariate techniques are more and more widespread within the ATLAS Collaboration and this search could benefit from such optimization methods. A multivariate approach was actually performed to assess the discovery and exclusion prospects at the high-luminosity LHC [101] for the considered scenario of the analysis.

For now, all eyes are on the fresh data: the LHC Run 2 has started. Proton–proton collisions are being taken at a record $\sqrt{s} = 13$ TeV, for the joy of experimentalists. Patience is required in the electroweak supersymmetric sector, as the sensitivity gain will require a large integrated luminosity. Strongly produced sparticles such as squarks and gluinos, however, have their cross sections increase by two to three orders of magnitude. Important effort is made in the ATLAS SUSY group towards targeting all possible scenarios and avoid any blind spot in the parameter space. If SUSY is around the corner, it will be spotted!

From a more general perspective, the LHC Run 2 will undeniably improve our understanding on matter and the Universe. Experimentalists and theorists are at a crest in human knowledge, overlooking the unknown. They are, together, writing the next physics textbooks and their future findings will soon make history.

Appendix A

ATLAS Liquid Argon Calorimeter Operation

During the data taking from April 2012 until February 2013, the author of this dissertation has been actively involved in the ATLAS Liquid Argon (LAr) calorimeter operations:

- first as a shifter, monitoring the calorimeter status in the ATLAS Control Room (ACR),
- then as a super-shifter, briefing and supervising the shifters in the ACR,
- on duty as Software On-call expert (424 hours overall),
- finally co-organizing and co-chairing the training session for future Software On-call experts.

The ATLAS Liquid Argon calorimeter operations during the 2012 data taking period are presented in the next section, with an emphasis on the author's contributions within the calorimeter team.

A.1 Basics of LAr signal reconstruction

Each one of the 1524 LAr front end board (FEB) amplifies, shapes and digitizes the signal of up to 128 channels simultaneously [102]. In order to achieve the required dynamic range, the amplification and shaping is performed in parallel with three different gains (of roughly 1, 9, and 80). But only the signal with the optimal gain is digitized by an analog to digital converter. After this treatment, five digitized samples[1] are sent for each cell to the readout driver (ROD) system [103] via optical links. The ROD boards can either transparently transmit the digitized samples to the data acquisition system (*transparent* mode), or compute the energy of the cell (*results* mode) to transmit only one number, hence reducing the data size and the offline processing time. In *results* mode, the cell energy is computed with a Digital Signal Processing (DSP) chip mounted on the ROD boards, using an online optimal filtering technique [104]. When the cell energy is above a defined threshold, additional information is sent: the time of the signal peak and the quality factor that reflects how much the pulse shape looks like an argon ionisation pulse shape. For cell energies above a second energy threshold, the five digitized samples are also transmitted. This allows the monitoring of the reliability of the DSP computation by performing an independent offline energy reconstruction or recompute the energy when the signal timing is not yet precisely adjusted. When a cell is no more operational (deteriorated signal routing in cryostat, dead readout channel, large noise, etc.), its energy is then estimated from the average energy of the eight neighbouring channels in the same calorimeter layer. The cell is masked offline, *i.e.* ignored in the event reconstruction. Regular calibration procedures in absence of collisions are the main input to identify problematic calorimeter channels [105]. Since the front end board's output is the basic detector information building block, a careful data integrity monitoring at the earliest stages of the processing chain is mandatory.

A.2 Responsibilities and mission as On-call expert

Information of all ATLAS sub-systems – also referred to as "partitions" – is available to the users by a Finite State Machine (FSM) software running in the ATLAS control room and also displayed on the web. An example is given in Figure A.1. Each table lists the different partitions in the first column, with their associated *state* and *status* on the second and third column respectively. Checkings are facilitated thanks to a colour-flag associated to the *state/status*.

The On-call expert main mission is to ensure the data taking of the three calorimeters (Forward, LAr and Tile) occurs smoothly. On top of being available and ready to intervene in the shortest delays, the On-call expert should frequently collect information about the current status of the detector. The On-call expert, along with

---

[1] in debugging/commissioning mode, up to 32 samples can be readout.

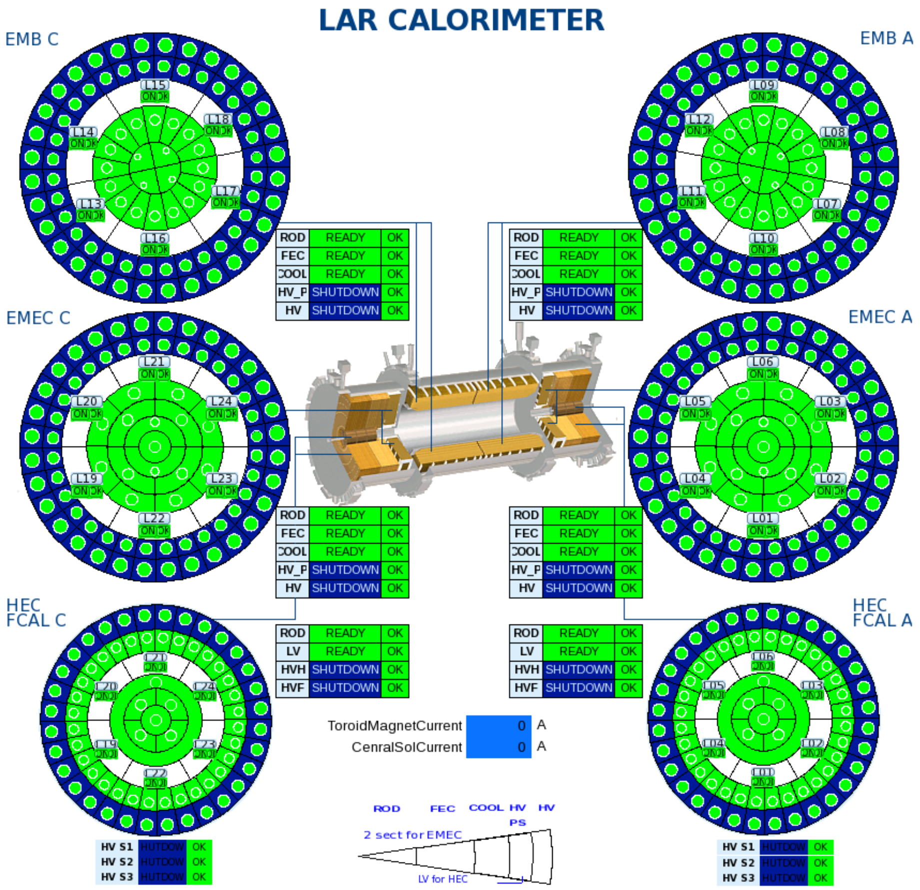

ROD	READY	OK
FEC	READY	OK
COOL	READY	OK
HV_P	SHUTDOWN	OK
HV	SHUTDOWN	OK

ROD	READY	OK
FEC	READY	OK
COOL	READY	OK
HV_P	SHUTDOWN	OK
HV	SHUTDOWN	OK

ROD	READY	OK
FEC	READY	OK
COOL	READY	OK
HV_P	SHUTDOWN	OK
HV	SHUTDOWN	OK

ROD	READY	OK
FEC	READY	OK
COOL	READY	OK
HV_P	SHUTDOWN	OK
HV	SHUTDOWN	OK

ROD	READY	OK
LV	READY	OK
HVH	SHUTDOWN	OK
HVF	SHUTDOWN	OK

ROD	READY	OK
LV	READY	OK
HVH	SHUTDOWN	OK
HVF	SHUTDOWN	OK

ToroidMagnetCurrent	0	A
CenralSolCurrent	0	A

HV S1	HUTDOWN	OK
HV S2	HUTDOWN	OK
HV S3	HUTDOWN	OK

HV S1	HUTDOWN	OK
HV S2	HUTDOWN	OK
HV S3	HUTDOWN	OK

Figure A.1: ATLAS Detector Online Status of the Liquid Argon Calorimeter.

the hardware and data quality experts, should give a summary of the last 24 hours activities to the Run Coordinator chairing the daily calorimeter meeting. All the experts of all subdetectors then attend the daily ATLAS meeting to learn about the ATLAS plan of the day.

How to react to a given problem is strongly influenced by the current run status. When ATLAS is collecting data under stable beam, the top priority is to maintain the system online, error-free and nominal. If stable beam is imminent, investigations are limited in time. However, the absence of stable beam permits longer inquiry to try new recovery methods not yet tested. The main tools available to Software On-call expert were the Logfile Viewer, listing all verbose records proper to a given machine, and the Logfile Manager. The latter stores all generated messages from any given run, past or current. Applying filters, the problem can be restricted by localising it more precisely (which RODs, FEBs are affected). It is also possible to look for past entries with similar errors and see how it was treated at that time. The first step is always to collect all information about the issue, and report them as soon as possible to the Run Coordinator. Each action is performed only after the Run Coordinator's approval. It can be a simple acknowledgement of an alarm (as considered unharmful for the run) until the complete restart of a partition, or the whole LAr system if the situation demands it.

A.2.1 Revision of Message Filter Liquid Argon software

One of the author contributions as a developer in the LAr software group was to improve an existing plugin called `MessageFilter`. This application prevents an already acknowledged warning or message from being displayed in the alarm panel. To perform this task, it is essential to know how the LAr software, referred to as the LargOnline framework, is structured.

Object-oriented programming (OOP) is a programming paradigm that represents concepts as “objects” that have data fields (attributes that describe the object) and associated procedures known as methods. A “class” defines an object type. It can be divided into sub-classes, all inheriting of the properties of the mother class. The software first creates the objects from their respective classes, generating “instances” of the class. Then objects methods are called to perform the programmed actions.

All the hardware components of the LAr system (readout electronics such as RODs, FEBs collecting the signal of all channels) are translated into instances of the main class `OnlineObject` in the LargOnline framework. Figure A.2 gives an overview of the class hierarchy. This main class `OnlineObject` is the root class of all high level components. It can propagate any data acquisition command to all `OnlineObject` instances, combining possible independent features (for instance an `OnlineObject` associated with a FEB is different as one matching a ROD, however they share common properties as all readout signal processing electronics).

The Object Oriented scheme is static. Object properties are fixed. The LargOnline framework follows Aspect Oriented Programming (AOP), which complements Object Oriented Programming by allowing the developer to dynamically modify the static OO model to create a system that can grow to meet new requirements. The `MessageFilter` plugin follows the Aspect Oriented paradigm. It intervenes everytime a method is called on an object, to prevent potential known error messages from being displayed in the alarm panel. The existing version used to be hard-coded: the

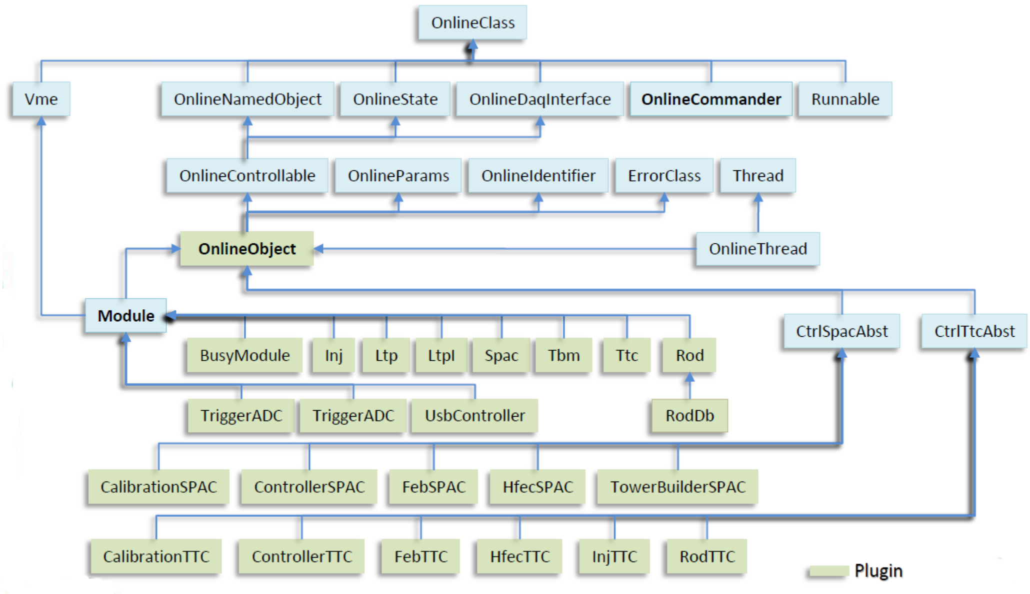

Figure A.2: Overview of the class hierarchy in the LargOnline framework.

known errors were directly written in the class header file.

A new patch was developed by the author so that the MessageFilter works in a more dynamic way, accessing the main database. Whenever an object transmits a warning or error message, the MessageFilter intercepts it and checks in the database the list of known messages for this object. If it matches with one of those, the message is removed from the list and hence will not be displayed on the alarm panel. This new patch has been successfully tested, implemented and documented in late summer 2012.

A.2.2 Web-portal project and realization

The calorimetry operation includes the three ATLAS calorimeters (Forward, LAr and Tile) which had their independent online documentation. The information was repeated and scattered on those pages, some of them were outdated. To better access links in the different Twiki pages, a web-portal project was suggested by the author, who coded, implemented and documented it.

The web-page design follows the main ATLAS Detector Operation page, but it is here specific to the calorimeters. The information is organized in different tabs. Each tab is dedicated to a role: shifter, super-shifter, expert, data quality. In this way, the operator only sees the relevant links specific to their tasks. The links are split in three columns, each for the calorimeter sub-systems. A common glossary defines the acronyms used. To visualize on a daily basis the current shifters and experts, the link “Calo Crew” accesses the database of ATLAS operations to display the names of the persons in charge along with their picture and contact information. Figure A.3 is a screenshot of the final version. A direct link from the main ATLAS Detector Operation page directs to this “Calo Portal”.

The Calo Portal has been in use as main entrance menu page on the computers in the ATLAS control room from August 2012 until the end of the Run 1 in February 2013. After minor updates, it now serves for the LHC Run 2.

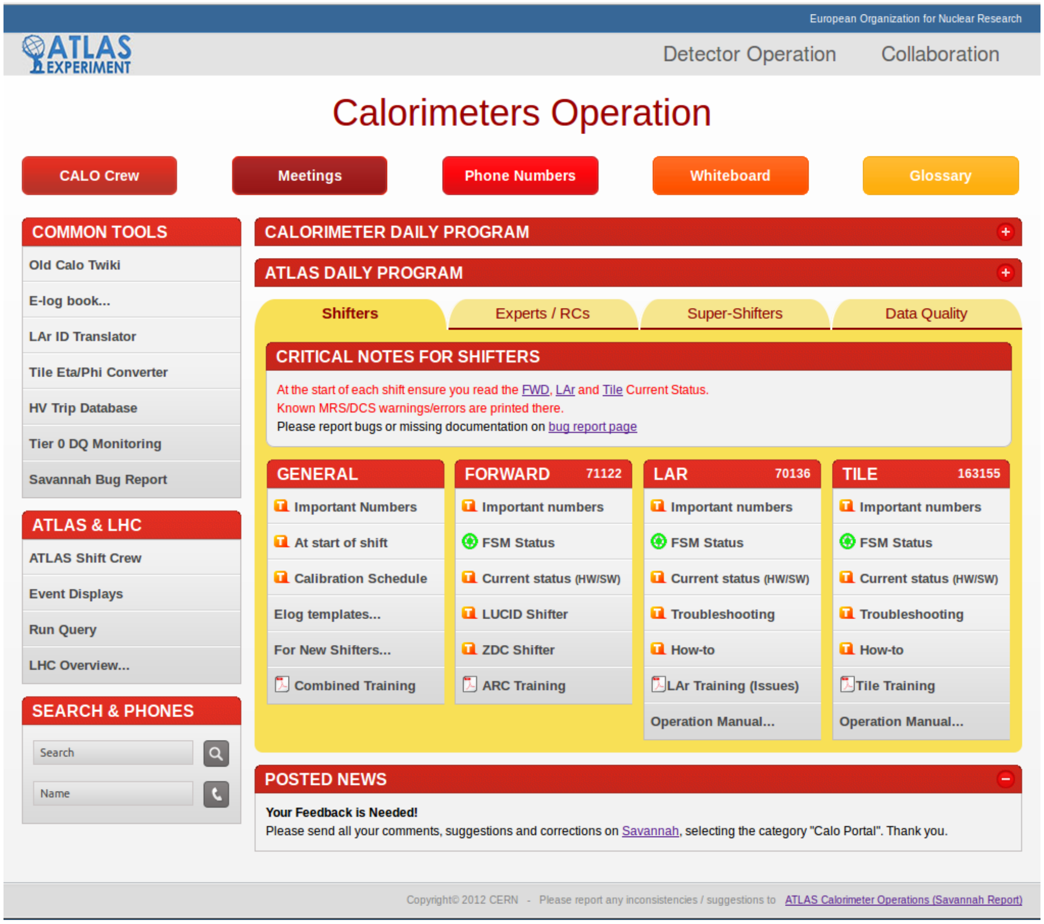

At the start of each shift ensure you read the FWD, LAr and Tile Current Status.
Known MRS/DCS warnings/errors are printed there.
Please report bugs or missing documentation on bug report page

Your Feedback is Needed!
Please send all your comments, suggestions and corrections on Savannah, selecting the category "Calo Portal". Thank you.

Copyright© 2012 CERN - Please report any inconsistencies / suggestions to ATLAS Calorimeter Operations (Savannah Report)

Figure A.3: Screenshot of the Calorimeter portal web-page.

Appendix B

Prescriptions for Theoretical Systematic Uncertainties

This appendix details how the theoretical systematic uncertainties are assessed for each of the main background processes considered in this thesis.

B.1 Top pair production

Generator The uncertainty on generator modelling is derived by comparing Powheg+Jimmy with MC@NLO+Jimmy.

Parton shower An uncertainty on the choice of the showering model is computed by comparing Powheg+Pythia6 with Powheg+Jimmy.

Radiation Uncertainties related to the emission of additional partons in the initial or final states are evaluated by comparing the AcerMC+Pythia6 "MorePS" samples with "LessPS".

Factorisation and Renormalisation scales An uncertainty on the generation of the NLO hard scattering is computed by varying the renormalisation and factorisation scales in Powheg+Pythia6 to half (samples "facsc05" and "rensc05") and twice (samples "facsc2" and "rensc2") the nominal scales.

PDFs The nominal $t\bar{t}$ sample uses the PDF set CT10 and contains 52 additional error sets.

B.2 Single-top production

ISR/FSR For each of the three channels (s, t and Wt) of the single-top background component, AcerMC+Pythia6 samples with ISR and FSR increased and decreased (separately) have been used to compute the relative difference among yields. The implementation follows the one for $t\bar{t}$ (see Equation 7.2).

Generator + Parton Shower comparison for s-channel The uncertainty on the generator on the single-top s is computed by comparing Powheg+Pythia6 with MC@NLO+Jimmy. The full difference in yields between the two Monte Carlo generators is evaluated and symmetrized.

Generator, parton shower and interference with $t\bar{t}$ for Wt-channel The Wt mode is well-defined at LO, but at NLO in QCD it receives large corrections and interferes with top pair production, especially if the invariant mass m_{Wb} of the final states W and b approaches the top quark mass. A first approach to compute these three variations is to derive the three following systematic uncertainties: the generator (estimating the full difference of yields between Powheg+Herwig and MC@NLO+Herwig), the parton shower (computing the full difference between Powheg+Pythia6 and Powheg+Herwig) and the interference with $t\bar{t}$, which is assessed using the "DR vs DS method". This method consists of taking the full difference between two Powheg+Pythia6 Monte Carlo samples, one produced with the Diagram Removal (DR) scheme and the other with the Diagram Substraction scheme (DS) [106]. In DR, the diagrams that also enter $t\bar{t}$ production are removed at amplitude level; the $t\bar{t}$ interferences with single-top Wt production are eliminated. In DS, the cross section is corrected with a substraction term that is adjusted to peak when the invariant mass m_{Wb} gets close to the top mass. In this process, the $t\bar{t}$ interferences are suppressed at cross section level. To cope with the very limited statistics, the generator, parton shower and DR/DS differences have all been estimated in a loose region, defined as: $m_{\mathrm{T}}> 40$ GeV, $E_{\mathrm{T}}^{\mathrm{miss}}> 100$ GeV, $m_{\mathrm{CT}}> 100$ GeV and $45 < m_{bb} < 195$ GeV. Figure B.1 shows the m_{bb} distributions for the single-top Wt-channel for the generator, parton shower and DR/DS systematics, estimated at reconstructed level in the loose region binned in number of b-jets.

A "new recommendation" for the single-top Wt systematic uncertainties, sug-

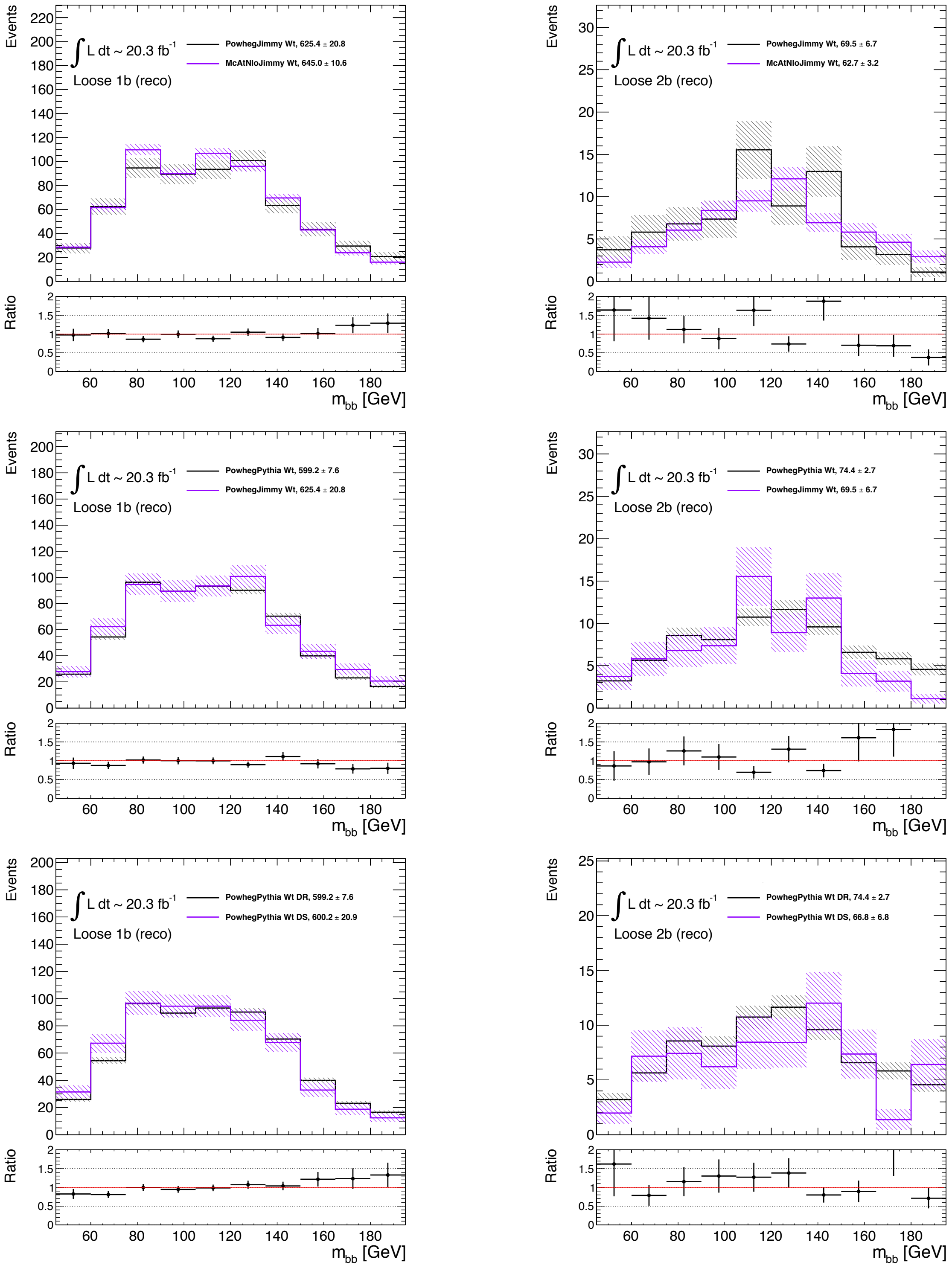

Figure B.1: The m_{bb} distributions for the single-top Wt-mode assessing the generator (first row), parton shower (middle row) and DR/DS systematic uncertainties (bottom row) in the loose pre-selection region with 1 b-jet (left) and 2 b-jets (right) requirements.

gested by the SUSY Working Group, was later studied. With this recipe, the generator, parton shower and $t\bar{t}$ interference systematic uncertainties are merged into one systematic error. For this, the nominal POWHEG+PYTHIA6 samples (using the Diagram Removal scheme), are compared to a LO production of $WWbb$ ACERMC composed of:

- Process 14 : $q + q \rightarrow (W\,W\,b\,b)$
- Process 20 : $g + g \rightarrow (W\,W\,b\,b)$,

which offers the best description of $WWbb$. We make three comparisons in total in order to assess the uncertainties due to the generator, the parton shower and the interference previously mentioned:

1. Comparison of POWHEG+PYTHIA6 $Wt + t\bar{t}$ (with the P2011C tune) with ACERMC+PYTHIA6 $WWbb$ processes 14 + 20
2. Comparison of MC@NLO+JIMMY Wt+$t\bar{t}$ with POWHEG+JIMMY Wt+$t\bar{t}$
3. Comparison of POWHEG+PYTHIA6 $Wt + t\bar{t}$ (with the P2011C tune) with POWHEG+JIMMY $Wt + t\bar{t}$

Just taking ACERMCLO cross sections directly (14.47 pb for process 14 and 63.2 pb for process 20) gives a large normalisation difference – almost a factor of 2 – between the ACERMC and POWHEG samples. We therefore calculate a single k-factor to apply to ACERMC using the POWHEG cross section.

$$k = \frac{0.543(253.00 + 20.461 \times 1.0933)}{14.478 + 63.2} \sim 1.925 \tag{B.1}$$

After applying this k-factor, we can compare the ACERMC predictions to POWHEG samples. The total generator+parton shower+interference with $t\bar{t}$ systematic is then computed by taking the maximum of 1 and 2 and adding 3 in quadrature:

$$\sigma^{\text{gen+PS+int}} = \sqrt{\max\left(\sigma_1, \sigma_2\right)^2 + \left(\sigma_3\right)^2}. \tag{B.2}$$

Figures B.2 show the m_{bb} distributions used to derive the values of σ_1, σ_2 and σ_3. Table B.1 shows the relative percentages obtained with the old (split systematics) and new (merged systematics) recommendations.

Given the large differences observed for the single-top Wt systematic uncertainties and in an effort of harmonization with other SUSY searches, the analysis

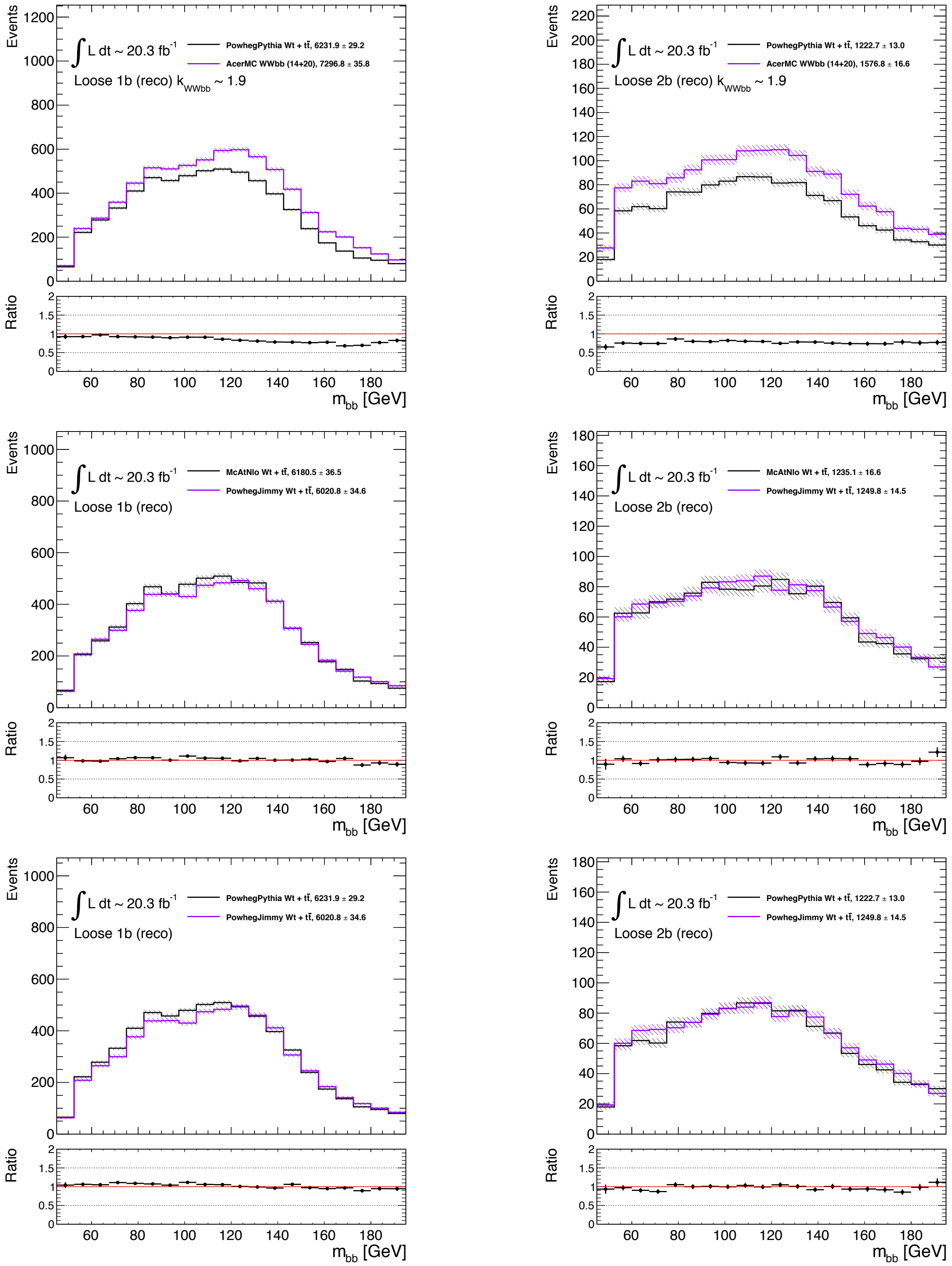

Figure B.2: The m_{bb} distributions for the single-top Wt-mode comparing the single-top $+t\bar{t}$ and $WWbb$ processes (top row), the generators (middle row) and the parton shower (bottom row), which are merged in a combined systematic uncertainty. The loose pre-selection region with 1 b-jet (left) and 2 b-jets (right) is the same as in the previous systematic derivation method.

Table B.1: Relative percentage of the systematics with respect to nominal yield of the single-top Wt-channel according to the old (three separate variations summed in quadrature) and new (all the three merged as explained in the text) recommendations.

	Old recommendation			
Region	Generator	Parton shower	Interference $t\bar{t}$	Quadratic sum
Loose 1 b-jet	3.57	4.37	0.17	5.65
Loose 2 b-jets	10.8	6.64	10.2	16.27
	New recommendation			
	σ_1	σ_2	σ_3	$\max(\sigma_1, \sigma_2) \bigoplus \sigma_3$
Loose 1 b-jet	17.10	2.58	3.39	17.43
Loose 2 b-jets	29.00	1.19	2.22	29.08

eventually opted for an evaluation of the systematics in a “normalization region” n, defined as the union of the two control regions CRT and CRW. The systematic uncertainties for the generator + $t\bar{t}$ interference are merged, whereas the one for parton shower modelling is estimated separately. All systematics were extrapolated from this normalization region “n”. For a given systematic variation i in a region r, the relative extrapolated systematic s_i^r in this region will be:

$$s_i^r = \frac{\left| N^r_{\mathrm{Up},i} \dfrac{N^n_{\mathrm{Nom},i}}{N^n_{\mathrm{Up},i}} - N^r_{\mathrm{Down},i} \dfrac{N^n_{\mathrm{Nom},i}}{N^n_{\mathrm{Down},i}} \right|}{N^r_{\mathrm{Nom},i}} = \frac{\left| \dfrac{N^r_{\mathrm{Up},i}}{N^n_{\mathrm{Up},i}} - \dfrac{N^r_{\mathrm{Down},i}}{N^n_{\mathrm{Down},i}} \right|}{\dfrac{N^r_{\mathrm{Nom},i}}{N^n_{\mathrm{Nom},i}}}, \tag{B.3}$$

where $N^r_{\mathrm{Nom},i}$ ($N^n_{\mathrm{Nom},i}$), $N^r_{\mathrm{Up},i}$ ($N^n_{\mathrm{Up},i}$) and $N^r_{\mathrm{Down},i}$ ($N^n_{\mathrm{Down},i}$) are the yields in the region r (n) for the nominal, the up and down systematic variations, respectively.

B.3 W+jets production

Instead of comparing alternate samples – which is CPU intensive with the large set of W+jets Monte Carlo samples – a reweighting procedure has been implemented, developed for the SUSY 0-lepton inclusive analysis [107]. This procedure consists of applying the Alpgen scale variations to Sherpa using a reweighting based on the number of truth jets with $p_{\mathrm{T}} > 30$ GeV. The resulting weights of this procedure are implemented in the Sherpa nominal samples of this analysis as event weights. They account for the uncertainty on the renormalisation, factorisation and matching scales and also the uncertainty linked with the heavy flavor overlap removal procedure[1].

B.4 Diboson production

The theoretical uncertainties on the total cross sections of diboson are 5% for WW, ZZ and 7% for WZ. The systematic variations samples are generated at the particle level with Sherpa using the same PDF set CT10 as the baseline samples. There are up to 2 extra partons in the matrix element. For the subprocesses $WW \to \ell\nu\ell\nu, WZ \to \ell\nu\ell\ell, ZZ \to \ell\ell\ell\ell$ and $ZZ \to \ell\ell\nu\nu$, the following cuts are applied: the lepton transverse momentum should be $p_T^{\mathrm{lepton}} > 5$ GeV and the invariant mass of the lepton pair should be $m_{\ell\ell} > 4$ GeV. For the subprocess $VV \to \nu\nu qq$, the transverse momentum of the two jets should be $p_T^{\mathrm{jets}} > 15$ GeV. For $VV \to e^+e^-qq, VV\mu^+\mu^-qq, VV \to \tau^+\tau^-qq, VV \to e\nu qq, VV \to \mu\nu qq$ and $VV \to \tau\nu qq$, the cut $m_{\ell\ell} > 7$ GeV is applied. The complete list of Monte Carlo sample can be found in Reference [52].

Due to the lack of statistics, the uncertainties are derived in an "inclusive" region, defined as: ≥ 1 b-jet, $m_{\mathrm{T}}>$ 40 GeV, $E_{\mathrm{T}}^{\mathrm{miss}}>$ 100 GeV, $m_{\mathrm{CT}}>$ 100 GeV and $45 < m_{bb} <$ 195 GeV.

B.5 Top pair production associated with vector boson

Following the recommendations of the background forum, a global 22% uncertainty on the $t\bar{t}V$ production cross section and, therefore, on the global normalisation of the $t\bar{t}V$ MC samples is considered.

---

[1] The W+jets production is split by processes, with multiple datasets for each jet flavor and extra parton multiplicity. A significant overlap exists between heavy b and c jets created in the parton shower and those originally in the matrix element calculation. An overlap removal procedure is necessary. It is based on angular distance between the simulated heavy flavor quarks [108].

Appendix C

Additional fit results

This section contains supporting information for Chapter 8.

C.1 Results of background-only fits

C.1.1 Tables and figures on fit parameters

The blinded fit results presented in Section 8.2.2 are expanded in Table C.1, which shows the expected and fitted MC yields for all the background components separately. Shown in Table C.2 are the MC predicted yields, before and after the unblinded background-only fit, for all background components separately. Table C.3 is the same as Table C.1, except that the blinded fit has been performed with the improved variables m_{bb}^{corr}. The corresponding unblinded fit results, with the use of m_{bb}^{corr} as fitted variable, is shown in Table C.4.

The fit results for the nuisance parameters are shown in Figures C.1 and C.2 for the published analysis using m_{bb} and for the modified search using m_{bb}^{corr} respectively.

The variations on the background estimate of the dominant systematics uncertainties in the published analysis and in the version using m_{bb}^{corr} are listed in Tables C.5 and Table C.6, respectively. In these tables all backgrounds have been grouped into a single component. Here the uncertainties on the Jet Energy Scale have been grouped together, as well as these on the electron and muon reconstruction. It is important to note that the individual uncertainties can be correlated, and do not necessarily add up quadratically to the total background uncertainty. The percentages show the size of the uncertainty relative to the total expected background.

Table C.1: Expected yields from the Monte Carlo simulation before and after the **blinded** background-only fit. The errors shown are the quadratic sum of the statistical and systematic uncertainties. Uncertainties on the fitted yields are symmetric by construction, where the negative error is truncated when reaching to zero event yield.

Yields in regions	**CRT**	**CRW**	**SRAsb**	**SRBsb**	**VRA**	**VRB**	**SRAh**	**SRBh**
Observed events	651	1547	14	10	885	235	4	3
MC yields after fit	642.01 ± 24.93	1558.04 ± 38.65	13.05 ± 2.40	8.81 ± 1.65	880.44 ± 85.54	245.19 ± 17.21	5.96 ± 1.29	2.77 ± 0.79
$t\bar{t}$	607.29 ± 25.27	676.62 ± 56.91	8.00 ± 2.44	3.10 ± 1.38	684.79 ± 85.57	141.01 ± 17.88	3.82 ± 1.22	1.36 ± 0.67
W+jets	11.13 ± 1.60	693.78 ± 59.83	2.66 ± 0.48	1.73 ± 0.32	99.18 ± 11.85	62.22 ± 8.44	0.58 ± 0.27	0.24 ± 0.13
Single top s	0.75 ± 0.15	2.96 ± 0.32	0.00 ± 0.00	0.00 ± 0.00	17.31 ± 2.56	0.26 ± 0.07	0.00 ± 0.00	0.00 ± 0.00
Single top t	2.51 ± 0.94	19.68 ± 2.71	0.25 ± 0.23	$0.09^{+0.15}_{-0.09}$	28.50 ± 5.42	5.03 ± 0.83	0.20 ± 0.04	0.00 ± 0.00
Single top Wt	16.25 ± 3.32	88.82 ± 12.97	1.61 ± 0.52	2.40 ± 1.14	34.18 ± 4.17	21.91 ± 3.56	1.08 ± 0.36	0.71 ± 0.37
Diboson	2.25 ± 0.35	64.44 ± 7.65	0.33 ± 0.11	1.10 ± 0.15	10.20 ± 1.48	8.99 ± 1.01	0.00 ± 0.00	0.21 ± 0.04
Z+jets	0.38 ± 0.08	7.03 ± 0.79	$0.02^{+0.02}_{-0.02}$	0.12 ± 0.06	1.95 ± 0.28	0.38 ± 0.07	0.03 ± 0.02	0.00 ± 0.00
WH	0.42 ± 0.04	3.65 ± 0.27	0.11 ± 0.02	0.05 ± 0.01	3.71 ± 0.31	5.12 ± 0.43	0.23 ± 0.03	0.12 ± 0.02
ZH	0.01 ± 0.00	0.03 ± 0.00	$0.00^{+0.00}_{-0.00}$	0.00 ± 0.00	0.04 ± 0.00	0.04 ± 0.00	0.00 ± 0.00	0.00 ± 0.00
$t\bar{t}V$	1.03 ± 0.26	1.02 ± 0.25	0.07 ± 0.03	0.22 ± 0.06	0.58 ± 0.14	0.21 ± 0.05	0.01 ± 0.01	0.12 ± 0.03
MC yields before fit	547.96 ± 101.78	1703.17 ± 90.93	11.23 ± 3.27	7.79 ± 2.00	830.35 ± 71.49	241.95 ± 25.62	4.98 ± 1.69	2.24 ± 0.94
$t\bar{t}$	511.65 ± 100.95	636.62 ± 93.49	5.83 ± 3.09	2.01 ± 1.55	617.17 ± 60.99	124.85 ± 23.76	2.79 ± 1.49	0.90 ± 0.75
W+jets	13.73 ± 1.59	880.52 ± 2.60	3.19 ± 0.55	2.18 ± 0.41	123.04 ± 9.15	76.63 ± 7.68	0.67 ± 0.39	0.30 ± 0.20
Single top s	0.71 ± 0.20	2.96 ± 0.36	0.00 ± 0.00	0.00 ± 0.00	16.08 ± 3.63	0.24 ± 0.10	0.00 ± 0.00	0.00 ± 0.00
Single top t	2.46 ± 1.11	19.42 ± 2.89	$0.19^{+0.24}_{-0.19}$	$0.14^{+0.33}_{-0.14}$	26.22 ± 8.01	4.83 ± 0.90	0.19 ± 0.04	0.00 ± 0.00
Single top Wt	15.51 ± 3.42	89.21 ± 13.97	1.47 ± 0.56	2.01 ± 1.16	32.62 ± 4.50	21.09 ± 3.88	1.05 ± 0.39	0.60 ± 0.35
Diboson	2.05 ± 0.45	62.80 ± 8.72	0.36 ± 0.17	1.07 ± 0.16	9.40 ± 1.98	8.73 ± 1.18	0.00 ± 0.00	0.21 ± 0.05
Z+jets	0.39 ± 0.11	6.89 ± 0.91	$0.02^{+0.03}_{-0.02}$	0.13 ± 0.08	1.83 ± 0.39	0.37 ± 0.08	0.03 ± 0.02	$0.00^{+0.02}_{-0.00}$
WH	0.40 ± 0.05	3.69 ± 0.37	0.10 ± 0.02	0.05 ± 0.01	3.57 ± 0.37	4.94 ± 0.55	0.22 ± 0.04	0.12 ± 0.02
ZH	0.01 ± 0.00	0.03 ± 0.00	$0.00^{+0.00}_{-0.00}$	0.00 ± 0.00	0.04 ± 0.01	0.04 ± 0.01	0.00 ± 0.00	0.00 ± 0.00
$t\bar{t}V$	1.05 ± 0.28	1.02 ± 0.25	0.07 ± 0.03	0.22 ± 0.06	0.56 ± 0.14	0.21 ± 0.06	0.01 ± 0.01	0.11 ± 0.04

Table C.2: Expected yields from the Monte Carlo simulation before and after the **unblinded** background-only fit. The errors shown are the quadratic sum of the statistical and systematic uncertainties. Uncertainties on the fitted yields are symmetric by construction, where the negative error is truncated when reaching to zero event yield.

Yields in regions	**CRT**	**CRW**	**SRAsb**	**SRBsb**	**SRAh**	**SRBh**
Observed events	651	1547	14	10	4	3
MC yields after fit	641.52 ± 24.91	1557.60 ± 38.64	12.50 ± 2.12	8.53 ± 1.53	5.69 ± 1.10	2.67 ± 0.69
$t\bar{t}$	606.80 ± 25.27	676.25 ± 56.56	7.48 ± 2.14	2.87 ± 1.20	3.57 ± 1.04	1.26 ± 0.57
W+jets	11.15 ± 1.60	694.16 ± 59.67	2.65 ± 0.48	1.72 ± 0.32	0.56 ± 0.25	0.25 ± 0.13
Single-top s	0.75 ± 0.15	2.97 ± 0.32	0.00 ± 0.00	0.00 ± 0.00	0.00 ± 0.00	0.00 ± 0.00
Single-top t	2.52 ± 0.93	19.71 ± 2.71	0.24 ± 0.22	$0.08^{+0.15}_{-0.08}$	0.19 ± 0.04	0.00 ± 0.00
Single-top Wt	16.22 ± 3.29	88.68 ± 12.79	1.60 ± 0.51	2.37 ± 1.12	1.07 ± 0.35	0.71 ± 0.36
Diboson	2.24 ± 0.35	64.13 ± 7.60	0.33 ± 0.11	1.09 ± 0.16	0.00 ± 0.00	0.21 ± 0.04
Z+jets	0.38 ± 0.08	7.01 ± 0.79	$0.02^{+0.02}_{-0.02}$	0.12 ± 0.06	0.03 ± 0.02	0.00 ± 0.00
WH	0.42 ± 0.04	3.65 ± 0.27	0.11 ± 0.02	0.05 ± 0.01	0.23 ± 0.03	0.12 ± 0.02
ZH	0.01 ± 0.00	0.03 ± 0.00	$0.00^{+0.00}_{-0.00}$	0.00 ± 0.00	0.00 ± 0.00	0.00 ± 0.00
$t\bar{t}V$	1.03 ± 0.26	1.02 ± 0.24	0.07 ± 0.03	0.22 ± 0.06	0.01 ± 0.01	0.12 ± 0.03
MC yields before fit	547.96 ± 101.78	1703.17 ± 90.93	11.23 ± 3.27	7.79 ± 2.00	4.98 ± 1.69	2.24 ± 0.94
$t\bar{t}$	511.65 ± 100.95	636.62 ± 93.49	5.83 ± 3.09	2.01 ± 1.55	2.79 ± 1.49	0.90 ± 0.75
W+jets	13.73 ± 1.59	880.52 ± 2.60	3.19 ± 0.55	2.18 ± 0.41	0.67 ± 0.39	0.30 ± 0.20
Single-top s	0.71 ± 0.20	2.96 ± 0.36	0.00 ± 0.00	0.00 ± 0.00	0.00 ± 0.00	0.00 ± 0.00
Single-top t	2.46 ± 1.11	19.42 ± 2.89	$0.19^{+0.24}_{-0.19}$	$0.14^{+0.33}_{-0.14}$	0.19 ± 0.04	0.00 ± 0.00
Single-top Wt	15.51 ± 3.42	89.21 ± 13.97	1.47 ± 0.56	2.01 ± 1.16	1.05 ± 0.39	0.60 ± 0.35
Diboson	2.05 ± 0.45	62.80 ± 8.72	0.36 ± 0.17	1.07 ± 0.16	0.00 ± 0.00	0.21 ± 0.05
Z+jets	0.39 ± 0.11	6.89 ± 0.91	$0.02^{+0.03}_{-0.02}$	0.13 ± 0.08	0.03 ± 0.02	$0.00^{+0.02}_{-0.00}$
WH	0.40 ± 0.05	3.69 ± 0.37	0.10 ± 0.02	0.05 ± 0.01	0.22 ± 0.04	0.12 ± 0.02
ZH	0.01 ± 0.00	0.03 ± 0.00	$0.00^{+0.00}_{-0.00}$	0.00 ± 0.00	0.00 ± 0.00	0.00 ± 0.00
$t\bar{t}V$	1.05 ± 0.28	1.02 ± 0.25	0.07 ± 0.03	0.22 ± 0.06	0.01 ± 0.01	0.11 ± 0.04

Table C.3: Expected yields from the Monte Carlo simulation before and after the **blinded** background-only fit **using $\boldsymbol{m_{bb}^{\text{corr}}}$**. The errors shown are the quadratic sum of the statistical and systematic uncertainties. Uncertainties on the fitted yields are symmetric by construction, where the negative error is truncated when reaching to zero event yield.

Yields in regions	**CRT**	**CRW**	**SRAsb**	**SRBsb**	**VRA**	**VRB**	**SRAh**	**SRBh**
Observed events	691	1592	15	11	905	242	6	3
MC yields after fit	681.21 ± 25.79	1602.80 ± 39.22	14.88 ± 2.56	9.32 ± 1.84	915.44 ± 91.43	262.38 ± 19.24	6.60 ± 1.44	3.12 ± 0.90
$t\bar{t}$	644.21 ± 26.30	702.51 ± 53.21	8.41 ± 2.55	3.36 ± 1.49	709.72 ± 89.69	144.51 ± 17.06	4.40 ± 1.39	1.45 ± 0.74
W+jets	12.49 ± 2.36	702.13 ± 58.75	3.16 ± 0.66	1.98 ± 0.49	106.76 ± 17.77	73.74 ± 14.09	0.56 ± 0.29	0.34 ± 0.15
Single top s	0.82 ± 0.16	3.03 ± 0.32	0.00 ± 0.00	0.00 ± 0.00	18.33 ± 2.46	0.26 ± 0.08	0.00 ± 0.00	0.00 ± 0.00
Single top t	2.78 ± 1.02	20.93 ± 2.91	$0.32^{+0.32}_{-0.32}$	$0.03^{+0.07}_{-0.03}$	29.35 ± 4.87	5.11 ± 0.95	0.20 ± 0.04	0.00 ± 0.00
Singe top Wt	16.92 ± 3.37	94.01 ± 13.11	1.65 ± 0.54	2.62 ± 1.19	34.34 ± 4.04	22.90 ± 3.46	1.16 ± 0.38	0.79 ± 0.41
Diboson	1.99 ± 0.35	68.50 ± 7.55	1.17 ± 0.47	0.92 ± 0.54	10.67 ± 1.16	9.67 ± 1.18	0.00 ± 0.00	0.27 ± 0.06
Z+jets	0.45 ± 0.11	6.65 ± 0.59	0.03 ± 0.01	0.10 ± 0.05	1.99 ± 0.41	0.59 ± 0.12	0.02 ± 0.01	0.02 ± 0.01
ZH	0.01 ± 0.00	0.03 ± 0.00	$0.00^{+0.00}_{-0.00}$	0.00 ± 0.00	0.04 ± 0.00	0.04 ± 0.00	0.00 ± 0.00	0.00 ± 0.00
WH	0.42 ± 0.04	3.88 ± 0.26	0.09 ± 0.01	0.05 ± 0.01	3.63 ± 0.27	5.32 ± 0.41	0.26 ± 0.03	0.13 ± 0.02
$t\bar{t}V$	1.11 ± 0.28	1.13 ± 0.27	0.06 ± 0.02	0.24 ± 0.06	0.60 ± 0.16	0.22 ± 0.06	0.01 ± 0.01	0.11 ± 0.03
MC yields before fit	577.74 ± 102.51	1695.73 ± 93.47	12.49 ± 3.57	7.86 ± 2.26	844.60 ± 73.41	253.83 ± 28.56	5.39 ± 1.87	2.44 ± 1.01
$t\bar{t}$	540.97 ± 101.75	665.84 ± 92.63	6.21 ± 3.29	2.07 ± 1.59	635.26 ± 62.43	130.26 ± 24.75	3.26 ± 1.73	0.98 ± 0.83
W+jets	13.90 ± 2.36	833.28 ± 3.15	3.56 ± 0.70	2.22 ± 0.57	117.22 ± 15.91	81.75 ± 14.06	0.58 ± 0.35	0.34 ± 0.15
Single top s	0.74 ± 0.18	3.06 ± 0.34	0.00 ± 0.00	0.00 ± 0.00	16.60 ± 3.06	0.24 ± 0.10	0.00 ± 0.00	0.00 ± 0.00
Single top t	2.44 ± 1.01	20.04 ± 2.89	$0.19^{+0.24}_{-0.19}$	$0.14^{+0.27}_{-0.14}$	27.13 ± 6.34	4.87 ± 1.03	0.19 ± 0.04	0.00 ± 0.00
Singe top Wt	16.02 ± 3.42	93.20 ± 13.79	1.41 ± 0.56	2.09 ± 1.17	32.32 ± 4.40	21.74 ± 3.75	1.09 ± 0.40	0.60 ± 0.37
Diboson	1.79 ± 0.46	68.80 ± 8.66	0.95 ± 0.46	0.95 ± 0.69	10.20 ± 1.29	9.07 ± 1.42	0.00 ± 0.00	0.25 ± 0.06
Z+jets	0.39 ± 0.11	6.56 ± 0.69	0.03 ± 0.01	0.09 ± 0.05	1.83 ± 0.44	0.56 ± 0.12	0.02 ± 0.01	0.02 ± 0.01
ZH	0.01 ± 0.00	0.03 ± 0.00	$0.00^{+0.00}_{-0.00}$	0.00 ± 0.00	0.04 ± 0.00	0.04 ± 0.01	0.00 ± 0.00	0.00 ± 0.00
WH	0.39 ± 0.05	3.81 ± 0.32	0.08 ± 0.02	0.05 ± 0.01	3.45 ± 0.33	5.07 ± 0.51	0.24 ± 0.04	0.13 ± 0.02
$t\bar{t}V$	1.07 ± 0.28	1.13 ± 0.28	0.06 ± 0.02	0.24 ± 0.07	0.56 ± 0.15	0.22 ± 0.06	0.01 ± 0.01	0.11 ± 0.03

Table C.4: Expected yields from the Monte Carlo simulation before and after the **unblinded** background-only fit **using $\boldsymbol{m_{bb}^{\text{corr}}}$**. The errors shown are the quadratic sum of the statistical and systematic uncertainties. Uncertainties on the fitted yields are symmetric by construction, where the negative error is truncated when reaching to zero event yield.

Yields in regions	**CRT**	**CRW**	**SRAsb**	**SRBsb**	**SRAh**	**SRBh**
Observed events	691	1592	15	11	6	3
MC yields after fit	680.91 ± 25.75	1602.91 ± 39.21	14.63 ± 2.38	9.12 ± 1.80	6.48 ± 1.28	3.07 ± 0.81
$t\bar{t}$	643.95 ± 26.26	703.18 ± 53.03	8.20 ± 2.33	3.24 ± 1.35	4.29 ± 1.24	1.41 ± 0.66
W+jets	12.50 ± 2.37	701.89 ± 58.73	3.16 ± 0.67	1.97 ± 0.50	0.55 ± 0.28	0.34 ± 0.14
Single top s	0.82 ± 0.15	3.02 ± 0.32	0.00 ± 0.00	0.00 ± 0.00	0.00 ± 0.00	0.00 ± 0.00
Single top t	2.79 ± 0.99	20.90 ± 2.88	$0.29^{+0.30}_{-0.29}$	$0.04^{+0.08}_{-0.04}$	0.20 ± 0.04	0.00 ± 0.00
Singe top Wt	16.87 ± 3.35	93.83 ± 13.01	1.65 ± 0.53	2.56 ± 1.17	1.15 ± 0.37	0.79 ± 0.40
Diboson	1.98 ± 0.35	68.41 ± 7.53	1.15 ± 0.46	0.91 ± 0.54	0.00 ± 0.00	0.27 ± 0.06
Z+jets	0.45 ± 0.11	6.65 ± 0.59	0.03 ± 0.01	0.10 ± 0.05	0.02 ± 0.01	0.02 ± 0.01
ZH	0.01 ± 0.00	0.03 ± 0.00	$0.00^{+0.00}_{-0.00}$	0.00 ± 0.00	0.00 ± 0.00	0.00 ± 0.00
WH	0.42 ± 0.04	3.88 ± 0.26	0.09 ± 0.01	0.05 ± 0.01	0.26 ± 0.03	0.13 ± 0.02
$t\bar{t}V$	1.12 ± 0.28	1.13 ± 0.27	0.06 ± 0.02	0.24 ± 0.06	0.01 ± 0.00	0.11 ± 0.03
MC yields before fit	577.74 ± 102.51	1695.73 ± 93.47	12.49 ± 3.57	7.86 ± 2.26	5.39 ± 1.87	2.44 ± 1.01
$t\bar{t}$	540.97 ± 101.75	665.84 ± 92.63	6.21 ± 3.29	2.07 ± 1.59	3.26 ± 1.73	0.98 ± 0.83
W+jets	13.90 ± 2.36	833.28 ± 3.15	3.56 ± 0.70	2.22 ± 0.57	0.58 ± 0.35	0.34 ± 0.15
Single top s	0.74 ± 0.18	3.06 ± 0.34	0.00 ± 0.00	0.00 ± 0.00	0.00 ± 0.00	0.00 ± 0.00
Single top t	2.44 ± 1.01	20.04 ± 2.89	$0.19^{+0.24}_{-0.19}$	$0.14^{+0.27}_{-0.14}$	0.19 ± 0.04	0.00 ± 0.00
Singe top Wt	16.02 ± 3.42	93.20 ± 13.79	1.41 ± 0.56	2.09 ± 1.17	1.09 ± 0.40	0.60 ± 0.37
Diboson	1.79 ± 0.46	68.80 ± 8.66	0.95 ± 0.46	0.95 ± 0.69	0.00 ± 0.00	0.25 ± 0.06
Z+jets	0.39 ± 0.11	6.56 ± 0.69	0.03 ± 0.01	0.09 ± 0.05	0.02 ± 0.01	0.02 ± 0.01
ZH	0.01 ± 0.00	0.03 ± 0.00	$0.00^{+0.00}_{-0.00}$	0.00 ± 0.00	0.00 ± 0.00	0.00 ± 0.00
WH	0.39 ± 0.05	3.81 ± 0.32	0.08 ± 0.02	0.05 ± 0.01	0.24 ± 0.04	0.13 ± 0.02
$t\bar{t}V$	1.07 ± 0.28	1.13 ± 0.28	0.06 ± 0.02	0.24 ± 0.07	0.01 ± 0.01	0.11 ± 0.03

C.1.2 Distributions before and after background-only fit

This section shows event distributions of background-only fits. The stacked background histograms of the single top samples (s-channel, t-channel, and Wt-channel) have been grouped into "Single top" and the negligible backgrounds $t\bar{t}V$, WH and ZH are grouped as well. The hashed areas represent the total uncertainties on the background estimates. The vertical bars on the data point account for the statistical uncertainty. The lower panels show the ratio of the data to the SM background prediction. The distributions of two signal points from the simplified model grid, $m(\tilde{\chi}_1^{\pm}\tilde{\chi}_2^0, \tilde{\chi}_1^0)$ = (130,0) GeV and $m(\tilde{\chi}_1^{\pm}\tilde{\chi}_2^0, \tilde{\chi}_1^0)$ = (250,0) GeV, are overlaid – not stacked – on the background for information.

Figures C.3 to C.5 show the event distributions in CRT, CRW, VRA, VRB, SRA and SRB before and after the unblinded fit (corresponding to the published version of the analysis). The reduction of systematic uncertainties after fit is visible in the reduced hashed areas.

Figures C.6 to C.8 show the event distributions in the same control, validation and signal regions before and after the unblinded fit performed using m_{bb}^{corr} as discriminating variables. For this fit setup, regions are defined using the same cuts as in the published analysis but on the m_{bb}^{corr} and $m_{\mathrm{CT}}^{\mathrm{corr}}$ variables.

C.1.3 Distributions before final cut

The validation of the extrapolation is shown in the event distributions in Figures C.9 to C.12.

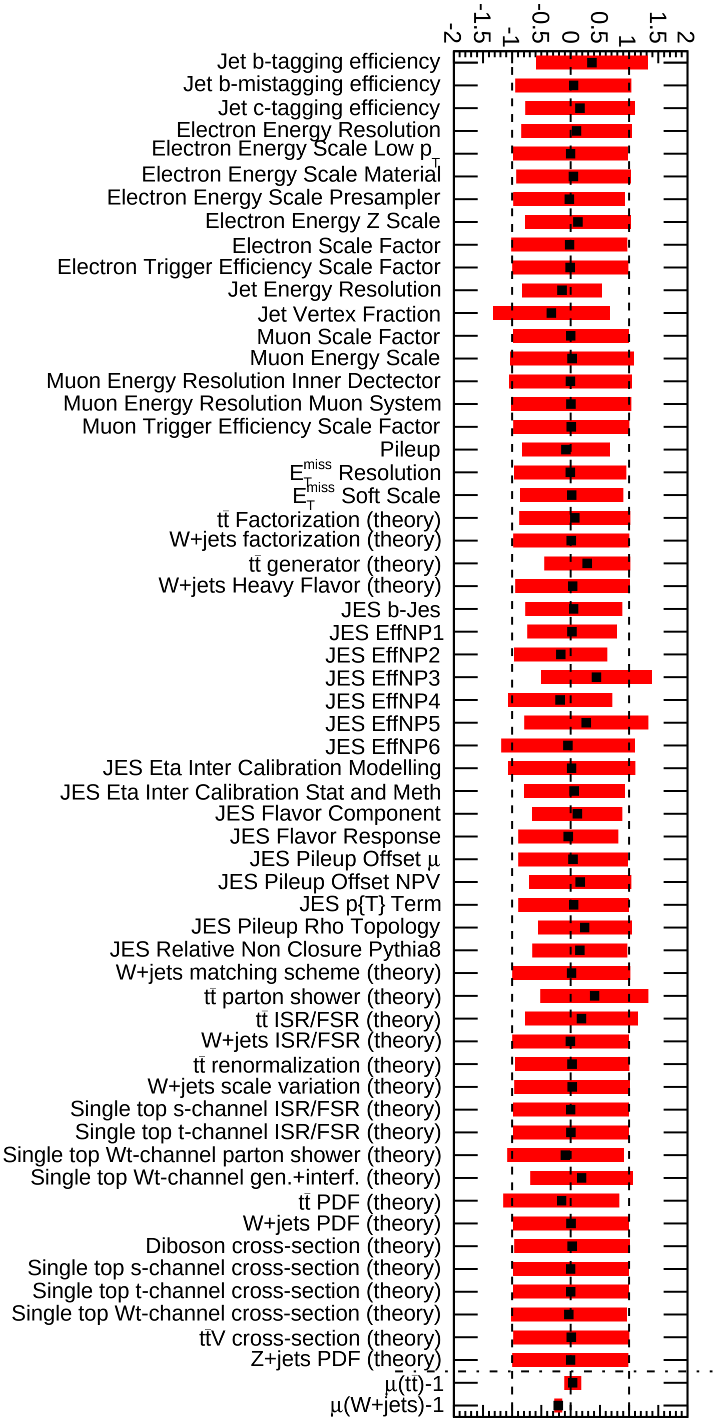

Figure C.1: Fit results for the nuisance parameters and the normalization factors $\mu_{t\bar{t}}$ and $\mu_{W\text{+jets}}$, in the background-only fit.

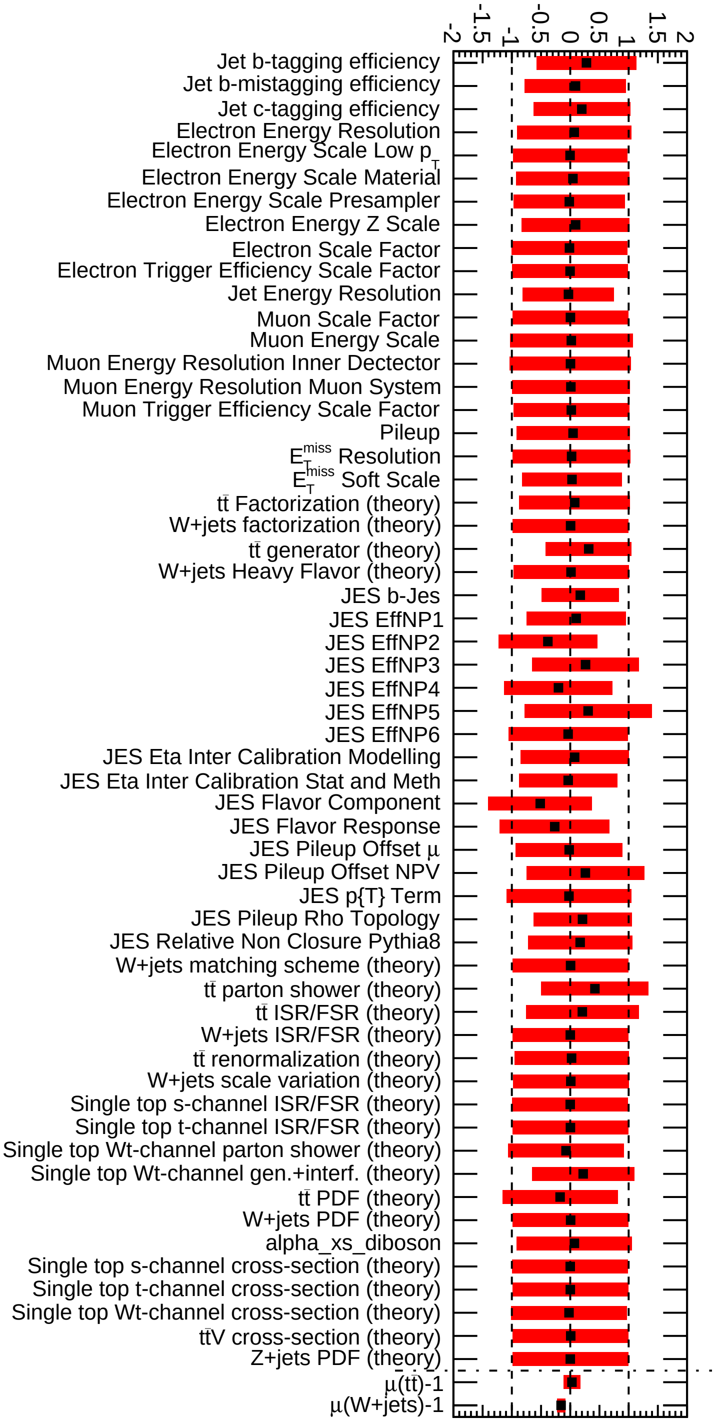

Figure C.2: Fit results for the nuisance parameters and the normalization factors $\mu_{t\bar{t}}$ and $\mu_{W\text{+jets}}$, in the background-only fit using m_{bb}^{corr} as discriminating variable.

Table C.5: Breakdown of the systematic uncertainties on background estimates after fit, with $\boldsymbol{m_{bb}}$ as discriminating variable. More information in text.

Uncertainty of channel(s)	**CRT**	**CRW**	**VRA**	**VRB**	**SRAh**	**SRBh**
Total background expectation	641.52	1557.60	874.17	243.21	5.69	2.67
Total statistical ($\sqrt{N_{\mathrm{exp}}}$)	±25.33	±39.47	±29.57	±15.60	±2.38	±1.63
Total background systematic	±24.91	±38.63	±84.58	±16.70	±1.10	±0.69
[in %]	[3.88%]	[2.48%]	[9.68%]	[6.87%]	[19.40%]	[25.71%]
$t\bar{t}$ normalization (fit)	±84.78	±94.49	±94.81	±19.43	±0.50	±0.18
$t\bar{t}$ parton shower (theory)	±80.03	±61.34	±7.91	±11.70	±0.31	±0.17
$t\bar{t}$ generator (theory)	±32.05	±32.54	±34.96	±12.77	±1.09	±0.57
$t\bar{t}$ ISR/FSR (theory)	±30.43	±22.36	±9.40	±1.42	±0.39	±0.14
Jet Energy Scale	±28.04	±21.41	±22.47	±1.63	±0.36	±0.35
Jet b-tagging efficiency	±13.17	±7.96	±17.99	±1.24	±0.06	±0.05
Jet Vertex Fraction	±7.73	±11.19	±3.86	±0.22	±0.03	±0.01
$t\bar{t}$ PDF (theory)	±5.97	±5.36	±6.68	±1.82	±0.09	±0.05
Electron reconstruction	±2.92	±2.89	±3.41	±1.14	±0.14	±0.09
Single top (Wt) parton shower (theory)	±2.42	±8.20	±0.45	±1.74	±0.13	±0.01
$E_{\mathrm{T}}^{\mathrm{miss}}$ Soft Scale	±2.41	±7.26	±1.96	±1.68	±0.16	±0.07
Single top (Wt) gen.+$WWbb$ (theory)	±1.48	±5.20	±1.83	±1.46	±0.25	±0.31
$t\bar{t}$ renormalization (theory)	±1.25	±0.78	±22.65	±0.95	±0.33	±0.05
Single top (Wt) cross-section (theory)	±1.09	±5.98	±2.30	±1.47	±0.07	±0.05
W+jets normalization (fit)	±0.96	±59.80	±8.55	±5.37	±0.05	±0.02
Muon reconstruction	±0.92	±1.49	±1.00	±0.36	±0.07	±0.02
Jet Energy Resolution	±0.84	±0.06	±2.26	±1.00	±0.06	±0.11
Luminosity	±0.66	±5.21	±2.68	±1.16	±0.04	±0.03
W+jets factorization (theory)	±0.58	±0.57	±5.20	±4.69	±0.04	±0.02
$t\bar{t}$ factorization (theory)	±0.57	±0.36	±13.82	±0.24	±0.48	±0.16
Single top (t) ISR/FSR (theory)	±0.28	±2.15	±3.11	±0.55	±0.02	±0.00
Jet c-tagging efficiency	±0.27	±5.73	±16.62	±13.95	±0.33	±0.11
$E_{\mathrm{T}}^{\mathrm{miss}}$ Resolution	±0.24	±0.81	±1.42	±0.43	±0.10	±0.08
$t\bar{t}V$ cross-section (theory)	±0.24	±0.23	±0.13	±0.05	±0.00	±0.03
Jet b-mistagging efficiency	±0.18	±1.91	±2.37	±1.61	±0.04	±0.01
Diboson cross-section (theory)	±0.15	±4.43	±0.70	±0.62	±0.00	±0.01
Pileup	±0.13	±0.53	±1.05	±0.16	±0.05	±0.04
Single top (t) cross-section (theory)	±0.10	±0.76	±1.10	±0.19	±0.01	±0.00
Single top (s) ISR/FSR (theory)	±0.05	±0.21	±1.25	±0.02	±0.00	±0.00
Single top (s) cross-section (theory)	±0.03	±0.11	±0.67	±0.01	±0.00	±0.00
W+jets PDF (theory)	±0.02	±0.02	±0.44	±0.16	±0.01	±0.01
Z+jets PDF (theory)	±0.01	±0.34	±0.12	±0.03	±0.00	±0.00
W+jets Heavy Flavor (theory)	±0.00	±0.00	±0.00	±0.00	±0.00	±0.00
Shape (statistical)	±0.00	±0.00	±0.00	±1.08	±0.48	±0.33
W+jets scale variation (theory)	±0.00	±0.00	±0.00	±0.00	±0.00	±0.00
W+jets ISR/FSR (theory)	±0.00	±0.00	±0.00	±0.00	±0.00	±0.00
W+jets parton shower/ME (theory)	±0.00	±0.00	±0.00	±0.00	±0.00	±0.00

Table C.6: Breakdown of the systematic uncertainties on background estimates after fit, with $\boldsymbol{m}_{\boldsymbol{bb}}^{\text{corr}}$ as discriminating variable. More information in text.

Uncertainty of channel(s)	**CRT**	**CRW**	**VRA**	**VRB**	**SRAh**	**SRBh**
Total background expectation	680.91	1602.91	913.52	261.86	6.48	3.07
Total statistical ($\sqrt{N_{\text{exp}}}$)	±26.09	±40.04	±30.22	±16.18	±2.55	±1.75
Total background systematic	±25.75	±39.21	±90.94	±18.89	±1.28	±0.81
[in %]	[3.78%]	[2.45%]	[9.96%]	[7.21%]	[19.69%]	[26.34%]
$t\bar{t}$ normalization (fit)	±89.92	±98.19	±98.86	±20.12	±0.60	±0.20
$t\bar{t}$ parton shower (theory)	±84.66	±63.60	±8.23	±12.09	±0.37	±0.19
$t\bar{t}$ generator (theory)	±34.03	±33.86	±36.49	±13.21	±1.30	±0.64
$t\bar{t}$ ISR/FSR (theory)	±32.25	±23.22	±9.79	±1.47	±0.47	±0.15
Jet Energy Scale	±25.92	±23.31	±29.14	±2.31	±0.40	±0.46
Jet b-tagging efficiency	±13.59	±8.41	±21.12	±3.11	±0.06	±0.06
$t\bar{t}$ PDF (theory)	±6.30	±5.60	±6.92	±1.89	±0.11	±0.06
Electron reconstruction	±2.96	±3.09	±3.75	±1.16	±0.15	±0.10
Single top (Wt) parton shower (theory)	±2.51	±8.65	±0.45	±1.82	±0.14	±0.01
$E_{\mathrm{T}}^{\text{miss}}$ Soft Scale	±2.30	±7.80	±2.07	±1.90	±0.15	±0.09
Single top (Wt) gen.+$WWbb$ (theory)	±1.54	±5.49	±1.84	±1.53	±0.26	±0.33
$t\bar{t}$ renormalization (theory)	±1.33	±0.81	±23.62	±0.98	±0.39	±0.05
Single top (Wt) cross-section (theory)	±1.14	±6.33	±2.31	±1.54	±0.08	±0.05
W+jets Heavy Flavor (theory)	±1.07	±0.94	±10.42	±7.61	±0.06	±0.04
W+jets normalization (fit)	±1.05	±59.05	±8.98	±6.21	±0.05	±0.03
Muon reconstruction	±0.90	±1.55	±1.08	±0.33	±0.09	±0.06
Jet Energy Resolution	±0.82	±0.12	±3.06	±1.87	±0.03	±0.18
Pileup	±0.70	±0.89	±1.84	±0.83	±0.16	±0.03
Luminosity	±0.68	±5.50	±2.75	±1.22	±0.05	±0.04
$t\bar{t}$ factorization (theory)	±0.60	±0.37	±14.38	±0.25	±0.58	±0.18
W+jets scale variation (theory)	±0.57	±0.50	±3.09	±6.16	±0.04	±0.03
$E_{\mathrm{T}}^{\text{miss}}$ Resolution	±0.49	±1.70	±1.34	±0.43	±0.01	±0.16
Jet c-tagging efficiency	±0.48	±4.98	±16.78	±13.25	±0.33	±0.10
W+jets factorization (theory)	±0.39	±0.34	±2.57	±3.88	±0.03	±0.02
W+jets matching scheme (theory)	±0.36	±0.32	±2.14	±3.77	±0.02	±0.02
Single top (t) ISR/FSR (theory)	±0.30	±2.28	±3.21	±0.55	±0.02	±0.00
$t\bar{t}V$ cross-section (theory)	±0.25	±0.26	±0.14	±0.05	±0.00	±0.03
Jet b-mistagging efficiency	±0.25	±1.72	±2.28	±1.06	±0.04	±0.01
Diboson cross-section (theory)	±0.14	±4.71	±0.73	±0.67	±0.00	±0.02
Single top (t) cross-section (theory)	±0.11	±0.81	±1.14	±0.20	±0.01	±0.00
Single top (s) ISR/FSR (theory)	±0.06	±0.22	±1.32	±0.02	±0.00	±0.00
W+jets ISR/FSR (theory)	±0.06	±0.05	±0.36	±0.58	±0.00	±0.00
Single top (s) cross-section (theory)	±0.03	±0.12	±0.71	±0.01	±0.00	±0.00
W+jets PDF (theory)	±0.02	±0.02	±0.47	±0.19	±0.01	±0.01
Z+jets PDF (theory)	±0.02	±0.32	±0.12	±0.04	±0.00	±0.00
Shape (statistical)	±0.00	±0.00	±0.00	±0.99	±0.54	±0.40
Jet Vertex Fraction	±0.00	±0.00	±0.00	±0.00	±0.00	±0.00

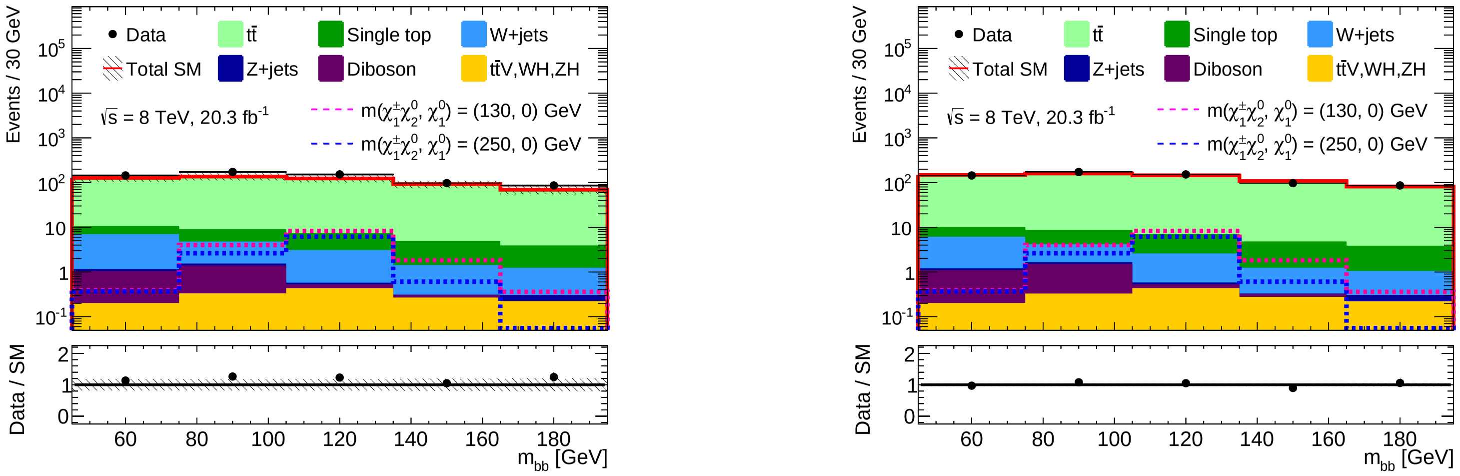

(a) m_{bb} distribution in CRT before fit.

(b) m_{bb} distribution in CRT after fit.

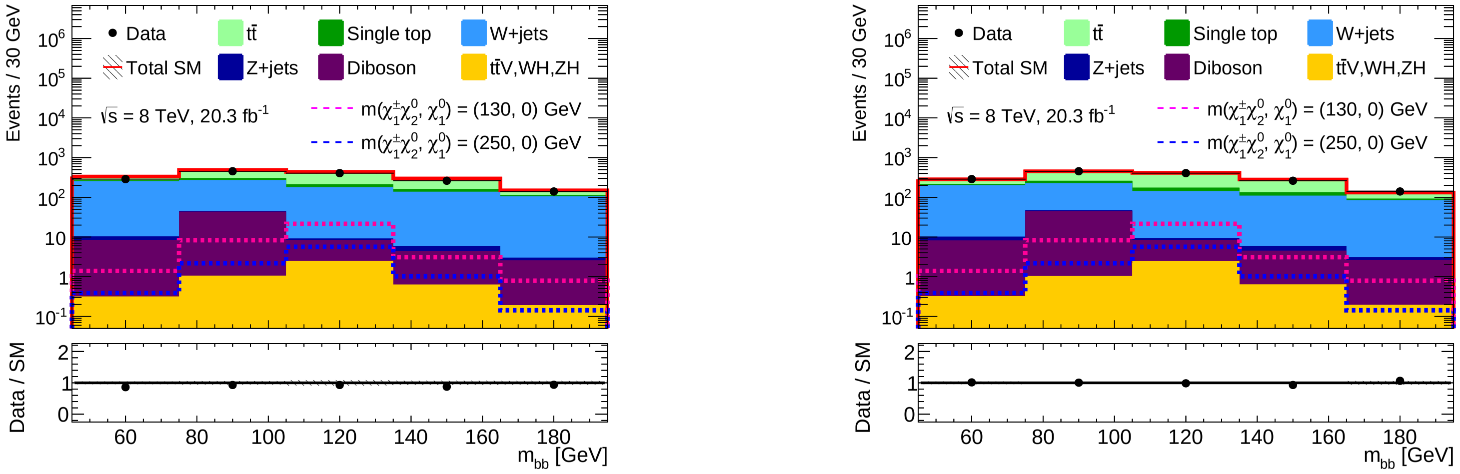

(c) m_{bb} distribution in CRW before fit.

(d) m_{bb} distribution in CRW after fit.

Figure C.3: m_{bb} distributions in the CRs before (left) and after (right) the unblinded background-only fit.

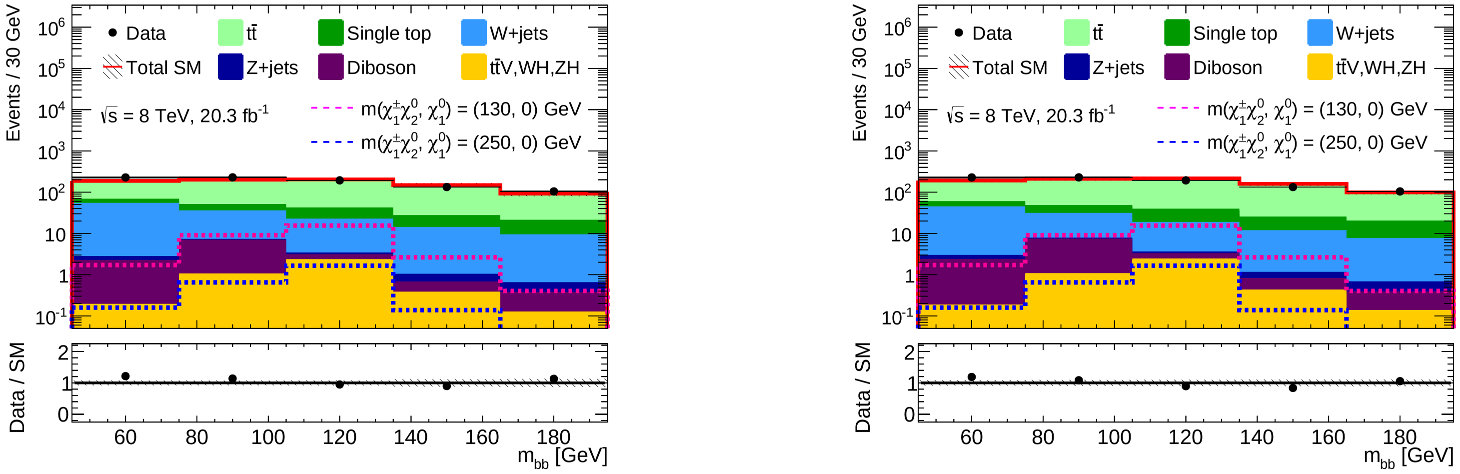

(a) m_{bb} distribution in VRA before fit.

(b) m_{bb} distribution in VRA after fit.

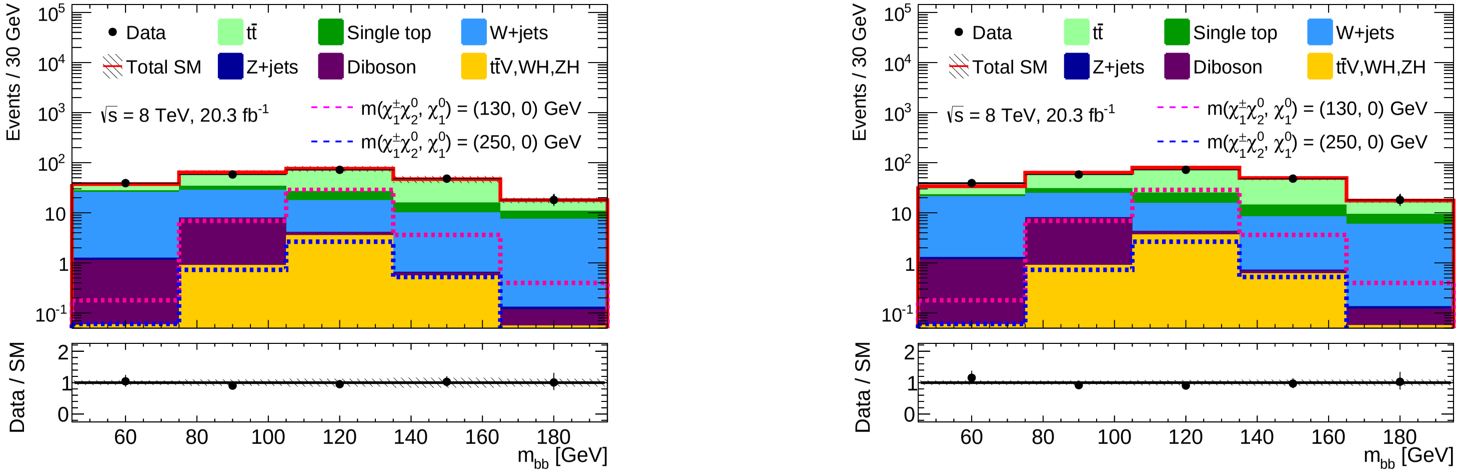

(c) m_{bb} distribution in VRB before fit.

(d) m_{bb} distribution in VRB after fit.

Figure C.4: m_{bb} distributions in the VRs before (left) and after (right) the unblinded background-only fit.

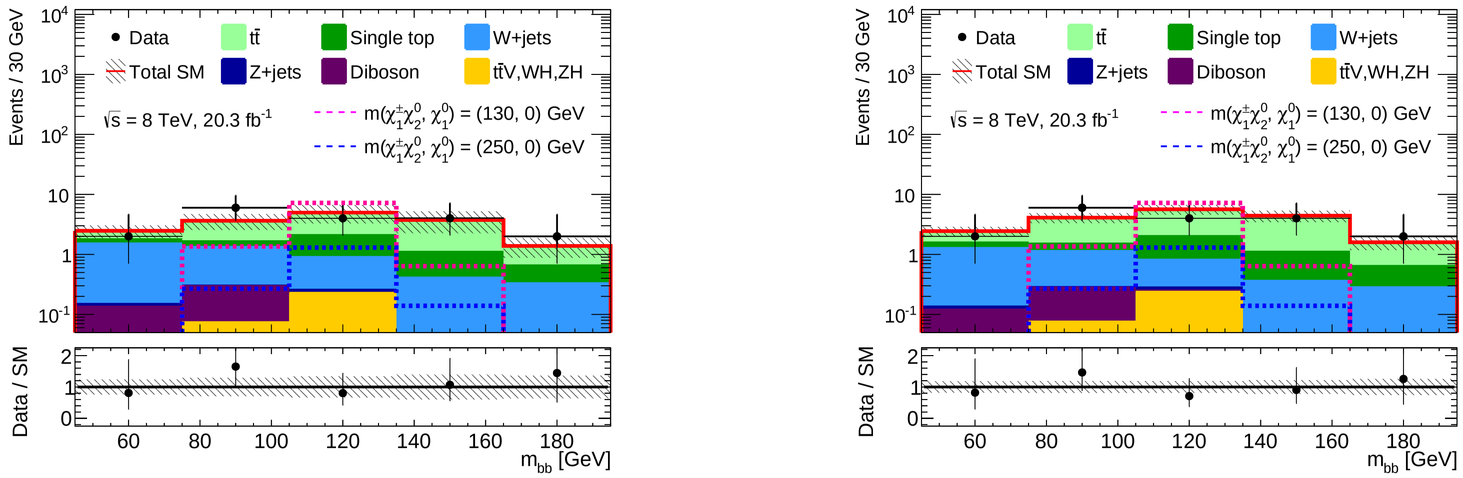

(a) m_{bb} distribution in SRA before fit.

(b) m_{bb} distribution in SRA after fit.

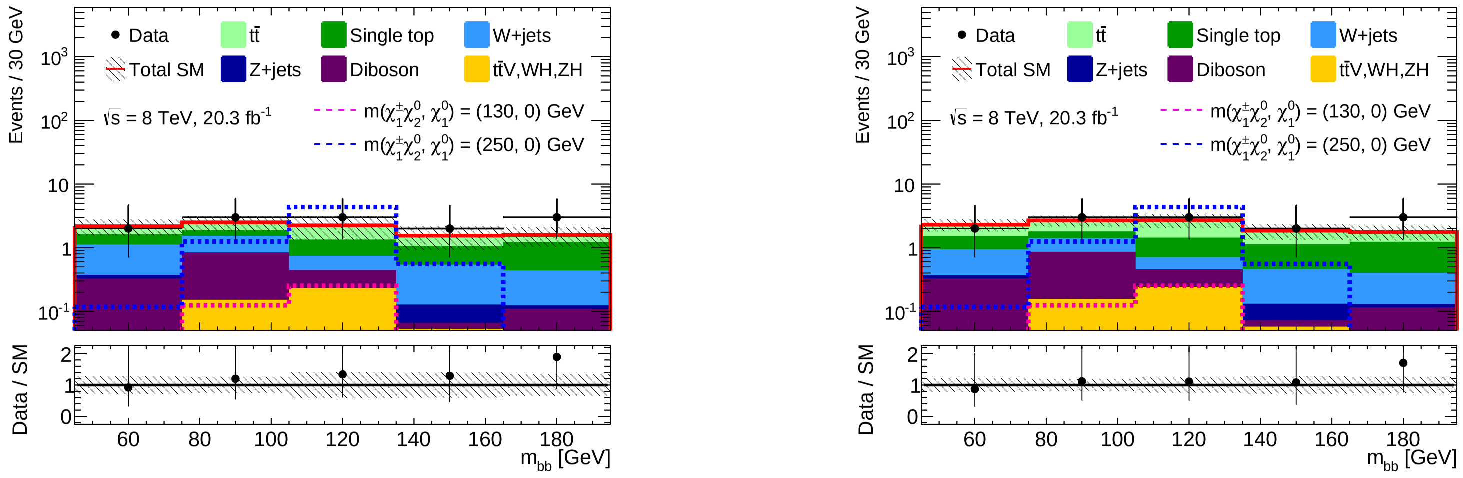

(c) m_{bb} distribution in SRB before fit.

(d) m_{bb} distribution in SRB after fit.

Figure C.5: m_{bb} distributions in the SRs before (left) and after (right) the unblinded background-only fit.

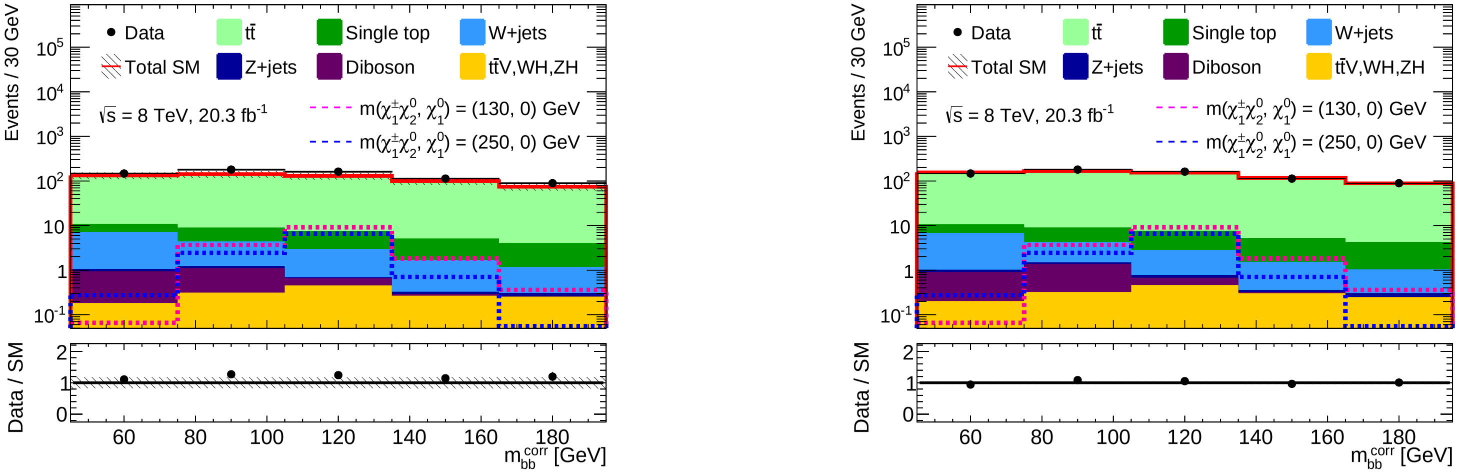

(a) m_{bb}^{corr} distribution in CRT before fit.

(b) m_{bb}^{corr} distribution in CRT after fit.

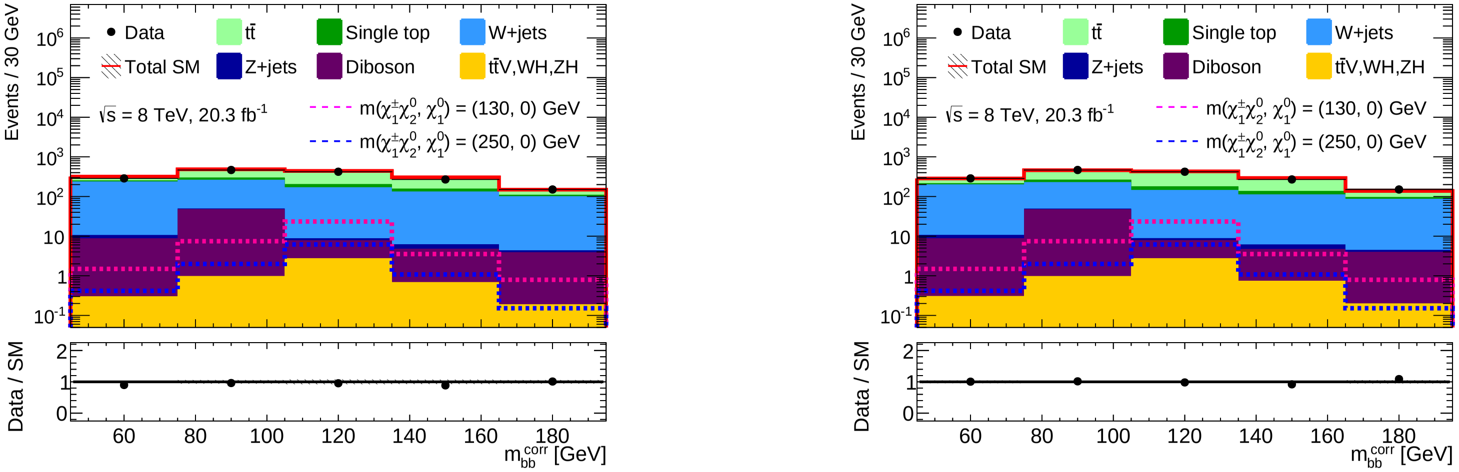

(c) m_{bb}^{corr} distribution in CRW before fit.

(d) m_{bb}^{corr} distribution in CRW after fit.

Figure C.6: m_{bb}^{corr} distributions in the CRs before (left) and after (right) the unblinded background-only fit.

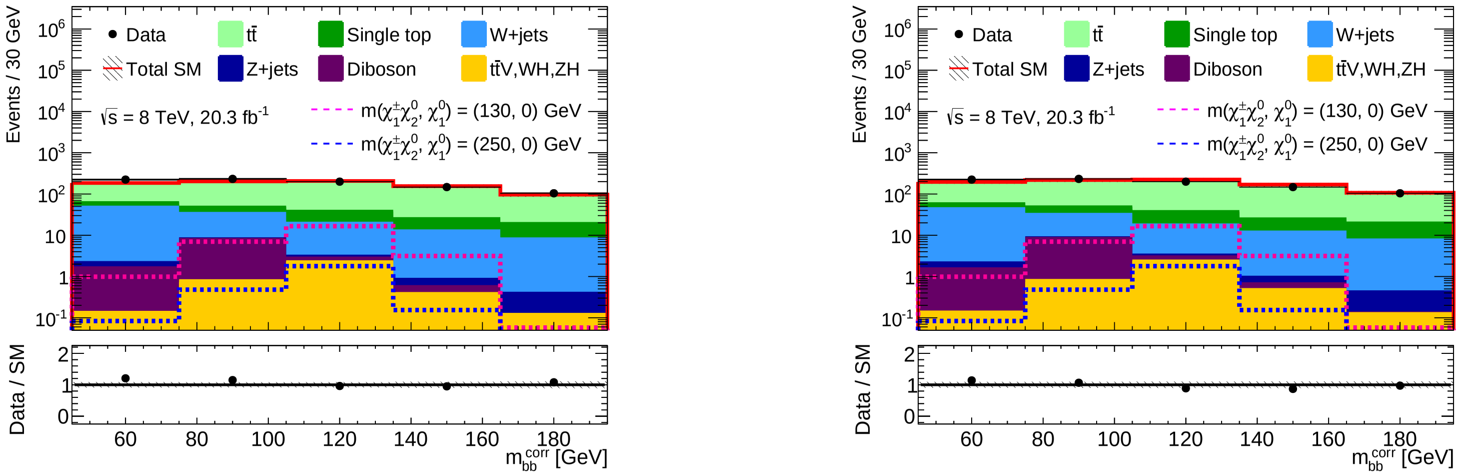

(a) m_{bb}^{corr} distribution in VRA before fit.

(b) m_{bb}^{corr} distribution in VRA after fit.

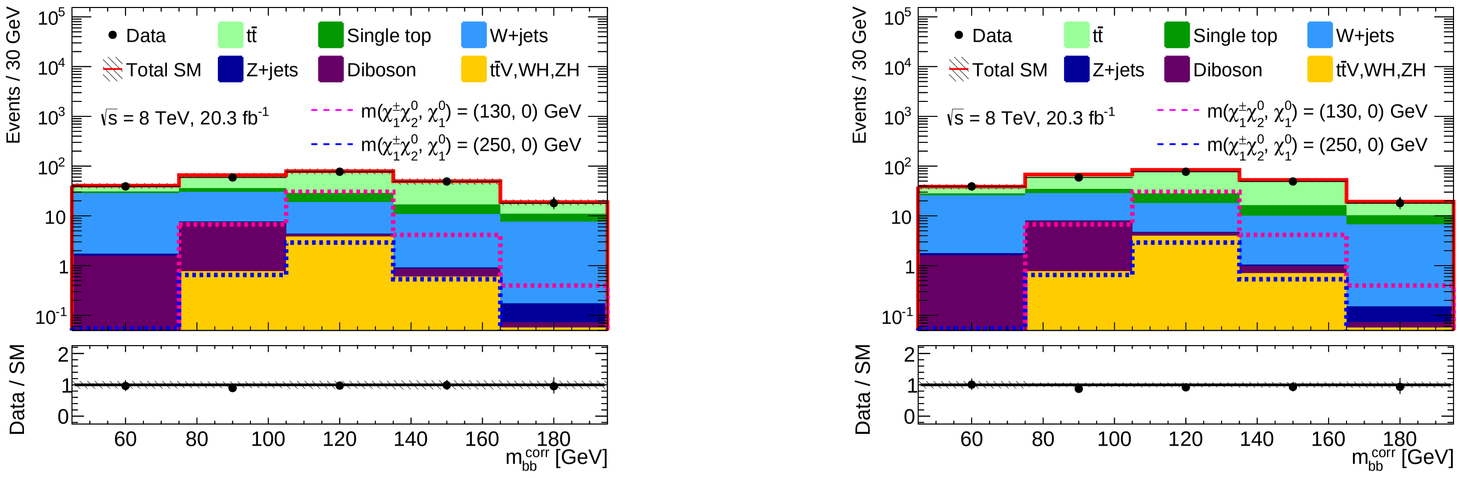

(c) m_{bb}^{corr} distribution in VRB before fit.

(d) m_{bb}^{corr} distribution in VRB after fit.

Figure C.7: m_{bb}^{corr} distributions in the VRs before (left) and after (right) the unblinded background-only fit.

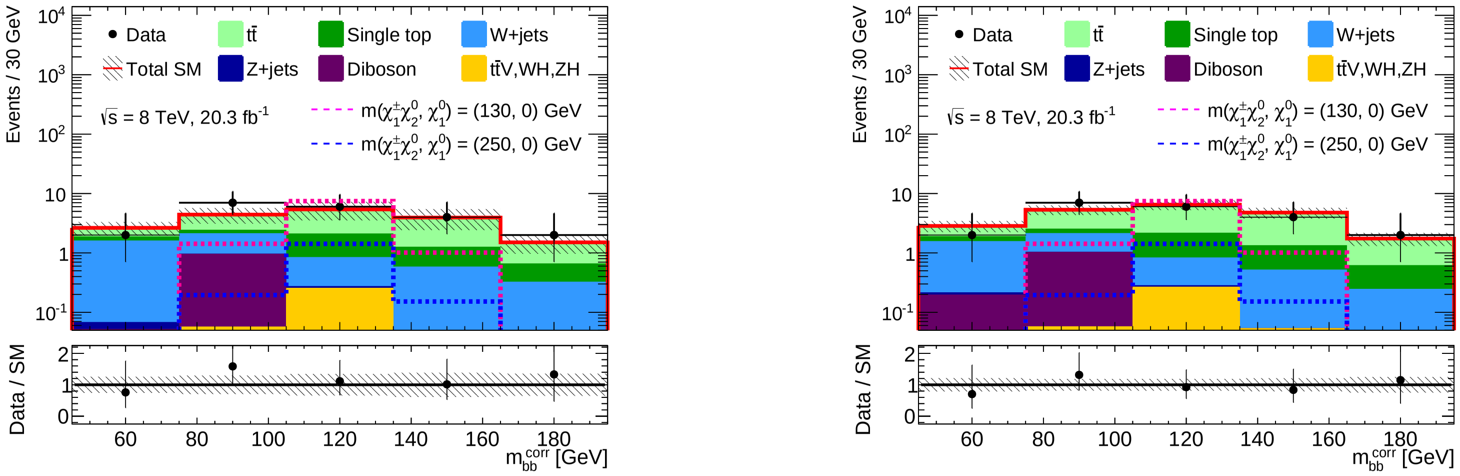

(a) m_{bb}^{corr} distribution in SRA before fit.

(b) m_{bb}^{corr} distribution in SRA after fit.

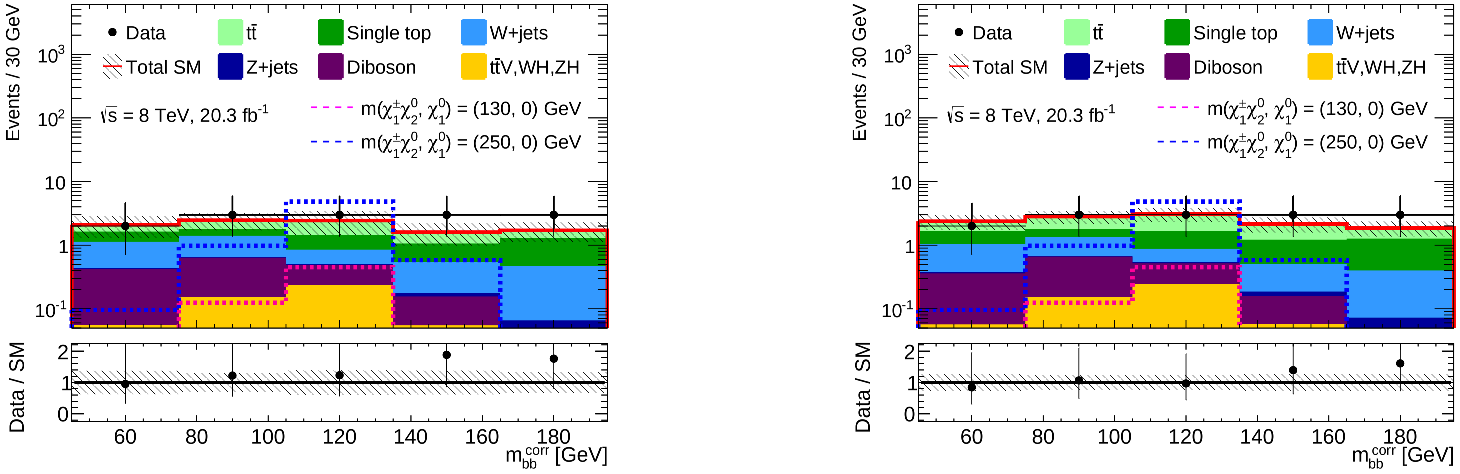

(c) m_{bb}^{corr} distribution in SRB before fit.

(d) m_{bb}^{corr} distribution in SRB after fit.

Figure C.8: m_{bb}^{corr} distributions in the SRs before (left) and after (right) the unblinded background-only fit.

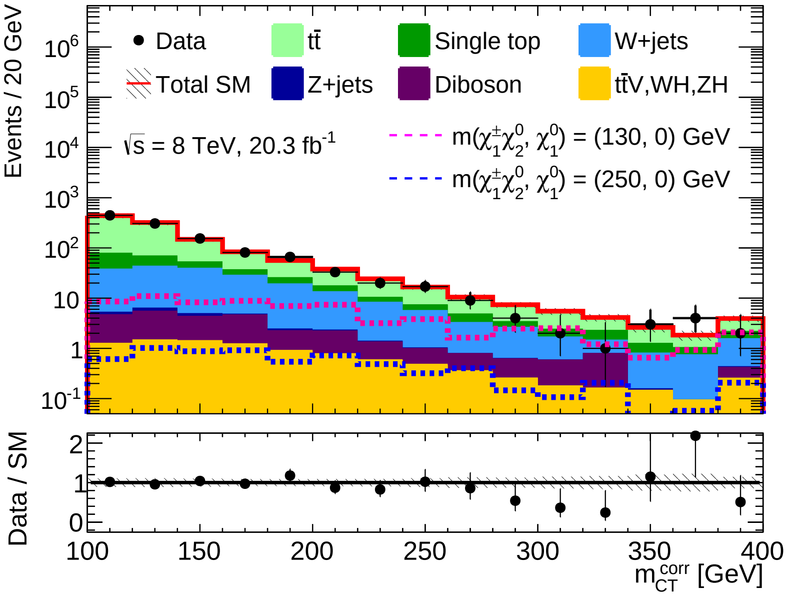

(a) $m_{\mathrm{CT}}^{\mathrm{corr}}$ distribution in VRA+VRB.

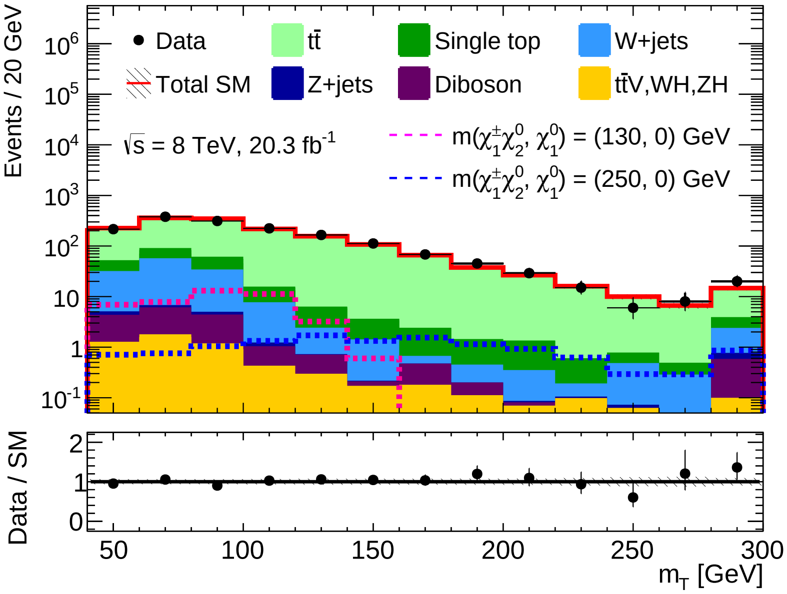

(b) m_{T} distribution in VRA+CRT.

Figure C.9: Distributions of $m_{\mathrm{CT}}^{\mathrm{corr}}$ (top) and m_{T} (bottom) after the background-only fit in VRA+VRB and VRA+CRT respectively. The rightmost bin includes overflow.

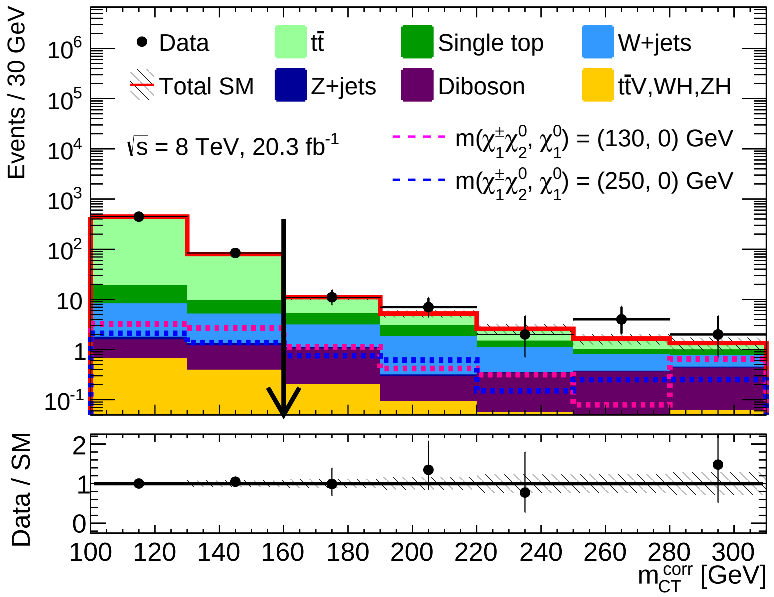

(a) $m_{\mathrm{CT}}^{\mathrm{corr}}$ distribution in CRT+SRAsb+SRBsb.

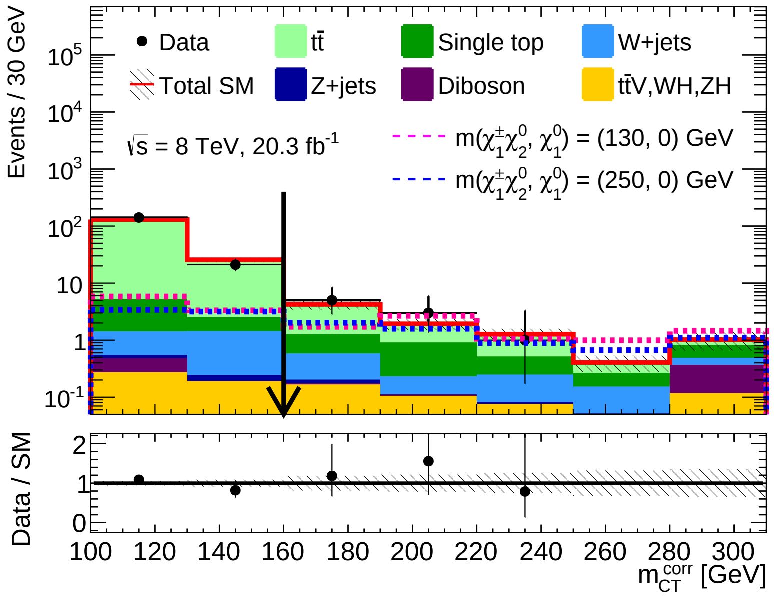

(b) $m_{\mathrm{CT}}^{\mathrm{corr}}$ distribution in CRT+SRAh+SRBh.

Figure C.10: Distributions of $m_{\mathrm{CT}}^{\mathrm{corr}}$ extrapolated from CRT to SRAsb+SRBsb (top) and SRAh+SRBh (bottom) after the background-only fit. The vertical arrows indicate the lower boundary of the signal regions. The rightmost bin includes overflow.

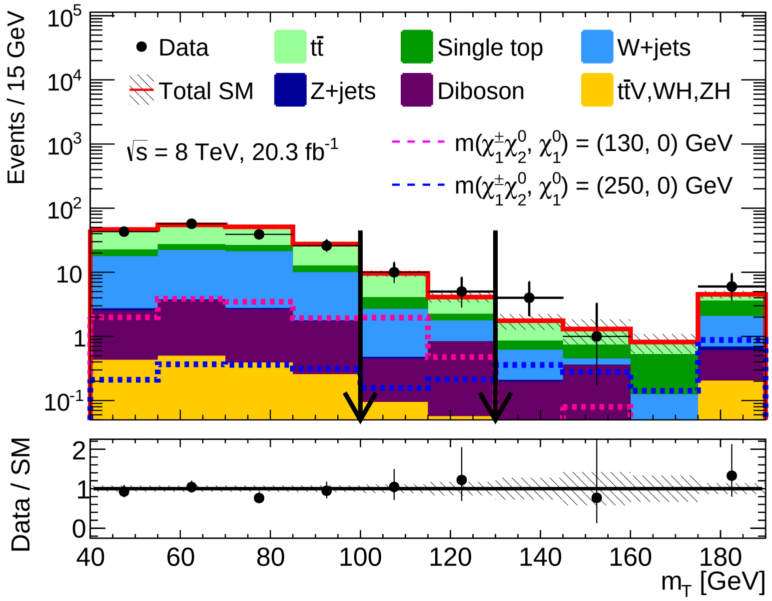

(a) m_{T} distribution in VRB+SRAsb+SRBsb.

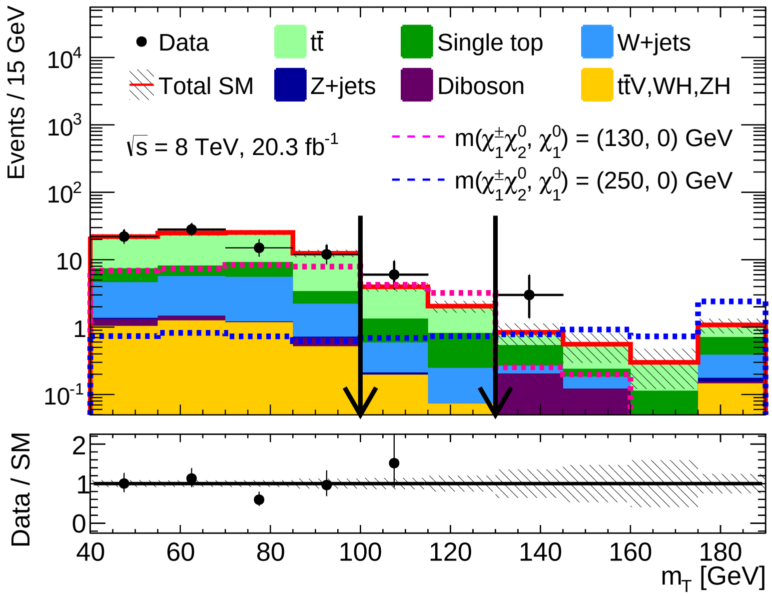

(b) m_{T} distribution in VRB+SRAh+SRBh.

Figure C.11: Distributions of m_{T} extrapolated from VRB to SRAsb+SRBsb (top) and SRAh+SRBh (bottom) after the background-only fit. The region between the two vertical arrows corresponds to SRA. The right vertical arrow indicates the lower boundary of SRB. The rightmost bin includes overflow.

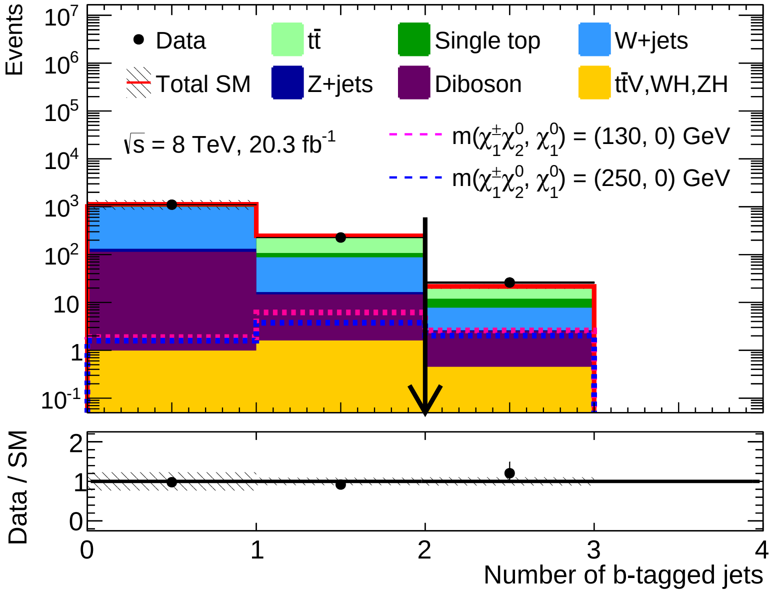

(a) Distribution of the b-jet multiplicity in the signal sidebands.

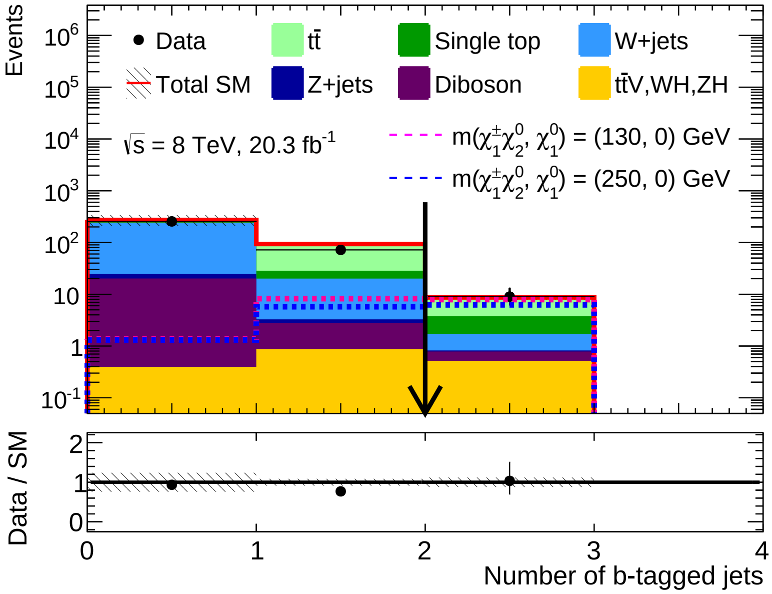

(b) Distribution of the b-jet multiplicity in the central bin.

Figure C.12: Distribution of the b-jet multiplicity after the background-only fit in a region defined by the union of SRA+SRB but without the b-jet multiplicity requirement applied. The rightmost bin after the arrow corresponds to the actual definition of SRAsb+SRBsb (top) and SRAh+SRBh (bottom), with $n^{b\text{-jet}} = 2$. The regions are defined using m_{bb}^{corr} and $m_{\text{CT}}^{\text{corr}}$.

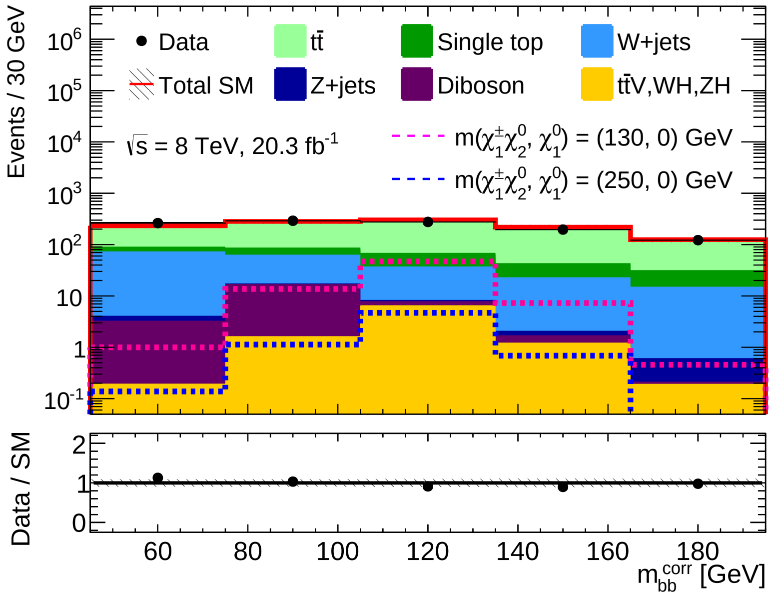

(a) m_{bb}^{corr} distribution in VRA+VRB.

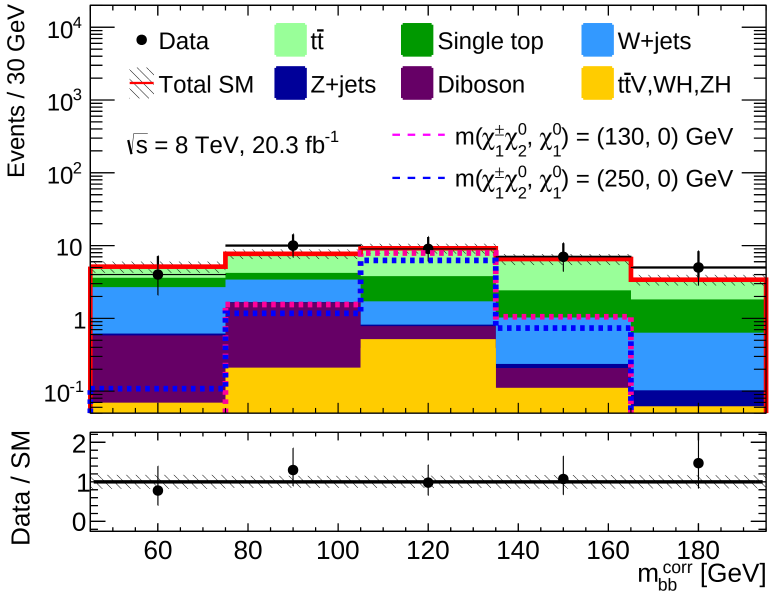

(b) m_{bb}^{corr} distribution in SRA+SRB.

Figure C.13: Distributions of m_{bb}^{corr} after the background-only fit in the union of validation regions VRA+VRB (top) and signal region SRA+SRB (bottom) over the five bins, *i.e.* the four sideband bins and the central signal bin.

C.2 Results of the model-dependent fits

This section provides additional figures that complete the ones presented in Section 8.3.3. For the model-dependent fits performed with the simplified model, the 95% CL exclusion region in the $m(\tilde{\chi}_1^0) - m(\tilde{\chi}_1^\pm, \tilde{\chi}_2^0)$ mass plane is shown in Figure C.14, with the expected and observed CL_s indicated for each signal point. Figure C.15 displays the exclusion region for the analysis performed with the corrected di-jet mass m_{bb}^{corr}. Expected and observed CL_s values are also shown. The exclusion results for the pMSSM grid are shown in Figure C.16 and C.17 for the published analysis with m_{bb} and the corrected version with m_{bb}^{corr}, respectively. Upper limits on the normalized signal cross section $\sigma/\sigma^{\mathrm{SUSY}}$ for the simplified model and pMSSM grids are shown in Figure C.18.

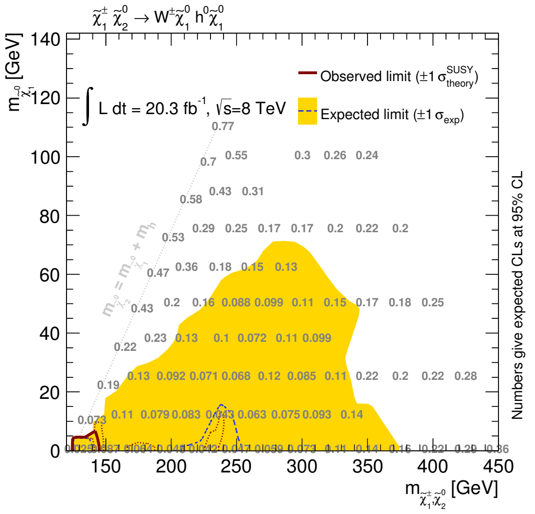

(a) Expected CL$_s$ at 95% CL. (b) Observed CL$_s$ at 95% CL.

Figure C.14: Exclusion in the $m(\tilde{\chi}_1^{\pm}, \tilde{\chi}_2^0) - m(\tilde{\chi}_1^0)$ mass plane for the published version of the analysis that uses m_{bb}. The grey numbers indicate the expected (left) and observed (right) CL$_s$ values obtained from the model-dependent fit.

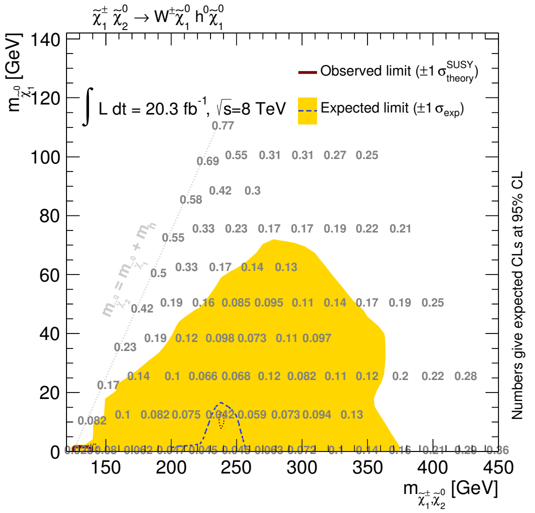

(a) Expected CL$_s$ at 95% CL. (b) Observed CL$_s$ at 95% CL.

Figure C.15: Exclusion in the $m(\tilde{\chi}_1^{\pm}, \tilde{\chi}_2^0) - m(\tilde{\chi}_1^0)$ mass plane for the corrected version of the analysis that uses m_{bb}^{corr}. The grey numbers indicate the expected (left) and observed (right) CL$_s$ values obtained from the model-dependent fit.

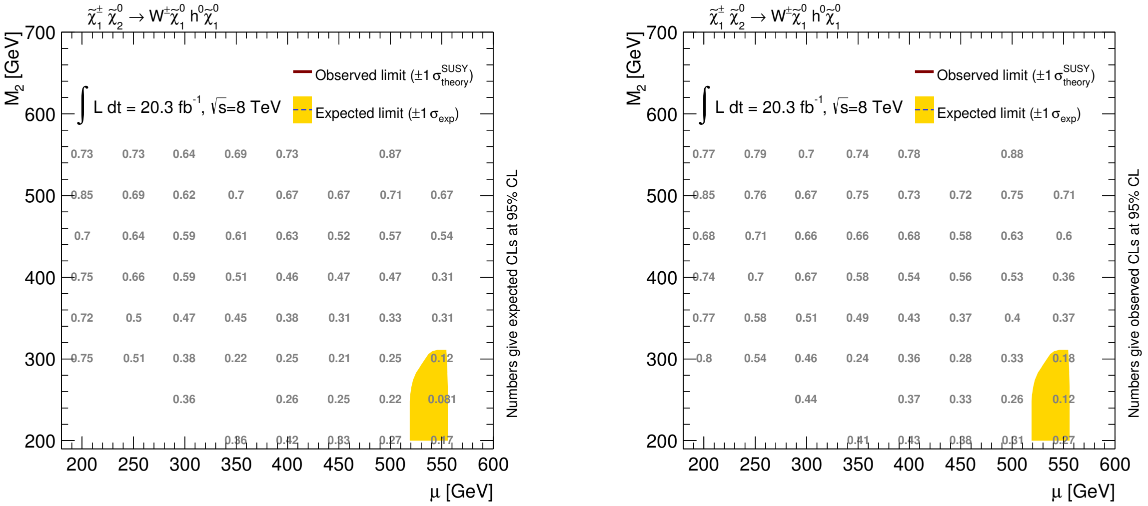

(a) Expected CL$_s$ at 95% CL.

(b) Observed CL$_s$ at 95% CL.

Figure C.16: Exclusion in the $mu - M_2$ plane for the published version of the analysis that uses m_{bb}^{corr}. The grey numbers indicate the expected (left) and observed (right) CL$_s$ values obtained from the model-dependent fit.

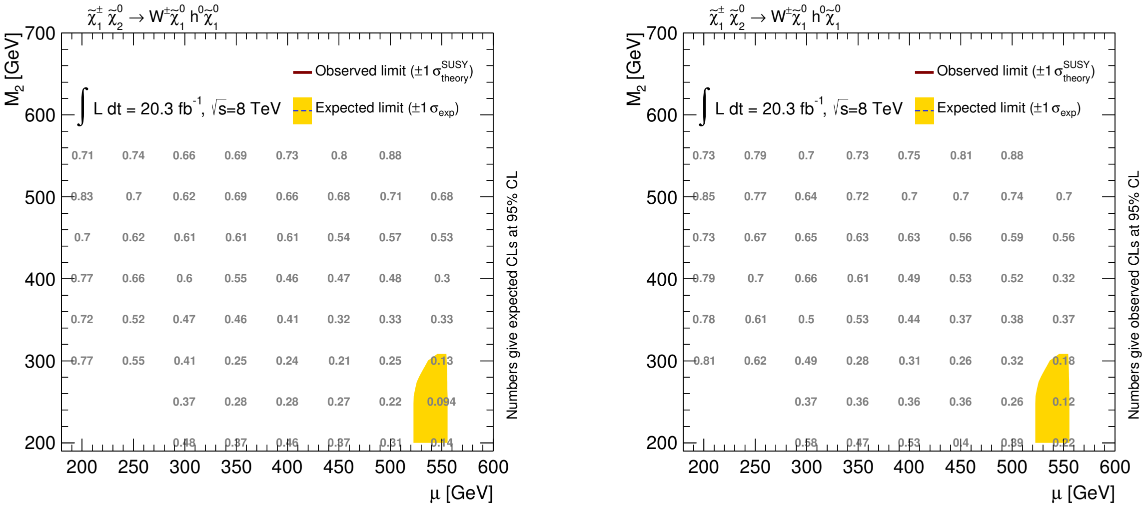

(a) Expected CL$_s$ at 95% CL.

(b) Observed CL$_s$ at 95% CL.

Figure C.17: Exclusion in the $mu - M_2$ plane for the corrected version of the analysis that uses m_{bb}^{corr}. The grey numbers indicate the expected (left) and observed (right) CL$_s$ values obtained from the model-dependent fit.

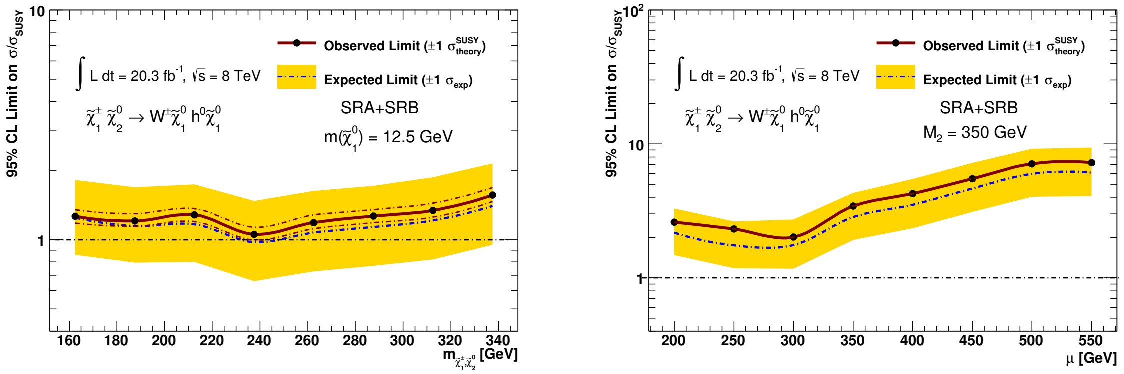

(a) Projection in the simplified model for $\tilde{\chi}_1^0 = 12.5$ GeV.

(b) Projection in the pMSSM for $\mu = 350$ GeV.

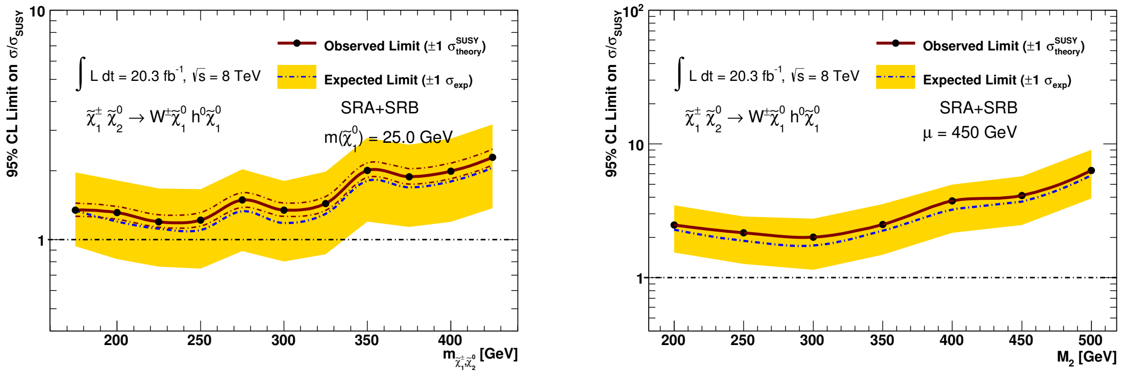

(c) Projection in the simplified model for $\tilde{\chi}_1^0 = 25$ GeV.

(d) Projection in the pMSSM for $\mu = 450$ GeV.

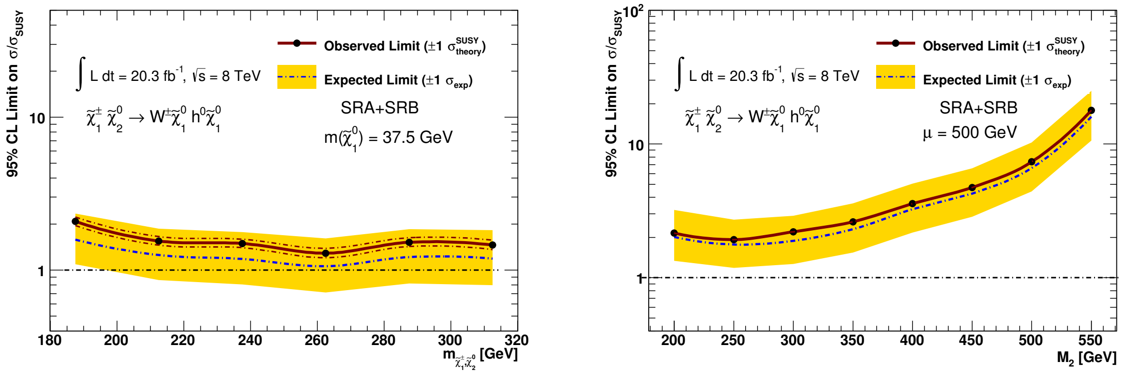

(e) Projection in the simplified model for $\tilde{\chi}_1^0 = 37.5$ GeV.

(f) Projection in the pMSSM for $\mu = 500$ GeV.

Figure C.18: Upper limits on the signal cross section normalized to the SUSY model prediction, $\sigma/\sigma^{\text{SUSY}}$ in the simplified model (left) and pMSSM (right) for different projection of the $m(\tilde{\chi}_1^0)$ and μ parameters, respectively.

Appendix D

Results of the ATLAS SUSY searches summary reinterpreted in the pMSSM

D.1 Exclusion limits from the ℓh analysis

The results of the ℓh analysis in the context of the pMSSM reinterpretation – detailed in Chapter 9 – are presented here. For each model point, the p-value p_0, expected and observed CLs are computed. The expected $\mathrm{CLs}^{\mathrm{exp}}$ has uncertainty bounds $\mathrm{CLs}^{-1\sigma}$ ($\mathrm{CLs}^{+1\sigma}$), which are obtained by varying the signal cross-section of -1σ ($+1\sigma$). The observed CLs is $\mathrm{CLs}^{\mathrm{obs}}$. Table D.1 shows the results for the sole model point with wino-like LSP while Table D.2 lists the results of the 63 pMSSM model points with a bino-like LSP.

Table D.1: Results from the exclusion fit of ℓh analysis performed for the pMSSM model point with a wino-like LSP. More details on the extracted variables in the text.

Model name	p_0	$\mathrm{CLs}^{\mathrm{exp}}$	$\mathrm{CLs}^{-1\sigma}$	$\mathrm{CLs}^{+1\sigma}$	$\mathrm{CLs}^{\mathrm{obs}}$
12381550	0.14	0.23	0.09	0.51	0.26

Table D.2: Results from the exclusion fit of ℓh analysis performed for the 63 pMSSM model points with a bino-like LSP. More details on the extracted variables in the text.

Model name	p_0	CLs$^{\text{exp}}$	CLs$^{-1\sigma}$	CLs$^{+1\sigma}$	CLs$^{\text{obs}}$
21268567	0.47	0.46	0.26	0.72	0.63
22966708	0.31	0.40	0.20	0.67	0.49
39193244	0.42	0.63	0.44	0.83	0.69
61683747	0.50	0.67	0.49	0.85	0.75
64451425	0.50	0.47	0.27	0.72	0.65
68547168	0.45	0.67	0.49	0.85	0.73
85043518	0.42	0.65	0.46	0.84	0.70
100367047	0.38	0.51	0.30	0.75	0.59
116598020	0.45	0.59	0.39	0.80	0.68
117941348	0.46	0.63	0.44	0.83	0.71
124523905	0.50	0.48	0.27	0.73	0.66
129860058	0.26	0.41	0.22	0.68	0.46
134477982	0.37	0.39	0.20	0.66	0.53
138686496	0.36	0.38	0.19	0.66	0.52
141079858	0.26	0.26	0.10	0.53	0.38
150059611	0.49	0.65	0.46	0.84	0.73
154547252	0.25	0.40	0.20	0.67	0.44
155907918	0.29	0.47	0.27	0.72	0.52
162566015	0.24	0.36	0.17	0.63	0.41
169799005	0.10	0.10	0.03	0.31	0.16
175215884	0.26	0.45	0.25	0.71	0.48
192541795	0.40	0.43	0.23	0.69	0.57
194217976	0.50	0.27	0.11	0.54	0.58
207692437	0.49	0.55	0.35	0.78	0.68
212303037	0.23	0.46	0.26	0.71	0.46
219933858	0.32	0.33	0.15	0.61	0.46
230784331	0.24	0.41	0.21	0.67	0.44
244174259	0.38	0.36	0.18	0.64	0.52
247474936	0.12	0.13	0.04	0.35	0.18
248986127	0.24	0.51	0.30	0.75	0.49
278011961	0.22	0.51	0.31	0.75	0.49

Continued on next page

Continued from previous page

Model name	p_0	$\mathrm{CLs}^{\mathrm{exp}}$	$\mathrm{CLs}^{-1\sigma}$	$\mathrm{CLs}^{+1\sigma}$	$\mathrm{CLs}^{\mathrm{obs}}$
284158078	0.16	0.22	0.08	0.49	0.27
287709877	0.17	0.19	0.06	0.44	0.27
303014332	0.42	0.40	0.21	0.67	0.57
309666028	0.50	0.59	0.39	0.81	0.71
311679864	0.21	0.30	0.13	0.57	0.35
319088156	0.30	0.37	0.18	0.64	0.46
319291200	0.27	0.34	0.16	0.61	0.42
320339638	0.32	0.32	0.15	0.60	0.45
326901592	0.24	0.26	0.10	0.53	0.36
339985460	0.50	0.81	0.68	0.92	0.84
355795643	0.42	0.42	0.23	0.69	0.58
362665045	0.33	0.31	0.14	0.59	0.46
370944698	0.41	0.62	0.42	0.82	0.68
398859326	0.33	0.52	0.31	0.76	0.56
401298695	0.50	0.67	0.49	0.85	0.75
412330086	0.27	0.47	0.26	0.72	0.50
414588510	0.11	0.13	0.04	0.36	0.18
418728841	0.23	0.29	0.13	0.57	0.37
424263145	0.27	0.51	0.31	0.75	0.52
427894273	0.27	0.48	0.28	0.73	0.51
432613790	0.50	0.71	0.54	0.87	0.78
432888422	0.22	0.39	0.20	0.66	0.41
449751773	0.30	0.36	0.18	0.64	0.46
453491214	0.38	0.50	0.29	0.74	0.59
454938790	0.28	0.28	0.12	0.56	0.40
457611219	0.33	0.27	0.11	0.54	0.44
463371753	0.43	0.58	0.38	0.80	0.66
466265931	0.25	0.16	0.05	0.41	0.33
466432540	0.42	0.48	0.28	0.73	0.61
471729364	0.28	0.36	0.17	0.63	0.44
475713692	0.33	0.25	0.10	0.52	0.43
486724955	0.42	0.45	0.25	0.71	0.59

D.2 Fraction of pMSSM model excluded by ATLAS SUSY searches

The overall fraction of model points within the pMSSM space excluded by each analysis for each of the LSP types is shown in Table D.3.

Table D.3: Fraction of models excluded (in percentage) by the individual analyses, with respect to the total number of models. More information on the listed searches can be found in the publication [97]

Analysis	All LSPs	Bino-like	Wino-like	Higgsino-like
0-lepton + 2–6 jets + $E_{\mathrm{T}}^{\mathrm{miss}}$	32.1	35.8	29.7	33.5
0-lepton + 7–10 jets + $E_{\mathrm{T}}^{\mathrm{miss}}$	7.8	5.5	7.6	8.0
0/1-lepton + 3b-jets + $E_{\mathrm{T}}^{\mathrm{miss}}$	8.8	5.4	7.1	10.1
1-lepton + jets + $E_{\mathrm{T}}^{\mathrm{miss}}$	8.0	5.4	7.5	8.4
Monojet	9.9	16.7	9.1	10.1
SS/3-leptons + jets + $E_{\mathrm{T}}^{\mathrm{miss}}$	2.4	1.6	2.4	2.5
$tau(\tau/\ell)$ + jets + $E_{\mathrm{T}}^{\mathrm{miss}}$	3.0	1.3	2.9	3.1
0-lepton stop	9.4	7.8	8.2	10.2
1-lepton stop	6.2	2.9	5.4	6.8
2b-jets + $E_{\mathrm{T}}^{\mathrm{miss}}$	3.1	3.3	2.3	3.6
2-leptons stop	0.8	1.1	0.8	0.7
Monojet stop	3.5	11.3	2.8	3.6
Stop with Z boson	0.4	1.0	0.4	0.5
tb+$E_{\mathrm{T}}^{\mathrm{miss}}$, stop	4.2	1.9	3.1	5.0
ℓh, electroweak	0.0	0.0	0.0	0.0
2-leptons, electroweak	1.3	2.2	0.7	1.6
2-τ, electroweak	0.2	0.3	0.2	0.2
3-leptons, electroweak	0.8	3.8	1.1	0.6
4-leptons	0.5	1.1	0.6	0.5
Disappearing Track	11.4	0.4	29.9	0.1
Long-lived particle	0.1	0.1	0.0	0.1
$H/A \to \tau^+\tau^-$	1.8	2.2	0.9	2.4
Total	40.9	40.2	45.4	38.1

Bibliography

[1] S. Glashow, "Partial-symmetries of weak interactions," *Prog. Theor. Phys.*, vol. 22, pp. 579–588, 1961.

[2] S. Weinberg, "A model of leptons," *Phys. Rev. Lett.*, vol. 19, pp. 1264–1266, 1967.

[3] A. Salam, "Weak and electromagnetic interactions," in *Proceedings of the 8th Nobel Symposium - Elementary Particle Theory: relativistic groups and analyticity, Aspenäsgøarden, Sweden, 19-25 May 1968* (N. Svartholm, ed.), (Stockholm), pp. 367–372, Almquist and Wiksells, 1969.

[4] K. A. Olive *et al.*, "Review of Particle Physics," *Chin. Phys.*, vol. C38, p. 090001, 2014.

[5] F. Englert and R. Brout, "Broken Symmetry and the Mass of Gauge Vector Mesons," *Phys. Rev. Lett.*, vol. 13, pp. 321–323, 1964.

[6] P. W. Higgs, "Broken symmetries, massless particles and gauge fields," *Phys. Lett.*, vol. 12, pp. 132–133, 1964.

[7] P. W. Higgs, "Broken Symmetries and the Masses of Gauge Bosons," *Phys. Rev. Lett.*, vol. 13, pp. 508–509, 1964.

[8] W. Commons, "Standard model of particle physics, most complete diagram by latham boyle," 2014.

[9] S. P. Martin, "A Supersymmetry primer," 2011. [Adv. Ser. Direct. High Energy Phys.18,1(1998)].

[10] V. C. Rubin, N. Thonnard, and W. K. Ford, Jr., "Rotational properties of 21 SC galaxies with a large range of luminosities and radii, from NGC 4605 /R = 4kpc/ to UGC 2885 /R = 122 kpc/," *Astrophys. J.*, vol. 238, p. 471, 1980.

[11] K. G. Begeman, A. H. Broeils, and R. H. Sanders, “Extended rotation curves of spiral galaxies: Dark haloes and modified dynamics,” *Mon. Not. Roy. Astron. Soc.*, vol. 249, p. 523, 1991.

[12] G. Bertone, D. Hooper, and J. Silk, “Particle dark matter: Evidence, candidates and constraints,” *Phys. Rept.*, vol. 405, pp. 279–390, 2005.

[13] H. Miyazawa, “Baryon Number Changing Currents,” *Prog. Theor. Phys.*, vol. 36, pp. 1266–1276, 1966.

[14] P. Ramond, “Dual Theory for Free Fermions,” *Phys. Rev.*, vol. D3, pp. 2415–2418, 1971.

[15] Y. Gol’fand and E. Likhtman, “Extension of the Algebra of Poincare Group Generators and Violation of p Invariance,” *JETP Lett.*, vol. 13, pp. 323–326, 1971.

[16] A. Neveu and J. Schwarz, “Factorizable dual model of pions,” *Nucl. Phys.*, vol. B31, pp. 86–112, 1971.

[17] A. Neveu and J. Schwarz, “Quark Model of Dual Pions,” *Phys. Rev.*, vol. D4, pp. 1109–1111, 1971.

[18] D. Volkov and V. Akulov, “Is the Neutrino a Goldstone Particle?,” *Phys. Lett.*, vol. B46, pp. 109–110, 1973.

[19] J. Wess and B. Zumino, “A Lagrangian Model Invariant Under Supergauge Transformations,” *Phys. Lett.*, vol. B49, p. 52, 1974.

[20] J. Wess and B. Zumino, “Supergauge Transformations in Four-Dimensions,” *Nucl. Phys.*, vol. B70, pp. 39–50, 1974.

[21] S. R. Coleman and J. Mandula, “All Possible Symmetries of the S Matrix,” *Phys. Rev.*, vol. 159, pp. 1251–1256, 1967.

[22] R. Haag, J. T. Lopuszanski, and M. Sohnius, “All Possible Generators of Supersymmetries of the s Matrix,” *Nucl. Phys.*, vol. B88, p. 257, 1975.

[23] S. Dimopoulos and H. Georgi, “Softly Broken Supersymmetry and SU(5),” *Nucl. Phys.*, vol. B193, p. 150, 1981.

[24] H. H. et al, “Supersymmetry, part i (theory),” *Journal of Physics*, vol. G 33, 2009.

[25] “Running coupling constants.” `http://www.nobelprize.org/nobel_prizes/physics/laureates/2004/popular.html`.

[26] G. Jungman, M. Kamionkowski, and K. Griest, “Supersymmetric dark matter,” *Phys. Rept.*, vol. 267, pp. 195–373, 1996.

[27] L. Evans *et al.*, *The Large Hadron Collider: a Marvel of Technology.* 2009.

[28] L. Evans and P. Bryant, “LHC Machine,” *JINST*, vol. 3, p. S08001, 2008.

[29] F. Marcastel, “CERN's Accelerator Complex. La chane des acclrateurs du CERN,” Oct 2013. General Photo.

[30] R. Alemany-Fernandez, E. Bravin, L. Drosdal, A. Gorzawski, V. Kain, M. Lamont, A. Macpherson, G. Papotti, M. Pojer, L. Ponce, S. Redaelli, G. Roy, M. Solfaroli Camillocci, W. Venturini, and J. Wenninger, “Operation and Configuration of the LHC in Run 1,” Nov 2013.

[31] ATLAS Collaboration, “ATLAS Luminosity Public Results.” `https://twiki.cern.ch/twiki/bin/view/AtlasPublic/LuminosityPublicResults`.

[32] ATLAS Collaboration, “The ATLAS Experiment at the CERN Large Hadron Collider,” *JINST*, vol. 3, p. S08003, 2008.

[33] W. Lampl *et al.*, “Calorimeter clustering algorithms: Description and performance,” Tech. Rep. ATL-LARG-PUB-2008-002, CERN, April 2008.

[34] ATLAS Collaboration, “Electron reconstruction and identification efficiency measurements with the ATLAS detector using the 2011 LHC proton-proton collision data,” *Eur. Phys. J.*, vol. C74, no. 7, p. 2941, 2014.

[35] ATLAS Collaboration, “Measurement of the muon reconstruction performance of the ATLAS detector using 2011 and 2012 LHC proton-proton collision data,” *Eur. Phys. J. C*, vol. 74, p. 3130, 2014.

[36] ATLAS Collaboration, “Expected Performance of the ATLAS Experiment - Detector, Trigger and Physics,” 2009.

[37] M. Cacciari, G. P. Salam, and G. Soyez, "The Anti-k(t) jet clustering algorithm," *JHEP*, vol. 04, p. 063, 2008.

[38] ATLAS Collaboration, "Jet energy measurement with the ATLAS detector in proton-proton collisions at $\sqrt{s} = 7$ TeV," *Eur. Phys. J.*, vol. C73, no. 3, p. 2304, 2013.

[39] ATLAS Collaboration, "Jet energy measurement and its systematic uncertainty in proton-proton collisions at $\sqrt{s} = 7$ TeV with the ATLAS detector," *Eur. Phys. J.*, vol. C75, p. 17, 2015.

[40] ATLAS Collaboration, "Jet energy resolution in proton-proton collisions at $\sqrt{s} = 7$ TeV recorded in 2010 with the ATLAS detector," *Eur. Phys. J.*, vol. C73, no. 3, p. 2306, 2013.

[41] A. Heister *et al.*, "Study of the fragmentation of b quarks into B mesons at the Z peak," *Phys. Lett.*, vol. B512, pp. 30–48, 2001.

[42] "Commissioning of the ATLAS high-performance b-tagging algorithms in the 7 TeV collision data," Tech. Rep. ATLAS-CONF-2011-102, CERN, Geneva, Jul 2011.

[43] "b-tagging in dense environments," Tech. Rep. ATL-PHYS-PUB-2014-014, CERN, Geneva, Aug 2014.

[44] G. Piacquadio and C. Weiser, "A new inclusive secondary vertex algorithm for b-jet tagging in ATLAS," *J. Phys. Conf. Ser.*, vol. 119, p. 032032, 2008.

[45] "Measurement of the b-tag Efficiency in a Sample of Jets Containing Muons with 5 fb^{-1} of Data from the ATLAS Detector," Tech. Rep. ATLAS-CONF-2012-043, CERN, Geneva, Mar 2012.

[46] ATLAS Collaboration, "Performance of missing transverse momentum reconstruction in proton-proton collisions at 7 TeV with ATLAS," *Eur. Phys. J. C*, vol. 72, p. 1844, 2012.

[47] ATLAS Collaboration, "Performance of Missing Transverse Momentum Reconstruction in ATLAS studied in Proton-Proton Collisions recorded in 2012 at 8 TeV," *ATLAS-CONF-2013-082*.

[48] ATLAS Collaboration, “Missing transverse energy performance in 2012 data.” `https://twiki.cern.ch/twiki/bin/view/AtlasPublic/JetEtmissApproved2013EtMiss`, 2013.

[49] ATLAS Collaboration, “How to clean jets.” `https://twiki.cern.ch/twiki/bin/view/AtlasProtected/HowToCleanJets`, 2011.

[50] ATLAS Collaboration, “Summary of the searches for squarks and gluinos using $\sqrt{s} = 8$ TeV pp collisions with the ATLAS experiment at the LHC,” 2015.

[51] H. Baer, V. Barger, S. Kraml, A. Lessa, W. Sreethawong, and X. Tata, “WZ plus missing-E_T signal from gaugino pair production at LHC7,” *JHEP*, vol. 03, p. 092, 2012.

[52] ATLAS Collaboration, “Search for Chargino and Neutralino Production in Final States with One Lepton, Two b-jets Consistent with a Higgs Boson, and Missing Transverse Momentum with the ATLAS detector in 20.3 fb^{-1} of $\sqrt{s} = 8$ TeV pp collisions,” Tech. Rep. ATL-COM-PHYS-2013-1640, 2014.

[53] ATLAS Collaboration, “Search for direct pair production of a chargino and a neutralino decaying to the 125 GeV Higgs boson in $\sqrt{s} = 8$ TeV pp collisions with the ATLAS detector,” *Eur.Phys.J.*, vol. C 75, no. 5, p. 208, 2015.

[54] W. Beenakker, R. Hopker, and M. Spira, “PROSPINO: A program for the production of supersymmetric particles in next-to-leading order QCD, hep-ph/9611232,” 1996.

[55] GEANT4 Collaboration, S. Agostinelli, *et al.*, “GEANT4: A simulation toolkit,” *Nucl. Instrum. Meth. A*, vol. 506, p. 250, 2003.

[56] ATLAS Collaboration, “The simulation principle and performance of the atlas fast calorimeter simulation fastcalosim,” *ATL-PHYS-PUB-2010-013*, 2010.

[57] M. Bahr *et al.*, “Herwig++ Physics and Manual,” *Eur. Phys. J. C*, vol. 58, p. 639, 2008.

[58] A. Djouadi, L. Maiani, A. Polosa, J. Quevillon, and V. Riquer, “Fully covering the MSSM Higgs sector at the LHC,” *JHEP*, vol. 06, p. 168, 2015.

[59] B. P. Kersevan and E. Richter-Was, “The Monte Carlo event generator AcerMC versions 2.0 to 3.8 with interfaces to PYTHIA 6.4, HERWIG 6.5 and ARIADNE 4.1,” *Comput. Phys. Commun.*, vol. 184, p. 919, 2013. Version 38.

[60] T. Sjöstrand, S. Mrenna, and P. Z. Skands, “PYTHIA 6.4 Physics and Manual,” *J. High Energy Phys.*, vol. 05, p. 026, 2006. Version 6.426.

[61] N. Kidonakis, “Next-to-next-to-leading-order collinear and soft gluon corrections for t-channel single top quark production,” *Phys. Rev. D*, vol. 83, p. 091503, 2011.

[62] ATLAS Collaboration, “ATLAS tunes of PYTHIA 6 and Pythia 8 for MC11,” *ATL-PHYS-PUB-2011-009*, 2011.

[63] J. Pumplin *et al.*, “New generation of parton distributions with uncertainties from global QCD analysis,” *J. High Energy Phys.*, vol. 07, p. 012, 2002.

[64] P. Nason, “A New method for combining NLO QCD with shower Monte Carlo algorithms,” *J. High Energy Phys.*, vol. 11, p. 040, 2004. Version r1556.

[65] S. Frixione, P. Nason, and C. Oleari, “Matching NLO QCD computations with Parton Shower simulations: the POWHEG method,” *J. High Energy Phys.*, vol. 11, p. 070, 2007.

[66] N. Kidonakis, “NNLL resummation for s-channel single top quark production,” *Phys. Rev. D*, vol. 81, p. 054028, 2010.

[67] P. Z. Skands, “Tuning Monte Carlo Generators: The Perugia Tunes,” *Phys. Rev. D*, vol. 82, p. 074018, 2010.

[68] H.-L. Lai *et al.*, “New parton distributions for collider physics,” *Phys. Rev. D*, vol. 82, p. 074024, 2010.

[69] N. Kidonakis, “Two-loop soft anomalous dimensions for single top quark associated production with a W- or H-,” *Phys. Rev. D*, vol. 82, p. 054018, 2010.

[70] M. Cacciari *et al.*, “Top-pair production at hadron colliders with next-to-next-to-leading logarithmic soft-gluon resummation,” *Phys. Lett. B*, vol. 710, p. 612, 2012.

[71] P. Baernreuther, M. Czakon, and A. Mitov, "Percent Level Precision Physics at the Tevatron: First Genuine NNLO QCD Corrections to $q\bar{q} \to t\bar{t} + X$," *Phys. Rev. Lett.*, vol. 109, p. 132001, 2012.

[72] M. Czakon and A. Mitov, "NNLO corrections to top-pair production at hadron colliders: the all-fermionic scattering channels," *J. High Energy Phys.*, vol. 12, p. 054, 2012.

[73] M. Czakon and A. Mitov, "NNLO corrections to top pair production at hadron colliders: the quark-gluon reaction," *J. High Energy Phys.*, vol. 01, p. 080, 2013.

[74] M. Czakon, P. Fiedler, and A. Mitov, "The total top quark pair production cross-section at hadron colliders through $O(\alpha_S^4)$," *Phys. Rev. Lett.*, vol. 110, p. 252004, 2013.

[75] M. Czakon and A. Mitov, "Top++: A Program for the Calculation of the Top-Pair Cross-Section at Hadron Colliders," *Comput. Phys. Commun.*, vol. 185, p. 2930, 2014.

[76] J. Alwall *et al.*, "MadGraph/MadEvent v4: The New Web Generation," *J. High Energy Phys.*, vol. 09, p. 028, 2007. Version 1.5.2.

[77] T. Gleisberg *et al.*, "Event generation with SHERPA 1.1," *J. High Energy Phys.*, vol. 02, p. 007, 2009. Version 1.4.1.

[78] T. Sjöstrand, S. Mrenna, and P. Z. Skands, "A Brief Introduction to PYTHIA 8.1," *Comput. Phys. Commun.*, vol. 178, p. 852, 2008. Version 8.160.

[79] LHC Higgs Cross Section Working Group, S. Heinemeyer, *et al.*, "Handbook of LHC Higgs Cross Sections: 3. Higgs Properties," 2013.

[80] ATLAS Collaboration, "Summary of ATLAS Pythia 8 tunes," *ATL-PHYS-PUB-2012-003*, 2012.

[81] D. R. Tovey, "On measuring the masses of pair-produced semi-invisibly decaying particles at hadron colliders," *J. High Energy Phys.*, vol. 04, p. 034, 2008.

[82] G. Polesello and D. R. Tovey, "Supersymmetric particle mass measurement with the boost-corrected contransverse mass," *J. High Energy Phys.*, vol. 03, p. 030, 2010.

[83] M. Oreglia, "A Study of the Reactions $\psi' \to \gamma\gamma\psi$," *SLAC-R-0236*, 1980.

[84] ATLAS Collaboration, "Measurement of the top quark-pair production cross section with ATLAS in pp collisions at $\sqrt{s} = 7$ TeV," *Eur. Phys. J.*, vol. C71, p. 1577, 2011.

[85] A. Ismail, R. Schwienhorst, J. S. Virzi, and D. G. E. Walker, "Deconstructed Transverse Mass Variables," *Phys. Rev.*, vol. D91, no. 7, p. 074002, 2015.

[86] ATLAS Collaboration, "Search for the $b\bar{b}$ decay of the Standard Model Higgs boson in associated $(W/Z)H$ production with the ATLAS detector," *JHEP*, vol. 01, p. 069, 2015.

[87] ATLAS Collaboration, "Improved luminosity determination in pp collisions at $\sqrt{s} = 7$ TeV using the ATLAS detector at the LHC," *Eur. Phys. J. C*, vol. 73, p. 2518, 2013.

[88] ATLAS Collaboration, "Electron and photon energy calibration with the ATLAS detector using LHC Run 1 data," *Eur. Phys. J.*, vol. C74, no. 10, p. 3071, 2014.

[89] ATLAS Collaboration, "Muon reconstruction efficiency and momentum resolution of the ATLAS experiment in proton-proton collisions at $\sqrt{s} = 7$ TeV in 2010," *Eur. Phys. J.*, vol. C74, no. 9, p. 3034, 2014.

[90] G. Cowan, K. Cranmer, E. Gross, and O. Vitells, "Asymptotic formulae for likelihood-based tests of new physics," *Eur. Phys. J.*, vol. C71, p. 1554, 2011. [Erratum: Eur. Phys. J.C73,2501(2013)].

[91] A. L. Read, "Presentation of search results: the cl s technique," *Journal of Physics G: Nuclear and Particle Physics*, vol. 28, no. 10, p. 2693, 2002.

[92] M. Baak, G. J. Besjes, D. Cte, A. Koutsman, J. Lorenz, and D. Short, "HistFitter software framework for statistical data analysis," *Eur. Phys. J.*, vol. C75, p. 153, 2015.

[93] S. S. Wilks, "The Large-Sample Distribution of the Likelihood Ratio for Testing Composite Hypotheses," *Annals Math. Statist.*, vol. 9, no. 1, pp. 60–62, 1938.

[94] A. Wald, “Tests of Statistical Hypotheses Concerning Several Parameters When the Number of Observations is Large,” *Transactions of the American Mathematical Society*, vol. 54, no. 3, pp. 426–482, 1943.

[95] ATLAS Collaboration, “Search for direct production of charginos, neutralinos and sleptons in final states with two leptons and missing transverse momentum in pp collisions at $\sqrt{s} = 8$ TeV with the ATLAS detector,” *JHEP*, vol. 05, p. 071, 2014.

[96] ATLAS Collaboration, “Search for direct production of charginos and neutralinos in events with three leptons and missing transverse momentum in $\sqrt{s} =$ 8TeV pp collisions with the ATLAS detector,” *JHEP*, vol. 04, p. 169, 2014.

[97] ATLAS Collaboration, “Summary of the ATLAS experiment’s sensitivity to supersymmetry after LHC Run 1 interpreted in the phenomenological MSSM,” *JHEP*, vol. 10, p. 134, 2015.

[98] ATLAS Collaboration, “Search for direct production of charginos, neutralinos and sleptons in final states with two leptons and missing transverse momentum in pp collisions at $\sqrt{s} = 8$ TeV with the ATLAS detector,” *JHEP*, vol. 05, p. 071, 2014.

[99] CMS Collaboration, “Searches for electroweak neutralino and chargino production in channels with Higgs, Z, and W bosons in pp collisions at 8 TeV,” *Phys. Rev.*, vol. D90, no. 9, p. 092007, 2014.

[100] “CERN Courier Volume 55, Number 9, November 2015,” 2015.

[101] S. A. Stucci, M. Weber, T. Lari, and F. Meloni, “Prospect for a search for direct pair production of a chargino and a neutralino decaying via a W boson and the lightest Higgs boson in final states with one lepton, two b-jets and missing transverse momentum at the high luminosity LHC with the ATLAS detector,” Tech. Rep. ATL-COM-PHYS-2015-838, CERN, Geneva, Aug 2015.

[102] N. e. a. Buchanan, “Design and implementation of the Front End Board for the readout of the ATLAS liquid argon calorimeters,” *JINST*, vol. 3, 2010.

[103] A. e. a. Bazan, “ATLAS liquid argon calorimeter back end electronics (RODs),” *JINST*, vol. 2, 2007.

[104] W. E. Cleland and E. Stern, "Signal Processing Considerations for Liquid Ionization Calorimeters in a High Rate Environment," *Nucl. Instrum. Methods*, vol. A, pp. 467–497, 1994.

[105] ATLAS Collaboration, "Monitoring and data quality assessment of the ATLAS liquid argon calorimeter," *JINST*, vol. 9, p. P07024, 2014.

[106] C. D. White, "Single Top Production in the Wt mode with MC@NLO," pp. 197–200, 2009.

[107] ATLAS Collaboration, "Search for squarks and gluinos using final states with jets and missing transverse momentum with the ATLAS experiment in $\sqrt{s} = 8$ TeV proton-proton collisions: supporting documentation," Tech. Rep. ATL-PHYS-INT-2012-063, CERN, Geneva, Sep 2012.

[108] ATLAS Collaboration, "Heavy Flavor Overlap Removal Tool." `https://twiki.cern.ch/twiki/bin/viewauth/AtlasProtected/HforTool`.